Development of NMR Tools to Investigate Aggregation Phenomena

Rebecca Emily Joyce

Submitted for the qualification of PhD

University of Sussex

May 2013

University of Sussex

Rebecca Emily Joyce

Thesis submitted for the qualification of PhD

Development of NMR Tools to Investigate Aggregation Phenomena

Summary

Chemistry and biology are full of examples of aggregation phenomena; from the useful applications in drug molecule stabilisation and tissue engineering, to the negative effects of causing diseases such as Alzheimer's and Parkinson's. NMR is a useful tool for probing aggregation as it can provide detail at the atomic scale; however, the molecular size of the aggregates can lead to poor resolution and spectral broadening, issues which require some development to solve. The research detailed in this thesis aims to develop NMR tools to investigate aggregation phenomena from two angles; firstly, to directly monitor aggregation using diffusion-ordered NMR spectroscopy and secondly to probe the effects of aggregates on biomimetic constructs using NMR techniques.

To achieve the first aim, diffusion-ordered NMR Spectroscopy in conjunction with a size-exclusion chromatography stationary phase was developed for the purpose of monitoring aggregation in a time-resolved manner. The size-exclusion stationary phases, commonly used to separate molecules of different sizes, such as proteins from salts, in liquid chromatography methods, provide an additional perturbation of the diffusion profile of molecules of different sizes when added to NMR samples for diffusion-ordered spectroscopy analysis. The development of this method and a selection of applications are detailed within two chapters of the thesis. These studies have been published in Journal of Magnetic Resonance[i] and Journal of Physical Chemistry C[ii].

A complementary study of the interactions between aggregates and biological structures such as biomimetic cell membranes using NMR methods such as time-resolved ^{31}P NMR and the implementation of paramagnetic shift reagents is discussed in the final two chapters. Changes in chemical shift caused by additional interactions between the shift reagent and the solvent are fully investigated and the method is applied to the study of membrane permeation by amyloid-β oligomers.

[i] R. E. Joyce and I. J. Day, *J. Magn. Reson.*, 2012, **220**, 1–7.
[ii] R. E. Joyce and I. J. Day, *J. Phys. Chem. C.*, 2013, **117**, 17503–17508.

Acknowledgements

I would first like to sincerely thank my supervisor, Dr Iain Day, for giving me the opportunity to perform the research detailed in this thesis and for the support and encouragement over the last three and a half years, as well as the multitude of corrections during the preparation of the thesis!

I would also like to thank all members of the Day group, past and present, especially Matt Renshaw for providing tips on sunset yellow purification and assistance in the creation of the pulse sequence figures and Jonathan Katz for several patient explanations of how the sunset yellow absorption coefficient was determined.

Much of the work involving Aβ could not have been done without the advice and expertise of my secondary supervisor, Professor Louise Serpell and members of her group, I greatly appreciate all of their assistance. In particular, Dr Tom Williams for teaching me the vesicle preparation and wash protocols, answering all sorts of questions regarding vesicle stability and acquiring some of the fluorescence data presented in the thesis. Also, Youssra Al-Hilaly for help with the preparation of Aβ and of samples for TEM imaging. On a related note, I would like to acknowledge the assistance of Dr Julian Thorpe on the acquisition of TEM images, also Dr Darren Thompson for the loan of an SEC column and Devyani Amin and Joanna Thorpe at the University of Greenwich for assistance in acquiring SEC data.

Thanks must also go to all those who I have shared an office with over the three years, for providing interesting conversations, entertaining pub Fridays and amazing cakes. Especially Laura Nicholls, who ran the Marathon des Sables while I was writing this thesis and inspired me to get on with it, because writing couldn't be half as bad as running through the desert all day!

In concluding these acknowledgements I need to thank my family and closest friends for all of their continuous support, despite not really understanding what my research was about. Finally, I would like to thank Gareth for the love and support throughout my PhD, particularly during the write-up process.

Contents

List of Figures

List of Tables

List of Abbreviations

Chemicals

Aβ	Amyloid-β peptide
HEPES	(4-(2-hydroxyethyl)-1-piperazineethanesulphonic acid)
(h)IAPP	(human)Islet Amyloid PolyPeptide
MTSL	(1-oxyl-2,2,5,5-tetramethylpyrroline-3-methyl)-methanesulphonate
NiEDDA	Nickel(II)-ethylenediamine-N,N′-diacetic acid
SSY	Sunset Yellow FCF
ThT	Thioflavin T
Tris	Tris(hydroxymethyl)aminomethane

Lipids

DMPC	1,2-dimyristoyl-sn-glycero-3-phosphocholine
DOPA	1,2-dioleoyl-sn-glycero-3-phosphate
DOPE	1,2-dioleoyl-sn-glycero-3-phosphoethanolamine
POPC	1-palmitoyl-2-oleoyl-sn-glycero-3-phosphocholine
POPG	1-palmitoyl-2-oleoyl-sn-glycero-3-phospho-glycerol
POPS	1-palmitoyl-2-oleoyl-sn-glycero-3-phospho-L-serine

Polymers

Poly(nipam) / Pnipam	Poly(*N*-isopropyl acrylamide)
Poly(allylamine) / Poly(aa) / Paa	Poly(allylamine hydrochloride)
PSS	Poly(stryene-4-sulphonate)

Techniques and Other Abbreviations

COSY	Correlation Spectroscopy
CSA	Chemical Shift Anisotropy
CTP	Coherence Transfer Pathway
DLS	Dynamic Light Scattering
DOSY	Diffusion-Ordered Spectroscopy
DSC	Differential Scanning Calorimetry
EPR	Electron Paramagnetic Resonance
GUV	Giant Unilamellar Vesicle
LUV	Large Unilamellar Vesicle
MAS	Magic Angle Spinning
MLV	Multi-Lamellar Vesicle
MW	Molecular Weight
NMR	Nuclear Magnetic Resonance
PFG	Pulsed Field Gradient
POC	Proof of Concept
SDSL	Site-Directed Spin Labelling
SEC	Size-Exclusion Chromatography
SEC-DOSY	Size-Exclusion Chromatography–Diffusion-Ordered Spectroscopy
SUV	Small Unilamellar Vesicle
TEM	Transmission Electron Microscopy

Chapter 1

Introduction

Aggregation phenomena are prevalent in a variety of chemical and biological situations. This thesis approaches the study of aggregation from two angles, firstly the direct analysis of aggregation using diffusion-ordered NMR spectroscopy and secondly the observation of the effects of aggregates on biomimetic membranes using NMR experiments.

In this chapter the importance of studying aggregation will be highlighted by a review of the broad range of aggregate systems and the established methods of investigation. This will be followed by a brief description of the basic theory of NMR and a full discussion of the main methods utilised in this thesis, diffusion-ordered spectroscopy and paramagnetic shift reagents. The application of NMR methods to aggregate systems will then be discussed in more detail. The investigation of interactions between aggregates and biomimetic membranes is the second topic of this research; this will be introduced by a discussion of model membrane systems and established methods for studying aggregate-membrane interactions. This chapter will be concluded with an outline of the remainder of the thesis.

1.1 Aggregation Phenomena

Aggregation is the self-association of molecules into large non-covalently bonded assemblies[1] and is important in several areas of chemistry and biology. Examples of molecules which exhibit aggregation behaviour include proteins,[2] aromatic drug[3] and dye[4] molecules and some polymers.[5] The consequences of aggregation can be positive or negative depending on the system in which the aggregation is observed, a selection of aggregate systems will be reviewed here.

1.1.1 Aromatic Molecules

A range of molecules with extended aromatic ring systems, including dye[4] and drug molecules,[3] have been shown to self-assemble into columnar aggregates in solution. These molecules are typically characterised by rigid, planar, multi-ring aromatic systems with solubilising functional groups around the edge,[6] examples include several dye molecules (e.g. sunset yellow,[7] bordeaux dye[8] and acid red[9]) and drug molecules (e.g. antiasthmatic drug disodium cromoglycate (DSCG) and antiallergic drug RU31156),[6] the structures of which are shown in Figure 1.1. Other examples include nucleic acids and antibiotics.[10]

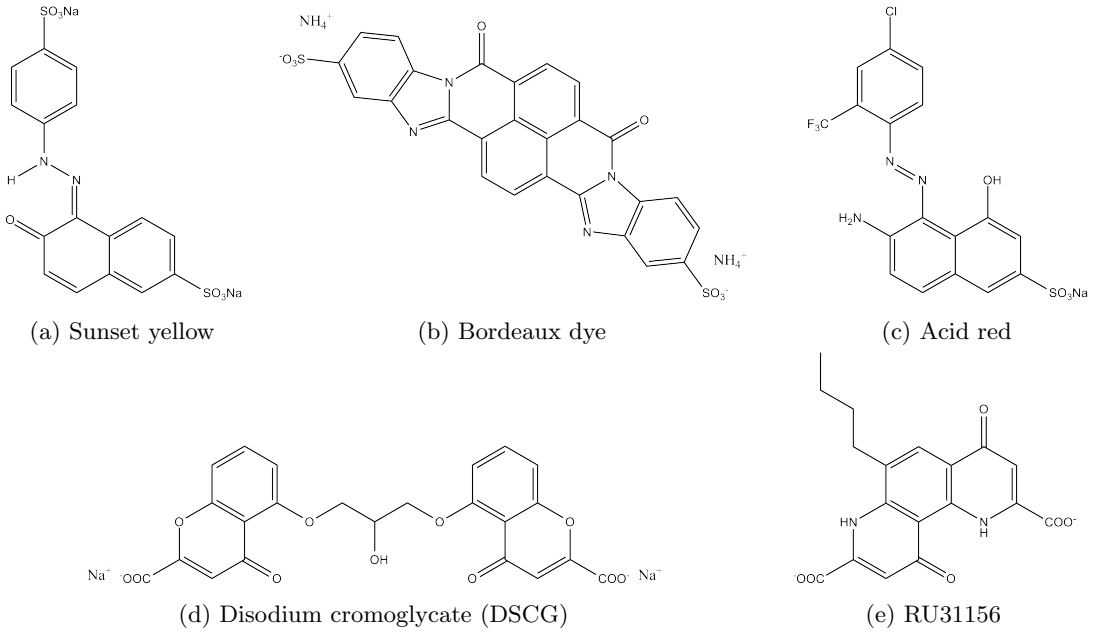

(a) Sunset yellow (b) Bordeaux dye (c) Acid red

(d) Disodium cromoglycate (DSCG) (e) RU31156

Figure 1.1: Structures of chromonic molecules. Dye molecules: a)-c), drug molecules: d) and e).

The columnar aggregates are stabilised by '$\pi - \pi$' interactions due to the parallel alignment of the π electron clouds either side of the aromatic ring,[6] the nature of these interactions have been described by Hunter and Sanders[11] as predominantly van der Waals interactions with $\pi - \sigma$ electrostatic attraction determining the geometry of the association. Aggregation of the molecules into columns is also facilitated by the reduction of the hydrophobic surface area in contact with the aqueous solution on aggregation.[10] Some of these aggregate systems undergo further association to form liquid crystal mesophases, described as chromonic phases.[12] Chromonic liquid crystalline phases are a type of lyotropic liquid crystal as they are both concentration and temperature dependent. There are two common chromonic mesophases, the nematic (N) phase is characterised by roughly parallel alignment of the columnar aggregates without any positional or orientational order, while the M phase is a hexagonal arrangement of the columns with long-range order.[13] Figure 1.2 shows diagrams of the positional and orientational order of molecule in the isotropic, nematic and hexagonal phases.

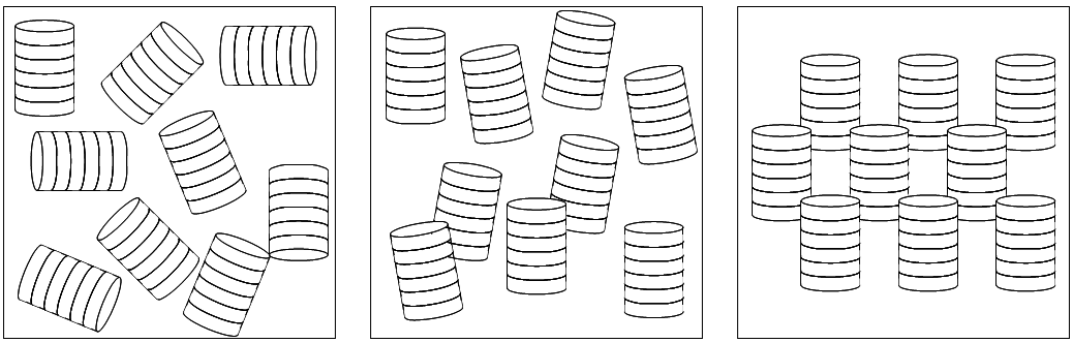

(a) Isotropic Solution (b) Nematic (N) Phase (c) Hexagonal (M) Phase

Figure 1.2: Schematic of phases of chromonic liquid crystals

There are a wide range of potential applications for aggregates which form chromonic mesophases,[12,14] including solar cells,[15] biosensors[12] and nanotubes.[14,16]

1.1.1.1 Methods of Investigation

The concentration and temperature dependent aggregation of aromatic molecules into $\pi - \pi$ stacked columns and onwards into chromonic mesophases has been studied using UV/Vis spectroscopy, NMR and X-ray diffraction.

X-ray scattering/diffraction studies of a range of chromonic liquid crystals provided evidence of columnar stacks, typically with a concentration independent repeat distance of 3.4 Å between the molecules.[17] Additional concentration dependent reflections in the diffraction patterns of the N and M mesophases were attributed to the spacings between the columnar aggregates.[8,18] Further analysis of X-ray data provided estimates for the cross-sectional area of the aggregate, typically 1–3 molecule areas.[17,19]

UV/Vis spectroscopy has frequently been used to study chromonic dye systems such as bordeaux dye,[8] sunset yellow[7] and acid red.[9,20] The absorption spectrum is affected by aggregation[17] typically displaying a decrease in absorption coefficient along with a shift in wavelength of the maximum absorption, consistent with exciton theory of coupling between molecules.[8] The decrease in absorption coefficient with increasing concentration can be used to determine the 'stacking free energy change', i.e. the free energy of a molecule in solution relative to that of a molecule in an aggregate, of a chromonic system.[8] This value is indicative of the propensity of the system to form aggregates, for example the 'stacking free energy changes' are 9.2 k_BT and 7.2 k_BT for bordeaux dye and sunset yellow respectively, the higher value for bordeaux dye is reflected in the formation of aggregates at a lower concentration.[8]

NMR was utilised in the studies of the azo dyes sunset yellow,[21–23] acid red[9] and orange II.[4] In these studies aggregation was monitored through changes in chemical shift and diffusion coefficients, as will be discussed in detail in section 1.3. The chemical shift values were also used to determine the relative orientation of molecules within the stacks, both orange II and sunset yellow were shown to stack in an antiparallel or 'head-to-tail' configuration,[4,21] whereas an ^{19}F NMR study of the CF_3 group of acid red, in combination with UV/Vis results, indicated a 50° twist between molecules such that the CF_3 substituent of the phenyl ring is located above the phenyl ring of the neighbouring molecule.

1.1.2 Drug Molecules

Many drug molecules are amphiphilic, i.e. contain both hydrophobic and hydrophilic groups, which leads to aggregation of the molecules in aqueous solution.[24] In the literature there are two descriptions of drug molecule aggregation, for amphiphilic molecules without extended aromatic systems the molecules aggregate into micelle formations, whereas molecules with large aromatic ring systems tend to form aggregate stacks through $\pi - \pi$ interactions, as described above.

The study of the self-association of drug molecules which aggregate by π-stacking is important because these molecules are also able to bind to DNA by intercalation.[3] Nucleic acids (e.g. DNA and RNA) are suggested to be liquid crystalline due to their flexibility in winding and unwinding, coupled with the inherent order of the system, DNA can be regarded as a mesogenic side chain polymer, where a chromonic stack of the base pairs is held together by the sugar-phosphate chains.[10] Co-solubilisation of chromonic compounds leads to stacks containing a mixture of both compounds rather than separate stacks of each compound,[12] this miscibility facilitates the intercalation of chromonic drug compounds between the bases of DNA. Studying the self-association of drug

molecules provides a better understanding of the mechanisms of interactions between drug molecules and nucleic acids,[3] thus elucidating the mechanism of action for this class of drug molecules.

The aggregation of drug molecules has consequences for the bioavailability of the drug.[25] The adsorption of a range of non-nucleoside reverse transcriptase inhibitors (NNRTIs), a class of anti-AIDS drugs, has been shown to be related to the size of the aggregate, which is determined by the concentration of the drug molecule and the pH of the system.

In some cases aggregation provides a mechanism for stabilisation of drug molecules, for example, colistin is an antibiotic which is administered as its prodrug colistin methanesulphonate (CMS), which is less toxic and non-active.[26] The micellisation of CMS protects the molecules from degradation to the active drug molecule at high concentrations (e.g. during storage) through the reduced mobility of water molecules at the micelle surface, which reduces the opportunity for hydrolysis of the sulphomethyl groups of the CMS to form colistin.[27] The colistin is only released upon dilution of the prodrug formulation i.e when administered to the patient and not in storage.

Aggregation can also cause issues in the drug discovery process, specifically in high-throughput screening, where aggregates display enhanced inhibition of enzyme targets due to encapsulation of the protein within colloid-like particles.[28]

1.1.2.1 Methods of Investigation

Aggregation of aromatic drug molecules which formed $\pi-\pi$ stacked aggregates have been investigated using the changes in chemical shift in ^{1}H NMR spectra[3] as described above for other chromonic systems.

The aggregation of drug molecules forming micellar assemblies were studied using dynamic light scattering to determine the size of the micelles.[25,27] Surface tension measurements were also acquired for solutions of colistin and colistin methanesulphonate, critical micelle concentrations were established and the reduction in surface tension of colistin was found to be comparable to that of cationic octyl-chain surfactants.[27] Images of NNRTIs were acquired by transmission electron microscopy (TEM) as a visual confirmation of micelle size distribution and concentration dependence.[25]

1.1.3 Proteins

Aggregation of proteins generally occurs through misfolding of the protein into a conformation that is not functionally relevant.[2] Accumulation of aggregates in cells is usually prevented by several biological responses, such as molecular chaperones which facilitate refolding of misfolded proteins[29] or degradation through the ubiquitin-proteasome pathway.[2] When these processes fail to remove the misfolded proteins, extensive aggregation can occur which leads to the formation of insoluble protein deposits.

More than 20 human diseases, including Alzheimer's and Parkinson's diseases are characterised by protein deposits in the form of amyloid fibrils and plaques. These diseases are classified as amyloidoses due to the common 'amyloid' structure of the deposits,[2] despite the differences in the size, amino acid sequence and native structure of the constituent proteins.[30] Amyloid fibrils are characterised by a cross-β structure with the polypeptide chains organised in β-sheets parallel to the fibril axis; formed by the stacking of proteins in a β-strand conformation. The β-strands

are arranged perpendicular to the fibril axis, as observed by X-ray diffraction[30] and shown in Figure 1.3.

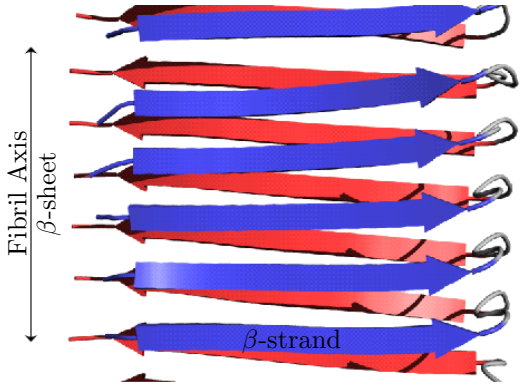

Figure 1.3: Cross-β structure

Proteins identified in amyloidosis diseases include Amyloid-β peptide (Aβ), a 40–42 residue peptide derived from amyloid precursor protein (APP) found in Alzheimer's disease sufferers, α-Synuclein in Parkinson's disease, Huntingtin in Huntington's disease and islet amyloid polypeptide (IAPP) in type II diabetes sufferers.[2,29,31] It was originally believed that the mature amyloid fibrillar aggregates were the pathogenic species due to their presence in diagnosed patients of a range of amyloidosis diseases; more recently many studies have shown that the oligomeric intermediates are more likely the pathogenic species.[2,32]

Amyloid formation is predominantly associated with diseases as discussed above, however there are also non-pathological amyloid conformations, sometimes called functional amyloids.[33] These amyloids are found in a variety of species, including bacteria, insects and mammals.[34] In bacteria functional amyloids include 'curli', an extracellular amyloid which aids bacterial surface attachment and colony growth, and 'chaplins' which aggregate into insoluble mats of fibres at air-water interfaces, lowering surface tension and aiding spore formation. Insects and fish employ chorion proteins as the main component of their eggshells, chorions have been shown to have an amyloid structure,[33,35] the mechanical strength and chemical stability of the fibrils are useful properties for protecting the embryo from environmental hazards such as temperature variations and mechanical pressure.[35] Another example of a functional amyloid is spider silk, formed by the protein spidroin, which has been shown to have an anti-parallel β-sheet structure, similar to that of amyloid fibrils.[36]

All of these functional amyloids require careful regulation to avoid the formation of pathological amyloids, these systems which utilise functional amyloids are generally highly regulated to avoid the formation of toxic aggregates. One example of a functional amyloid found in humans is composed of a peptide derived from the protein Pmel17.[37] The amyloid, designated Mα, has been shown to have cross-β sheet structure and facilitates the formation of melanin by acting as a template for the polymerisation of the melanin precursors. Melanin is a biopolymer which defends the body against a wide range of toxicity including UV radiation, pathogens and toxic small molecules. Toxicity of the Mα amyloid is regulated by fast fibril assembly. Recombinant Mα was shown to fibrilise four times faster than Aβ and α-Synuclein and this avoids the formation of significant populations of small toxic intermediates. The formation of amyloid from Mα is localised within the melanosome compartment. In order to avoid cell damage, the full-length Pmel17, which is unable to form aggregates, is maintained until the protein is contained within the melanosome.

The presence of these functional amyloids in a range of organisms indicates that amyloid structures

are not always toxic and it has been suggested that studies of these systems, especially of the regulatory mechanisms, could provide solutions in the treatment of amyloidosis diseases.[37] The formation of amyloids through self-assembly of a variety of different proteins and peptides is also of interest in the design of new nanomaterials due to the stability and strength of the fibrils and the ability to introduce additional functionality through changes in protein sequence.[38]

The aggregation of proteins can cause difficulties in the production of proteins for therapeutic purposes[39] due to the range of different conditions to which the protein is exposed during the production and purification processes. Aggregation leads to a decreased refolding yield in the production of recombinant proteins.[40] One protein known to have issues with aggregation in the production, storage and delivery processes is insulin.[41] Purification of insulin involves pH levels of 1–3 and transportation involves significant agitation of the insulin solution, both of these are known to promote aggregation.

Self-assembly of some proteins is beneficial, for example collagens are composed of three chains which associate into triple helical structures as the basis for larger assemblies.[42] Collagen is the most abundant protein in mammals and a major component in skin, bone and cartilage.[43] Collagens form a range of suprastructures such as fibrils and networks which have a range of functional roles including tissue development and providing structural integrity to organs.[42]

Aggregation is also an important process in the production of cheese, the addition of rennet to milk causes the aggregation of casein micelles into a gel-like network which is further processed to produce cheese.[44,45]

1.1.3.1 Methods of Investigation

X-ray fibre diffraction has been used to elucidate the structure of various amyloid fibrils including insulin,[46] Aβ[47] and α-synuclein.[48] Amyloid fibrils have a characteristic diffraction pattern relating to the cross-β structure composed of β-sheets parallel to the fibril axis which in turn are composed of β-strands which lie perpendicular to the fibril axis.[30]

Solid state NMR provides structural parameters which can be used in creating structural models of amyloid fibrils. These experiments are typically carried out on peptides which are isotopically labelled with ^{13}C and/or ^{15}N. Solid state NMR methods used to obtain structural constraints for Aβ fibrils include multiple quantum NMR,[49] ^{13}C–^{13}C and ^{15}N–^{13}C dipolar recoupling,[50,51] and ^{15}N–^{13}C rotational echo double resonance (REDOR).[50]

Circular dichroism (CD) is frequently used to study the secondary structure of proteins,[52] the CD spectra are different for the α-helix and β-sheet conformations and CD allows the determination of the fraction of the type of secondary structure present in the protein.[53] Circular dichroism has been used to monitor changes in secondary structure of proteins on formation of amyloid fibrils.[54,55]

Microscopy techniques including transmission electron microscopy (TEM), scanning electron microscopy (SEM) and atomic force microscopy (AFM), are used to study the morphology of protein assemblies.[52] Electron microscopy images show mature amyloid fibrils to be straight and unbranched with diameters of ∼100 Å.[56] One advantage of using AFM rather than EM is the ability to monitor changes in the aggregation state over time[57] allowing dynamics of aggregation to be determined, AFM has been used for this purpose with a range of amyloids including amylin,[57] Aβ[58,59] and insulin.[60]

The formation of amyloid fibrils can be followed by fluorescence by using Thioflavin T (ThT), where

the fluorescence of this molecule is increased in the presence of amyloid fibrils.[61] The mechanism of ThT binding to amyloid fibrils has been proposed as an electrostatic interaction between ThT micelles and the fibrils[62] or as the binding of ThT molecules into channels formed along the length of the fibrils.[63] The channel model has since been supported by molecular dynamics simulations and studies using peptide self-assembly mimics (PSAMs).[64] ThT fluorescence has been used to monitor the aggregation of a range of amyloid proteins including, but not limited to, insulin,[65] α-synuclein,[66] curli protein CsgA[66] and β-lactoglobulin.[67,68] The aggregation of amyloid proteins into fibrils in solution has been shown to occur via a nucleation polymerisation pathway,[31] with a lag phase in which oligomeric 'nuclei' are formed followed by a phase of rapid exponential growth where monomers or oligomers are associated with the nucleus.[69] The sigmoidal function of ThT fluorescence in the presence of amyloid proteins provides evidence for this nucleation pathway and has been observed in the fibrillisation of many amyloid proteins.[65–68,70]

1.1.4 Hydrogels

Hydrogels are formed by either chemical or physical cross-linking of water-soluble polymers to produce a three-dimensional network.[5] Formation of a hydrogel by physical cross-linking is a form of self-assembly and can be influenced by changes in environment such as temperature, pH and ionic strength. Physical cross-linking mechanisms include hydrophobic interactions, hydrogen bonding and interactions between charged polymers.[5] Hydrogels can absorb large amounts of water without dissolving[71] and are potentially useful as drug-delivery systems due to the porous structure of the network which allows the loading of drug molecules and high water content promoting biocompatibility.[5] Many polymers and hydrogels are stimuli-responsive, such that they undergo property changes e.g. changes in hydration state, volume, solubility or conformation, on experiencing an external stimulus such as a change in temperature or pH.[72] This is particularly useful for targeted release of drug molecules. Poly(*N*-isopropylacrylamide) is a thermo-responsive polymer which undergoes a volume phase transition at 30–34 °C, from a swollen state to a collapsed globule formation.[72] This polymer has been used as a copolymer in a hydrogel for the oral delivery of insulin and calcitonin. Polymers and hydrogels which are pH-responsive are also useful in targeted drug delivery due to the range of pH values within the body, for example tumour tissue has an extracellular pH of 6.5–7.2, which is slightly lower than normal tissue.[72] A pH-responsive drug delivery system provides the opportunity for controlled drug release in the correct location by tuning the hydrogel to release the drug within the pH range of the tumour tissue.

The self-association of polymers into hydrogel networks is an important form of aggregation with a range of potential applications including drug delivery,[5,72] and as sensors.[73] The properties of the hydrogels are influenced by several factors including polymer composition, solvent, temperature, and salt concentration,[72] which produces a range of hydrogel systems to be studied.

Proteins and polypeptides can be considered as natural polymers and as such can also form hydrogels. Examples of naturally occurring proteins being studied for hydrogel formation include gelatin and globular proteins such as bovine serum albumin and lysozyme.[74] Natural polypeptides typically have good biocompatibility and biodegradability, however the sample composition and therefore gel properties can differ between sources and the physical cross-linking can lead to weak hydrogels. Synthetic polypeptides with biomimetic segments can be prepared with the biofunctionality of a natural polypeptide and additional strength by the promotion of additional cross-linking.[74] Hydrogels have been prepared using polypeptides based on a range of protein structures including coiled-coil and β-sheet, as well as elastin-like polypeptides which include

a characteristic pentapeptide sequence from elastin, and peptide amphiphiles that combine a hydrophilic peptide sequence with a hydrophobic alkyl chain.[74] Peptide-based hydrogels have potential applications in drug delivery, microfluidics and tissue engineering.[74]

1.1.4.1 Methods of Investigation

Hydrogels have been studied using techniques such as rheology,[75] luminescence[76] and NMR.[77] One important property of a hydrogel is the swelling percentage, which can be determined by difference in weight between dry and swollen gels. The swelling percentage is proportional to the water uptake of the hydrogel which affects the rate of diffusion of solutes within the polymer network.[75] This has consequences in the efficiency of hydrogels as drug delivery systems, hydrogels with high water content allow rapid diffusion and release of drug molecules within hours or days.[5]

Rheology is the study of the deformation and flow of matter and provides information on the effects of stress and strain on a material.[78] Rheology is used to study the mechanical properties of hydrogels, an important factor in the optimisation of a hydrogel system for a particular application.[79] For example a hydrogel with shear thinning properties (decreasing viscosity with increasing rate of shear[80]) and rapid self-healing (returns to solid form once stress is removed), is required for injections.[74] Typical rheological measurements of hydrogels include small deformation tests, such as small amplitude oscillatory shear (SAOS), creep and creep recovery measurements which provide values of the shear storage modulus G', loss modulus G'' and the loss factor δ.[74] The shear storage modulus G' is a measure of the stiffness of the material and the loss modulus G'' is a measure of the liquid-like response of the material, the relative magnitudes of G' and G'' indicate whether the hydrogel behaves as an elastic solid or a viscous liquid.[74]

Luminescence studies of hydrogels provide information regarding the interior of the hydrogel, for example the distribution of hydrophilic and hydrophobic domains and the diffusion of molecules within the hydrogel. One method employs luminescent probes mixed in the hydrogel solution or bonded to the polymer chains to characterise the hydrophobic/hydrophilic environments within a hydrogel.[76] This requires probe molecules with a fluorescence spectrum dependent on its environment, for example pyrene is sensitive to aqueous and non-aqueous solvent conditions with changes in the fluorescence intensity and lifetime in the different environments. On inclusion in a hydrogel the fluorescence spectrum is composed of an aqueous component and a non-aqueous component, the latter is used as a measure of the size of any hydrophobic domains within the hydrogel. Other probe molecules are sensitive to viscosity and temperature and probe molecules attached to the polymer chains can be used to monitor changes in the polymer chain conformation on formation of the hydrogel. Other luminescence methods for studying hydrogels include luminescence quenching and fluorescence polarisation.

NMR studies of hydrogels have mainly used ^{13}C experiments due to overlapping broad peaks in the ^{1}H spectra.[77] Other NMR methods include relaxation studies of the water inside the hydrogel and nuclear Overhauser enhancements (NOE) used to identify intermolecular interactions within the hydrogel network.[81] The semi-solid nature of hydrogels produces spectra with broad unresolved peaks, as such magic angle spinning (MAS) is frequently implemented in NMR studies of hydrogels.[77,81]

1.2 Nuclear Magnetic Resonance

1.2.1 NMR Theory

NMR relies on two intrinsic properties of atomic nuclei, the spin angular momentum ($\boldsymbol{I}$) and the magnetic moment ($\boldsymbol{\mu}$), which are vector quantities proportional to each other through Equation 1.1.[82]

$$\boldsymbol{\mu} = \gamma \boldsymbol{I} \tag{1.1}$$

Where γ is the gyromagnetic ratio of the nucleus. As vector quantities both $\boldsymbol{I}$ and $\boldsymbol{\mu}$ have magnitudes and directions which are quantised. The magnitude of the spin angular momentum is given by $[I(I+1)]^{\frac{1}{2}}\hbar$ where I is the nuclear spin quantum number, which is determined by the number of protons and neutrons in the nucleus and the configuration of the nuclear ground state.[83] I can take integer and half-integer values including zero, i.e. $I = 0, \frac{1}{2}, 1, \frac{3}{2}, 2\ldots$, nuclei with $I = 0$ include ^{12}C and ^{14}N and are NMR silent, nuclei with $I = \frac{1}{2}$ include ^{1}H, ^{13}C and ^{31}P and are the only nuclei used in this thesis, finally nuclei with $I > \frac{1}{2}$ such as ^{2}H and ^{14}N ($I = 1$) are known as quadrupolar nuclei, the NMR of these nuclei is more complicated than the $I = \frac{1}{2}$ nuclei[83] and will not be discussed in this thesis.

The direction of $\boldsymbol{I}$ on an arbitrarily chosen axis (e.g. the z axis) has $2I + 1$ possible orientations given by $I_z = m\hbar$, where m is the magnetic quantum number which takes values from $-I$ to $+I$ in integer steps (i.e. $m = -I, -I+1, \ldots I-2, I-1, I$). In the absence of a magnetic field there is no directional preference and the $2I + 1$ orientations are degenerate, this degeneracy is lifted in the presence of a strong magnetic field and the quantisation axis is aligned with the direction of the magnetic field.[82] The energy of the orientations is given by Equation 1.2.

$$\begin{aligned} E &= -\boldsymbol{\mu} \cdot \boldsymbol{B} \\ &= -\mu_z B \\ &= -m\hbar\gamma B \end{aligned} \tag{1.2}$$

For a spin-½ nucleus, such as ^{1}H, there are 2 values of m, $+\frac{1}{2}$ and $-\frac{1}{2}$, these are sometimes referred to as the α and β states respectively. At thermal equilibrium the population of these two states is described by the Boltzmann distribution (Equation 1.3).[82]

$$\frac{n_\beta}{n_\alpha} = \exp -\Delta E / k_B T \tag{1.3}$$

Where n_α and n_β are the populations of the α and β states, ΔE is the difference in energy between the two states (i.e. $E_\beta - E_\alpha$), k_B is the Boltzmann constant (1.381×10^{-23} J K^{-1}) and T is the absolute temperature in Kelvin. At thermal equilibrium there is a slight preference for the α state where the magnetic moments are aligned with the magnetic field, this creates a net magnetisation along the z axis. The distribution between the α and β states is dependent on the strength of the magnetic field and the temperature. With a magnetic field strength of 14.1 T and temperature of 298 K, $n_\beta/n_\alpha = 0.999903$, this gives a population difference of 1 in approximately 21000. There is no magnetisation in the x or y directions due to the random distribution of magnetic moments in these directions leading to an average of zero over the whole sample.[82]

The selection rule for transitions in NMR is $\Delta m_I = \pm 1$,[82] i.e. allowed transitions are those where the magnetic quantum number m changes by $+1$ or -1, as is the case for the transition between the

α and β states.[84] Transition between these two energy levels requires radiation with a frequency (ν) to match the difference in energy between the two levels, as shown in Equation 1.4.[84]

$$\begin{aligned} \Delta E &= E_\beta - E_\alpha \\ &= [-(-\frac{1}{2})\hbar\gamma B] - [-(+\frac{1}{2})\hbar\gamma B] \\ \Delta E &= \hbar\gamma B = h\nu \\ \nu_{\alpha\to\beta} &= \frac{\gamma B}{2\pi} \end{aligned} \tag{1.4}$$

With a magnetic field strength of 14.1 T and a gyromagnetic ratio for the ^{1}H nuclei of 26.75×10^7 T^{-1} s^{-1}, the frequency of electromagnetic radiation required is 600 MHz which is within the radio frequency range.

The magnetic moment precesses around the static magnetic field, the frequency of precession is called the Larmor frequency and is dependent on the field strength and gyromagnetic ratio of the nucleus (Equation 1.5).[84] The Larmor frequency can be expressed in units of Hz (ν_0) or rad s^{-1} (ω_0), the conversion from Hz to rad s^{-1} is achieved by the multiplication by 2π. The Larmor frequency is the same as the frequency of radiation corresponding to the energy gap, as derived above, the minus sign indicates that, for nuclei with positive gyromagnetic ratios, the direction of precession is negative, i.e. clockwise when looking down the z axis (the axis of the applied magnetic field).[84]

$$\omega_0 = -\gamma B \text{ in rad s}^{-1} \quad \text{or} \quad \nu_0 = -\frac{\gamma B}{2\pi} \text{ in Hz} \tag{1.5}$$

Application of a radio frequency pulse perpendicular to the static magnetic field with a frequency close to the Larmor frequency creates an oscillating magnetic field in resonance with the Larmor precession which causes the magnetisation to move away from the z axis.[84] The angle through which the magnetisation is tipped depends on the length of the RF pulse (Equation 1.6).[82]

$$\begin{aligned} \beta &= \omega_1 t_p \\ &= \gamma B_1 t_p \end{aligned} \tag{1.6}$$

Where β is the flip angle in radians, ω_1 the frequency of the applied RF field (in rad s^{-1}), determined by γ and B_1, the strength of the radiofrequency field, and t_p is the duration of the pulse in seconds.

When considered in a reference frame which rotates about the z axis at the transmitter frequency of the spectrometer (ω_1), the applied RF field appears static and the apparent frequency of precession is the difference between the Larmor frequency and the transmitter frequency (Equation 1.7), called the offset (Ω).[84]

$$\Omega = \omega_0 - \omega_1 \tag{1.7}$$

A 90° pulse ($\beta = \pi/2$) along the x axis will rotate the magnetisation from the z axis to the -y axis. The magnetisation continues to precess about the z axis, with an observed frequency Ω in the rotating frame, this precession creates a current in the RF coil which produces signals for the x- and y-components of the magnetisation which are detected simultaneously and form the complex Free Induction Decay (FID) which takes the form of Equation 1.8.[84]

$$S(t) = S_0 \exp(i\Omega t) \exp(-R_2 t) \tag{1.8}$$

Where R_2 is the transverse relaxation rate which determines the rate at which the transverse magnetisation decays back to zero.

The FID is a function of time, Fourier transformation of the FID converts the signal to a function of frequency i.e. a spectrum. The signal is complex and therefore has a real and imaginary part (Equation 1.9), the real part produces a peak with an absorption mode Lorentzian lineshape and the imaginary part has a dispersion mode lineshape.[84]

$$\begin{aligned} S(t) &\overset{\text{FT}}{\rightarrow} S(\omega) \\ S_0 \exp(i\Omega t)\exp(-R_2 t) &\overset{\text{FT}}{\rightarrow} \underbrace{\frac{S_0 R_2}{R_2^2 + (\omega-\Omega)^2}}_{\textbf{real}} + i\underbrace{\frac{-S_0(\omega-\Omega)}{R_2^2 + (\omega-\Omega)^2}}_{\textbf{imaginary}} \end{aligned} \tag{1.9}$$

The Fourier transform produces a spectrum with a peak of intensity S_0, at a frequency Ω and a width dependent on the relaxation rate R_2. When there are several resonances the time-domain signal is the sum of each of the resonances (Equation 1.10) and the Fourier transform extracts each signal separately.[84]

$$\begin{aligned} S(t) =& S_0^{(1)} \exp(i\Omega^{(1)} t)\exp(-R_2^{(1)} t) \\ &+ S_0^{(2)} \exp(i\Omega^{(2)} t)\exp(-R_2^{(2)} t) \\ &\ldots + S_0^{(n)} \exp(i\Omega^{(n)} t)\exp(-R_2^{(n)} t) \end{aligned} \tag{1.10}$$

1.2.1.1 Chemical Shift

The strength of the magnetic field experienced by a particular nucleus is different to that of the external magnetic field due to the shielding effect of the electrons in bonds surrounding the nucleus.[82] The magnitude of the shielding effect and therefore the effective magnetic field experienced by the nucleus is dependent on the distribution of electrons around the nucleus and is characteristic of the environment in which the nucleus is situated (Equation 1.11).

$$\begin{aligned} B &= B_0 - B' \\ &= B_0(1-\sigma) \end{aligned} \tag{1.11}$$

Where B is the magnetic field experienced by the nucleus, B_0 is the strength of the external magnetic field, B' is the strength of the field generated by the electrons and σ is the shielding constant ($\sigma = B'/B_0$). The Larmor frequency of a particular nucleus is therefore dependent on its local environment as well as its gyromagnetic ratio and the strength of the external magnetic field.

$$\nu = -\frac{\gamma B_0(1-\sigma)}{2\pi} \tag{1.12}$$

The effect of shielding is more conveniently expressed as the difference in frequency between the nucleus of interest and a reference nucleus, this dimensionless parameter is called the chemical shift (δ), expressed in parts per million (ppm) and is independent of magnetic field strength (Equation 1.13).[82]

$$\delta = 10^6 \frac{(\nu - \nu_{\text{ref}})}{\nu_{\text{ref}}} \tag{1.13}$$

Chemical shift increases with a decrease in shielding, for example protons in aliphatic functional groups appear at low chemical shift and protons on aromatic groups appear at a larger chemical

shift.

1.2.1.2 J-coupling

Multiplet patterns arise in NMR spectra due to coupling between inequivalent adjacent nuclei. The spin-state of an adjacent nucleus contributes to the local magnetic field experienced by the nucleus being observed. For a spin-$^1/_2$ nucleus the magnetic moment can be aligned with or against the static magnetic field (i.e. occupy the α or β spin state) which opposes or adds to the external magnetic field and therefore decreases or increases the resonance frequency respectively.[84] The presence of one adjacent spin-$^1/_2$ nucleus produces a doublet splitting pattern due to the two possible spin states of the adjacent nucleus. Increasing the number of adjacent nuclei increases the amount of peak splitting, coupling to n nuclei (all of which are equivalent) produces an $n + 1$ splitting pattern with binomial intensities.[82] More complicated multiplet patterns arise from increasing numbers of adjacent nuclei in different environments. J-coupling is a useful tool in the application of NMR to the elucidation of chemical structures.[84]

1.2.1.3 Relaxation

Relaxation is the re-establishment of the thermal equilibrium of the magnetisation after the application of an RF pulse.[84] Relaxation effects can be separated into two components, spin-lattice and spin-spin relaxation.

Spin-lattice (longitudinal) relaxation, characterised by the spin-lattice relaxation time T_1, describes the return of the bulk magnetisation to its thermal equilibrium position along the z axis. The value of T_1 characterises how long it takes for bulk z magnetisation to be established on initial application of the external magnetic field as well as to be re-established after a pulse.[83] Longitudinal relaxation occurs through an exchange of energy from the nuclear spin system to the surroundings, facilitated by local fields within the sample. Local fields are generated by nearby spins and thermal agitation of the molecules causes the magnitude and orientation of the local field to vary over time, if the local field oscillates with a frequency close to the Larmor frequency it can change the orientation of the magnetic moment of the nucleus experiencing the local field.[84] Random fluctuations of local fields leads to random orientations of the individual magnetic moments and zero bulk magnetisation along the z axis. The equilibrium position of the bulk magnetisation along the z axis is acquired by the slight energetic preference of alignment with the magnetic field. The rate of longitudinal relaxation depends on the spectral density at the Larmor frequency ($J(\omega_0)$) as well as the gyromagnetic ratio (γ) and the mean square value of the local fields ($\langle B^2 \rangle$) (Equation 1.14).[82,84]

$$\frac{1}{T_1} = \gamma^2 \langle B^2 \rangle J(\omega_0) \tag{1.14}$$

Spin-spin (transverse) relaxation, characterised by the spin-spin relaxation time T_2, describes the decay of the transverse magnetisation to zero. Transverse relaxation occurs through varying local fields which change the precession frequencies of the spins leading to loss of phase-coherence of the spins and a decrease in net transverse magnetisation. The value of T_2 determines the time the loss of coherence takes, this relaxation process affects the linewidth of the signals (Equation 1.15). A small T_2 value indicates rapid loss of phase-coherence which leads to a range of precession frequencies and broadening of the peak.

$$\text{Linewidth} \propto \frac{1}{\pi T_2} \tag{1.15}$$

The local field effects described for longitudinal relaxation can also contribute to the transverse relaxation, as such $T_2 \leq T_1$.[85] The rate of transverse relaxation is therefore dependent on two contributions, the relaxation due to local fields oscillating at the Larmor frequency (as described above for spin-lattice relaxation) which is dependent on the spectral density at the Larmor frequency and the relaxation due to the loss of phase coherence of the spins (Equation 1.16).[82] The latter contribution is dependent on the spin density at zero frequency because random motion at any frequency reduces the efficiency of the relaxation mechanism.

$$\frac{1}{T_2} = \frac{1}{2}\gamma^2\langle B^2\rangle J(\omega_0) + \frac{1}{2}\gamma^2\langle B^2\rangle J(0) \tag{1.16}$$

Fast motion (molecular tumbling) causes the local fields to vary rapidly with time, such that the spin experiences a time-average local field, increased motion leads to more complete averaging of the local fields across the sample and therefore a reduction in the dephasing of spin coherence.[84]

Equations 1.14 and 1.16 include the spectral density function $J(\omega)$, which is proportional to the probability of random motion occurring with a frequency ω and is described by Equation 1.17.[82]

$$J(\omega) = \frac{2\tau_c}{1 + \omega^2\tau_c^2} \tag{1.17}$$

Where τ_c is the rotational correlation time, the average time for a molecule to rotate one radian, which increases with increasing molecular size or solvent viscosity and decreases on increasing temperature.[82]

From this it is clear that both T_1 and T_2 relaxation are dependent on the molecular tumbling rate of the molecules and therefore the size of the molecule. The dependence of the relaxation time T_1 and T_2 on the rotational correlation time are shown in Figure 1.4.

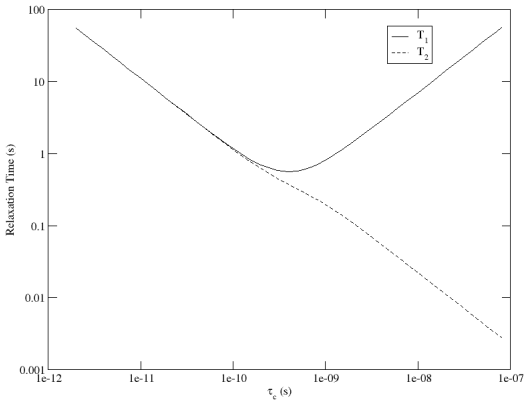

Figure 1.4: Dependence of T_1 and T_2 on the rotational correlation coefficient τ_c. These curves were calculated using Equations 1.14 and 1.16 with values of $\gamma^2\langle B^2\rangle = 4.5 \times 10^9$ s^{-2} and $\omega_0/2\pi = 400$ MHz. Figure adapted from Reference 82.

T_1 relaxation has a minimum when the rotational correlation time is equal to the inverse Larmor frequency i.e. when $\tau_c = \frac{1}{\omega_0}$ or $\tau_c\omega_0 = 1$, while T_2 decreases with increasing τ_c.[82] When molecular tumbling is fast compared to the resonance frequency ($\omega_0\tau_c \ll 1$) T_2 is equal to T_1, however as τ_c increases the contribution of loss of phase coherence increases leading to a decrease in T_2. As T_2 is related to the linewidth of a peak, it is clear that larger molecules, with longer rotational correlation times give rise to broader peaks due to the increased contribution of phase coherence effects to the relaxation time.

1.2.1.4 Phase Cycling

Phase cycling is used to select coherence transfer pathways and to correct for imperfections in the receiver or RF pulses.[86,87] This is most frequently required when a pulse sequence involves more than one pulse which can create additional unwanted signals. For example, a pulse sequence which consists of a 90° pulse followed by a delay t_1 and then a second pulse with any flip angle. The second pulse acts on all magnetisation present at the end of t_1, this includes z-magnetisation which may be present due to spin-lattice relaxation during t_1 or imperfections in the first 90° pulse, this produces unwanted 'axial' peaks at zero frequency in the indirect dimension of a 2D experiment.[87] The second pulse also acts on transverse magnetisation in two ways to give two coherence pathways, known as N-type and P-type pathways, it is sometimes necessary to separate these two pathways in order to improve spectral quality.[87]

Product operators can be used to describe the state of the spin system during an NMR experiment.[86] For example, for a single spin, I_z represents z magnetisation and I_x and I_y represent transverse magnetisation along the x and y axes respectively. Additional operators are used to describe other spins (e.g. S_z, S_x and S_y) and the product operators (e.g. $2I_zS_z$, $2I_zS_x$ and $2I_zS_y$) are used when spins are coupled. Each product operator has one or more associated coherence orders (p), which is determined by the effect of a z-rotation through an angle φ on the spin state.[84] Z-magnetisation, with the operator I_z, has a coherence order of $p = 0$ as it is unaffected by a rotation along the z-axis. Transverse magnetisation, such as I_x and I_y, are both rotated by $-\varphi$ and have coherence orders of $p = \pm 1$, these are known as single quantum coherences. Other product operators with $p = 0$, ± 2 are called zero- and double-quantum coherences respectively. Some product operators are mixtures of quantum coherences, such as $2I_xS_x$ which is a mixture of zero- and double-quantum coherences.

For a particular pulse sequence, a coherence transfer pathway (CTP) diagram can be drawn to illustrate the coherence order wanted at each step. The coherence order of z-magnetisation is $p = 0$ so a coherence transfer pathway always begins at 0. The coherence order is not affected by free precession and can only be changed by the RF pulses. Only single quantum coherence of the order $p = -1$ is observable, so the coherence transfer pathway must end at -1. The pulse sequence and three possible coherence transfer pathways for the COSY (COrrelation SpectroscopY) experiment are shown in Figure 1.5. COSY is a 2D experiment which shows correlations between J-coupled spins.[86] Coherence transfer pathway a) selects N-type signals, where the N stands for 'negative', so called because the coherence order has opposite signs during the time delays t_1 and t_2. CTP b) gives a P-type spectrum, with the P standing for 'positive' due to the coherence order being of the same sign during t_1 and t_2. CTP c) selects both N- and P-type signals to give amplitude modulated spectra.[84]

Phase cycling relies on the fact that if a coherence order is changed from p_1 to p_2 by application of a pulse, then shifting the phase of the pulse by $\Delta\varphi$ leads to a phase shift in the coherence order of $-\Delta p\Delta\varphi$. Where Δp is the change in coherence order ($\Delta p = p_2 - p_1$).[84] This means that different pathways acquire different phase shifts, allowing the differentiation and selection of different pathways. For example, in CTP a) of Figure 1.5, $\Delta p = +1$ for the first pulse. If the phase of this pulse is cycled through the sequence 0°, 90°, 180°, 270°, the coherence pathway with $\Delta p = +1$ acquires the phase 0°, 270°, 180°, 90°, as shown in Table 1.1.

The $\Delta p = +1$ pathway can be selected by changing the phase of the receiver to match the phase shift acquired by the coherence order. As φ_1 cycles through the sequence 0°, 90°, 180°, 270°, the receiver phase (φ_{rx}) should be cycled through the sequence 0°, 270°, 180°, 90°. The phase of the

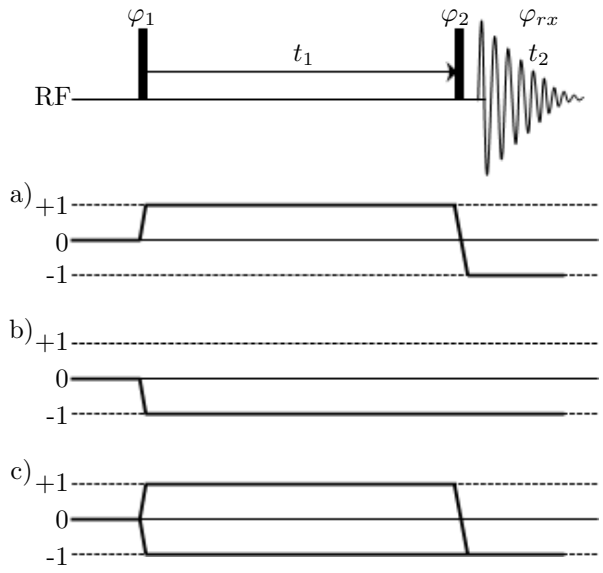

Figure 1.5: Pulse sequence and coherence transfer pathway diagrams for COSY experiment. φ_1, φ_2 and φ_{rx} represent the phase of the two RF pulses and the receiver respectively. CTP a) selects N-type coherence transfer, CTP b) gives P-type coherence transfer and CTP c) selects both N- and P-type signals. Figure adapted from Reference 87.

Table 1.1: Table of Phase Shifts for $\Delta p = +1$

Pulse Phase ($\Delta\varphi$)	Phase Shift of Coherence ($-\Delta p\Delta\varphi$)	Equivalent ($0° - 360°$)
0°	$-(+1)(0°) = 0°$	0°
90°	$-(+1)(90°) = -90°$	270°
180°	$-(+1)(180°) = -180°$	180°
270°	$-(+1)(270°) = -270°$	90°

second pulse remains constant throughout this sequence, as the coherence order is already selected to be $p = +1$ during t_1 and the only coherence observable is $p = -1$ there is no need to specifically select the $\Delta p = -2$ transfer for the second pulse. Combination of the results of the four steps of this phase cycle leads to the signals from the selected pathway adding constructively while signals from other pathways, which experienced different phase shifts will cancel out.

A different phase cycle is used for CTP b), in this case the change in coherence order required for the first pulse is $\Delta p = -1$. Using the equation for the acquired phase shift of $-\Delta p\Delta\varphi$ with $\Delta p = -1$ and pulse phase shifts of 0°, 90°, 180°, 270°, it can be found that the receiver phase should also be 0°, 90°, 180°, 270° in order to select this pathway. Thus, by changing the cycling of the receiver phase relative to that of the RF pulse phase a particular coherence transfer pathway can be selected.

In CTP c) of Figure 1.5, both $\Delta p = +1$ and $\Delta p = -1$ are required at the first pulse, as these are the only coherence orders achievable for a pulse applied to equilibrium magnetisation, no phase cycling is required for this sequence.

Phase cycling is an important tool in NMR, especially in the acquisition of 2D data, where the ability to separate N- and P-type signals and the suppression of axial peaks leads to significant improvements in the quality of spectra.[87] One consequence of the use of phase cycling is the number of scans required, an integral number of cycles must be completed in order to fully combine signals

from the selected coherence pathway and cancel those from the unwanted coherence pathways. It is therefore standard practice to acquire spectra with 2^n transients (e.g. 8,16,128,256, or 1024) in order to ensure completion of any phase cycles.

1.2.2 Diffusion NMR

The measurement of translational diffusion by NMR is achieved using pulsed field gradients and the spin or stimulated echo sequences first described by Hahn.[88] In 1954 Carr and Purcell described the effect of diffusion on the spin echo sequence composed of a 90° pulse followed by a 180° pulse[89] and presented the measurement of the self-diffusion coefficient of water in the presence of a continuous field gradient. Later, Stejskal and Tanner proposed the use of pulsed field gradients in place of the steady field gradient used by Carr and Purcell.[90] The use of pulsed field gradients overcomes several experimental limitations of the steady gradient method.[90] Firstly, the presence of a gradient during acquisition causes increased linewidths, with larger gradients causing greater broadening, this hinders the analysis of multiple peaks,[91,92] the use of pulsed field gradients avoids this complication. Secondly, because the linewidth is not affected by pulsed field gradients, larger gradients can be used without the need to increase the RF power, which allow the measurement of smaller diffusion coefficients.[91] Finally, because the gradients are applied as pulses, the diffusion delay is well defined which is important where restricted diffusion is measured.[92]

1.2.2.1 Effect of Magnetic Field Gradients

Magnetic field gradients introduce a spatial dependence to the magnetic field strength (Equation 1.18),[93] for example, with a magnetic field gradient along the z axis with its origin at the centre of the sample tube, the magnetic field strength increases on moving up the z axis from the centre and decreases on moving down the z axis from the centre.

$$B(\mathbf{r}) = B_0 + \mathbf{g} \cdot \mathbf{r} \tag{1.18}$$

where $B(\mathbf{r})$ indicates that the magnetic field strength depends on the spatial position ($\mathbf{r}$), B_0 is the strength of the static magnetic field and $\mathbf{g}$ describes the magnetic field gradient. In diffusion NMR experiments the gradient applied is spatially homogeneous in that it produces a linear change in the magnetic field along the direction of the gradient, the gradient is typically one-dimensional along the z axis.[92] Magnetic field gradients in two- and three-dimensions are used in imaging experiments (e.g. magnetic resonance imaging) and other diffusion experiments.[83]

As the Larmor frequency of a nucleus is dependent on the magnetic field strength (Equation 1.5), the application of a magnetic field gradient introduces spatial dependency to the Larmor frequency (Equation 1.19).

$$\begin{aligned} \omega(\mathbf{r}) &= -\gamma B(\mathbf{r}) \\ &= -\gamma(B_0 + \mathbf{g} \cdot \mathbf{r}) \\ &= \omega_0 - \gamma(\mathbf{g} \cdot \mathbf{r}) \end{aligned} \tag{1.19}$$

In a diffusion NMR experiment the magnetic field gradient is applied as a pulse with gradient strength g and duration δ. After a 90° RF pulse to transfer the magnetisation into the x-y plane, the application of the gradient pulse gives the nuclei a position-dependent phase angle (ϕ, Equation 1.20)

which can be visualised as a helix (Figure 1.6).[93]

$$\phi = -\gamma g \delta z \tag{1.20}$$

Equation 1.20 describes the phase angle acquired when the gradient pulse is square, equations for other shapes of gradient require the inclusion of a shape factor to determine the phase angle.

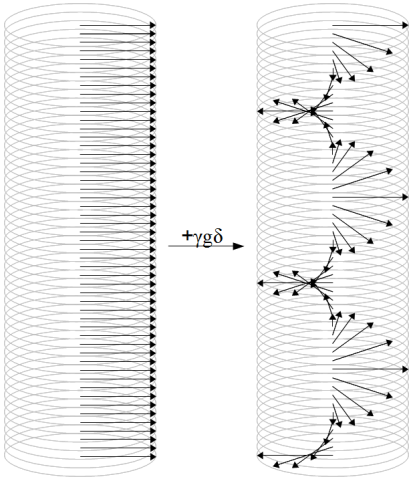

Figure 1.6: Schematic of nuclear spins after 90° pulse and after application of a magnetic field gradient. Each arrow represents nuclei in a particular layer along the z-axis, on application of the magnetic field gradient, nuclei precess with different frequencies depending on position such that after the duration of the gradient (δ) the nuclei acquire a phase shift of $-\gamma g \delta z$. Figure adapted from References 83 and 93.

1.2.2.2 Measuring Diffusion Coefficients

To measure diffusion coefficients using pulsed field gradients a diffusion delay (Δ) is included in the pulse sequence followed by another gradient to undo the spatial encoding established by the first gradient. Pulsed field gradient (PFG) NMR experiments are based on either the Hahn spin echo or the stimulated echo sequences, shown in Figure 1.7.

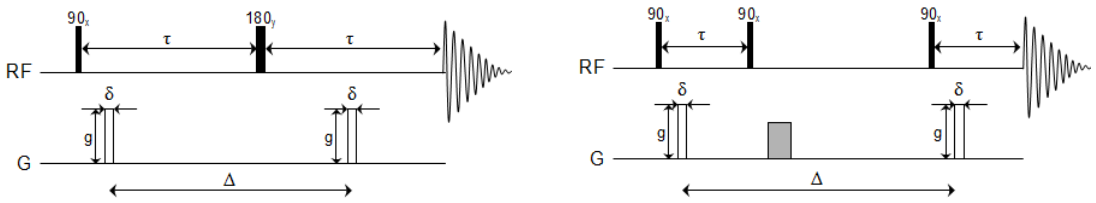

(a) Spin Echo (b) Stimulated Echo

Figure 1.7: Spin echo and Stimulated echo pulse sequences

In the spin echo sequence (Figure 1.7a) the effect of the 180° pulse along the y axis is to flip the spins by 180° about the y axis which reverses the sign of the phase angle during the subsequent τ period. Dephasing of the spins through different precession frequencies (due to applied gradients or field inhomogeneity) is refocussed forming an echo at time τ after the 180° pulse (where τ is the time between the 90° and 180° pulses). This is shown in Figure 1.8 using a vector representation of the magnetisation for the spin echo sequence without magnetic field gradients.

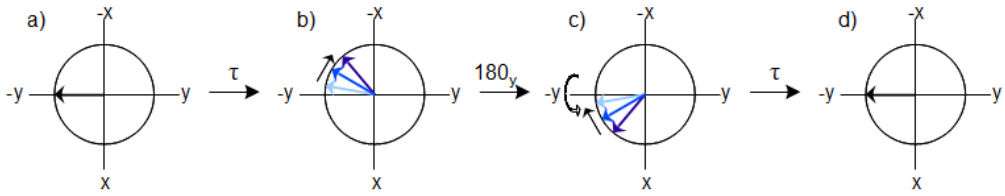

Figure 1.8: Vector representation of magnetisation during a spin echo sequence. a) the 90° pulse transfers the magnetisation onto the -y axis, b) the spins precess about the z axis during period τ, c) the 180° pulse flips the magnetisation around the y axis, d) the spins precess about the z axis during the second τ period and are refocussed at a time = 2τ. Figure adapted from Reference 82.

The stimulated echo sequence (Figure 1.7b) uses three 90° pulses to generate a stimulated echo at time τ after the third pulse (where τ is the time between the first and second pulses). The evolution of the magnetisation vectors during the stimulated echo sequence in the absence of magnetic field gradients is shown in Figure 1.9. The phase change caused by the second and third 90° pulses is the same as that caused by the 180° pulse in the spin echo sequence.[94] The formation of additional spin echoes by the magnetisation not affected by the second 90° pulse can be avoided by application of a 'crusher' gradient during the diffusion delay, as shown by the grey gradient in Figure 1.7b.[94]

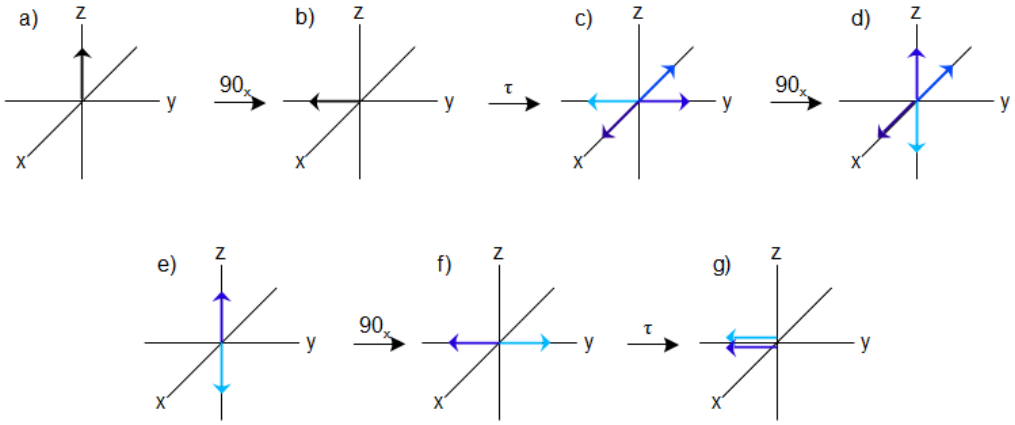

Figure 1.9: Vector representation of magnetisation during a stimulated echo sequence. a,b) The 90° pulse transfers the magnetisation onto the -y axis, c) the spins precess about the z axis during period τ, d) the second 90° pulse along the x axis transfers the y-component of the magnetisation into the $\pm$z axis, e) the x component is unaffected by a pulse along the x axis, these spins refocus to form other spin echoes, f) the third 90° pulse transfers the magnetisation back onto the $\pm$y axis g) the spins precess about the z axis and are refocussed after the second τ period. Figure adapted from Reference 94.

In the absence of diffusion the effect of the first gradient is completely reversed by the second gradient and the spins are all refocussed, however when diffusion occurs the strength of the magnetic field experienced on application of the second gradient will be different to that experienced in the first gradient and the phase shift acquired during the first gradient will not be completely refocussed by the second gradient.[91] The phase shift acquired by diffusing spins is random and when averaged over the whole sample results in signal attenuation. The amount of signal attenuation depends on the diffusion coefficient of the molecule and the strength of the gradients, the diffusion coefficient can be determined by increasing the gradient strength and recording the signal attenuation. The signal attenuation follows an exponential decay described by the Stejskal-Tanner equation (Equation 1.21).[92]

$$\frac{S(g)}{S(0)} = \exp\left(-\gamma^2 g^2 D\delta^2(\Delta - \delta/3)\right) \tag{1.21}$$

Where $S(g)$ is the signal with gradient strength g, $S(0)$ is the signal in the absence of gradients, γ is the gyromagnetic ratio of the nucleus, g is the gradient strength, D is the diffusion coefficient, δ is the length of the gradient pulse and Δ is the length of the diffusion delay (the period between gradient pulses). The subtraction of $\delta/3$ from the diffusion delay Δ is a correction factor for the finite length of the gradient pulses and the diffusion which occurs while the gradient pulse is applied. Equation 1.21 is the form related to the use of square gradients and slight modifications are required when non-square shaped gradients are used.

The presence of flow (e.g. due to convection) introduces coherent motion within the sample, in this case the phase shift acquired is not random and leads to a net phase change in the resulting spectrum.[91]

As discussed in Section 1.2.1.3, large molecules have short T_2 relaxation times due to slow molecular tumbling and reduced averaging of local field effects which leads to peak broadening and loss of signal. In the spin echo sequence the magnetisation is stored in the transverse xy plane during the diffusion delay and is therefore subject to transverse relaxation. The advantage of the stimulated echo sequence over the spin echo is that the second 90° pulse stores the y-component of the magnetisation in the z-direction during the diffusion delay, loss of signal through transverse relaxation only occurs during the two τ periods and is therefore minimised.[93] A consequence of storing only the y-component of the magnetisation in the z-direction is that the signal acquired using the stimulated echo sequence is reduced by a factor of 2 compared to the spin echo sequence, however when $T_2 \ll T_1$ the loss of signal due to transverse relaxation in the spin echo is likely to be greater than the factor of 2 reduction in the stimulated echo.

1.2.2.3 Pulse Sequence Adaptations

A range of pulse sequences based on the spin and stimulated echo sequences have been developed for the purpose of diffusion NMR, designed to reduce unwanted effects such as eddy currents, J-modulation and convection which can alter the apparent diffusion coefficient of a molecule.[93]

Eddy currents are generated in conducting surfaces surrounding the gradient coils by the rapid rise and fall of the gradient pulses and can cause signal distortions such as phase changes or gradient-induced broadening in the spectra.[93,95] Eddy current effects are reduced by two pulse sequence alterations, longitudinal eddy current delay (LED) and bipolar pulse pairs (BPP). LED sequences include a longitudinal eddy current delay period at the end of the stimulated echo sequence, in this period the eddy currents decay while the magnetisation is stored in the longitudinal direction. Bipolar pulse pairs involve the replacement of the single gradient pulse of length δ with two gradient pulses each of length $\delta/2$ with opposite sign separated by a 180° RF pulse.[96] The presence of the 180° pulse means that the two gradients have an additive effect on the phase of the spins rather than the second gradient undoing the phase change caused by the first gradient. The 180° pulse does not affect the eddy currents and the eddy currents created by the first gradient pulse are cancelled by the second gradient.[95] The BPP-LED sequence incorporating both of these features is shown in Figure 1.10.[97]

J-modulation occurs when scalar coupling exists between nuclei, the precession frequency of the nuclei is influenced by the magnitude of the coupling constant, J,[95] also the spin states of coupled nuclei can be exchanged by RF pulses,[93] both of which affect the refocussing of the spins and therefore the signal-to-noise ratio of the echo. The peaks in J-modulated spectra have absorption and dispersion components.[98] J-modulation is not refocussed in a spin echo experiment[84] but the effects

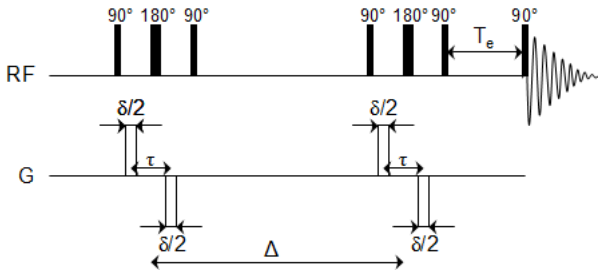

Figure 1.10: Bipolar pulse pair - longitudinal eddy-current delay (BPP-LED) pulse sequence.

can be minimised in the stimulated echo sequence by reducing the time that the magnetisation is transverse, i.e. by minimising τ, the period between the first and second 90° pulses, best results are acquired when $\tau \ll 1/J$.[95] Another method for the suppression of J-modulation effects is the implementation of a 45° pulse at the end of the spin echo just before signal acquisition which removes antiphase terms which cause phase distortion, as demonstrated by Botana et al. with the Oneshot45 pulse sequence.[98]

Coherent motion within a sample, due to thermal gradients, causes additional motion of the molecules during the diffusion delay which can lead to increased signal attenuation and an increased apparent diffusion coefficient. A convection compensated sequence described by Jerschow and Müller[99] is the double stimulated echo sequence where an additional set of pulses and gradients are included in the middle of the diffusion delay (Figure 1.11). This set of pulses and gradients are the same as the spatial encoding sets at the beginning and end of the sequence, but there are two gradients between the pulses instead of one. The purpose of this sequence is to transfer the magnetisation back into the transverse plane, refocus the magnetisation with the first gradient before spatial encoding the spins in the opposite direction with the second gradient and returning the magnetisation into the longitudinal direction for the remainder of the diffusion delay. The phase changes caused by convection in the first half of the sequence are cancelled out in the second half, because diffusion is a random process it is not affected. One disadvantage of this sequence is the 50% reduction in signal intensity compared to the sequence without convection compensation.

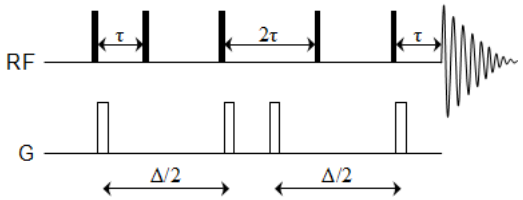

Figure 1.11: Stimulated echo sequence with convection compensation.

1.2.2.4 Multicomponent Analysis

Issues arise in the analysis of multicomponent mixtures when the peaks overlap in the chemical shift domain and have similar diffusion coefficients. Monoexponential fitting of overlapping peaks results in a diffusion coefficient value which is an average of the two actual values.[100] When the diffusion coefficients of two components are significantly different biexponential fitting can be used to obtain the diffusion coefficients of the individual components. However, care must be taken with biexponential fitting as multiple diffusion coefficients can be obtained for a single component peak due to non-uniformity of the pulsed field gradients which presents as a similar decay.[100] For

multicomponent analysis the best practice is to employ non-uniform gradient correction.

There are a range of techniques which can be used to analyse multicomponent data.[92] Univariate methods, such as biexponential fitting,[100] SPLMOD[101] and CONTIN,[101] involve the analysis of each signal individually.[92] Multivariate methods, including (S)CORE[102,103] and DECRA,[104] resolve the entire spectrum of a component through utilisation of the covariance between signals of the component.[92]

1.2.2.5 Diffusion-Ordered Spectroscopy

Diffusion-ordered spectroscopy (DOSY) is a specific presentation of diffusion NMR data as a 2-dimensional spectrum with the chemical shift domain on one axis and the diffusion domain on the other axis.[105] For this analysis, the signal attenuation of each peak is fitted to an exponential decay, e.g. the Stejskal-Tanner equation (Equation 1.21).[106] Each peak in the diffusion domain is presented as a Gaussian, centered on the diffusion coefficient extracted from the fitting of the signal attenuation, with a width determined by the residual error of the fit.[107]

This presentation of data is particularly useful for mixtures as each component appears in a different position along the diffusion axis. Figure 1.12 shows an example DOSY plot of an isotropic solution of sunset yellow containing ethanol (from the purification process) and a component relating to the residual protonated solvent (HOD). Diffusion NMR data in this thesis will be presented as DOSY plots.

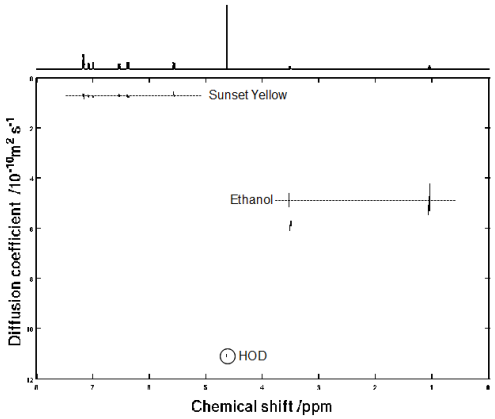

Figure 1.12: DOSY plot of a mixture.

1.2.3 Paramagnetic Ions in NMR

Paramagnetic ions have been used in NMR as shift and broadening reagents. In this thesis a paramagnetic shift reagent is utilised to differentiate between the interior and exterior environments of lipid vesicles, as discussed in Section 1.4.1.2.

Paramagnetic ions have unpaired electrons which interact with nearby nuclei and cause perturbation of the normal response of the nucleus to NMR. The electron is a spin-$^1/_2$ particle with a magnetic moment which can align with or against the magnetic field ($m_S = \pm\frac{1}{2}$). The magnitude of the electron magnetic moment is 658 times that of the proton resulting in larger local fields and much faster relaxation rates for the electron.[85]

1.2.3.1 Paramagnetic Shift Reagents

The nucleus experiences the average magnetic moment $\langle\mu\rangle$ of the unpaired electrons which contributes to the magnetic field experienced by the nucleus. The effect of this contribution to the chemical shift is called the hyperfine shift and is measured relative to the chemical shift in the presence of a diamagnetic analogue.[85] There are two mechanisms for the effect of unpaired electrons on the chemical shift of a nucleus - the Fermi contact interaction and the dipolar interaction.

Fermi Contact Shift

The Fermi contact shift is caused by the electron magnetic moment located at the nucleus, either by the unpaired electron occupying an s orbital (or a molecular orbital with s character) or through spin-polarisation of paired electrons by an unpaired electron in a p or d orbital. The contact contribution to the chemical shift is given by Equation 1.22.[85]

$$\delta^{con} = \frac{A}{\hbar}\frac{g_e\mu_B S(S+1)}{3\gamma_I k_B T} = \frac{A}{\hbar\gamma_I B_0}\langle S_z\rangle \qquad (1.22)$$
$$A = \frac{2\mu_0}{3}\hbar\gamma_I g_e \mu_B \rho$$

Where A is the contact coupling constant which expresses how much the nucleus and electron 'sense' each other[85] and is proportional to the electron spin density at the nucleus (ρ). g_e is the free electron g value, μ_B is the electron Bohr magneton, S is the electron spin quantum number, γ_I is the gyromagnetic ratio for the nucleus, k_B is the Boltzmann constant, T is the temperature and $\langle S_z\rangle$ is the expectation value of S_z.

Pseudocontact Shift

The dipolar or pseudocontact shift arises from interactions between the nuclear magnetic moment and the electron magnetic moment located outside of the resonating nucleus i.e. on the nucleus of a nearby atom, e.g. a paramagnetic metal.[85] This can be described using the metal-centered point-dipole approximation which places the unpaired electron on the metal nucleus in a paramagnetic complex. Dipolar interactions depend on both the distance between the magnetic moments and their orientation with respect to the magnetic field.[108]

In Section 1.2.1 the magnetic moment of the nucleus $\boldsymbol{\mu}$ was shown to be proportional to the spin angular momentum $\boldsymbol{I}$. The magnetic moment of the electron is also influenced by its spin angular momentum $\mathbf{S}$, but there is also an orbital contribution $\mathbf{L}$, the effect of which is to introduce an orientational dependence (anisotropy) to the magnetic moment.[85]

The average induced magnetic moment is related to the magnetic susceptibility χ through Equation 1.23.

$$\chi = \frac{\mu_0\langle\mu\rangle}{B_0} \qquad (1.23)$$

Where the magnetic susceptibility χ is the proportionality constant between the magnetisation of a substance and the applied magnetic field and is independent of the magnetic field strength.[109]

The anisotropy of the magnetic susceptibility and therefore the magnetic moment of the electron can be visualised as a set of ellipsoids, as shown in Figure 1.13 and described by the tensor $\boldsymbol{\chi}$, the principal values of which are given in Equation 1.24.

$$\chi_{kk} = \mu_0\mu_B^2 g_{kk}^2 \frac{S(S+1)}{3kT} \qquad (1.24)$$

Where g_{kk} is the principal value of the $\mathbf{g}$ tensor, such that $g_{kk}^2 = g_{xx}^2\cos^2\alpha + g_{yy}^2\cos^2\beta + g_{zz}^2\cos^2\gamma$

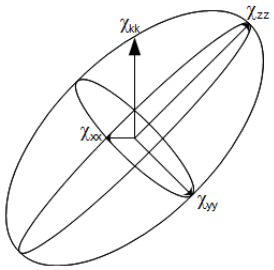

Figure 1.13: Ellipsoid representation of the magnetic susceptibility tensor $\boldsymbol{\chi}$. Figure adapted from Reference 85.

and $\cos\alpha$, $\cos\beta$ and $\cos\gamma$ are the direction cosines of the kk vector,[85] i.e. the cosines of the angles between the kk vector and the xx, yy and zz vectors respectively.

For a molecule or complex containing a paramagnetic metal ion, the ellipsoid is centered on the metal atom. The dipolar interaction between the electron magnetic moment and the magnetic moment of a nucleus within the molecule is described by the metal-nucleus vector $\mathbf{r}$, as shown in Figure 1.14.

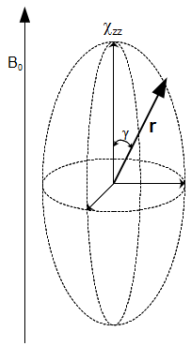

Figure 1.14: Ellipsoid representation of the magnetic susceptibility tensor $\boldsymbol{\chi}$ with an electron-nucleus dipole interaction vector $\mathbf{r}$

When the external magnetic field is aligned with the χ_{zz} direction of the molecule, as shown in Figure 1.14, the energy of the dipolar interaction can be described by Equation 1.25.[85]

$$E^{dip} = -\frac{B_0}{4\pi r^3}\hbar\gamma_I I_z \chi_{zz}(3\cos^2\gamma - 1) \tag{1.25}$$

Where r is the distance between the nuclear and electron magnetic moments (i.e. the modulus of the metal-nucleus vector), γ_I is the gyromagnetic ratio of the nucleus, χ_{zz} is the zz component of the molecular susceptibility tensor $\boldsymbol{\chi}$ and γ is the angle between the external magnetic field and the metal-nucleus vector.

When the molecule is orientated in a generic direction with respect to the external magnetic field, Equation 1.25 is expanded to include a full description of orientation of the metal-nucleus vector relative to the external magnetic field, with reference to the geometric arrangement shown in Figure 1.15.

Where $\boldsymbol{\kappa}$, $\boldsymbol{\nu}$ and $\boldsymbol{\iota}$ represent vectors along the z, x and y axes of a cartesian coordinate frame and $\boldsymbol{\kappa}$ is coincident with the external magnetic field. The molecular z axis, i.e. the direction of the χ_{zz} molecular anisotropy tensor, is defined by the vector $\boldsymbol{\lambda}$ and the metal-nucleus vector is described by $\mathbf{r}$. The angle α between $\boldsymbol{\kappa}$ and $\boldsymbol{\lambda}$ is therefore the angle between the external magnetic field and

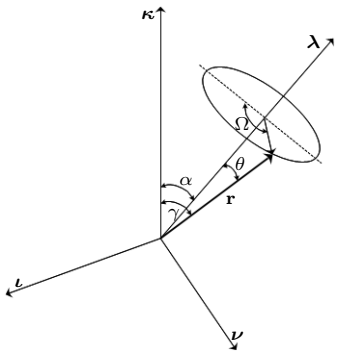

Figure 1.15: Geometric description of metal-nucleus vector arrangement. Figure adapted from Reference 85.

the χ_{zz} direction of the molecular anisotropy tensor and the angle θ describes the angle between the χ_{zz} direction and the metal-nucleus vector. The angle γ is defined as the angle between the external magnetic field ($\boldsymbol{\kappa}$) and the metal-nucleus vector $\mathbf{r}$ and is equal to θ when the χ_{zz} axis is aligned with the external magnetic field, as shown in Figure 1.14. On rotation of the molecule about the $\boldsymbol{\lambda}$ axis, the vector $\mathbf{r}$ creates a cone around $\boldsymbol{\lambda}$, the position of $\mathbf{r}$ on this cone is defined by the angle Ω.[85]

The dipolar shift equation (Equation 1.26) is derived from the expansion of Equation 1.25.

$$\begin{aligned}\delta^{dip} =& \frac{1}{4\pi r^3}[\chi_{\parallel}\cos^2\alpha(3\cos^2\theta-1)+\chi_{\perp}\sin^2\alpha(3\sin^2\theta\cos^2\Omega-1)\\ &+\frac{3}{4}(\chi_{\parallel}-\chi_{\perp})\sin 2\alpha\sin 2\theta\cos\Omega]\end{aligned} \tag{1.26}$$

Where $\chi_{\parallel}$ and $\chi_{\perp}$ are the magnetic susceptibility parallel and perpendicular to the magnetic field respectively, α, θ and Ω are the angles which describe the position of the metal-nucleus vector as shown in Figure 1.15.

Equation 1.26 describes the case in the solid state where the molecules all have the same orientation. In solution all molecular orientations are possible, the pseudocontact shift (Equation 1.27) is therefore derived by integration of Equation 1.26 over all orientations of the molecule.[85]

$$\delta^{pc} = \frac{1}{12\pi r^3}(\chi_{\parallel}-\chi_{\perp})(3\cos^2\theta-1) \tag{1.27}$$

Where θ is the angle between the χ_{zz} axis and the metal-nucleus vector.

Equation 1.27 clearly shows that the pseudocontact shift is inversely proportional to the distance r^3 between the unpaired electron and the nucleus and is also dependent on the orientation of the metal-nucleus vector (θ) within the molecule.

When the molecular susceptibility tensor $\boldsymbol{\chi}$ is isotropic, i.e. $\chi_{\parallel} = \chi_{\perp}$ the pseudocontact shift in the solution state disappears, whereas in the solid state the dipolar shift exists in a reduced form of $\delta^{dip} = \frac{1}{4\pi r^3}\chi(3\cos^2\gamma-1)$.

These equations for the dipolar and pseudocontact shifts hold for a molecule which is axially symmetric about the χ_{zz} axis (i.e. $\chi_{xx} = \chi_{yy}$), if this is not the case Equation 1.27 is expanded to Equation 1.28.

$$\delta^{pc} = \frac{1}{12\pi}\frac{1}{r^3}[\Delta\chi_{ax}(3\cos^2\theta-1)+\frac{3}{2}\Delta\chi_{rh}\sin^2\theta\cos 2\Omega] \tag{1.28}$$

$$\text{where } \Delta\chi_{ax} = \chi_{zz} - \frac{\chi_{xx} + \chi_{yy}}{2}$$
$$\text{and } \Delta\chi_{rh} = \chi_{xx} - \chi_{yy}$$

Where θ is the angle between the χ_{zz} axis and the metal-nucleus vector and ω is the angle between the χ_{xx} axis and the projection of the metal-nucleus vector onto the $\chi_{xx} - \chi_{yy}$ plane.

The pseudocontact shift is only present when the magnetic susceptibility and therefore the induced electron magnetic moment is anisotropic.[110] The anisotropy of the induced electron magnetic moment is due to an orbital contribution to the magnetic moment which is dependent on the orientation of the molecule within the magnetic field and leads to different splitting of the energy levels in different orientations.[85] The pseudocontact shift is therefore expected for paramagnetic atoms with strong spin-orbit coupling, as well as those with S$> \frac{1}{2}$ (more than 1 unpaired electron) due to zero-field splitting (ZFS) effects.

1.2.3.2 Paramagnetic Relaxation Agents

As discussed in Section 1.2.1.3, nuclear relaxation is caused by random fluctuations of the local magnetic field experienced by the nucleus. The dipolar mechanism, where the local field is generated by nearby magnetic moments (e.g. other nuclei or unpaired electrons), is dominant for spin-$^1/_2$ nuclei[84] and the electron-nucleus dipolar interaction causes both paramagnetic relaxation enhancements and the dipolar shift described above.[108] The energy of the dipolar interaction between the nucleus and an unpaired electron is much greater than that between two nuclei because the magnetic moment of the electron is 658 times that of the nucleus[108] and therefore produces larger local fields, which provide an efficient source of relaxation.[84]

Fluctuations in the local field produced by an unpaired electron can occur in three ways; 1) a change in the orientation of the electron-nucleus vector, through rotation of the complex with respect to the magnetic field, 2) a change in the direction of the electron magnetic moment, through electron spin relaxation or 3) a change in the distance between the electron and the nucleus, typically through exchange.[85] Each of these processes has a correlation time which contributes to the overall correlation time of the system, τ_c (Equation 1.29).

$$\tau_c^{-1} = \tau_s^{-1} + \tau_r^{-1} + \tau_M^{-1} \tag{1.29}$$

Where τ_s is the correlation time for electron spin relaxation and has typical values of 10^{-7}–10^{-13} s, τ_r is the correlation time for molecular rotation, which depends on the size of the molecule and ranges between 10^{-11} s for hexaaqua metal complexes in water and 10^{-6} s for large macromolecules with molecular weights of $\approx 10^6$ g mol^{-1} and τ_M is the correlation time for exchange which depends on the bond strength and can be as short as 10^{-10} s. The process with the smallest correlation time is the most dominant contribution to τ_c, such that if $\tau_s \ll \tau_r$ and there is no exchange i.e. τ_M is large, the correlation time is dependent only on τ_s, i.e. $\tau_c \cong \tau_s$.[108]

Longitudinal and transverse nuclear relaxation are dependent on the spectral density at the Larmor frequency (T_1 and T_2) and zero frequency (T_2 only), as discussed in Section 1.2.1.3 (Equations 1.14 and 1.16). The spectral density is in turn dependent on the correlation time τ_c (Equation 1.17). Nuclear relaxation in the presence of unpaired electrons is therefore influenced by electron spin relaxation, molecular rotation or chemical exchange, depending on the relative size of the correlation times for these processes. Larger τ_c values cause larger nuclear relaxation rates and therefore

increased line broadening, this is especially the case for paramagnetic relaxation agents, such as Cr^{3+}, Mn^{2+} and Gd^{3+}, which have τ_s values of 5×10^{-9}–5×10^{-10} s, $\approx 10^{-8}$ s and 10^{-8}–10^{-9} s respectively.[85]

A separate contribution to nuclear relaxation arises from the interaction of the nuclear spin with the average induced magnetic moment $\langle\mu\rangle$, which is generated by the slight preference for the $m_S = -\frac{1}{2}$ electron energy level according to the Boltzmann distribution.[85] $\langle\mu\rangle$ is a static magnetic moment related to the expectation value of S_z (i.e. $\langle S_z\rangle$). In this case the correlation time for the dipolar coupling is determined only by molecular rotation and cannot be modulated by the electron spin relaxation because $\langle S_z\rangle$ is an average over the ensemble of electron spin states.[108] This is called Curie spin relaxation or magnetic susceptibility relaxation and becomes important when electron relaxation is much faster than molecular rotation[110] and at high magnetic fields due to the dependence of Curie spin relaxation on $\langle S_z\rangle^2$ which is linearly dependent on the external magnetic field.[108]

Both of these relaxation enhancements described here are caused by dipolar interactions and as such are dependent on the distance between the nucleus and the unpaired electron as described in the case of dipolar shift reagents. Paramagnetic relaxation enhancement is more sensitive to distance than the paramagnetic shift effect, with a distance dependence of r^{-6} for relaxation compared to r^{-3} for shift.[110]

1.3 NMR Methods for Investigating Aggregation

1.3.1 Changes in Chemical Shift

Changes in the chemical shift of peaks has been shown to occur on formation of $\pi - \pi$ stacked aggregates of sunset yellow,[21] and orange II.[4] A decrease in chemical shift is observed on increasing concentration, i.e. with increasing aggregate size, the upfield shift is attributed to shielding effects from the aromatic rings of neighbouring molecules in the aggregate stack.[21] The magnitude of the change in chemical shift for each of the protons in the molecule has been used to determine the orientation of the molecules within the stacks.[4,21] The concentration dependence of the chemical shifts can also be used to determine equilibrium constants for the stacking process.[22] The upfield shift on stacking has also been observed in the NMR spectra of nucleic bases, such as purine and its nucleoside derivatives inosine and adenosine.[111]

Self-association can be described by a set of successive equilibria with associated equilibrium constants (Equation 1.30).[111]

$$\begin{aligned} A + A &\rightleftharpoons A_2 & K_2 &= [A_2]/[A]^2 \\ A_2 + A &\rightleftharpoons A_3 & K_3 &= [A_3]/[A_2][A] = [A_3]/K_2[A]^3 \\ A_3 + A &\rightleftharpoons A_4 & K_4 &= [A_4]/[A_3][A] = [A_4]/K_2K_3[A]^4 \\ A_{i-1} + A &\rightleftharpoons A_i & K_i &= [A_i]/[A_{i-1}][A] = [A_i]/(K_2 \ldots K_{i-1})[A]^i \end{aligned} \tag{1.30}$$

There are two frequently used models, the equal K or isodesmic model and the attenuated K model. In the equal K (EK) model all equilibrium constants are equal ($K_E = K_2 = K_3 = K_i$), whereas in the attenuated K (AK) model the equilibrium coefficient decreases with increasing aggregate size ($K_A = 2K_2 = 3K_3 = iK_i$). Both of these models can be adapted to allow the dimer formation

step to have a different equilibrium constant to the following steps. In the EK model the ratio ρ is defined as K_2/K_E, such that $K_E = K_2/\rho = K_3 = K_i$, when $\rho > 1$ dimer formation is easier than the formation of larger aggregates, if $\rho < 1$ dimer formation is more difficult and $\rho \ll 1$ describes a nucleation process. A similar ratio is employed in the attenuated K model, $\tau = 2K_2/K_A$ where dimer formation is favoured if $\tau > 2/3$.

The modelling of the chemical shifts of nucleic bases and nucleosides using the equal K and attenuated K models to determine equilibrium coefficients for the stacking process has been discussed in detail by Martin et al.[111] Analysis of ^{1}H and ^{13}C chemical shift data for purine yielded K_E values of 2.3 and 3.0 for the different nuclei using the EK model and K_A values of 6.2 and 7 using the AK model. The values for the two nuclei are in good agreement and differences between the models are expected due to differences in the set up of the relative equations, from the equation for the equilibrium constant of a trimer, ($K_3 = K_E = K_A/3$), K_A is expected to be approximately equal to $3K_E$.[111] Analysis of ^{1}H chemical shift data for other purine derivatives and $\pi - \pi$ stacking molecules yielded K_E values ranging from 4.1 for 6-methyl purine to 41 for 1,10-phenanthroline with corresponding K_A values of 12 and 119 for the same compounds and these are consistent with the approximation of $K_A \approx 3K_E$.[111]

Simplified analysis of the chemical shift data of sunset yellow using the isodesmic (EK) model, without factoring in a different equilibrium constant for dimer formation or the difference in chemical shift expected for molecules at the end of stacks compared to those in the centre, yielded different equilibrium constants depending on which end of the concentration scale the fit of the data was optimised.[22] Equilibrium constants obtained in this analysis were $K = 36$ for concentrations close to the formation of the liquid crystal and $K = 311$ at very low concentrations, when aggregates were close to monomeric. The deviations from the isodesmic model at intermediate concentrations indicates that this model is not suitable for the aggregation of sunset yellow.[22]

Changes in chemical shift values have also been used in studies of protein aggregates, Comellas et al. used changes in ^{13}C chemical shift values of α-synuclein incubated for different periods of time as indication of a change from α-helix to β-sheet structure.[112]

1.3.2 Diffusion NMR

The translational diffusion coefficient measured in diffusion NMR experiments is related to molecular size through the Einstein-Sutherland equation (Equation 1.31).

$$D = \frac{k_B T}{b\pi\eta r_S} \tag{1.31}$$

Where D is the diffusion coefficient, η is the viscosity of the solution and r_S is the hydrodynamic radius of the molecule. b represents the boundary conditions (the interaction between the analyte molecule and the solvent) and varies between 4 and 6. When $b = 6$ the denominator of Equation 1.31 is called the Stokes law and Equation 1.31 is referred to as the Stokes-Einstein equation.[92]

The formation of aggregates results in an increase in size of the molecular assembly, this leads to a decrease in the diffusion coefficient, through the Einstein-Sutherland equation, which can be followed using diffusion NMR methods such as pulsed-field gradient NMR (PFG-NMR) or diffusion-ordered spectroscopy (DOSY).

Several studies have used PFG-NMR to determine the oligomeric state of a protein in solution[113,114]

either by comparing the diffusion coefficient of a protein suspected to be an oligomer with that of a known monomeric protein of a similar size,[113] or by monitoring changes in the diffusion coefficient on addition of a detergent.[114] PFG-NMR was also used to study the aggregation state of lysozyme at a range of concentrations in varying temperature, pH and salt concentration.[115]

Diffusion NMR has also been used to determine the length distributions of amyloid fibrils[116] formed of an $(SH3)_2$ domain with an apo-cytochrome attached.[117] The apo-cytochrome remains unfolded and mobile even on formation of fibrils allowing the acquisition of well-resolved ^{1}H peaks not available for pure $(SH3)_2$ fibrils.[117] In this study, due to the large size of the fibrils, the effective diffusion coefficient measured by the NMR experiment was considered as a combination of translational and rotational diffusion. In large molecules where the displacement due to translation diffusion is comparable to the radius, the rotation of the molecule will contribute to the displacement observed during the diffusion NMR experiment and lead to an underestimation of the translational diffusion coefficient unless the rotational diffusion is included in the analysis.[118] The fibril length obtained in this analysis was found to be comparable to those found in TEM and AFM images, whereas analysis without inclusion of rotational diffusion produced underestimated fibril lengths.[117]

Diffusion-ordered spectroscopy, has been applied to studies of $\pi - \pi$ stacked aggregates.[23,119,120] Studies of chloroacetamides such as metolachlor and acetochlor showed ^{1}H spectra with separate signals for the aggregates and monomers at concentrations above the reported solubility. The DOSY plots gave smaller diffusion coefficients for the aggregate signals compared to the monomer signals, consistent with an increased molecule size.[119,120] The diffusion coefficients obtained from DOSY plots of acetochlor, metolachlor and pretilachlor were used to calculate the hydrodynamic radii of the monomeric and aggregate forms using the Stokes-Einstein equation.[120] In contrast to the study of the chloracetamides, the ^{1}H spectra of sunset yellow showed a single peak, as observed for other azo dye aggregates[4,9] and the DOSY experiments yielded a single diffusion coefficient, this was attributed to fast exchange between the monomers and aggregates.[23] In the study of sunset yellow the DOSY data was used to model the aggregation behaviour using a thermodynamic model of aggregation to determine the interaction energy between monomer units.[23]

1.4 Investigating the Interactions between Aggregates and Biological Systems

The interaction of protein aggregates with cell membranes is an important consideration in investigating the cause of amyloidosis diseases, such as Alzheimer's and Parkinson's. The degradation of cellular function in neurodegenerative diseases is thought to be a consequence of the interaction between protein aggregates and cell membranes.[2] There is evidence that the interaction is mutually disruptive to both the protein and the lipid membrane; the lipid-water interface promotes aggregation and the protein aggregates perturb the structure of the bilayer, which *in vivo* causes increased membrane permeability and disrupts the ionic balance.[121] There are several proposed mechanisms for the permeation of membranes by amyloid aggregates, including pore formation, nonspecific binding and detergent-like solubilisation.[31,121] Increased understanding of the interaction between amyloid aggregates and phospholipid membranes will improve the understanding of the amyloidosis diseases and therefore aid the development of treatments for these diseases.

1.4.1 Modelling Biological Systems

Biological cells are complex constructs, the cell membrane is a bilayer composed of a range of phospholipids[43] containing membrane proteins, functional additives, such as sterols (e.g. cholesterol),[122] and other lipids such as sphingolipids and glycolipids. The fluid mosaic model of the cell membrane (Figure 1.16) where globular proteins are embedded in a phospholipid matrix was proposed by Singer and Nicholson in 1972 and described as 'two-dimensional solutions of oriented globular proteins and lipids'.[123] The proteins are arranged such that ionic and polar groups occur at the surface of the membrane and non-polar groups are buried within the hydrophobic core of the phospholipid bilayer.

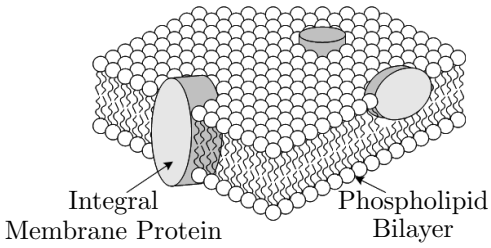

Figure 1.16: Fluid mosaic model of a cell membrane

A model system for a cell membrane should mimic the properties of the membrane as close as possible while reducing the complexity of the system. Vesicles prepared from phospholipids provide a simple model of a cell membrane, with physical properties which can be systematically altered by changes in composition.

1.4.1.1 Phospholipid Vesicles as Biomimetic Membranes

Phospholipids are amphiphilic molecules composed of a polar phosphate head group attached to hydrophobic fatty acid chains through a glycerol linker unit. Figure 1.17 shows the structure of 1-palmitoyl-2-oleoyl-sn-glycero-3-phosphocholine (POPC), a phospholipid frequently found in cell membranes, where the fatty acid chains are palmitic acid (hexadecanoic acid) and oleic acid (*cis*-9-octadecenoic acid). The common head groups and fatty acid chains are summarised in Table 1.2a and 1.2b respectively. Throughout the remainder of this thesis phospholipids will be referred to by four letter abbreviations, the first two denoting the fatty acid chains and the latter two the headgroup as given in these tables. Phospholipids with two identical fatty acid chains are identified by an abbreviation beginning with D, e.g. DMPC is 1,2-dimyristoyl-sn-glycero-3-phosphocholine.

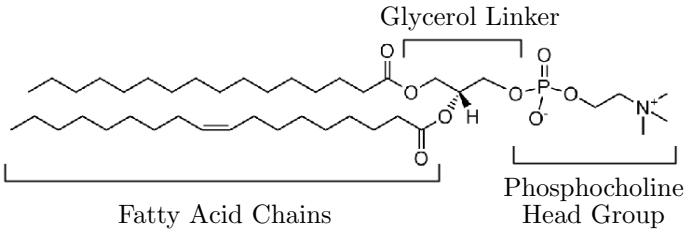

Figure 1.17: Structure of a phospholipid

Phospholipids assemble into bilayer and vesicular structures in aqueous solution in order to reduce unfavourable interactions between the hydrophobic chains and the aqueous solution. The preference for a bilayer structure compared to a micellar structure favoured by single chain amphiphiles

Table 1.2: Structural Information for Phospholipids

(a) Head Groups[124]

Head Group	Abbreviation	Structure
Phosphate	PA	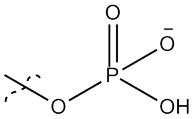
Choline	PC	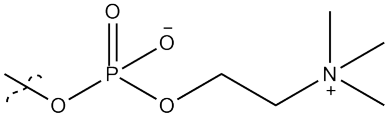
Ethanolamine	PE	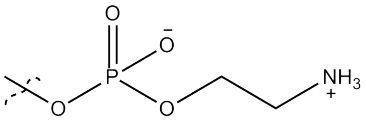
Glycerol	PG	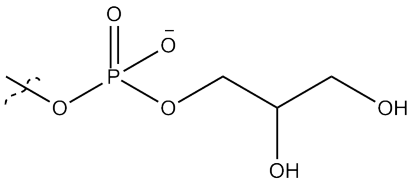
Serine	PS	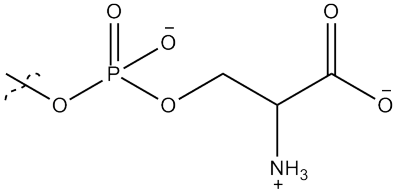

(b) Fatty Acid Chains[125]

Fatty Acid	Abbreviation	Formula	Systematic Name
Myristic	M	$C_{14}H_{27}COOH$	tetradecanoic acid
Palmitic	P	$C_{16}H_{31}COOH$	hexadecanoic acid
Stearic	S	$C_{18}H_{35}COOH$	octadecanoic acid
Oleic	O	$C_{18}H_{33}COOH$	*cis*-9-octadecenoic acid
Linoleic	L	$C_{18}H_{31}COOH$	*cis,cis*-9,12-octadecadienoic acid

(such as lyso-phospholipids and surfactants) is a consequence of the steric hindrance of the two hydrocarbon chains.

There are several types of bilayer structure formed by phospholipids, shown in Figure 1.18. A multilamellar vesicle (MLV) is formed on dissolving the phospholipid in aqueous solution (Figure 1.18a), unilamellar vesicles of varying size (Figure 1.18b) can be prepared from MLV solutions. Large unilamellar vesicles (LUVs) with diameters of approximately 100 nm are formed by extrusion, small unilamellar vesicles (SUVs) with diameters of 20–50 nm are formed by sonication. Vesicles with larger diameters of 1–100 μm are called giant unilamellar vesicles (GUVs) and can be prepared by controlled hydration of a dry lipid film with minimal agitation.[126] Unilamellar vesicles are considered as the most biologically relevant membrane model due to the encapsulation of an aqueous solution and spherical shape.[31] Another form of phospholipid bilayer sometimes used as a model membrane is the planar lipid bilayer which is a short bilayer formed between two solid supports (Figure 1.18c), these bilayers are used in conductance measurements of ion transport across the membrane.[31]

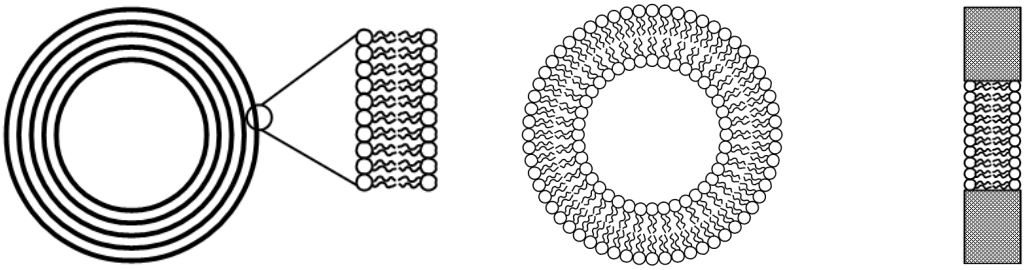

(a) Multilamellar Vesicle (MLV) (b) Unilamellar Vesicle (c) Planar Bilayer

Figure 1.18: Types of bilayer structures

1.4.1.2 Physical Studies of Phospholipid Vesicles

The similarity of the unilamellar phospholipid vesicle with the cell membrane makes it a useful model with which to study the physical properties of membranes. A wide range of techniques have been applied to the study of phospholipid vesicles, yielding information regarding parameters such as structure, size and stability under varying conditions.

Methods for determining the size of vesicles, or the size distribution, include light scattering (e.g. dynamic light scattering/photon correlation spectroscopy),[127,128] gel filtration chromatography[128] and sedimentation velocity measurements.[129] Photon correlation spectroscopy was used to determine the minimum hydrodynamic radius of sonicated vesicles formed by phospholipids with hydrocarbon chains of increasing length.[127] These methods can be used to determine the effect of additives, such as cholesterol, on the vesicle size. Electron microscopy has also been used for size determination; images of phospholipid vesicles were used to demonstrate the decrease in vesicle size after sonication.[130]

The bilayer has two significant phases, the gel phase where the hydrocarbon chains are crystalline[131] and the liquid-crystalline phase where the organisation of the hydrocarbon chains is more liquid-like.[132] The temperature of the phase transition is determined by differential scanning calorimetry (DSC)[131] and is influenced by the polar head group, the length of the hydrocarbon chains and the presence of double bonds in the hydrocarbon chains.[128] The phase transition temperature is sensitive to alterations in the packing of the bilayer, as occurs on incorporation of additives, such as proteins or drug molecules, into the bilayer.[128] The effect on the transition temperature of an

additive is dependent on its position in the bilayer, high-sensitivity DSC (HSDSC) is therefore a useful method for the prediction of protein location within a lipid bilayer.[128]

The thickness of the bilayer is an important factor in biological membranes, mismatch between the length of the hydrophobic core of the bilayer and the hydrophobic segment of an intrinsic membrane protein can affect protein insertion and function as well as lipid organisation.[133] Information regarding the bilayer thickness can be obtained using small-angle neutron scattering,[134,135] neutron diffraction[136] and X-ray scattering.[137] It has been shown, for vesicles formed by a single phospholipid, that the bilayer thickness is dependent on the length of the hydrocarbon chains of the phospholipid, increasing linearly as the number of carbons per chain increases.[137] Small-angle neutron scattering showed an increase in bilayer thickness on incorporation of three sterols, cholesterol, ergosterol and lanosterol, in the vesicle bilayer.[135]

The distribution of lipids between the interior and exterior leaflet of the bilayer and the effect of additives such as cholesterol or lyso-phospholipids has frequently been determined by NMR. Separation of ^{1}H NMR peaks belonging to molecules on the interior and exterior leaflets of sonicated lecithin (phospholipid extract from egg yolk[138]) dispersions by addition of paramagnetic ions was first described by Bystrov et al. in 1971.[139] The $N^{+}(CH_3)_3$ signal of molecules on the exterior surface of the phospholipid vesicles were broadened on addition of Mn^{2+} ions and shifted upfield by Eu^{3+} ions, when the paramagnetic ion was added to the exterior volume of the vesicles. The effect of a range of lanthanide ions as shift and broadening reagents in studies of model membranes[140] indicated a predominantly dipolar mechanism for both the shifting caused by Pr^{3+}, Eu^{3+}, Tb^{3+}, Dy^{3+} and Tm^{3+} and the significant broadening caused Tb^{3+}, Dy^{3+} and Gd^{3+}. In addition, this study showed that praseodymium caused greater shifting than europium (although downfield rather than upfield) and less broadening with comparable Ln^{3+} concentrations. The separation of the interior and exterior signals allows the quantification of the relative amount of phospholipid in each leaflet through comparison of peak areas,[141] a range of studies using ^{1}H, ^{13}C and ^{31}P NMR spectra with different paramagnetic ions yielded outside/inside ratios of 1.7-2.1 for sonicated egg phosphatidylcholine vesicles.[142] The asymmetry of vesicles containing charged phospholipids,[143,144] lyso-phospholipids[145] and cholesterol[146,147] have also been determined using this method.

Transport of cations across the cell membrane is an important process in biology, usually enabled by two classes of membrane proteins known as channels and pumps.[43] Insight into ion transport has been gained through studies of membrane-active antibiotics,[148] with model membranes, such as planar lipid bilayers[148] and vesicles.[149,150] A wide range of antibiotics have been studied, such as alamethicin and gramicidin which form channels or pores in the membrane and valinomycin and nonactin which act as carriers.[151] Conductivity studies using planar lipid bilayers measure the current across the membrane when a constant potential is applied, the fluctuations in the current give an insight into the ion transport across the membrane by the incorporated antibiotic.[148] NMR studies of ion transport utilising phospholipid vesicles were developed as an analogous method to the planer lipid bilayer studies.[149] In these studies the differentiation of the interior and exterior volumes was achieved using paramagnetic ions, as described above. Initially, the transport of paramagnetic lanthanide ions was monitored using the phospholipid signals of the vesicles.[149] This method had two disadvantages, firstly, small vesicles had to be used in order to maintain resolved resonances, secondly, the use of lanthanide ions as surrogates for the cations observed in nature was not compatible with highly selective membrane transporting proteins.[150] The solution to these problems was the use of lanthanide complexes, such as $Dy(NTA)_2^{3-}$, which binds to the Na^{+} cations producing an upfield shift.[152] When added to the exterior volume of phospholipid

vesicles the differentiation of interior and exterior ^{23}Na peaks was achieved.[150] Exchange between the interior and exterior volumes on incorporation of a range of ionophores (e.g. gramicidin,[150,153] monensin[154,155] and lasalocid A[156]) in phospholipid vesicles has been studied by montoring relative intensities of the two resonances[150] or by magnetisation transfer experiments.[157]

1.4.2 Studies of Aggregate-Membrane Interactions

The interaction of amyloid-forming proteins with membranes has two aspects, firstly, the promotion of aggregation by the lipid surface and secondly, the disruption of the membrane caused by the aggregates. Both of these are key factors in the study of amyloidosis diseases and have therefore been the focus of a large number of studies, utilising a range of techniques including fluorescence, microscopy, EPR and NMR.[31] A selection of these studies, the methods used and the conclusions drawn will be presented here.

The physiological concentration of amyloid proteins is typically far lower than the concentrations studied *in vitro* which show nucleation fibrillisation pathways above a critical concentration. It is suggested that *in vivo* fibrillisation occurs via a template-assisted mechanism where the cell membrane is a likely catalyst.[31] The binding of the amyloid proteins to the membrane surface increases the local protein concentration, promoting the shift to β-sheet conformation and aggregation.[31]

Membrane mediated protein misfolding has been shown to take place via α-helical intermediates.[31] The membrane-bound form of α-synuclein as an α-helix lying parallel to the curved surface of a vesicle[158] and the insertion of IAPP into an LUV, also as an α-helix parallel to the membrane surface[159] were both determined using site-directed spin labelling (SDSL) and EPR. In SDSL the proteins are labelled with spin labels (e.g. MTSL ((1-oxyl-2,2,5,5-tetramethylpyrroline-3-methyl)-methanethiosulfonate)[159]) in specific positions and EPR spectra in the presence of lipid vesicles are acquired. For IAPP and α-synuclein in the presence of phospholipid vesicles α-helix structures were derived from measures of accessibility to paramagnetic quenchers. Sites exposed to the membrane are more accessible to O_2 and solvent-exposed sites are more accessible to nickel(II)-ethylenediamine-N,N′-diacetic acid (NiEDDA). Accessibility parameters Π for O_2 and NiEDDA which are periodic and out of phase indicate asymmetrically solvated helices where one side (NiEDDA accessible) is exposed to the solvent and the other side (O_2 accessible) is exposed to the membrane.

Fluorescence techniques, such as fluorescence microscopy,[160–162] tryptophan fluorescence[163] and fluorescence of lipophilic probes[164,165] have been widely employed in studies of aggregate-membrane interactions. Incorporation of fluorescently labelled lipid molecules, such as DOPE-Rhod[i][162] and BODIPY-PC[ii][161] into bilayer preparations and fluorescent labelling of proteins allows the acquisition of images of the membrane-protein system by fluorescence microscopy.[161,162] Fluorescence microscopy of DOPE-Rhod labelled GUVs (giant unilamellar vesicles) and fluorescently labelled α-synuclein showed binding of the α-synuclein to GUVs formed of the negatively charged POPG, DOPA and POPS lipids but not to GUVs formed of the neutral lipid POPC.[162] The same study showed that α-synuclein has a preference for less densely packed lipids. In vesicles where DOPE-Rhod was segregated into disordered (Ld) domains, fluorescence microscopy showed that α-synuclein was accumulated in the same location.[162] Fluorescence microscopy has also been used to show the co-localisation of hIAPP and membrane lipids in both GUVs and rat insulinoma tumour cells,

[i] 1,2-dioleoyl-phosphatidylethanolamine-(lissamine rhodamine B)
[ii] 1-hexadecanoyl-2-(4,4-difluoro-5-methyl-4-bora-3a,4a-diaza-s-indacene-3-dodecanoyl)-glycero-3-phosphocholine

as well as the disruption and leakage of GUV membranes on addition of hIAPP, followed by the incorporation of the lipid molecules into hIAPP aggregates.[160]

Proteins containing tryptophan, tyrosine and phenylalanine have intrinsic fluorescence which can be used for determination of protein structure and dynamics.[166] Tryptophan fluorescence is most commonly used due to its sensitivity to its environment compared to tyrosine and its strong fluorescence in comparison to phenylalanine. Tryptophan residues can be utilised as site-specific intrinsic fluorescent probes in studies of proteins. The emission spectrum of tryptophan fluorescence is blue shifted when the environment is changed from an aqueous solution to a hydrophobic environment, such as a lipid bilayer, tryptophan fluorescence can therefore be used to study membrane insertion.[163] The insertion of Aβ into SUV membranes was studied by tryptophan fluorescence, the preference of Aβ for anionic membranes was shown by a greater blue shift for DPPC/PG SUVs (15 nm) than for DPPC SUVs (3 nm). The same observation was made for POPC/PG vs POPC SUVs, these lipids are liquid-crystalline at room temperature compared to DPPC/PG which are in the gel phase. This observation indicated that Aβ insertion is not dependent on the membrane fluidity.

Incorporation of fluorescent probe molecules, such as 1,6-diphenylhexatriene (DPH)[165] and 6-dodecanoyl-2-dimethylnaphthalene (Laurdan),[164,165] into lipid bilayers provides access to information regarding the lipid chain dynamics and fluidity of the membrane.[31] DPH acts as a sensor for perturbations in the packing of the acyl chains[167] and Laurdan is polarity-sensitive and used to measure lipid order[164] and phase transitions.[165] Both DPH and Laurdan were used in a study of lipid packing of phospholipid vesicles with α-synuclein, binding of the α-synuclein was shown to increase the phase transition temperature of DPPC vesicles, evidenced by fluorescence anisotropy of DPH and a shift in maximum fluorescence wavelength of Laurdan.[165]

Dye leakage assays are a common method for detecting membrane permeation,[31] this is usually achieved through encapsulation of fluorescent dyes which undergo a change in fluorescence as they leak from the interior of the vesicle due to the weakening of the bilayer. Dye leakage assays do not provide the mechanism of membrane disruption as any mechanism which produces defects in the bilayer can lead to dye leakage,[31] however size selectivity in dye leakage is indicative of a pore-like mechanism of membrane disruption and can be used to determine the size of the pores.[31,168]

Typical probe molecules in dye leakage assays include the self-quenching fluorophores, carboxyfluorescein[163] and calcein,[162,169] where the fluorescence increases on reduction of concentration below the self-quenching concentration and fluorescent dye complexes, e.g. Tb^{3+}/DPA and Ca^{2+}/Fura-2,[168,170] where the fluorescence of the dye increases on complexation to the cation. Dye leakage assays have been used to study membrane permeation by a range of amyloid proteins, including Aβ,[163,169] IAPP,[168] and α-synuclein[162,170,171]

A dye-leakage study of Aβ using carboxyfluorescein showed that permeation occurred with vesicles in the liquid-crystalline phase, but not the gel phase, indicating that membrane permeation is dependent on the fluidity of the membrane.[163] The ability of Aβ to cause membrane permeation of calcein-encapsulated LUVs was also shown to depend on incubation time of the peptide, with shorter incubation times producing greater calcein leakage, indicating the greater potency of the smaller oligomers of Aβ.[169]

Calcein leakage caused by α-synuclein was shown to depend on the composition of the lipid headgroup; LUVs formed of 1:1 POPC/DOPA showed an increase in calcein fluorescence on addition of α-synuclein, but those formed of 1:1 POPC/POPG were not permeabilised and therefore

showed no fluorescence increase.[162] Studies of PG vesicles with Fura-2 encapsulated inside and Ca^{2+} in the exterior solution showed an increase in fluorescence on addition of α-synuclein protofibrils, but not monomers or fibrils.[171] The increased fluorescence was attributed mainly to influx of calcium rather than efflux of Fura-2, based on fluorescence measurements after separation of vesicles from the exterior solution by gel filtration and comparison with the results of complete permeabilisation by ionomycin and Triton X-100.[171] A subsequent study by the same group used this process to monitor the size selectivity of vesicle permeabilisation by α-synuclein, it was shown that there was an inverse correlation between the extent of leakage of a range of fluorescent molecules (e.g. cytochrome c, FITC-dextran and dopamine) and the molecular mass. This observation indicated a pore-like mechanism of permeation for α-synuclein in the presence of calcium.[170] Size selectivity in the membrane permeation of vesicles has also been shown for IAPP, the degree of permeation increased for molecules of decreasing size indicating a pore-like mechanism.[168]

Membrane permeation by a range of amyloidosis aggregates has been suggested to occur via a pore-like mechanism.[31,172] Ion-permeable channels formed by Aβ were first described by Arispe et al.;[173] ion-channel activity was shown by discrete changes in conductance on incorporation of Aβ into a planar lipid bilayer.[173–175] Ion channels have also been detected, typically by current measurements through lipid bilayers,[176] in other amyloid peptides, including IAPP, α-synuclein and polyglutamine (related to huntingtin toxicity).[172] The conductance data have since been supported by the visualisation of annular structures in AFM and EM images of protofibrillar aggregates of Aβ,[176–178] α-synuclein[176,178,179] and other amyloid proteins[176] in the absence and presence of membranes.

Solid state NMR studies of amyloid protein interactions with membranes have typically employed ^{31}P and ^{2}H NMR to obtain information on the effect of protein binding on the order and dynamics of the phospholipids of the membrane. These studies usually utilise multilamellar vesicles because the smaller diameter of LUVs allows motional averaging of the ^{31}P chemical shift anisotropy (CSA) and the ^{2}H quadrupolar splitting.[180,181] The ^{31}P nuclei of the phospholipid headgroups provide a naturally abundant probe for the organisation of the lipids within the bilayer, the appearance of the solid state spectrum is dependent on the phase of the phospholipid assembly.[182] Spectra of bilayers appear as powder patterns with a high field peak and low field shoulder, whereas hexagonal phases have a low field peak with a high field shoulder and phases where isotropic motion is prevalent, e.g. small vesicles or micelles, display narrow symmetric peaks.[183] ^{2}H spectra can provide information on the motion of either the headgroups,[182,184] or the acyl chains,[181,185] depending on the position of deuteration of the lipid. The quadrupolar splitting of the ^{2}H peak is used as a measure of the orientation and ordering of the labelled section.[184]

Studies of Aβ and α-synuclein using solid state NMR have shown varying degrees of interaction between the protein and the phospholipid bilayer. ^{31}P spectra and ^{2}H quadrupolar splitting values of dPOPC/POPG MLVs presented by Terzi et al. showed no difference with or without Aβ(1–40).[184] In a separate study by Lau et al. addition of Aβ(1–42) to dPOPC/POPS MLVs also resulted in only minor changes to the ^{31}P CSA and ^{2}H quadrupolar splitting, however incorporation of the Aβ into the bilayer lead to the appearance of an isotropic component indicating reduced stability of the bilayer.[181] The addition of α-synuclein to MLVs composed of DMPC-d4, deuterated at the methylene positions of the headgroup and mixed MLVs of DMPC-d4/DOPG, DMPC-d4/DOPS and DMPC-d4/BPI[iii], caused changes to the ^{31}P and ^{2}H NMR spectra depending on the lipids in the MLV.[182] There was no effect on the DMPC MLVs, consistent with documented observations that α-

[iii] BPI is bovine L-α-phosphatidylinositol

synuclein only interacts with negatively charged membrane surfaces.[162] The addition of α-synuclein to MLVs containing DOPG, DOPS and BPI caused changes to the quadrupolar splittings of both methylene resonances as well as changes to the lineshape of the ^{31}P spectra, with DMPC/DOPG MLVs showing the most change with a narrowing of the ^{31}P spectrum indicating disruption of the lamellar structure into small vesicles.[182]

A wide range of biophysical techniques have been applied to the investigation of aggregate-membrane interactions and the mechanism of membrane permeation, a selection of which have been highlighted here. While there is general consensus that the oligomeric or protofibrillar aggregates are the cytotoxic species,[32] the precise structure of the aggregate and the mechanism of membrane disruption is unresolved, with evidence presented for both a pore-like mechanism and a non-specific or detergent-like mechanism.[31] Ongoing investigation of aggregate-membrane interactions and membrane permeation is clearly an important step in the understanding and potential treatment of the amyloidosis diseases.

1.5 Thesis Outline

This thesis is concerned with the development of NMR methods for the purpose of investigating aggregation, through direct observation of aggregating molecules and by monitoring the effects of aggregates on model membrane systems.

Chapter 2 will outline the experimental methods and materials used in this thesis.

Chapters 3 and 4 focus on the development and application of diffusion-ordered spectroscopy in the presence of a size-exclusion chromatography stationary phase, described as SEC-DOSY. Chapter 3 describes the development of SEC-DOSY, using polymers, polymer mixtures and a range of poly(styrene-4-sulphonate) molecular weight reference standards. In Chapter 4 the method of SEC-DOSY is applied to two aggregate systems, firstly the concentration dependent aggregation of the $\pi - \pi$ stacked system of sunset yellow, secondly the time-dependent aggregation of insulin under acidic and high temperature conditions.

Chapters 5 and 6 cover the investigation of phospholipid vesicles as biomimetic membranes and their use in studying membrane permeation by Amyloid-β (Aβ) aggregates. Chapter 5 focusses on the optimisation of a phospholipid vesicle system for NMR analysis including preparation methods and membrane composition, followed by time-resolved stability and peak shifting studies and the examination of a positive control of membrane permeation through solubilisation by detergent. Chapter 6 presents experiments investigating membrane permeation by Aβ, using the established method of calcein leakage monitored by fluorescence and by monitoring the changes in ^{31}P NMR peaks.

Chapter 2

Materials and Methods

This chapter will detail the materials used in experiments and their sources, methods of sample preparation and methods of data acquisition and analysis used throughout this work.

2.1 Materials

2.1.1 Chemicals

For the diffusion NMR experiments (chapters 3 and 4), all polymers were acquired from Sigma Aldrich, except the poly(styrene-4-sulphonate) molecular weight reference standards which were from Kromatek.

The size-exclusion stationary phases used in these experiments were all acquired from Sigma Aldrich. Sephadex is a dextran matrix cross-linked with epichlorohydrin supplied as a powder and Superdex is a composite of cross-linked agarose and dextran, supplied as suspensions in 20% aqueous ethanol. All Sephadex phases were 'superfine' with particle sizes of 20–50 μm and the Superdex phases were 'prep grade' with particle sizes of 22–44 μm. The fractionation ranges and other pertinent information for the stationary phases used in this thesis are detailed in Table 2.1.

Table 2.1: Properties of Stationary Phases[186]

Stationary Phase	Particle size (μm)	Fractionation Range (kDa)		Bed Volume (ml g^{-1} dry Sephadex)
		Globular Proteins	Dextrans	
Sephadex G-50	20–50	1.5–30	0.5–10	9–11
Sephadex G-75	20–50	3–70	1–50	12–15
Sephadex G-100	20–50	4–100	1–100	12–15
Superdex 75	22–44	3.0–70	0.5–30	–
Superdex 200	22–44	10–600	1.0–100	–

Other chemicals used in chapters 3 and 4, including α-lactalbumin from bovine milk (purity 85–87%), sunset yellow FCF (purity 95.7%) and insulin from bovine pancreas, were obtained from Sigma Aldrich.

The phospholipids, 1,2-dimyristoyl-sn-glycero-3-phosphocholine (DMPC) and 1-palmitoyl-2-oleoyl-sn-glycero-3-phosphocholine (POPC) used for vesicle experiments in chapters 5 and 6 were obtained

from Avanti Polar Lipids Inc, with additional POPC obtained from Sigma Aldrich. The purity of the phospholipids was ≥99% from both sources. Amyloid-β peptide (Aβ) was gratefully received from the group of Professor Louise Serpell, and acquired from rPeptide. Praseodymium chloride hydrate was obtained from Sigma Aldrich with a purity of 99.9% (based on rare earth analysis). Triton X-100[i] was also obtained from Sigma Aldrich.

2.1.2 Solvents

Deuterium oxide was obtained from Goss Scientific with a purity of 99.94%D. Ethanol, methanol and chloroform were 'analytical grade' and acquired from Fisher Scientific. Where water was used to prepare samples it was always distilled water.

Phosphate buffer solutions for polymer experiments were prepared using sodium phosphate monobasic dihydrate ($NaH_2PO_4 \cdot 2\,H_2O$) and sodium phosphate dibasic (Na_2HPO_4), both of which were acquired from Sigma Aldrich with purities ≥98%.

Tris buffer solutions for vesicle experiments were prepared by dissolving tris(hydroxymethyl) aminomethane (Tris) in distilled water to a concentration of 20 mM and addition of 1M HCl to adjust the solution to pH 7.4, followed by addition of sodium chloride (Fisher Scientific) to give a concentration of 150 mM. Tris(hydroxymethyl)aminomethane (purity ≥99.8%) and hydrochloric acid (1.0 N) were obtained from Sigma Aldrich.

HEPES buffer solutions for vesicle studies were prepared by dissolving 4-(2-hydroxyethyl)-1-piperazineethanesulphonic acid (HEPES) in distilled water to a concentration of 10 mM before adjusting to pH 7.4 with a 10 M solution of sodium hydroxide and adding sodium chloride at a concentration 100 mM. HEPES (purity ≥99.5%) and sodium hydroxide (purity 98.5%) were obtained from Sigma Aldrich.

2.2 Sample Preparation

2.2.1 Stationary Phases and Polymers

Sephadex G-50 was prepared for use by swelling the powder for ∼3 hours in 11 ml of solvent per gram of dry Sephadex as specified by the supplier,[186,187] after this time more solvent was added to form a 60 mg ml^{-1} suspension. This suspension was then washed at least three times with the required solvent to remove residual ethanol. 60 mg ml^{-1} was found to be the minimum concentration, so that when settled in a 5mm NMR tube, the stationary phase covered the RF coil region.

Superdex 75 and 200 were supplied as 20% aqueous ethanol suspensions, the stationary phase was re-suspended in the bottle and the required volume removed by pipette. This suspension was then washed three times with the same volume of the required solvent to remove the ethanol. Once settled under gravity the volume of the stationary phase was ∼80% of the total volume.

Samples of stationary phases with analyte were prepared by replacing 200 μl of supernatant from the 1 ml samples of settled stationary phases with 200 μl of analyte stock solution. The stationary phase was then resuspended by vortexing to ensure thorough mixing of the analyte and stationary

[i]Triton X-100 is 4-(1,1,3,3-Tetramethylbutyl)phenyl-polyethylene glycol

phase and transferred into an NMR tube. The suspensions were allowed to settle for at least 30 minutes before NMR acquisition.

2.2.2 Sunset Yellow

2.2.2.1 Purification

Sunset yellow was supplied at a purity of ~90%[188] and was further purified by ethanol precipitation, vacuum filtration and drying overnight in a 50°C vacuum oven. A nominal 900 mM stock solution in D_2O was prepared and the concentration corrected for the presence of additional impurities using UV-vis measurements with a molar extinction coefficient 8277 M^{-1} cm^{-1} at the isosbestic point of 523 nm.

The molar extinction coefficient was determined by Jonathan Katz of the Day group. The absorbance was measured between 300 and 600 nm for a range of concentrations. These absorbance values were used to calculate the experimental extinction coefficients using the Beer-Lambert law (Equation 2.1).

$$A = \varepsilon c l \tag{2.1}$$

Where A is the absorbance, ε is the extinction coefficient, c is the concentration and l is the path length of the light through the solution (taken as the width of the cuvette).

The wavelength where the experimental extinction coefficient is the same for all concentrations is called the isosbestic point, this point is identified in Figure 2.1 as the point where the extinction coefficient plots intersect. The molar extinction coefficient was taken as the average extinction coefficient for each concentration, as calculated from the absorbance measurements at the isosbestic point.

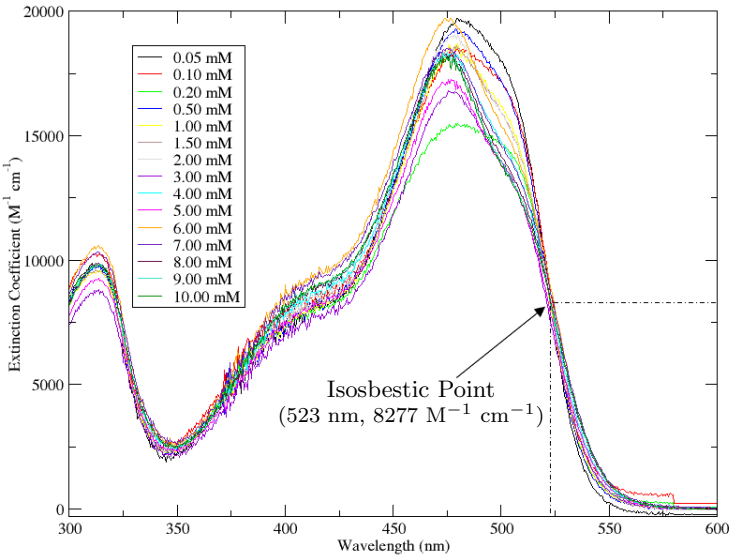

Figure 2.1: Extinction coefficients of a range of sunset yellow concentrations, across a wavelength range of 300–600 nm. Data acquired by Jonathan Katz of the Day group.

2.2.2.2 Sample Preparation

The stock solution with a corrected concentration of 833 mM was used to prepare a range of concentrations from 10 to 800 mM. 2.4 ml aliquots of each concentration (10, 25, 50, 75, 100, 200, 300, 400, 500, 600, 700 and 800 mM) were prepared and divided between four sample tubes to form the four samples: no Sephadex, Sephadex G-50, Sephadex G-75 and Sephadex G-100.

The samples with stationary phases were prepared by swelling the Sephadex stationary phases directly in the sunset yellow solutions. 36 mg of each Sephadex was weighed into 12 individual 1.5 ml sample tubes, 600 μl of a specific concentration of sunset yellow was added and the solution was vortexed and left for the stationary phase to swell for ∼3 hours. The final concentration of stationary phase was 60 mg ml^{-1} as with the polymer experiments with Sephadex G-50 described in Section 2.2.1. This concentration equates to a swelling volume of 16.67 ml per gram of dry Sephadex, above the range required for Sephadex G-75 and within the required range for Sephadex G-100. As with the polymer experiments, the samples were resuspended and transferred to NMR tubes and allowed to settle for at least 30 minutes before NMR acquisition.

2.2.3 Phospholipid Vesicles

2.2.3.1 Formation By Extrusion

10-20 mg of lipid was dissolved in 2:1 chloroform/methanol (v/v). Lipid films were then prepared by evaporating the solvent under nitrogen. These films were stored in a vacuum desiccator overnight to ensure complete removal of the solvent. If not immediately required, the lipid films were stored in a freezer at -20°C until use. The films were rehydrated with the appropriate solvent for the experiment i.e. D_2O or buffer solution (either HEPES or Tris) and vortexed to create a suspension. This was then passed 11 or 19 times through polycarbonate membranes of 50–400 nm using an Avestin extruder.

2.2.3.2 Formation By Sonication

Lipid suspensions were prepared as described for the extrusion method and then sealed in a round bottomed flask and sonicated in a water bath at 35°C for ∼3 hours or until clear.

2.2.3.3 Addition of Paramagnetic Shift Reagent

Praseodymium(III) chloride hydrate was added to the vesicles in order to induce a paramagnetic shift. For experiments where the exterior ^{31}P signal was shifted the $PrCl_3$ was added to the vesicle solution after vesicle formation. Where the interior ^{31}P signal was to be shifted the $PrCl_3$ was added prior to sonication. Any $PrCl_3$ remaining on the outside of the vesicles after vesicle formation was removed by a mini-column wash process (see Section 2.2.3.5).[128,169]

2.2.3.4 Vesicles for Calcein Leakage Experiments

Vesicles for calcein leakage experiments were prepared by sonication of the lipid suspension in 50 mM calcein, after sonication any non-encapsulated calcein was removed using the mini-column

wash described below. 50 mM calcein solutions were prepared in both 20 mM Tris HCl + 150 mM NaCl and 10 mM HEPES + 100 mM NaCl buffer solutions at pH 7.4.

2.2.3.5 Mini-column Wash Process

The mini-column wash process was used to prepare vesicles with $PrCl_3$ or calcein on the inside only, non-encapsulated material was trapped on the column while the vesicles were eluted. Mini-columns were prepared by swelling Sephadex G-50 at 10 mg ml^{-1}, once swelled the Sephadex was resuspended and added to a 1 ml syringe with a glass microfibre filter at the bottom of the barrel to support the gel, taking care to avoid air bubbles. Excess solvent was removed by a 3 minute centrifugation at 2000 rpm in a Mikro 22R centrifuge, temperature controlled at 4°C. 200 μl of vesicle solution was added to the top of the mini-column and allowed to absorb into the gel. This was then spun at 2000 rpm for 3 minutes, the vesicles were eluted and nonencapsulated material, such as exterior $PrCl_3$, remained on the column. A 40 μl stacker of solvent was added to the top of the centrifuged mini-column and the column was spun again. The eluted vesicle solution was transferred to a clean mini-column and the process repeated three times in total to ensure removal of exterior material.

2.2.4 Fibrils

2.2.4.1 Insulin

Insulin fibrils were prepared by incubating a 2 mM solution of insulin in pH 2 HCl (D_2O) at 60°C in a water bath for 48 hours. For time-resolved diffusion studies the insulin was incubated in the spectrometer, with diffusion measurements acquired every hour.

2.2.4.2 Aβ

A 20 mg aliquot of Aβ was dissolved in 200 μl hexafluoro-2-propanol (HFIP), the mixture was then vortexed for 60 s and sonicated in a bath sonicator for 5 minutes. The solvent was removed using dry nitrogen and the resulting film was vacuum dessicated for 30 minutes. The Aβ was resolubilised in DMSO at a concentration of 1 mg ml^{-1}, the solution was then vortexed for 60 s and sonicated for 5 minutes. The solvent was then exchanged for 10 mM HEPES, 100 mM NaCl, pH 7.4 solution (referred to as HEPES buffer) using a 2 ml Zeba buffer exchange spin column. The column was first equilibrated with HEPES buffer by addition of 1 ml of buffer to the column and a centrifuge cycle at 4°C and 1000 g for 2 minutes, this was repeated several times to ensure column equilibration. The solvent of the Aβ sample was exchanged by addition of the 200 μl of Aβ in DMSO to the column, followed by a 40 μl stacker of HEPES buffer, the column was then spun at 4°C and 1000 g for 2 minutes and the eluent collected in a cooled eppendorf. The eluted Aβ solution was then centrifuged at 4°C and 16000 g for 30 minutes to remove any fibrillar material and contaminants. The supernatant was transferred to a pre-cooled clean non-stick eppendorf and stored on ice until use to minimise fibrillation. The concentration of the Aβ was determined by absorbance measurements at 280 nm and a molar extinction coefficient of 1490 M^{-1} cm^{-1} using an Eppendorf Biophotometer (Eppendorf UK Ltd.,Cambridge,UK).

2.3 NMR

All experiments were performed on a Varian VNMRS 600 spectrometer (Agilent Technologies) using VnmrJ software (versions 2.2C and 3.1A). Two probes were used in these experiments, all standard liquid experiments were acquired using a 16 mm X{^{1}H} broadband probe equipped with an actively-shielded z-gradient coil capable of producing 72 G cm^{-1}. Experiments requiring magic angle spinning were acquired with a 4 mm HR-MAS ^{1}H{X} probe equipped with a magic angle gradient coil with a maximum gradient of 138 G cm^{-1} (NanoProbe™). The sample temperature was maintained at 298 K unless specified otherwise.

1D spectra were processed using MestreNova (version 6.1.1-6384). Diffusion data were analysed using DOSY Toolbox (version 0.8).[107] Time-resolved diffusion data were analysed using NMRPipe.[189]

2.3.1 1D Experiments

2.3.1.1 ^{1}H

Proton NMR spectra were acquired at a frequency of 599.7 MHz with a spectral width of 9615 Hz, 32768 data points and up to 128 transients. Where required, solvent suppression was applied using presaturation.[190,191]

2.3.1.2 ^{31}P

Phosphorus NMR spectra were acquired at a frequency of 242.8 MHz with a spectral width of 14705 Hz, 32768 data points and ^{1}H decoupling applied during acquisition. Spectra were typically acquired with 128, 256 or 1024 transients.

Time-resolved studies were acquired by arraying the pre-acquisition delay, the number of spectra to be acquired depended on the length of the study and the frequency of acquisition (typically every 30 minutes or 60 minutes), the length of the pre-acquisition delay was calculated from the difference between the time between acquisitions and the length of spectrum acquisition. For example, a 68 hour study with spectral acquisition of 128 transients (270 s) every hour gives a pre-acquisition delay of 3330 s ($60 \times 60 - 270$ s) with 69 increments, the first of which has a 0 s pre-acquisition delay.

2.3.2 Diffusion NMR Experiments

The pulse sequence used for diffusion-ordered spectroscopy experiments in this work was the One-shot pulse sequence developed by Pelta et al.[192] This pulse sequence is based on the bipolar pulse pair stimulated echo (BPPSTE) sequence[97,193] with the gradient strength of the bipolar pulses unbalanced to remove the need for phase cycling and additional gradient pulses to refocus the lock signal and maintain constant energy in the coil throughout the experiment. The pulse sequence is depicted in Figure 2.2. The equation which describes the signal attenuation of the diffusion experiment is called the Stejskal-Tanner equation, as given in Equation 1.21. The Stejskal-Tanner equation is modified for the One-shot pulse sequence to correct for the difference in the finite gradient pulse duration and signal attenuation caused by the introduction of additional gradients

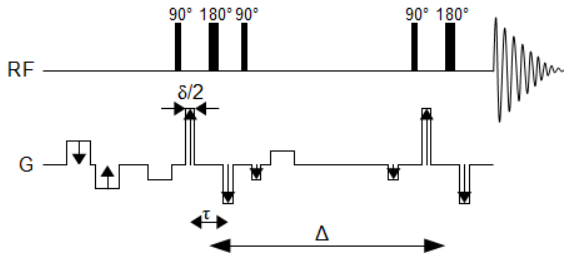

Figure 2.2: One-shot pulse sequence, arrows indicate incrementation of gradients.[192]

and unbalancing of the bipolar gradients. This modified equation is given in Equation 2.2.[192]

$$\frac{S(g)}{S(0)} = \exp\left(-\gamma^2 g^2 D\delta^2 \left[\Delta + \frac{\delta(\alpha^2-2)}{6} + \frac{\tau(\alpha^2-1)}{2}\right]\right) \tag{2.2}$$

In this equation γ is the gyromagnetic ratio of the observed nucleus, g is the strength of the applied gradient, in this case the average amplitude of the four diffusion-encoding gradients, D is the diffusion coefficient, δ is the length of the diffusion-encoding gradient (each individual pulse has a duration of $\delta/2$), Δ is the diffusion delay, the time between the two diffusion-encoding periods, τ is time between the midpoints of the pulse pairs within each diffusion-encoding period and α the factor by which the gradient strength of the bipolar pulse pairs are unbalanced.

Acquisition parameters were optimised for each set of experiments, with typical values of 0.2 s for the diffusion encoding delay (Δ), 5 ms for the gradient pulse length (δ) and sixteen gradient strengths from 4.5 to 56.25 G cm^{-1}, in equal increments with respect to g^2, α is set to 0.2 in all experiments. In DOSY experiments with MAS the gradient strengths were arrayed from 1.02 to 50.8 G cm^{-1} also in equal increments with respect to g^2.

2.3.3 Magic Angle Spinning

The glass rotors used in the magic angle spinning probe have a sample volume of 40 μl. The magic angle in the HR-MAS probe is factory set and was not adjusted in any of these experiments. Spin rates of 2000–2500 Hz were applied, selected to minimise overlap of the spinning sidebands with analyte signals.

2.3.3.1 Stationary Phase Samples for MAS

Samples with stationary phase were prepared as described above. To fill the rotor the sample was re-suspended and 60 μl pipetted into the rotor, the suspension filled the sample cavity and the space above. The stationary phase was allowed to settle for ~20 minutes before 20 μl of supernatant was removed so that all of the sample was within the sample cavity of the rotor, the rotor was sealed with the Teflon plug and the drive ring attached. Figure 2.3 shows a schematic of the rotor filling process. This protocol ensured that the rotor was filled with stationary phase with minimum excess solvent so that when spun there was little disturbance of the settled stationary phase.

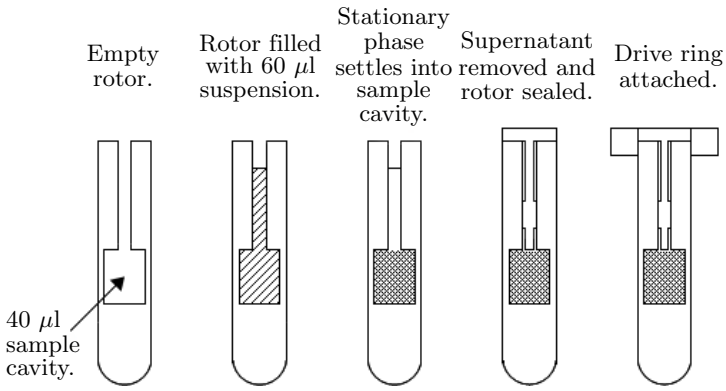

Figure 2.3: Schematic of filling process for the 40 μl rotors used in the HR-MAS probe

2.4 Other Physical Techniques

2.4.1 Size-Exclusion Chromatography

Size-exclusion chromatography (SEC) was performed at the University of Greenwich with the assistance of Professor Martin Snowden, Devyani Amin and Joanna Thorne. SEC data were obtained for each of the poly(styrene-4-sulphonate) molecular weight reference standards using a Superdex 200 10/300 GL column, borrowed from Dr Darren Thompson, on an Agilent 1200 LC system with UV detection at 254 nm. The mobile phase was 50 mM sodium phosphate and 150 mM NaCl in H_2O, 20 μl injections of the 10 mg ml^{-1} samples were used for each chromatographic run with a flow rate of 0.5 ml min^{-1}.

2.4.2 Dynamic Light Scattering

Dynamic Light Scattering (DLS) was used to assess the homogeneity and dimensions of the prepared vesicles. For these measurements the lipid vesicle solution was diluted to 1 mg ml^{-1} and transferred to a disposable cuvette. The cuvette was placed in the DLS instrument and measurements were acquired in triplicate with a viscosity value of 0.89 cP. The DLS data were acquired at 25°C using a Malvern Instruments Ltd Zetasizer Nano-S, (Model: ZEM1600) and were analysed using Dispersion Technology Software (version 5.10) by Malvern Instruments. Size distributions are given as both intensity and volume distributions.

2.4.3 Fluorescence Spectroscopy

Fluorescence measurements of calcein encapsulated vesicles were carried out on a Varian Cary Eclipse Fluorimeter with the Scan Application (version 1.1) as detailed by Williams et al.[169] Samples were transferred to a 1 cm path length quartz cuvette (Starna) with a nominal sample volume of 160 μl. Calcein fluorescence was measured using an excitation wavelength of 490 nm, emission was monitored between 500 and 600 nm, maximum fluorescence intensity occurred around 520 nm. Temperature was controlled at 20°C. Excitation and emission slits were set to 10 nm, the scan rate was set to 100 nm/min with 0.833nm data intervals and an averaging time of 0.55 s.

2.4.4 Transmission Electron Microscopy

Samples for TEM analysis were prepared on formvar/copper grids (Agar Scientific) at a typical concentration of 1 mg ml^{-1} by incubating a 4 μl drop of sample for 1 minute, followed by a 1 minute wash with H_2O and two subsequent 1 minute stains using 2% uranyl acetate. Images were taken on a Hitachi-7100 TEM with axially mounted Gatan Ultrascan 1000 CCD camera by Dr Julian Thorpe of The Sussex Centre for Advanced Microscopy.

Chapter 3

Diffusion NMR with Size-Exclusion Stationary Phases

Diffusion-ordered spectroscopy (DOSY) is the application of the pulsed-field gradient stimulated echo pulse sequence to produce a pseudo-two dimensional spectrum with a ^{1}H domain and diffusion coefficient domain.[105] The translational diffusion coefficient is related to molecular size through the Einstein-Sutherland equation (Equation 3.1).

$$D = \frac{kT}{f} \tag{3.1}$$

Assuming infinite dilution, for a spherical molecule with hydrodynamic radius r_S, the friction coefficient $f = f_{sphere} = b\pi\eta r_S$, where η is the dynamic viscosity of the solution and b depends on the boundary conditions and theoretically varies from 4 under 'slip' boundary conditions to 6 in 'stick' boundary conditions.[92] For molecular shapes other than spheres the Perrin factor $F = {}^{f}/_{f_{sphere}}$ can be applied, however closed analytical expressions for the friction coefficient, f, are only available for simple shapes such as cylinders and ellipsoids.[92]

Diffusion-ordered spectroscopy is a useful tool for the visual separation of mixtures, however issues arise in separating similar sized molecules leading to poor resolution in the diffusion domain. Several examples in the literature have shown that the addition of chromatographic stationary phases, such as silica,[194,195] or co-solutes, such as surfactants[196,197] and polymers,[198,199] improve the resolution of multicomponent mixtures in the diffusion domain.

The addition of silica aided the separation of components of varying polarity in the same way as in HPLC, polar analytes interact more strongly with the silica leading to a greater reduction in the diffusion coefficient.[194] The susceptibility broadening caused by the addition of the solid silica phase has been dealt with in two ways. Studies by Viel,[194,200] Pages[201] and Caldarelli[202] used magic angle spinning (HR-MAS) to reduce the line broadening. In contrast, Hoffman et al.[195,203] minimised the linewidth of the peaks by adjusting the magnetic susceptibility of the solvent to match that of the silica. In both cases good separation was shown for mixtures of similar hydrodynamic radius but different affinities for the stationary phase.

In the case of surfactants the incorporation of an analyte within a micelle is dependent on its hydrophobicity, more hydrophobic analytes spend more time within the micelle leading to a greater reduction in diffusion coefficient, this method was shown to separate three dihydroxybenzene

isomers.[197] The observed diffusion coefficients in the presence of micelles is described by $D_{obs} = pD_{mic} + (1-p)D_{free}$ where p is the degree of solubilisation for the analyte in the micelle.[196] A range of surfactants have been used for this application including dodecyltrimethylammmonium bromide (DTAB),[196] sodium dodecyl sulfate (SDS)[196,197,204,205] and sodium bis(2-ethylhexyl) sulfosuccinate (AOT) which forms reversed micelles.[197] An extension of the use of micelles is the application of microemulsions.[203,206,207] Microemulsions are formed by a mixture of two immiscible liquids and consist of roughly mono-disperse thermodynamically stable nano-droplets.[207] The diffusion of the analyte is altered depending on the phase of the microemulsion which it binds with. This has been succesfully applied to polyoxyethylene iso-octylphenyl, a polymer with a range of lengths on the polyethyleneoxide chain[206] and to a range of fragrance molecules with similar molecular weights.[207]

Studies by Kavakka et al. used soluble polymers to alter the diffusion of analytes.[198,199] Resolution of similar sized analytes was achieved through differences in polymer-analyte interactions, the large molecular weight of the polymer lead to a significant decrease in observed diffusion coefficients for analytes which interact with the polymer. These studies used polyvinylpyrrolidone (PVP) and polyethyleneglycol (PEG) as polymer additives, both of these polymers bind most strongly to polar analytes.

The initial hypothesis in this work was that a similar diffusion altering effect should be seen with size-exclusion chromatography (SEC) media. These media are frequently used in protein desalting and polymer molecular weight characterisation and are composed of porous, cross-linked dextran networks.[186] In SEC separation occurs based on the molecular size of the analytes, with smaller analytes being retained on a column for longer due to greater access to and longer residence time in the pore system.[208]

This chapter develops the use of size-exclusion chromatography media in chromatographic diffusion NMR. Assessment of the effect of the stationary phase on polymers and polymer mixtures is followed by characterisation of the effect of the stationary phases using polymer standards with well-defined molecular weights and low polydispersity. This method will be referred to as **S**ize **E**xclusion **C**hromatography - **D**iffusion **O**rdered **S**pectroscop**y** or by the acronym SEC-DOSY. The majority of the results presented in this chapter have been published in the Journal of Magnetic Resonance,[209] the article is included in Appendix A.1.

3.1 Parameter Optimisation

A selection of experiments were used to determine the optimum conditions for measuring polymer diffusion. These experiments were designed to indicate the dependence of the observed diffusion coefficient on sample concentration and two parameters of the DOSY experiment, the diffusion delay and the gradient length.

3.1.1 Concentration

An optimum concentration of polymer was determined by acquiring the DOSY data for samples of 25 kDa poly(*N*-isopropyl acrylamide) with a range of concentrations from 0.04 mM to 0.4 mM. The apparent diffusion coefficient of the samples decreased with increasing concentration (as shown in Figure 3.1). This is predominantly due to the increase in viscosity of the solution as the concentration increases, however, there may be some contribution from polymer chain tangling.

This result would promote the use of a low concentration, where interactions between neighbouring polymer chains are minimised; however, the error associated with the apparent diffusion coefficient decreases as the concentration increases due to improved s/n. At low concentrations the polymer peaks can also be obscured by the large broad peaks of the stationary phase leading to unreliable data.

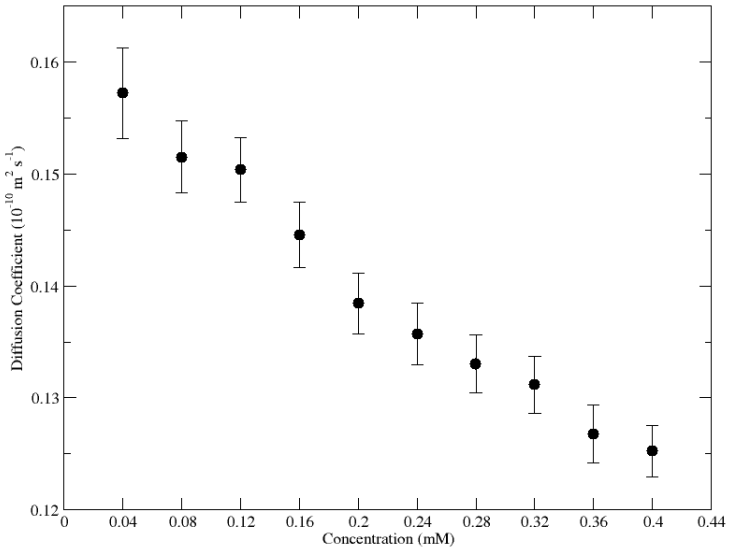

Figure 3.1: Diffusion coefficients of 25 kDa poly(*N*-isopropyl acrylamide) at concentrations of 0.04 - 0.4 mM.

The volume occupied by a polymer can be approximated by a sphere with a radius R_g (the radius of gyration), the concentration where these spheres fill the solution volume is called the overlap concentration, c^*.[210] The overlap concentration can be calculated from the intrinsic viscosity using Equation 3.2.

$$c^* = \frac{1}{[\eta]} \tag{3.2}$$

The intrinsic viscosity of the 25 kDa poly(*N*-isopropyl acrylamide) was determined from dynamic viscosity measurements, as detailed in Section 3.3.2.2, to be 31.94 ml g^{-1}. From this the overlap concentration for this polymer is 1.25 mM, indicating that significant overlap does not occur over the concentration range used in this study. This does not mean that the polymers do not come into contact or that there is no polymer chain tangling, only that the polymer chains are not completely overlapped and entangled.[210] The decrease in diffusion coefficient is therefore mainly caused by the increase in viscosity associated with the increase in concentration.

A concentration of 0.2 mM was selected for following experiments. This concentration was a compromise between visible peaks in the presence of stationary phase (Figure 3.2) and minimal polymer chain interaction.

Figure 3.2 shows that the poly(*N*-isopropyl acrylamide) peak at $\sim$ 3.9 ppm is directly under the broad peaks of the Sephadex G-50; the diffusion coefficient of this peak is not available in the presence of the stationary phase, due to the peak overlap the signal attenuation cannot be reliably extracted from that of the very low diffusion of the stationary phase. An additional effect of the stationary phase is the increased broadening of the signals. This is due to differences in the magnetic susceptibility between the stationary phase and the solvent causing an inhomogeneous magnetic field within the sample.[211] In the case of silica stationary phases, susceptibility matching

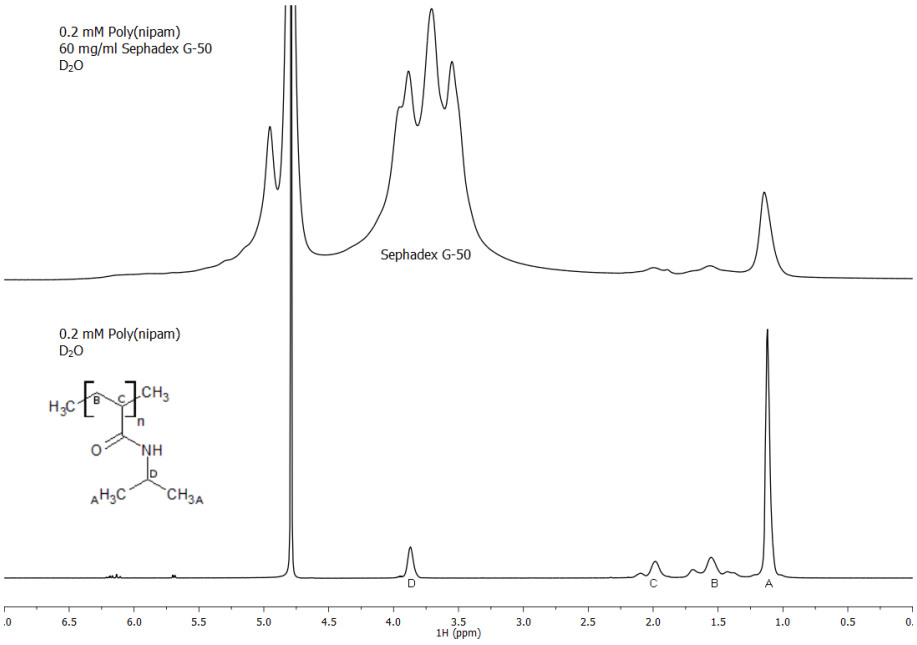

Figure 3.2: Extracts from ^{1}H NMR spectra of 0.2 mM poly(*N*-isopropyl acrylamide) with (top) and without (bottom) Sephadex G-50 in D_2O.

the solvent and stationary phase has been suggested by Hoffman et al.[195,212] as a solution to the inhomogeneity issue. This approach was found to be unsuitable for the dextran based media used for size-exclusion chromatography because the media are only stable in aqueous solutions allowing limited access to changes in magnetic susceptibilities. An alternative solution to the problem of line broadening is magic angle spinning[201,202,213,214] which will be discussed in section 3.4.

3.1.2 DOSY Parameters

The effect of changing pulse sequence parameters was investigated using the 0.04 mM, 0.2 mM and 0.4 mM samples of 25 kDa poly(*N*-isopropyl acrylamide) without stationary phase. The molecular weight (MW) of this polymer put it in the middle of the range of molecular weights of the polymers available for this study making it ideal for determining the most suitable parameters to use in ongoing experiments.

3.1.2.1 Diffusion Delay

The diffusion delay (Δ) is the period between the spatial encoding gradient pulses, during which time the molecules diffuse freely in solution. DOSY experiments were performed with diffusion delays of 0.1, 0.15, 0.2, 0.25 and 0.3 s. Figure 3.3 shows that for each concentration the diffusion coefficient decreases as the diffusion delay is increased. The error associated with the diffusion coefficient also increases with the diffusion delay.

Each of the concentrations show a similar trend across the range of diffusion delays. The decrease in apparent diffusion coefficient across the range of diffusion delays is $\sim$1.8 $\times 10^{-12}$ m^2 s^{-1} for all three concentrations. Also, the difference between the diffusion coefficients of each concentration is consistent across all five diffusion delay times ($\sim$1.8 $\times 10^{-12}$ m^2 s^{-1} from 0.04 mM to 0.2 mM and $\sim$1.4 $\times 10^{-12}$ m^2 s^{-1} from 0.2 mM to 0.4mM). This indicates that although the absolute value of

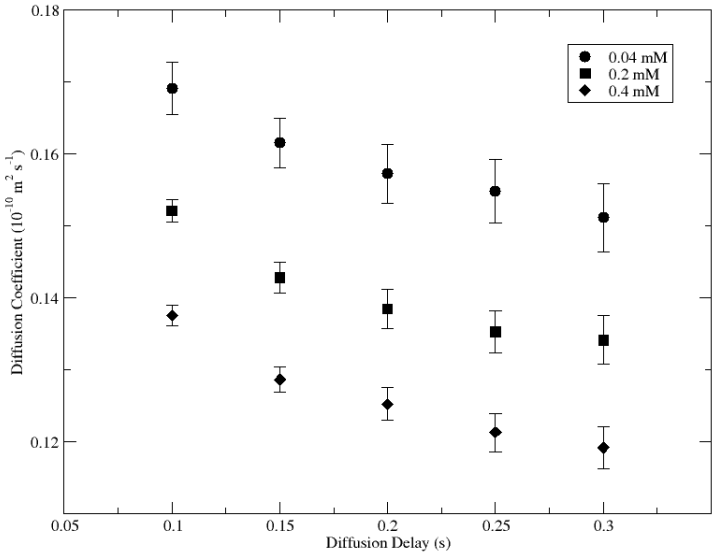

Figure 3.3: Diffusion coefficients of poly(*N*-isopropyl acrylamide) at concentrations of 0.04, 0.2 and 0.4 mM with diffusion delays of 0.1, 0.15, 0.2, 0.25 and 0.3 s.

the diffusion coefficient changes with different diffusion delays, comparisons can be made between data sets with the same diffusion delay.

The difference in apparent diffusion coefficients with different diffusion delays is possibly due to restricted motion caused by interactions between neighbouring polymer chains. As the diffusion delay is increased there is more chance for the polymer molecule to meet another which alters the root mean square (RMS) displacement experienced by the molecule during the diffusion delay.

3.1.2.2 Gradient Duration

The gradient duration refers to the time that the gradient pulses are applied for, DOSY experiments were performed with gradient lengths of 4, 5, 6, 7 and 8 ms. Figure 3.4 shows that for each concentration the diffusion coefficient decreases as the gradient length is increased. The error associated with the diffusion coefficient increases with gradient length; this is due to the faster signal decay and poor s/n of the later increments with higher gradient strengths.

3.1.2.3 Summary

Changing the diffusion delay from 0.1 s to 0.3 s leads to an average decrease in diffusion coefficient of 1.8×10^{-12} m^2 s^{-1}, a change in gradient length from 4 ms to 8 ms gives an average decrease of 1.9×10^{-12} m^2 s^{-1}. In comparison, the increase in concentration from 0.04 mM to 0.4 mM caused an average decrease of 3.0×10^{-12} m^2 s^{-1} in the diffusion coefficient. Although the effects are small compared to the observed diffusion coefficients, for best comparison between samples care was taken to use the same concentration, diffusion delay and gradient length for each set of experiments. Parameters for ongoing experiments were a concentration of 0.2 mM, diffusion delay of 0.2 s, and gradient length of 6 ms. These DOSY parameters gave a reasonable signal decay such that only ∼20% signal remained at the maximum gradient strength.

The other variable DOSY parameter, not discussed here, is the range of the arrayed gradient strengths. This was always set as 16 increments increased linearly by g^2 from 0.0452 to 0.5650 T

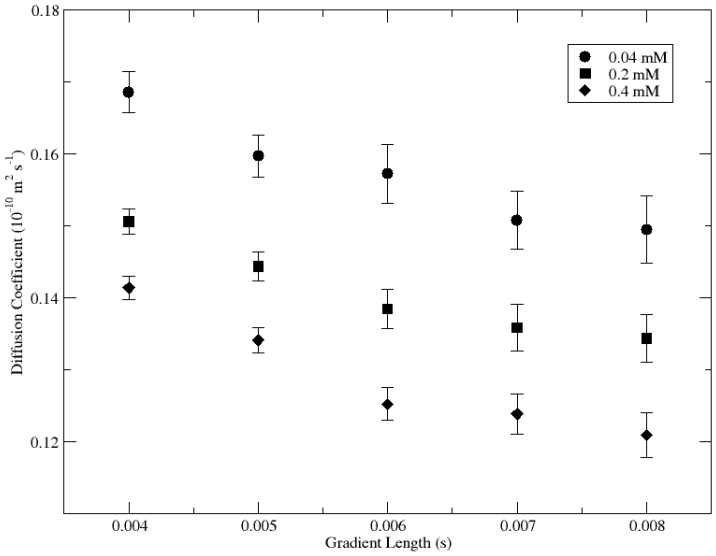

Figure 3.4: Observed diffusion coefficients of poly(*N*-isopropyl acrylamide) at concentrations of 0.04, 0.2 and 0.4 mM with varying gradient lengths.

m^{-1}. The initial gradient is small enough for limited attenuation of the D_2O solvent peak, useful for referencing spectra and the range of the gradient strengths allows for a good signal decay of a range of molecules.

3.2 Proof of Concept Experiments

Initial studies to establish the effect of a size-exclusion chromatography stationary phase in diffusion NMR were performed with a range of different polymers using the One-shot pulse sequence,[192] in the presence and absence of the size-exclusion chromatography (SEC) stationary phase, Sephadex G-50. It was anticipated that the effect of the stationary phase on the apparent diffusion coefficient should be related to the size, and therefore the molecular weight profile, of the polymer.

3.2.1 Individual Polymers

Three polymers were used for the proof of concept experiments; 15 kDa poly(allylamine hydrochloride) (15Paa), 25 kDa poly(*N*-isopropyl acrylamide) (25Pnipam) and 56 kDa poly(allylamine hydrochloride) (56Paa). The structures of these polymers are shown in Figure 3.5. In the remainder of this thesis the poly(allylamine hydrochloride) polymers will be referred to as poly(allylamine) or Paa and poly(*N*-isopropyl acrylamide) will be abbreviated to poly(nipam) or Pnipam.

3.2.1.1 Effect of Solvent

At a concentration of 0.2 mM in D_2O the diffusion coefficient decreased with increasing molecular weight (Figure 3.6), as expected given the inverse relationship between molecular size and diffusion coefficient (Einstein-Sutherland equation (Equation 3.1)). The same trend was observed in 150 mM NaCl, (D_2O), however the diffusion coefficients of the poly(allylamine) samples were larger than in D_2O while the diffusion coefficient of the poly(nipam) remained the same.

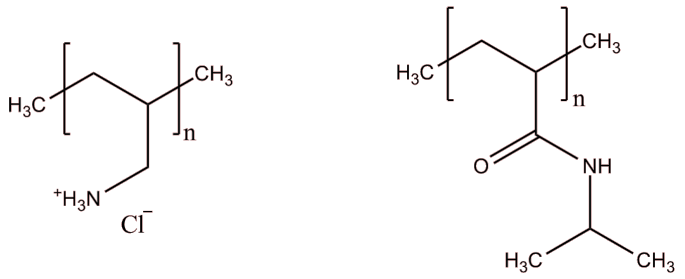

(a) Poly(allylamine hydrochloride) (b) Poly(*N*-isopropyl acrylamide)

Figure 3.5: Repeat units of the polymers used for proof of concept experiments

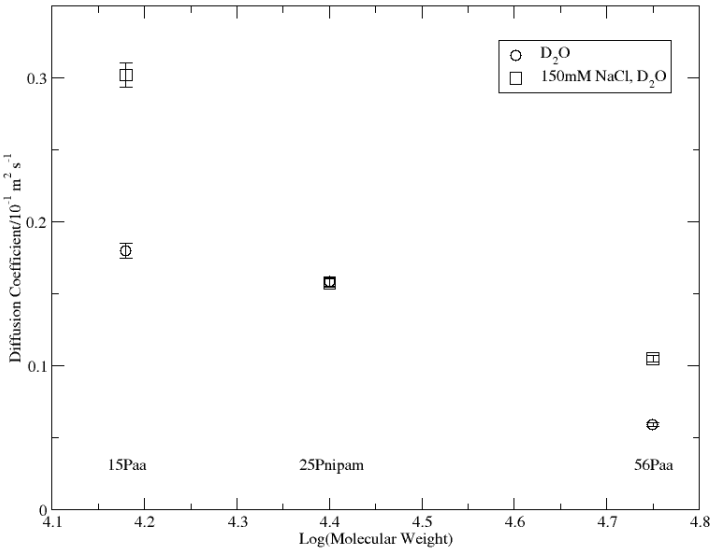

Figure 3.6: Trend in diffusion coefficient with molecular weight. 0.2 mM samples of 15 kDa poly(allylamine hydrochloride) (15Paa), 25 kDa poly(*N*-isopropyl acrylamide) (25Pnipam) and 56 kDa poly(allylamine hydrochloride) (56Paa) in D_2O and 150 mM NaCl(D_2O).

This change in sample composition to 150 mM NaCl in D_2O was directed by literature on size-exclusion chromatography, in gel filtration a salt concentration up to 150 mM NaCl is recommended to reduce ionic interactions between the analytes and stationary phase.[186] In addition, the increased ionic strength decreases the chain expansion of polyelectrolytes,[208] such as poly(allylamine hydrochloride) (Figure 3.5a). In neutral solutions, such as D_2O, the counterions diffuse away from the charged polymer backbone, Coulomb repulsion between the charges on the backbone lead to chain expansion and a decreased diffusion coefficient due to the larger effective size of the polymer. Poly(*N*-isopropyl acrylamide) is not affected to the same extent by the change in solvent because it is a neutral polymer (Figure 3.5b) and therefore does not undergo chain expansion.

3.2.1.2 Addition of Sephadex G-50

In 150mM NaCl, D_2O the addition of Sephadex G-50 to a 0.2 mM sample of 15 kDa poly(allylamine) reduced the apparent diffusion coefficient from 3.02×10^{-11} m^2 s^{-1} to 2.20×10^{-11} m^2 s^{-1}, a decrease of 8.22×10^{-12} m^2 s^{-1}. In comparison, the diffusion coefficient of a sample of 25 kDa poly(nipam) was reduced from 1.58×10^{-11} m^2 s^{-1} to 1.34×10^{-11} m^2 s^{-1} on addition of the same stationary phase, a decrease of only 2.34×10^{-12} m^2 s^{-1}. Similarly, the diffusion coefficient of the 56 kDa poly(allylamine) was reduced from 1.05×10^{-11} m^2 s^{-1} to 8.43×10^{-12} m^2 s^{-1}, a decrease

of 2.06×10^{-12} m^2 s^{-1}.

The DOSY plots for these 3 polymers with and without Sephadex G-50 are shown in Figures 3.7, 3.8 and 3.9 in order of increasing molecular weight. On the left is the DOSY plot of each polymer without Sephadex G-50, on the right is the DOSY plot of the same polymer in the presence of Sephadex G-50. All 6 plots have the same axis scales to facilitate comparison, the chemical shift increases from right to left as with conventional NMR spectra, the diffusion coefficient increases from top to bottom such that small diffusion coefficients appear higher up in the plot. The addition of Sephadex G-50 to poly(nipam) obscures the peak at $\sim \delta_H$ 3.9 ppm as it is overlapped by signals from the stationary phase.

The diffusion coefficients of the polymers decrease as the molecular weights increase, this occurs both with and without the addition of stationary phase and is expected from the increased molecular size. The magnitude of the observed change in diffusion coefficient decreases with increasing molecular weight, this is most clearly seen by comparing the differences between (a) and (b) for the 15 kDa and 56 kDa poly(allylamine)s (Figures 3.7 and 3.9). Samples in D_2O show similar results for the magnitude of change in diffusion coefficient, however the diffusion coefficients for all of the poly(allylamine)s are lower due to the chain expansion effects discussed above. Data extracted from the DOSY plots for all three polymers in both 150 mM NaCl (D_2O) and D_2O are summarised in Table 3.1.

Table 3.1: Summary of Proof of Concepts Data - Sephadex G-50

Solvent	Polymer	MW (kDa)	$D_{(\text{Polymer Only})}$* ($10^{-10}$ m^2 s^{-1})	$D_{(\text{Sephadex})}$* (10^{-10} m^2 s^{-1})	ΔD (10^{-10} m^2 s^{-1})
D_2O	Poly(aa)	15	0.180(0.005)	0.0839(0.004)	0.0962
	Poly(nipam)	25	0.158(0.003)	0.134(0.003)	0.0247
	Poly(aa)	56	0.0591(0.001)	0.0378(0.0009)	0.0213
150mM NaCl Solution	Poly(aa)	15	0.302(0.008)	0.220(0.006)	0.0822
	Poly(nipam)	25	0.158(0.003)	0.134(0.003)	0.0234
	Poly(aa)	56	0.105(0.002)	0.0844(0.002)	0.0205

*Errors given in brackets

The results show that the effect of the addition of stationary phase decreases with increasing molecular weight, consistent with the smaller polymer spending more time inhabiting the pores of the stationary phase, in a similar manner to separation achieved by a size-exclusion chromatographic column.

A complete quantitative comparison between these polymers cannot be conveniently drawn from these data due to differences in polymer structure and polydispersity, which may lead to different properties in solution which would affect diffusion. The difference in diffusion behaviour on changing the ionic strength of the solvent is one example of this issue. High polydispersity of the polymers would lead to skewing of the data and misrepresentation of the effect of the stationary phase, for example if a sample has a high proportion of smaller units, the effect of the stationary phase will appear greater due to the higher fraction of polymer in the pores. Polydispersity also invalidates the assumption of mono-exponential signal decay used to extract the diffusion coefficient as the decay would then be a weighted average of all polymers in solution.[215] The use of molecular weight polymer standards with the same structure and low polydispersity were therefore used for full characterisation of the stationary phases which is discussed in Section 3.3.

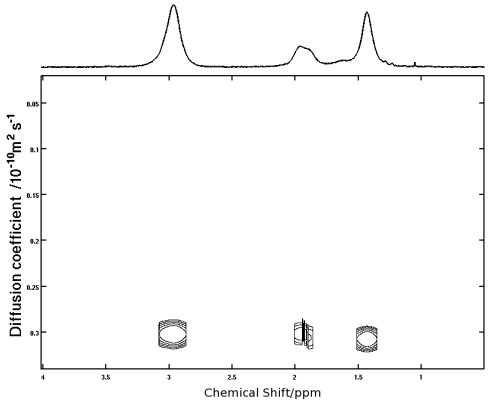

(a) 15 kDa Poly(allylamine hydrochloride)

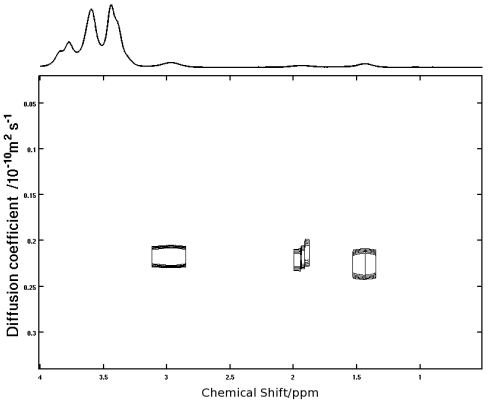

(b) 15 kDa Poly(allylamine hydrochloride) + Sephadex G-50

Figure 3.7: 15 kDa Poly(allylamine hydrochloride) with and without Sephadex G-50 in 150 mM NaCl (D_2O)

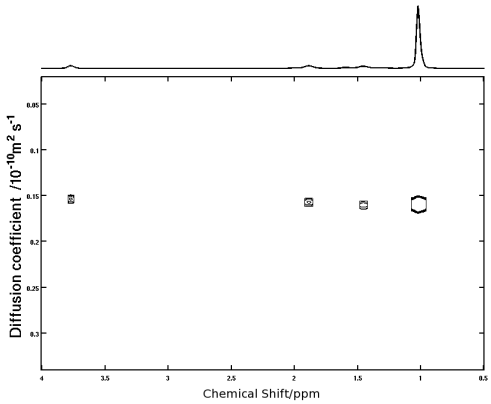

(a) 25 kDa Poly(nipam)

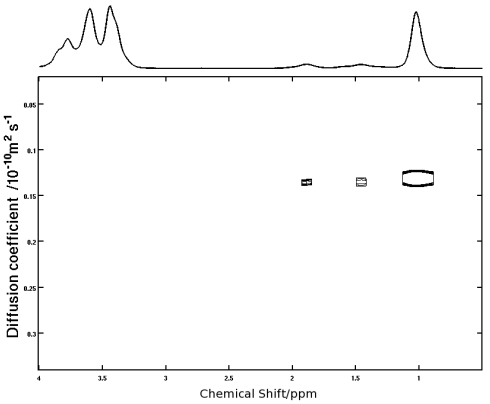

(b) 25 kDa Poly(nipam) + Sephadex G-50

Figure 3.8: 25 kDa Poly(nipam) with and without Sephadex G-50 in 150 mM NaCl (D_2O)

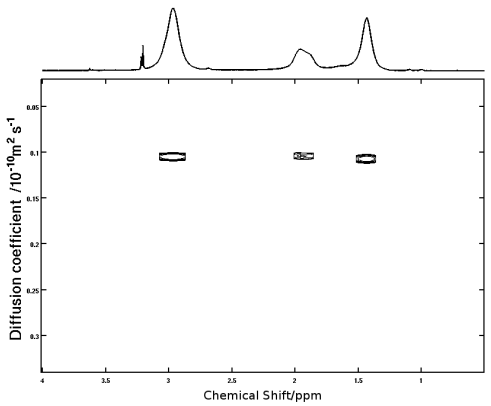

(a) 56 kDa Poly(allylamine hydrochloride)

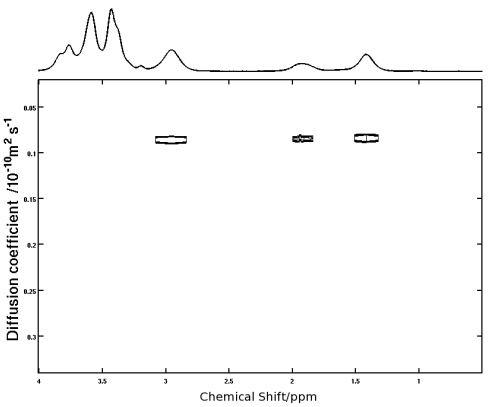

(b) 56 kDa Poly(allylamine hydrochloride) + Sephadex G-50

Figure 3.9: 56 kDa Poly(allylamine hydrochloride) with and without Sephadex G-50 in 150 mM NaCl (D_2O)

3.2.1.3 Other Stationary Phases

Other stationary phases were also tested with the proof of concept polymers (15 and 56 kDa poly(allylamine)s and 25 kDa poly(nipam)), Superdex 75 and Superdex 200 are cross-linked agarose and dextran composites, in comparison to Sephadex G-50 which is a dextran cross-linked with epichlorohydrin.[186] The fractionation ranges for these stationary phases are detailed in Table 3.2.

Table 3.2: Properties of Stationary Phases[186]

Stationary Phase	Particle size (μm)	Fractionation Range (kDa)	
		Globular Proteins	Dextrans
Sephadex G-50	20–50	1.5–30	0.5–10
Superdex 75	22–44	3.0–70	0.5–30
Superdex 200	22–44	10–600	1.0–100

The diffusion coefficients of the three polymers with these stationary phases in both D_2O and 150 mM NaCl (D_2O) are summarised in Table 3.3 and 3.4. For all sets of data there is a decrease in the effect of the stationary phase with increasing molecular weight, this is demonstrated most clearly in the case of Superdex 75 in D_2O where the fractionation range covers all three polymers (Figure 3.10).

Table 3.3: Summary of Proof of Concepts Data - Superdex 75

Solvent	Polymer	MW (kDa)	$D_{(\text{Polymer Only})}$* ($10^{-10}$ m^2 s^{-1})	$D_{(\text{Superdex 75})}$* (10^{-10} m^2 s^{-1})	ΔD (10^{-10} m^2 s^{-1})
D_2O	Poly(aa)	15	0.180(0.005)	0.125(0.008)	0.0552
	Poly(nipam)	25	0.158(0.003)	0.111(0.002)	0.0473
	Poly(aa)	56	0.0591(0.001)	0.0464(0.0005)	0.0128
150mM NaCl Solution	Poly(aa)	15	0.302(0.008)	0.183(0.06)	0.119
	Poly(nipam)	25	0.158(0.003)	0.114(0.002)	0.0434
	Poly(aa)	56	0.105(0.002)	0.0642(0.001)	0.0409

*Errors given in brackets

Table 3.4: Summary of Proof of Concepts Data - Superdex 200

Solvent	Polymer	MW (kDa)	$D_{(\text{Polymer Only})}$* ($10^{-10}$ m^2 s^{-1})	$D_{(\text{Superdex 200})}$* ($10^{-10}$ m^2 s^{-1})	ΔD (10^{-10} m^2 s^{-1})
D_2O	Poly(aa)	15	0.180(0.005)	0.154(0.01)	0.0265
	Poly(nipam)	25	0.158(0.003)	0.0995(0.002)	0.0588
	Poly(aa)	56	0.0591(0.001)	0.0494(0.0007)	0.00973
150mM NaCl Solution	Poly(aa)	15	0.302(0.008)	0.171(0.005)	0.131
	Poly(nipam)	25	0.158(0.003)	0.103(0.003)	0.0539
	Poly(aa)	56	0.105(0.002)	0.0586(0.001)	0.0465

*Errors given in brackets

The fractionation range of the stationary phase is the range of molecular weights that can be separated by high resolution fractionation in size-exclusion chromatography. This region has a linear selectivity curve of K_{av} against Log(Mw) and typical K_{av} values between 0.1 and 0.7, where K_{av} is the partition coefficient and a measure of the volume of the stationary phase available to a molecule.[186] In size-exclusion chromatography, molecules above the fractionation range are too large to access the pores, are not separated from one another and elute in the void volume,

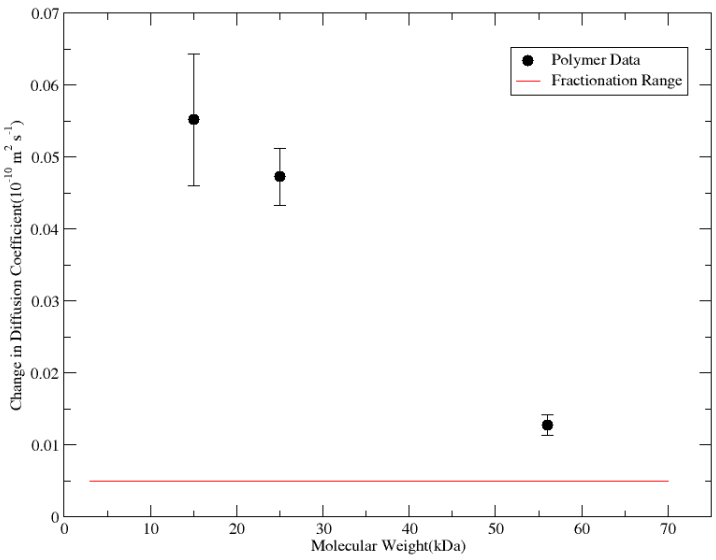

Figure 3.10: Change in diffusion coefficient on addition of Superdex 75 to 0.2 mM samples of 15 kDa poly(allylamine hydrochloride), 25 kDa poly(*N*-isopropyl acrylamide) and 56 kDa poly(allylamine hydrochloride) in D_2O.

molecules smaller than the lower limit of the fractionation range have access to a large volume of the pores and tend to elute at the full volume of the column. In these diffusion experiments the fractionation range indicates the range of molecular weights which will be affected by the stationary phase. In Figure 3.10 all three polymers are within the fractionation range of Superdex 75. Within this range the volume of the pore available to the polymers and therefore the effect of the stationary phase on the diffusion coefficient is lower for larger polymers. Above the fractionation range, the polymer is only affected by the restricted motion and increased viscosity caused by the addition of the stationary phase. The change in diffusion coefficient across the range of polymers for Superdex 75 is linear. In Sephadex G-50, where the largest polymer is above the fractionation range of the stationary phase the change in diffusion coefficient is less linear. For this range of polymers Superdex 75 is the most effective stationary phase, causing a decrease in diffusion coefficient which is linearly related to the molecular weight of the polymer.

3.2.2 Polymer Mixtures

Two equimolar mixtures of the polymers used in the proof of concept experiments were studied, 15 kDa poly(allylamine hydrochloride) + 25 kDa poly(*N*-isopropyl acrylamide) and 25 kDa poly(*N*-isopropyl acrylamide) + 56 kDa poly(allylamine hydrochloride), designated low MW mix and high MW mix respectively. A mix of the two poly(allylamine)s was not prepared due to the significant peak overlap of these polymers (Figure 3.11).

Only one peak of each polymer was used in the analysis of the polymer mixtures with stationary phase, δ_H 3.10 ppm for the poly(allylamine)s and δ_H 1.17 ppm for the poly(nipam). The two peaks at δ_H ~1.6 and ~2.1 ppm belong to the backbone CH_2 protons of both polymers. When peak overlap is too great the two individual signal decays cannot be separated, the diffusion coefficient extracted for peaks which overlap is a weighted average of the diffusion coefficients of the individual components.[107]

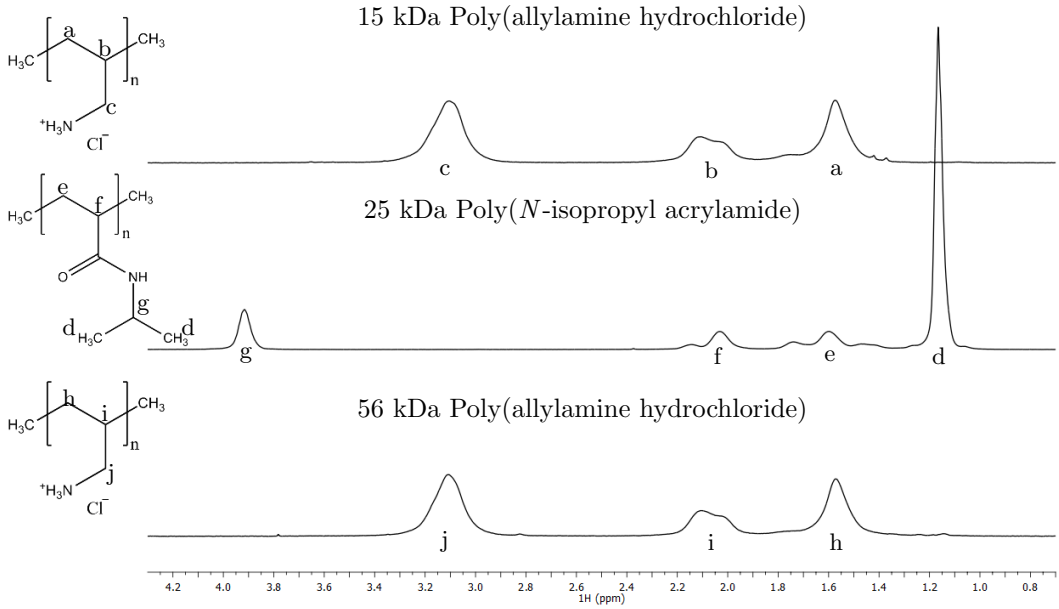

Figure 3.11: Extracts of ^{1}H spectra for 15 kDa poly(allylamine hydrochloride) (top), 25 kDa poly(*N*-isopropyl acrylamide) (middle) and 56 kDa poly(allylamine hydrochloride)(bottom) with peak assignments.

3.2.2.1 Polymer Mixtures in D_2O

In the absence of a stationary phase the diffusion coefficient of each polymer component was lower than in the single polymer samples as shown in Figure 3.12, this is due to increased viscosity and polymer chain entanglement caused by the effective doubling of concentration.[210]

On addition of Sephadex G-50 to the low MW mix, the diffusion coefficient of the 15 kDa poly(allylamine) is reduced more than the larger poly(nipam) due to greater access to the pores of the stationary phase, the effect is great enough to reverse the ordering of the polymers in the diffusion dimension (Figure 3.13a and b).

The separation of molecules by size-exclusion chromatography relies on smaller molecules accessing a greater volume of the pores and therefore taking longer to travel through a column. Without flow, the diffusion of the polymer is hindered by the walls of the pores, the more time spent in the pore or the higher fraction of polymer in the pore, the greater the change in the diffusion coefficient. In the case of an equimolar mixture of different sized polymers, the smaller polymer would have access to more of the pore leading to a greater decrease in apparent diffusion coefficient. When the effect of the stationary phase on the smaller polymer is greater than the separation of the polymers without stationary phase and the effect of the stationary phase on the larger polymer, this leads to a reversal of order in the DOSY plot.

The same effect is seen to a lesser extent with Superdex 75 (Figure 3.13c), the 15 kDa polymer is affected more than the 25 kDa polymer, but in this case the diffusion coefficient of the poly(allylamine) is only slightly lower than the poly(nipam).

With Superdex 200 there is no reversal of peak ordering in the diffusion domain and the effect of the stationary phase on the diffusion coefficient is similar for both polymers (Figure 3.13d), this is most likely due to the large fractionation range of the stationary phase in comparison to the molecular weights of the polymers. The large fractionation range for this stationary phase (10–600

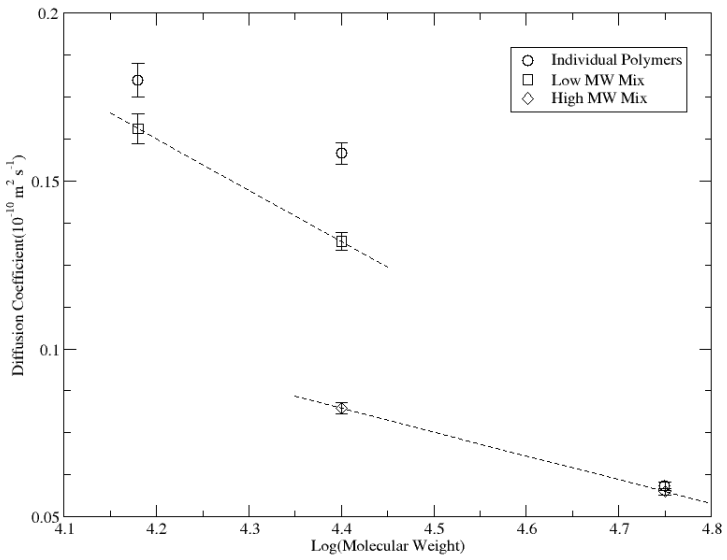

Figure 3.12: Comparison of diffusion coefficients for individual polymers and polymers in mixtures. Individual polymers (Circles): 0.2 mM 15 kDa poly(allylamine hydrochloride), 25 kDa poly(*N*-isopropyl acrylamide) and 56 kDa poly(allylamine hydrochloride). Low MW mix (Squares): 0.2 mM 15 kDa poly(allylamine hydrochloride) + 0.2 mM 25 kDa poly(*N*-isopropyl acrylamide). High MW mix (Diamonds): 0.2 mM 25 kDa poly(*N*-isopropyl acrylamide) + 0.2 mM 56 kDa poly(allylamine hydrochloride). Dashed lines connect the two polymers of each mixture. All samples were prepared in D_2O.

kDa for globular proteins[186]) indicates large pores accessible to a wide range of molecule sizes. The polymers in the mixture can access similar volumes of the pores leading to similar attenuation of the diffusion coefficient.

In the case of the high MW mixture, the higher molecular weight poly(allylamine) has a greater change in diffusion coefficient on addition of both Sephadex G-50 and Superdex 75 than poly(nipam). This is not the trend expected based on size-exclusion theory or the data from the individual polymers. This could be due to additional interactions between the poly(allylamine) and the stationary phase which causes greater attenuation of the diffusion coefficient than predicted for pure size-exclusion effects.

Data for the low MW mix and high MW mix are given in Table 3.5 and Table 3.6 respectively.

Table 3.5: Summary of Polymer Mixtures Data - Low MW Mix - D_2O

Stationary Phase	Polymer	MW (kDa)	$D_{(Polymer\ Only)}$* (10^{-10} m^2 s^{-1})	$D_{(S)}$* (10^{-10} m^2 s^{-1})	ΔD_S (10^{-10} m^2 s^{-1})
Sephadex G-50	Poly(aa)	15	0.166(0.004)	0.0671(0.004)	0.0985
	Poly(nipam)	25	0.132(0.003)	0.114(0.003)	0.0178
Superdex 75	Poly(aa)	15	0.166(0.004)	0.0935(0.005)	0.0721
	Poly(nipam)	25	0.132(0.003)	0.106(0.002)	0.0263
Superdex 200	Poly(aa)	15	0.166(0.004)	0.130(0.009)	0.0352
	Poly(nipam)	25	0.132(0.003)	0.0951(0.002)	0.0370

*Errors given in brackets

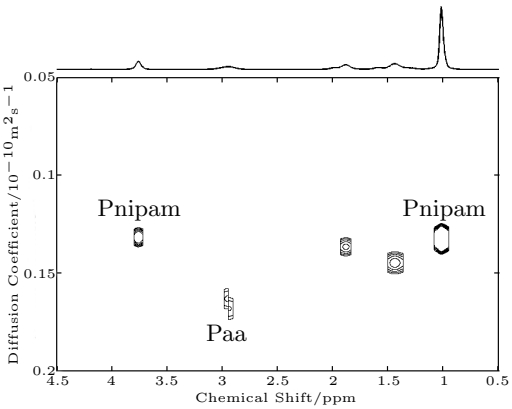

(a) 15 kDa Poly(aa) + 25 kDa Poly(nipam)

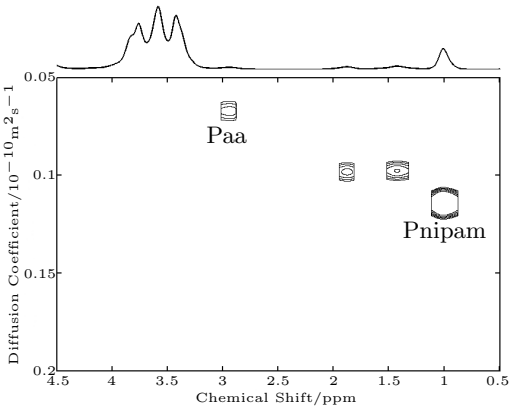

(b) 15 kDa Poly(aa) + 25 kDa Poly(nipam) with Sephadex G-50

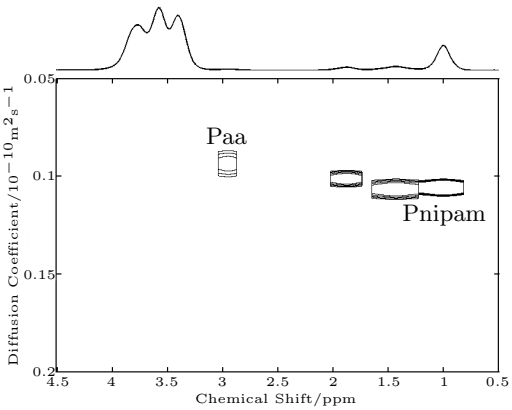

(c) 15 kDa Poly(aa) + 25 kDa Poly(nipam) with Superdex 75

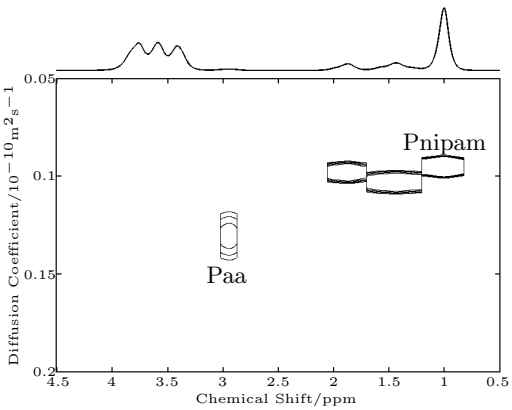

(d) 15 kDa Poly(aa) + 25 kDa Poly(nipam) with Superdex 200

Figure 3.13: 15 kDa poly(allylamine hydrochloride) + 25 kDa poly(*N*-isopropyl acrylamide), 0.2 mM each, a) D_2O, b) + Sephadex G-50, c) + Superdex 75 and d) + Superdex 200

Table 3.6: Summary of Polymer Mixtures Data - High MW Mix - D_2O

Stationary Phase	Polymer	MW (kDa)	$D_{(Polymer\ Only)}$* (10^{-10} m^2 s^{-1})	$D_{(S)}$* (10^{-10} m^2 s^{-1})	ΔD_S (10^{-10} m^2 s^{-1})
Sephadex G-50	Poly(nipam)	25	0.0823(0.002)	0.0678(0.002)	0.0144
	Poly(aa)	56	0.0575(0.001)	0.0321(0.0008)	0.0253
Superdex 75	Poly(nipam)	25	0.0823(0.002)	0.0673(0.0009)	0.0150
	Poly(aa)	56	0.0575(0.001)	0.0377(0.0004)	0.0198
Superdex 200	Poly(nipam)	25	0.0823(0.002)	0.0594(0.001)	0.0229
	Poly(aa)	56	0.0575(0.001)	0.0412(0.0007)	0.0163

*Errors given in brackets

3.2.2.2 Polymer Mixtures in 150 mM NaCl Solution

Following the observation of altered diffusion of the poly(allylamine)s in 150 mM NaCl, the low MW and high MW polymer mixtures were also prepared in 150 mM NaCl (D_2O). As with the individual polymers, the diffusion coefficients of each component in the mixtures are larger in 150 mM NaCl mixtures than the corresponding mixtures in D_2O.

The trend observed in D_2O for the low MW mix where the order in the diffusion domain is switched is not seen in the 150 mM NaCl samples, this could suggest the presence of additional interactions between polymer and stationary phase in the D_2O samples causing a greater attenuation of diffusion coefficient. For Sephadex there are several examples in the literature of ionic interactions between charged analytes and the Sephadex leading to additional adsorption effects which alter the elution profile of the analytes,[216,217] this has been attributed to a small amount of negative charges due to carboxyl groups which interact with the analytes. As the poly(allylamine) is positively charged some binding is likely to occur to the stationary phase which would enhance the decrease in diffusion coefficient seen on addition of the stationary phase. The inclusion of 150 mM NaCl in the solution will reduce these effects by screening the ionic interactions.[218]

The DOSY plots for the low MW mix are shown in Figure 3.14. As with the D_2O data, all scales are the same for convenient comparison, however the range of the diffusion domain is larger than in the D_2O data.

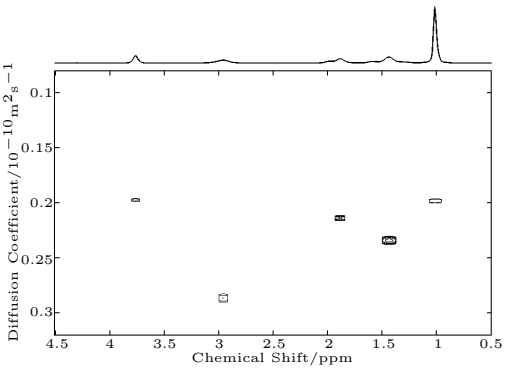

(a) 15 kDa Poly(aa) + 25 kDa Poly(nipam)

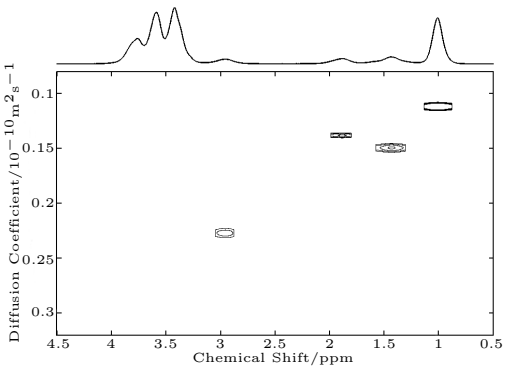

(b) 15 kDa Poly(aa) + 25 kDa Poly(nipam) with Sephadex G-50

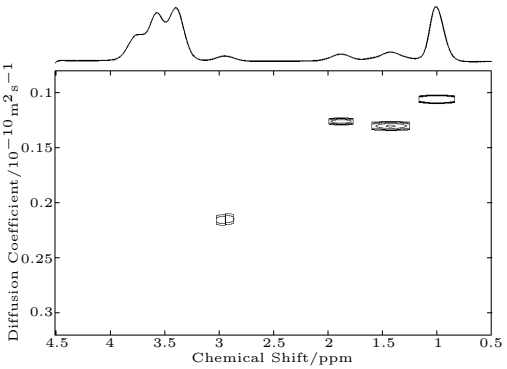

(c) 15 kDa Poly(aa) + 25 kDa Poly(nipam) with Superdex 75

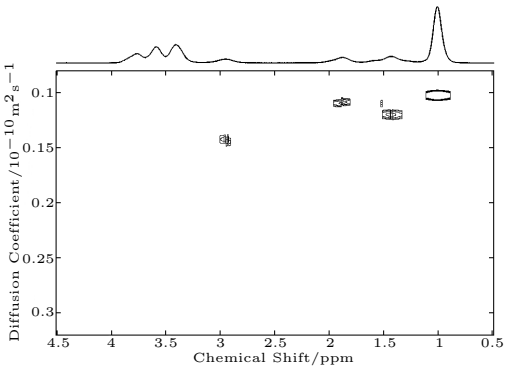

(d) 15 kDa Poly(aa) + 25 kDa Poly(nipam) with Superdex 200

Figure 3.14: 15 kDa poly(allylamine hydrochloride) + 25 kDa poly(*N*-isopropyl acrylamide), 0.2 mM each, a) 150 mM NaCl (D_2O), b) + Sephadex G-50, c) + Superdex 75 and d) + Superdex 200

The data for these mixtures are summarised in Table 3.7 and Table 3.8 for the low MW and high

MW mixtures respectively.

Table 3.7: Summary of Polymer Mixtures Data - Low MW Mix - 150 mM NaCl (D_2O)

Stationary Phase	Polymer	MW (kDa)	$D_{(Polymer\ Only)}$* (10^{-10} m^2 s^{-1})	$D_{(S)}$* (10^{-10} m^2 s^{-1})	ΔD (10^{-10} m^2 s^{-1})
Sephadex G-50	Poly(aa)	15	0.298(0.004)	0.230(0.003)	0.0681
	Poly(nipam)	25	0.200(0.001)	0.117(0.003)	0.0827
Superdex 75	Poly(aa)	15	0.298(0.004)	0.217(0.003)	0.0813
	Poly(nipam)	25	0.200(0.001)	0.115(0.005)	0.0843
Superdex 200	Poly(aa)	15	0.298(0.004)	0.152(0.005)	0.147
	Poly(nipam)	25	0.200(0.001)	0.108(0.003)	0.0913

*Errors given in brackets

Table 3.8: Summary of Polymer Mixtures Data - High MW Mix - 150 mM NaCl (D_2O)

Stationary Phase	Polymer	MW (kDa)	$D_{(Polymer\ Only)}$* (10^{-10} m^2 s^{-1})	$D_{(S)}$* (10^{-10} m^2 s^{-1})	ΔD (10^{-10} m^2 s^{-1})
Sephadex G-50	Poly(nipam)	25	0.105(0.001)	0.0860(0.003)	0.0188
	Poly(aa)	56	0.0956(0.001)	0.0778(0.001)	0.0178
Superdex 75	Poly(nipam)	25	0.105(0.001)	0.0763(0.003)	0.0285
	Poly(aa)	56	0.0956(0.001)	0.0574(0.001)	0.0382
Superdex 200	Poly(nipam)	25	0.105(0.001)	0.0796(0.002)	0.0253
	Poly(aa)	56	0.0956(0.001)	0.0595(0.002)	0.0360

*Errors given in brackets

The data obtained for these polymer mixtures in both D_2O and 150 mM NaCl (D_2O) indicate that resolution of different components using this method is not straight forward. Firstly there is the problem of overlapping peaks, which is made worse by the line broadening caused by the stationary phase. Secondly, there is no significant improvement in separation of the two components in the diffusion domain. Finally, additional information is required about the structure of the components to compensate for potential interactions with the stationary phase. For example the presence of charges on the analyte molecule could lead to additional ionic interactions with the stationary phase which would alter the diffusion profile to a different degree than expected from purely size-exclusion effects.

3.3 Characterisation of the Stationary Phases

For characterisation of the stationary phases five poly(styrene-4-sulphonate) reference standards with known molecular weights of 10.6, 14.9, 20.7, 32.9 and 63.9 kDa and low polydispersity (<1.2) were used. The use of polymers with the same structure removes any differences in interaction with the stationary phase caused by changes in the polymer structure, therefore allowing direct comparison of the change in diffusion coefficient caused by the stationary phase for polymers of different molecular weight. Low polydispersity allows the confirmation of the correlation between molecular weight and effect of stationary phase and maintains the validity of the assumption of a mono-exponential decay of the echo intensity.

DOSY data acquired for the 5 polymer standards without stationary phase shows a decrease in diffusion coefficient with increasing molecular weight. As with the poly(allylamine) samples, the

poly(styrene-4-sulphonate) samples showed a larger diffusion coefficient in 50 mM sodium phosphate buffer + 150 mM NaCl (pH 9) in comparison to D_2O, as shown in Figure 3.15, due to intramolecular chain expansion. The diffusion coefficients quoted for the polymer standards are average values of the three peaks at δ_H 1.47, 6.68 and 7.57 ppm. 150 mM NaCl in D_2O has a similar effect on the diffusion coefficient as the phosphate buffer. The phosphate buffer was implemented for the same reason as the 150 mM NaCl solution for the proof of concept (POC) polymers, following suggested protocols for size-exclusion chromatography.[186] 150 mM NaCl (D_2O) was used for comparisons with the POC polymers; phosphate buffer could not be used in this situation due to the positive charge on the poly(allylamine) causing precipitation in the presence of phosphate.

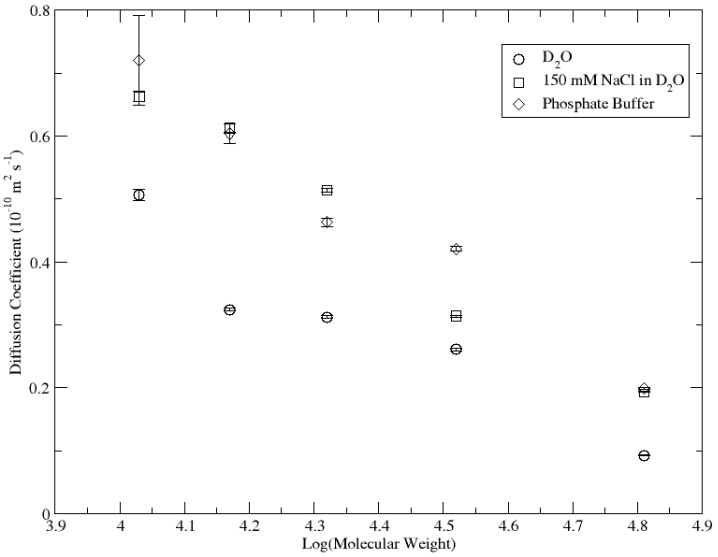

Figure 3.15: Comparison of the diffusion coefficient of polymer standards in different solvents. 0.2 mM poly(styrene-4-sulphonate) samples with molecular weights 10.6, 14.9, 20.7, 32.9 and 63.9 kDa. Solvents are D_2O(Circles), 150 mM NaCl in D_2O(Squares) and 50 mM Sodium Phosphate Buffer (pH 9) + 150 mM NaCl.(Diamonds)

As with the proof of concept experiments, the addition of stationary phases reduced the diffusion coefficient of the polymers. As an example, Figure 3.16 shows the DOSY plot for the 33 kDa polymer standard in the absence (a) and presence (b) of Superdex 75.

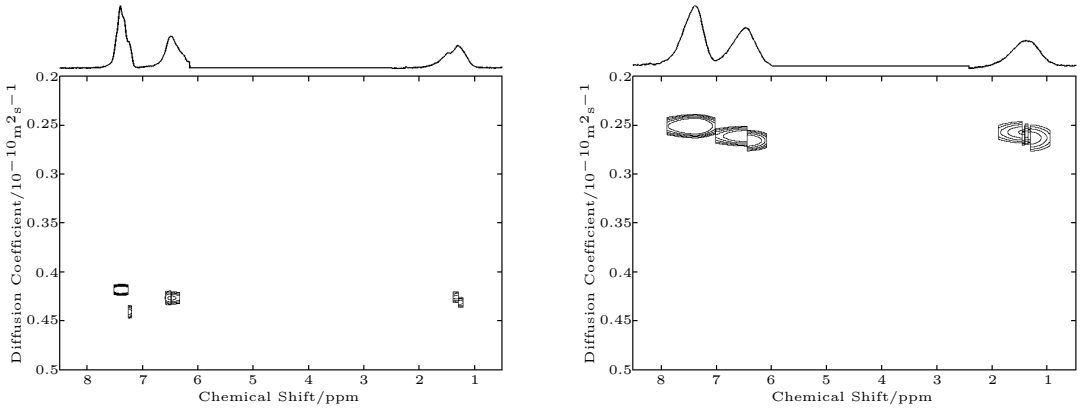

(a) 30 kDa PSS

(b) 30 kDa PSS with Superdex 75

Figure 3.16: DOSY plots of 30 kDa poly(styrene-4-sulphonate) (0.2 mM) with (b) and without (a) Superdex 75

The observation of a mono-exponential signal decay indicates that the diffusion data can be interpreted in terms of the fact that the polymer is in fast exchange between being in free solution and being trapped within the pores of the stationary phase. The observed diffusion coefficient (D_{obs}) is therefore a weighted average between the diffusion in free solution (D_f) and diffusion in the pores (D_p) as given in Equation 3.3, where f_f and f_p represent the fraction of polymer in free solution and in the pores respectively.

$$D_{obs} = f_f D_f + f_p D_p = (1 - f_p) D_f + f_p D_p \tag{3.3}$$

Diffusion in free solution in the presence of a stationary phase may be slightly lower than that observed in the absence of stationary phase, this is due to increased viscosity and a reduction in the volume caused by the addition of the stationary phase particles. The void volume is typically ~30% in a packed column,[186] however, it may be slightly greater in the NMR experiments as the stationary phase is allowed to settle naturally under gravity rather than being packed by flow. Diffusion within the pores is likely to appear much slower, the polymer may bounce around the pore giving a lower mean free path during the diffusion delay and therefore a smaller apparent diffusion coefficient. As molecular weight increases, the fraction of the polymer solution small enough to fit in the pores of the stationary phase (f_p) decreases, reducing the contribution of D_p to the observed diffusion coefficient.

Diffusion within the pore is likely to be affected by restriction, depending on the geometry and size of the pore (e.g. a sphere of radius a), the diffusion coefficient of the molecule in free solution and the length of the diffusion delay (Δ). The influence of restriction on the diffusion measurement can be characterised by the dimensionless parameter ξ, (Equation 3.4), and split into three regimes depending on the value of ξ.[92]

$$\xi = \frac{D\Delta}{a^2} \tag{3.4}$$

When $\xi \ll 1$, diffusion is not restricted as the displacement during the diffusion delay is smaller than the pore size, this is known as the 'short time' or 'free diffusion' limit. When $\xi \approx 1$, some molecules are restricted by the walls of the pores and the diffusion coefficient varies as a function of Δ. As the diffusion delay is increased, the molecules diffuse further and more are restricted by the pores causing a decrease in observed diffusion coefficient. In the 'long time' limit, when $\xi \gg 1$ or Δ is large, all molecules are restricted by the pores and the observed diffusion coefficient is dependent on the pore size.

Pore sizes for the stationary phases are ~3 nm for Sephadex G-50,[219] ~6 nm for Superdex 75 and ~13 nm for Superdex 200.[220] For the smallest polymer, likely to be the least restricted, $D = 0.53 \times 10^{-10}$ m^2 s^{-1} (for Sephadex G-50 in phosphate buffer) and $\Delta = 200$ ms, this gives a value $\xi = 1.2 \times 10^6$. This value is much greater than 1, confirming restricted diffusion within the pores, the observed diffusion coefficient is therefore related to the size and shape of the pores.

Figure 3.17 shows graphs of the diffusion coefficient values of the polymer standards in the presence of Sephadex G-50 (a), Superdex 75 (b) and Superdex 200 (c) in sodium phosphate buffer. The diffusion coefficient data for the polymer only samples is included on each graph for comparison. Samples prepared in 150 mM NaCl (D_2O) show similar trends, as shown in Figure 3.18. The data for these samples, as well as a set prepared in D_2O only, are summarised in Table 3.9. Data for Superdex 200 in D_2O were not acquired; the data from the other solvents showed that this stationary phase was the least effective. Combined with the polymer chain expansion shown to occur in D_2O, it was not considered as a useful experiment.

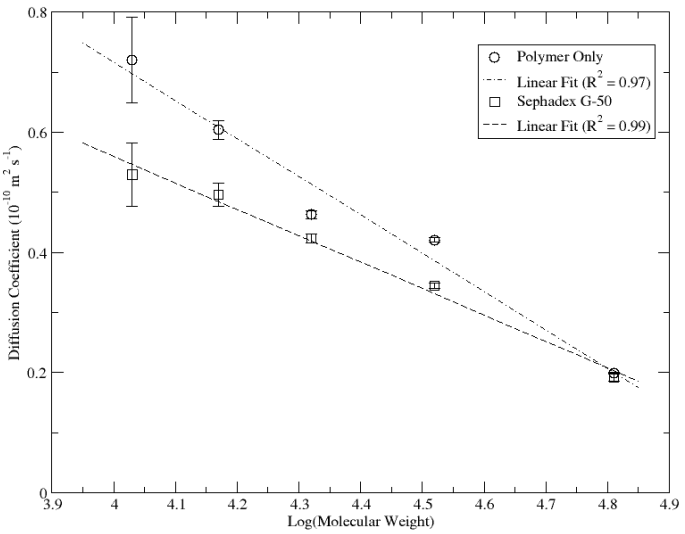

(a) Sephadex G-50

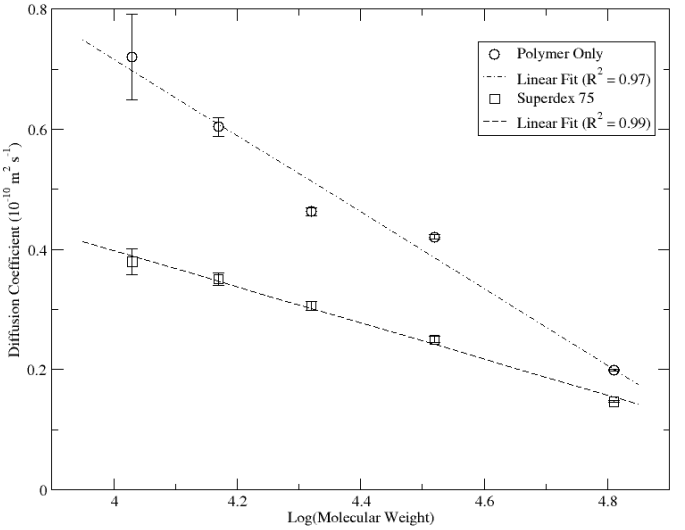

(b) Superdex 75

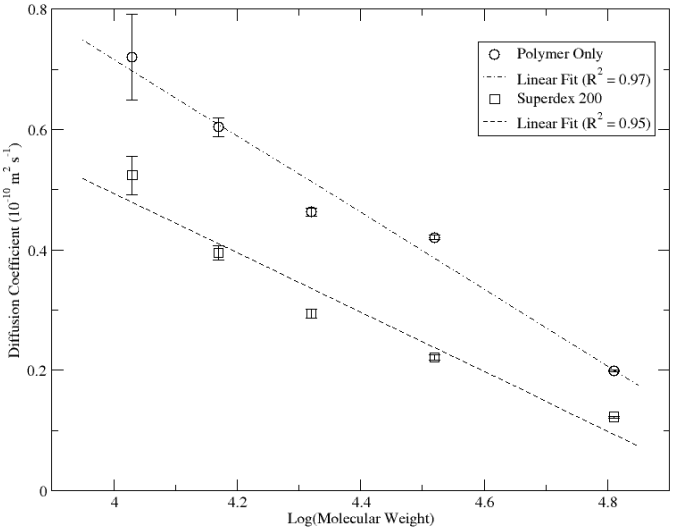

(c) Superdex 200

Figure 3.17: Graphs of diffusion coefficients of poly(styrene-4-sulphonate) with and without stationary phases in 50 mM sodium phosphate + 150 mM NaCl

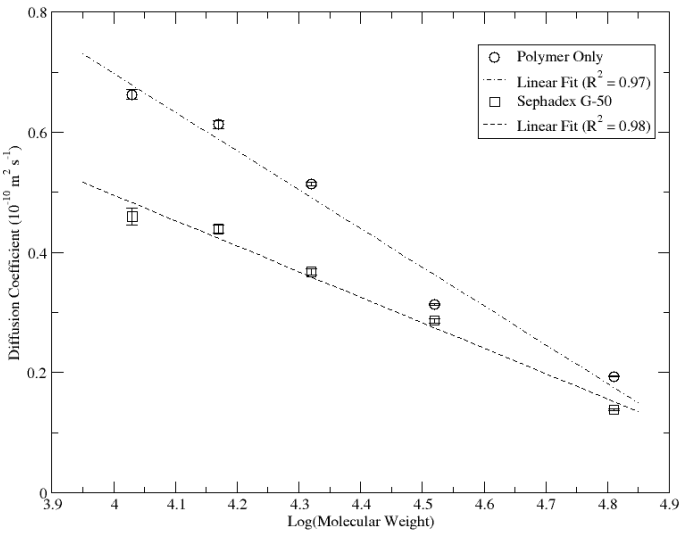

(a) Sephadex G-50

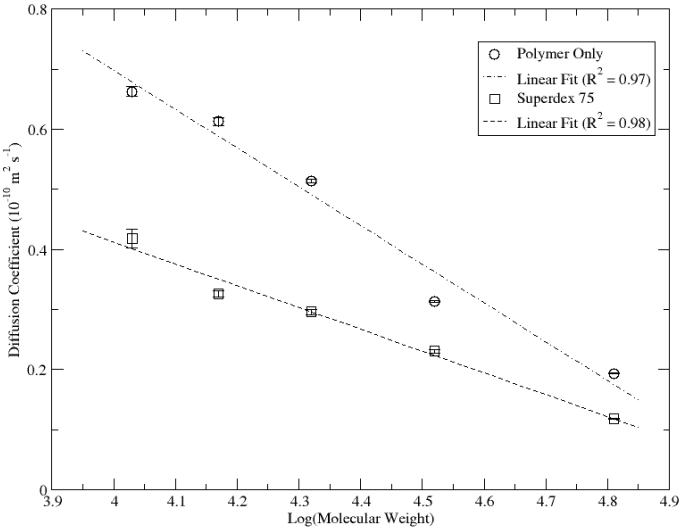

(b) Superdex 75

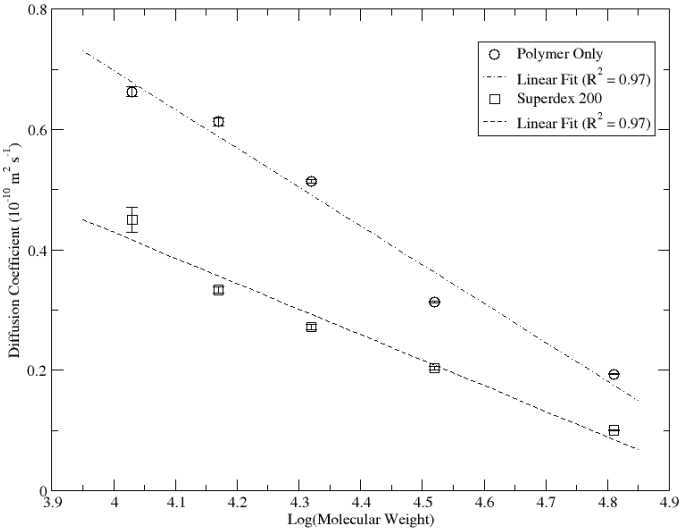

(c) Superdex 200

Figure 3.18: Graphs of diffusion coefficients of poly(styrene-4-sulphonate) with and without stationary phases in 150 mM NaCl

Table 3.9: Diffusion Coefficients of Poly(styrene-4-sulphonate) Standards

(a) 50 mM Sodium Phosphate + 150 mM NaCl

MW (kDa)	Polymer* (10^{-10} m^2 s^{-1})	Sephadex G-50* (10^{-10} m^2 s^{-1})	Superdex 75* (10^{-10} m^2 s^{-1})	Superdex 200* (10^{-10} m^2 s^{-1})
10.6	0.721(0.07)	0.530(0.05)	0.380(0.02)	0.524(0.03)
14.9	0.604(0.02)	0.496(0.02)	0.351(0.01)	0.395(0.01)
20.7	0.463(0.006)	0.424(0.008)	0.306(0.007)	0.294(0.008)
32.9	0.421(0.004)	0.344(0.004)	0.250(0.005)	0.222(0.005)
63.9	0.199(0.002)	0.192(0.005)	0.147(0.001)	0.123(0.001)

*Errors given in brackets

(b) 150 mM NaCl

MW (kDa)	Polymer* (10^{-10} m^2 s^{-1})	Sephadex G-50* (10^{-10} m^2 s^{-1})	Superdex 75* (10^{-10} m^2 s^{-1})	Superdex 200* (10^{-10} m^2 s^{-1})
10.6	0.663(0.008)	0.460(0.01)	0.418(0.02)	0.450(0.02)
14.9	0.613(0.006)	0.439(0.007)	0.326(0.005)	0.333(0.006)
20.7	0.514(0.003)	0.368(0.005)	0.296(0.004)	0.272(0.004)
32.9	0.314(0.002)	0.287(0.004)	0.231(0.003)	0.204(0.002)
63.9	0.193(0.001)	0.138(0.001)	0.118(0.0008)	0.100(0.0008)

*Errors given in brackets

(c) D_2O

MW (kDa)	Polymer* (10^{-10} m^2 s^{-1})	Sephadex G-50* (10^{-10} m^2 s^{-1})	Superdex 75* (10^{-10} m^2 s^{-1})
10.6	0.507(0.009)	0.317(0.005)	0.287(0.003)
14.9	0.324(0.002)	0.163(0.003)	0.162(0.003)
20.7	0.312(0.002)	0.197(0.003)	0.141(0.002)
32.9	0.261(0.003)	0.143(0.008)	0.106(0.001)
63.9	0.0926(0.0005)	0.0660(0.0005)	0.0538(0.0003)

*Errors given in brackets

In all cases the diffusion coefficient is lower in the presence of the stationary phase, however as the molecular weight increases the difference in the observed diffusion coefficient decreases. This is consistent with the assignment of the observed diffusion coefficient as a weighted average of free and in pore species. The larger polymers have a lower fraction within the pores of the stationary phase, which reduces the contribution of D_p, the low diffusion coefficient related to diffusion within the pores of the stationary phase, to D_{obs}. The point where the 'polymer only' trend line meets that of the 'polymer + stationary phase' occurs at increasing log(MW) values across the series of Sephadex G-50, Superdex 75 and Superdex 200, as expected due to the increase in upper limit of the fractionation ranges of the stationary phases, as detailed previously in Table 3.2.

The data in Figures 3.17 and 3.18 are plotted as log(molecular weight) against diffusion coefficient in a similar presentation as for size-exclusion chromatography calibration curves where log(molecular weight) is typically plotted against elution volume. The linear fits to these data can be rearranged to have the general form of:

$$\log(MW) = a_0 - a_1 D \tag{3.5}$$

This is similar to the equations presented by Determann and Michel for size-exclusion chromatography of globular proteins by Sephadex ($\log(MW) = M_0 - (k_1 - k_2 d)V_e/V_0$)[221] as well as Anderson and Stoddart ($V_e = -b' \log(MW) + c'$ which rearranges to $\log(MW) = c'/b' - V_e/b'$).[222] Parameters acquired from fitting each set of data shown above to Equation 3.5 are given in Table 3.10 along with the R^2 values. Values obtained from the NaCl data are similar to those from the phosphate buffer. Data from the D_2O samples have much lower R^2 values indicating less of a clear trend, possibly due to varying levels of intramolecular chain expansion. The values for a_0 are lower in D_2O than for the phosphate or NaCl samples, this is a consequence of the lower diffusion coefficients as a result of the intramolecular chain expansion, the values for a_1 are higher than the corresponding values from the phosphate or NaCl data indicating less change in diffusion coefficient across the range of molecular weights.

The a_0 values obtained from these measurements for the phosphate buffer and 150 mM NaCl solution are close to M_0 values obtained by Determann,[221] the increase in a_1 from 1.50×10^{10} s m^{-2} without stationary phase to 2.0–3.3×10^{10} s m^{-2} on addition of stationary phase indicates a smaller range of diffusion coefficients covered in the presence of stationary phase, which confirms that small molecules are affected more than larger molecules; this is consistent with size-exclusion effects.

An alternative presentation of this data is shown in Figure 3.19, the ratio of D/D_0 (where D is the diffusion with the stationary phase and D_0 is the diffusion in the absence of stationary phase) vs logM shows how the root mean square free path of the polymers changes with molecular weight. D/D_0 tends to 1 as the effect of the stationary phase decreases. This figure shows more clearly the difference between the Sephadex G-50 and Superdex 75 stationary phases. However, it also highlights a limitation of using Equation 3.5 for modelling this data, in the case of Superdex 200 the D/D_0 values tend to decrease due to the extracted a_0 value being lower than in the polymer only case. These results suggest that SEC-DOSY is most useful for small to medium sized systems. The stationary phase should be selected to have a fractionation range which encompasses the whole range of molecule sizes, but does not greatly exceed the size of the largest molecule.

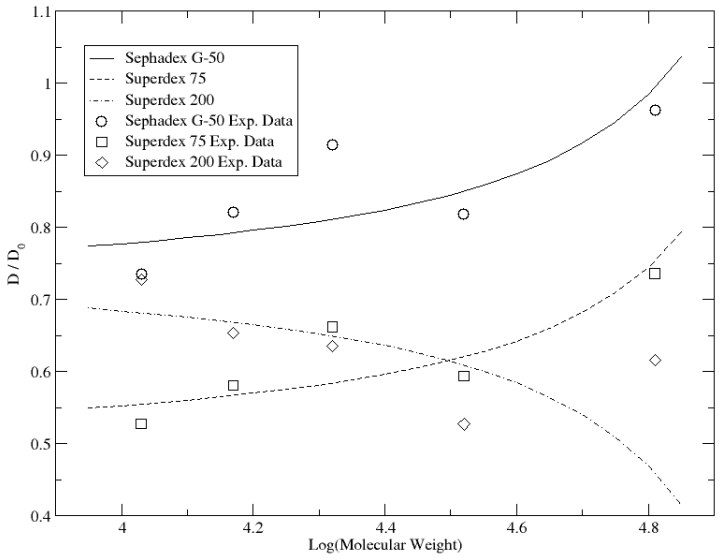

(a) 50 mM Phosphate + 150 mM NaCl

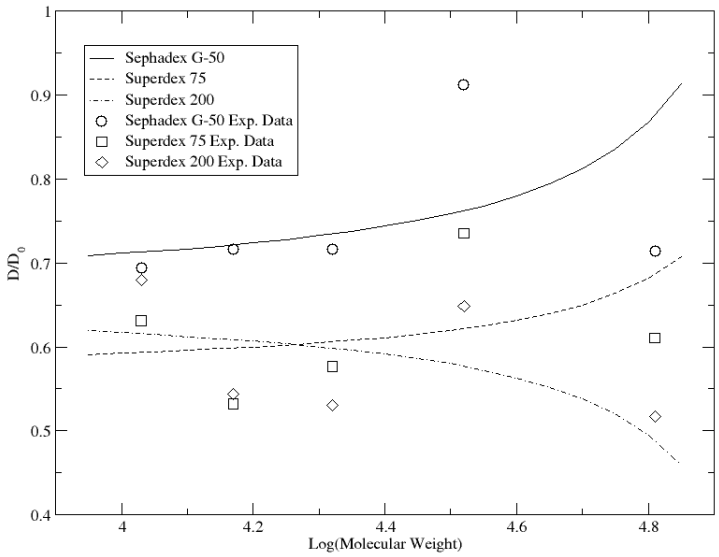

(b) 150 mM NaCl (D_2O)

Figure 3.19: D/D_0 graphs for polymer standards in phosphate and NaCl solutions

Table 3.10: Parameters extracted from Linear Fits of Equation 3.5

(a) 50 mM Sodium Phosphate + 150 mM NaCl

Sample	a_0	a_1 (10^{10} s m^{-2})	R^2
Polymer Standards	5.13	1.57	0.97
With Sephadex G-50	5.27	2.27	0.99
With Superdex 75	5.32	3.32	0.99
With Superdex 200	5.00	2.03	0.95

(b) 150 mM NaCl

Sample	a_0	a_1 (10^{10} s m^{-2})	R^2
Polymer Standards	5.08	1.55	0.97
With Sephadex G-50	5.17	2.36	0.98
With Superdex 75	5.14	2.76	0.98
With Superdex 200	5.01	2.35	0.97

(c) D_2O

Sample	a_0	a_1 (10^{10} s m^{-2})	R^2
Polymer Standards	5.01	2.15	0.91
With Sephadex G-50	5.03	3.72	0.80
With Superdex 75	4.94	3.82	0.85

3.3.1 Comparison with Size-Exclusion Chromatography

Size-exclusion chromatography was performed on the poly(styrene-4-sulphonate) standards in order to confirm that the samples behaved as expected. A Superdex 200 column and UV detection at 254 nm were used with a flow rate of 0.5 ml min^{-1} in 50 mM sodium phosphate buffer + 150 mM NaCl (pH 9). The graph of log(molecular weight) vs elution volume in Figure 3.20 shows a clear linear decrease in elution volume with increasing molecular weight. The elution volume is calculated from the elution time and the flow rate. This result is as predicted for these five polymers since all molecular weights are well within the fractionation range of the stationary phase. The lower molecular weight polymers are smaller and can access more of the pore volume and therefore spend longer on the column, resulting in a greater elution volume.

In size-exclusion chromatography, the elution volume is related to the volumes outside and inside the pores (V_o and V_i respectively) and the distribution coefficient (K_{SEC}) through Equation 3.6. The distribution coefficient, K_{SEC}, is the ratio of concentration of the polymer inside the pores to the concentration outside the pores, which varies from 0 for full exclusion from the pores to 1 for total permeation.

$$V_e = V_o + K_{\mathrm{SEC}} V_i \tag{3.6}$$

Size-exclusion chromatography is an entropy driven process, in comparison to other liquid chromatography methods which are enthalpy driven through absorption or adsorption with the stationary phase.[208] Distribution of the polymers between the mobile phase and the stagnant phase within the pores of the stationary phase approximates to thermodynamic equilibrium under normal

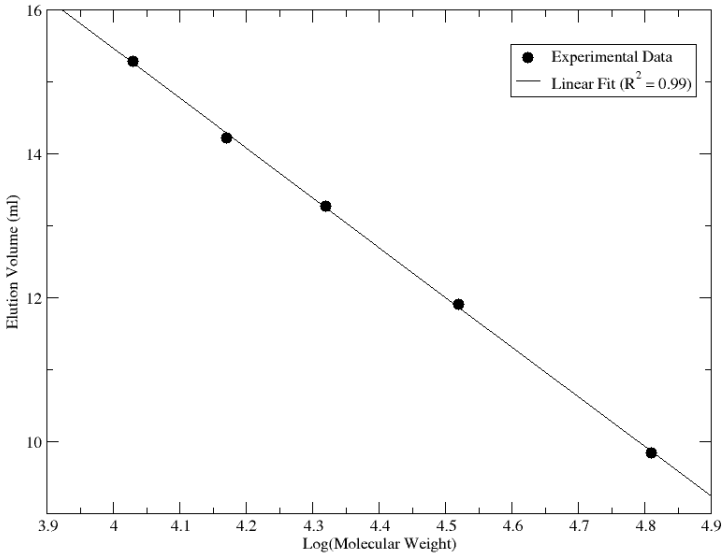

Figure 3.20: Size-exclusion chromatography of poly(styrene-4-sulphonate) standards

chromatographic conditions (Equation 3.7).[223]

$$\begin{aligned} \Delta G^\circ &= -kT \ln K_{\mathrm{SEC}} \\ &= \Delta H^\circ - T\Delta S^\circ \\ K_{\mathrm{SEC}} &= e^{-\Delta H^\circ/kT} e^{\Delta S^\circ/k} \end{aligned} \tag{3.7}$$

Where k is the Boltzmann constant and T is the absolute temperature in Kelvin.

In SEC, interactions with the stationary phase are minimised by use of inert columns and solvents with high ionic strength to screen ionic interactions. With no interactions between the analytes and the stationary phase $\Delta H^\circ \simeq 0$, this simplifies the equation for K_{SEC} to Equation 3.8. Partitioning of the polymer into the interior volume (V_i) of the pores involves a decrease in entropy due to the restriction in mobility caused by the pores, as such ΔS is negative and K_{SEC} is less than 1, this is consistent with the definition of K_{SEC} as a partition coefficient and a value of 1 indicating total permeation.

$$K_{\mathrm{SEC}} \simeq e^{\Delta S^\circ/k} \tag{3.8}$$

The main difference between size-exclusion chromatography and the diffusion NMR experiments in the presence of a stationary phase presented here is the use of flow. In size-exclusion chromatography, although the flow rate does not affect the elution volume,[208] the application of flow maintains the movement of the polymers through the porous network. The elution volume is directly related to the size of the molecule because smaller molecules have a higher K_{SEC} and will spend longer in the pores and therefore elute later. In this case, although diffusion is present within the system,[92] it is the flow coupled with the porous network that facilitates the separation of different sized molecules.

In the DOSY experiments there is no flow, however the polymers will equilibrate between the volume outside the pores and the volume within the pores available to that size of molecule as shown by static SEC experiments by Chang.[224] As discussed previously, the observed diffusion coefficient in the presence of the stationary phase is a weighted average of the polymer in the pore and polymer in free solution (Equation 3.3). The distribution coefficient (K_{DOSY}) can be defined as the ratio of the fraction of polymer in the pores to the fraction in free solution, this is comparable

to K_{SEC} for size-exclusion chromatography (Equation 3.9).

$$
\begin{aligned}
K_{\mathrm{DOSY}} &= \frac{f_p}{f_f} \\
f_p = \frac{C_p}{C_t}; \quad f_f &= \frac{C_f}{C_t} \\
\frac{f_p}{f_f} = \frac{C_p}{C_t} \times \frac{C_t}{C_f} &= \frac{C_p}{C_f} = K_{\mathrm{SEC}} \\
K_{\mathrm{DOSY}} = \frac{f_p}{f_f} &= K_{\mathrm{SEC}}
\end{aligned} \tag{3.9}
$$

Where C_p, C_f and C_t represent the 'in pore', 'free' and total concentrations respectively.

In conclusion, resolution of components by SEC-DOSY should be comparable to separation by SEC as both are dependent on the distribution coefficient between in pore and free components. This comparison is subject to some assumed conditions, such as the minimisation of interactions between the analyte and the stationary phase.

3.3.2 Comparison with Other Polymers

In the absence of a stationary phase, the diffusion coefficients for the polymers used in the proof of concept experiments do not fit to the data obtained using the polymer standards. The ∼15 kDa poly(allylamine) has a much lower diffusion coefficient than the 14.9 kDa poly(styrene-4-sulphonate) despite the similar molecular weight (Figure 3.21a). This is most likely due to differences in the hydrodynamic properties of the polymers, as the diffusion coefficient is related to the hydrodynamic radius of the molecule.

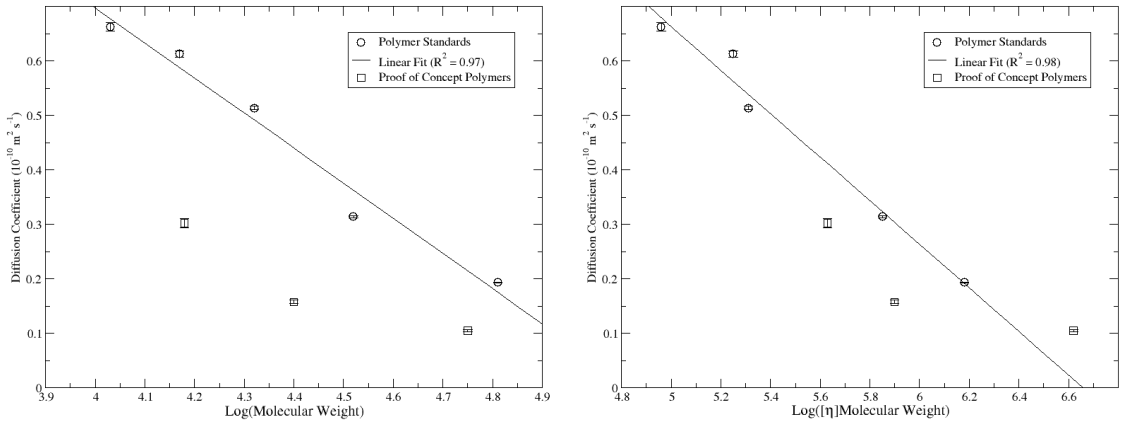

(a) Before Viscosity Adjustment

(b) After Viscosity Adjustment

Figure 3.21: Diffusion coefficients of polymers before and after viscosity adjustment

In size-exclusion chromatography the difference between the molecular size and molecular weight is overcome by introducing the intrinsic viscosity ($[\eta]$). The product of the intrinsic viscosity and molecular weight is equivalent to the hydrodynamic radius of the molecule. A plot of $[\eta]$MW against elution volume forms the universal calibration curve.[225] In order to test this approach for the DOSY data, viscosity measurements were acquired for all polymers and the intrinsic viscosity was calculated.

3.3.2.1 Types of Viscosity

There are several measurements of viscosity used in obtaining the intrinsic viscosity of a polymer, these are described in the following section and in Table 3.11.

Dynamic viscosity is measured using a viscometer and indicates the internal resistance to flow. Liquids with higher dynamic viscosity flow more slowly because a greater force is required.[210]

Relative viscosity is the dynamic viscosity of a solution relative to the pure solvent.

Specific viscosity (more accurately known as the relative viscosity increment[80]) is the ratio of the difference between the dynamic viscosities of the polymer solution and the viscosity of the pure solvent, or the relative viscosity minus 1. This gives the increase in viscosity on addition of that particular concentration of polymer. When divided by the concentration this becomes the *reduced viscosity* which is a measure of the polymer's ability to increase the solution viscosity per concentration unit.

The *inherent viscosity* is the natural logarithm of the relative viscosity ($ln(\eta_r)$) divided by the concentration. When there is no polymer in solution (i.e. concentration = 0) the relative viscosity is equal to 1 giving a $ln(\eta_r)$ value of zero for pure solvent. As concentration is increased the value of $ln(\eta_r)$ increases, dividing $ln(\eta_r)$ by concentration gives the incremental viscosity per concentration unit of polymer.

Both the reduced and inherent viscosities are 0 for the pure solvent; extrapolation of data from a range of concentrations back to zero concentration gives the *intrinsic viscosity*, a measure of the volume occupied per unit mass of polymer.

Table 3.11: Definitions of Viscosities

Viscosity	Symbol	Equation	Units	
Dynamic	η		kg m^{-1} s^{-1}	
Relative	η_r	$\frac{\eta}{\eta_0}$		η_0 is the viscosity of the solvent
Specific	η_{sp}	$\frac{\eta - \eta_0}{\eta_0} = \eta_r - 1$		
Reduced	η_{red}	$\frac{\eta_{sp}}{c}$	ml g^{-1}	c is the concentration in g ml^{-1}
Inherent	η_{inh}	$\frac{ln(\eta_r)}{c}$	ml g^{-1}	
Intrinsic	$[\eta]$	$\lim_{c\to 0} \eta_{red}$ $\lim_{c\to 0} \eta_{inh}$	ml g^{-1}	

3.3.2.2 Measuring Viscosity

First, the dynamic viscosity was measured using an Ostwald viscometer (Figure 3.22) and applying the Poiseuille formula (Equation 3.10).[210]

$$\eta = \frac{\pi r^4 t \Delta P}{8Vl} = A\rho t \qquad (3.10)$$
$$\Delta P = \rho g l; \quad \frac{\pi r^4 g}{8V} = A$$

Where r is the radius of the capillary, t is the time taken for volume V to flow through the capillary, V is the volume of the bulb between point **A** and **B** in Figure 3.22, l is the length of the capillary and ΔP is the pressure difference caused by gravity. A is a constant for the viscometer and ρ is the density of the liquid.

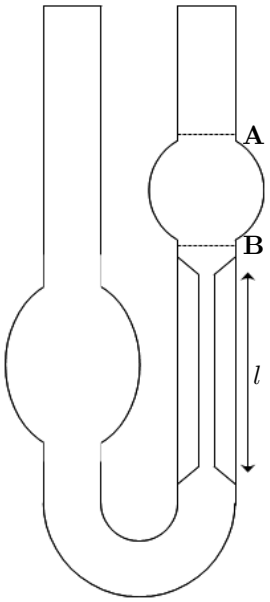

Figure 3.22: Schematic of an Ostwald viscometer. Solution is drawn up the right hand side through the capillary, past point **A**, the time taken for the solution to fall from **A** to **B** is measured.

The viscometer was calibrated with water ($\eta = 1.0 \times 10^{-3}$ kg m^{-1} s^{-1}) to obtain the constant A (2.8×10^{-8} m^2 s^{-2}), the dynamic viscosity of the pure solvent (150 mM NaCl, H_2O), η_0 was obtained and used for calculations of the relative, reduced and inherent viscosities.

The dynamic viscosity was obtained for each polymer (proof of concept and standard polymers) across a range of concentrations. The intrinsic viscosity $[\eta]$ can be obtained from the y-intercept of the inherent viscosity and reduced viscosity against concentration, Figure 3.23 shows a representative example of the viscosity data obtained for the 56 kDa poly(allylamine). The values plotted on the graph are calculated using the average result of three time measurements; the difference in y intercept (i.e. intrinsic viscosity) between the inherent viscosity data and reduced viscosity data is due to experimental error.

3.3.2.3 Viscosity Adjustment of the DOSY Data

The intrinsic viscosity was calculated and log$[\eta]$MW used in place of logMW to plot the diffusion data previously obtained (Figure 3.21b). The viscosity of the polymers used in the proof of concept experiments was greater than the polymer standards. The diffusion coefficient is inversely proportional to the dynamic viscosity (Einstein-Sutherland equation), this explains why the diffusion coefficients were lower for the more viscous proof of concept polymers than the polymer standards with similar molecular weight. Figure 3.21 shows the comparison of the diffusion coefficients of the polymer standards and proof of concept polymers before (a) and after (b) the inclusion of the intrinsic viscosity.

This adjustment improves the correlation between the polymer standards and the proof of concept polymers but not completely. The remaining differences could be due to the unknown polydispersity

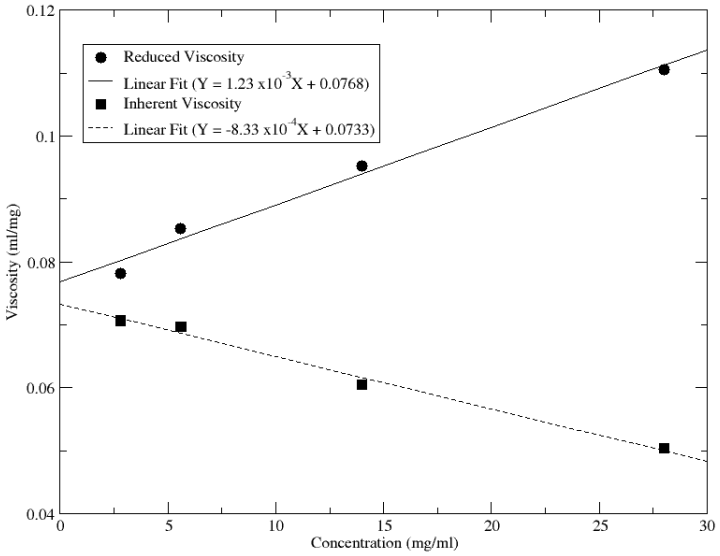

Figure 3.23: Inherent and reduced viscosities of 56 kDa poly(allylamine hydrochloride)

of the proof of concept polymers compared to the low polydispersity of the polymer standards. Higher polydispersity indicates a greater range of molecular weights; the diffusion data is analysed assuming a mono-exponential signal decay relating to a single component, increased polydispersity will lead to failure of this assumption and under or over estimation of the diffusion coefficient (depending on the precise shape of the molecular weight distribution). The diffusion coefficients for the 15 kDa poly(allylamine hydrochloride) and the 25 kDa poly(*N*-isopropyl acrylamide) are lower than the calibration curve, this could suggest the presence of larger polymer units in the sample than indicated by the molecular weight.

Comparison of the diffusion coefficients in the presence of stationary phase would be affected by the charges of the poly(allylamine hydrochloride) polymers and the poly(styrene-4-sulphonate) standards as well as the differences in hydrodynamic radii. The positively charged poly(allylamine) polymers are likely to interact with the hydroxyl groups of the stationary phase whereas the negatively charged poly(styrene sulphonate) polymers will not. The difference in the electrostatic interactions complicate the comparison of the diffusion coefficients of the different polymers in the presence of the stationary phase, necessitating the use of the polymer standards for the characterisation of the stationary phases.

3.4 Data Acquisition Using Magic Angle Spinning

The addition of the stationary phases used in this study causes line broadening due to differences in magnetic susceptibility leading to inhomogeneity of the magnetic field within the sample. Magic angle spinning (MAS) has been shown to reduce magnetic susceptibility broadening.[226]

The effect of magic angle spinning on line broadening caused by addition of Sephadex G-50 is demonstrated in Figure 3.24 where the spectra of 2 mM Lactalbumin with and without Sephadex G-50 is compared with and without MAS. The addition of the stationary phase without the use of MAS causes significant broadening such that the peaks are no longer visible, the same sample using MAS has clearly resolved peaks similar to the spectrum without stationary phase.

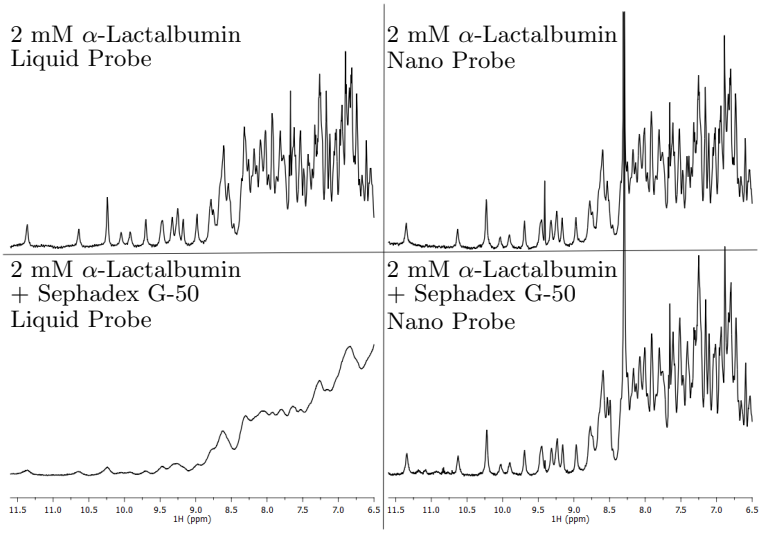

Figure 3.24: Extracts of ^{1}H spectra for 2 mM α-lactalbumin; top left: No Sephadex G-50, No MAS; bottom left: Sephadex G-50, No MAS; top right: No Sephadex G-50, MAS; bottom right: Sephadex G-50, MAS. Spectra were all acquired with 128 scans, MAS spectra were acquired with a spin rate of 2200 Hz.

3.4.1 Application of MAS to SEC-DOSY

The application of MAS to the SEC-DOSY experiments was intended to improve the resolution of the ^{1}H domain in the presence of stationary phase, therefore allowing the separation of complex mixtures. Figure 3.24 shows that MAS reduces the line broadening of a sample of the ∼14 kDa protein Lactalbumin in the presence of Sephadex G-50 .

Data obtained for 0.4 mM samples of the poly(styrene-4-sulphonate) polymer standards used for characterisation of the stationary phase in 50 mM sodium phosphate buffer + 150 mM NaCl in D_2O using the HR-MAS probe with a spin rate of 2.5 kHz showed significant variation from the results previously obtained. Figure 3.25 shows the diffusion coefficient values for the poly(styrene-4-sulphonate) samples in 50 mM sodium phosphate buffer + 150 mM NaCl acquired in a 5 mm NMR tube (no MAS) and a 40 μl rotor (2.5 kHz MAS). The concentration of the samples was increased due to the low volume of the MAS rotor leading to poor sensitivity, however this should decrease the diffusion coefficient in comparison to 0.2 mM samples, as shown in previous experiments (see Figure 3.1).

The cause of the difference in diffusion coefficient between the liquids probe and the HR-MAS probe is not fully understood. A study by Bradley et al. suggested that the spinning of the sample causes vortexing which can lead to fluctuations in signal intensity in the ^{1}H dimension.[227] Due to the random nature of the fluctuations caused by sample vortexing, the variations in signal intensity were shown to be improved for dilute mixtures by increased signal averaging.

In a separate study of magic angle spinning in self-diffusion measurements of liquids by Viel et al.[228] low volume rotors were implemented to improve the reliability of diffusion measurements using MAS. A rotor with a 12 μl active volume showed consistent diffusion coefficient results over a range of spin rates for distilled water but overestimated the diffusion coefficient of acetonitrile at spin rates of 2 and 8 kHz. In comparison, a 50 μl rotor overestimated the diffusion coefficient of distilled water at spin rates above 5 kHz and the values obtained for the less viscous acetonitrile were far greater than the literature value for all spin rates above 2 kHz.

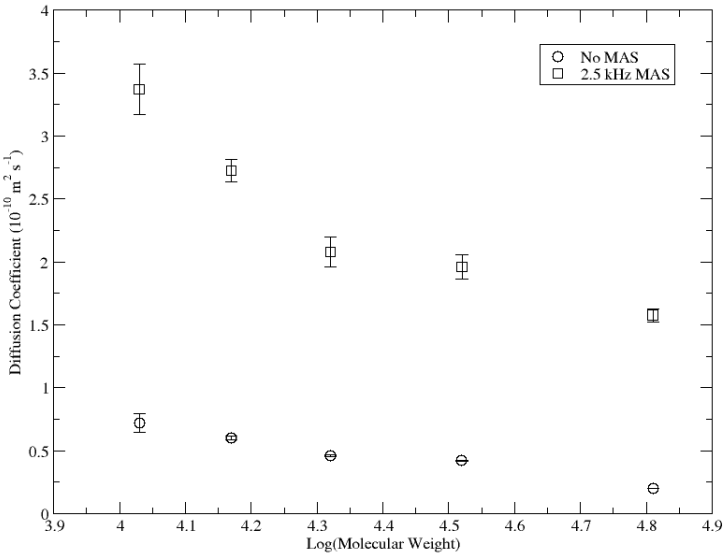

Figure 3.25: Diffusion coefficients for poly(styrene-4-sulphonate) samples (MW: 10 - 63 kDa) in 50 mM sodium phosphate buffer + 150 mM NaCl. Circles: 0.2 mM samples in 5 mm NMR tubes, no MAS. Squares: 0.4 mM samples in 40 μl rotors, 2.5 kHz MAS.

The diffusion coefficient data acquired with the HR-MAS probe are larger than those acquired with the standard liquids probe, this is comparable to the increased diffusion coefficients (compared to literature values) shown by Viel et al.[228] in 50 μl rotors. The erratic signal decay shown by Bradley et al.[227] is also apparent in the data obtained in this study suggesting that vortexing effects could be present. Spinning the rotor causes additional motion of the sample solution, this has the potential to disrupt the free diffusion of the molecules and lead to larger observed diffusion coefficients. Another consideration shown to affect the quality of spectra acquired using MAS is the synchronisation of the gradient length and diffusion delay to the rotor period.[229] The duration of the diffusion period should be equal to an integer number of rotations of the rotor so that the rotor is in the same position when the encoding and decoding gradients are applied and any displacement of the molecule is due to diffusion only. Without synchronisation, the apparent diffusion coefficient can appear to be larger, this is caused by the physical displacement of the molecule caused by rotation leading to additional signal attenuation.[230]

Studies of SEC-DOSY using MAS were inconclusive within the time-frame of this research. Further investigations into the effect of magic angle spinning on a sample and the acquisition of DOSY data is required.

3.5 Conclusions

In this chapter the development of diffusion-ordered spectroscopy with size-exclusion chromatography media has been presented. The effect of three stationary phases has been demonstrated with a range of polymer systems. This method is not suitable for improving resolution of mixtures as initially intended; the smaller molecules which have the larger diffusion coefficient without stationary phase are most affected on addition of stationary phase, this leads to a reduction in the range of diffusion coefficients covered.

It has been shown that on addition of a size-exclusion chromatography stationary phase to a

polymer solution the polymer equilibrates between the free solution outside the pores and a volume inside the pores dependent on the size of the polymer. The diffusion spectroscopy data of these samples are modelled by a population weighted average of the in pore and free components. Data obtained for polymer standards can be modelled by the equation $logM = a_0 - a_1 D$ and the values extracted for a_0 and a_1 show good correlation with data derived for size-exclusion chromatography by Determann and Michel.[221]

For comparison between polymers with different hydrodynamic properties, the intrinsic viscosity gives the volume of the polymer per mass unit, the product of the intrinsic viscosity and the molecular weight gives an estimation of the hydrodynamic radius. Viscosity adjustment of the DOSY data leads to better correlation between the polymer standards and the proof of concept polymers.

Finally, the use of MAS to reduce the line broadening caused by the addition of stationary phase leads to issues in the diffusion experiment. This is most likely due to vortexing effects caused by the spinning and the requirement of rotor synchronisation of the gradient length and diffusion period.

Studies of molecules with particularly small diffusion coefficients are limited by the gradient strengths available on the probe used. A potential improvement of this research would be the implementation of stronger gradients, this would allow access to smaller diffusion coefficients, improve the accuracy of the observed diffusion coefficients in the presence of stationary phases and allow better analysis of the change in diffusion coefficient on addition of stationary phase.

Chapter 4

Application of SEC-DOSY to Aggregating Species

The use of size-exclusion chromatography media with diffusion-ordered spectroscopy was shown in the previous chapter to alter the diffusion profile of polymers depending on their molecular weight. In the case of aggregating species, where there is a distribution of aggregate sizes, SEC-DOSY has the potential to resolve the signals of the monomers and small assemblies from the those of the large aggregates through the partitioning effect of the porous network.

In this chapter SEC-DOSY is applied to two aggregate systems with differing results. Sunset yellow shows good resolution in the diffusion domain of monomeric units from larger aggregates and a thorough discussion of conclusions drawn from this is included in this chapter. Application of the method to the time dependent aggregation of insulin shows a reduction in diffusion coefficient but no resolution of small and large aggregates, the reasons behind this will also be discussed. Comparison of the two systems allows conclusions to be drawn as to the potential utility of this method. The results of the sunset yellow study have been published in The Journal of Physical Chemistry C[231] and the article is included in Appendix A.2.

4.1 Sunset Yellow

Sunset yellow is the common name for disodium 6-hydroxy-5-[(4-sulphonatophenyl)azo]naphthalene-2-sulphonate, Figure 4.1 shows the azo (a) and hydrazone (b) forms of sunset yellow; the hydrazone tautomer is the most stable.[21]

Sunset yellow is a monoazo dye which is known to form lyotropic, chromonic liquid crystals above a certain concentration.[7,17,18,21] The sunset yellow molecules form aggregate stacks with increasing concentration, the columnar assemblies are stabilised by $\pi - \pi$ interactions between the naphthalene and phenyl rings, these stacks then undergo further association between aggregates to give nematic (N) and hexagonal (M) mesophases.[13] Molecules which form chromonic phases are characterised by large, planar, aromatic regions with hydrophilic groups at the edge.[10] Many studies of sunset yellow have focussed on characterising the liquid crystal phases,[21,232–234] using a variety of techniques including X-ray diffraction,[21,232,233] optical microscopy,[21] rheology[232] and NMR.[21] Studies of the isotropic phase of sunset yellow using UV-vis spectroscopy,[7] molecular dynamics simulations[235]

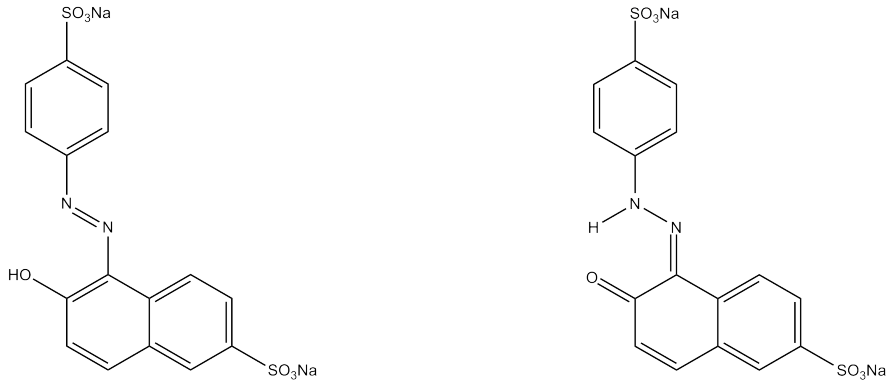

(a) azo tautomer (b) hydrazone tautomer

Figure 4.1: Structures of the azo and hydrazone tautomers of sunset yellow

and NMR[23] show that aggregation also occurs at low concentrations in the isotropic phase.

4.1.1 Studies without Stationary Phase

Diffusion NMR studies of sunset yellow in the isotropic phase and in the absence of any stationary phase have been previously undertaken and published by Renshaw and Day.[23] Similar experiments were performed in this research, firstly to confirm that results from a separately purified batch of sunset yellow were consistent with previous data, and secondly to facilitate direct comparison between samples with and without stationary phase by using the same solutions of purified sunset yellow. The results of ^{1}H and diffusion NMR experiments on sunset yellow samples without the addition of stationary phase are consistent with those shown by Renshaw and Day[23] and will be discussed here before continuing on to the SEC-DOSY studies.

4.1.1.1 ^{1}H NMR

The ^{1}H NMR spectra of sunset yellow at all concentrations in the isotropic phase show a single set of peaks indicating there is fast exchange between monomers and aggregates on the NMR timescale. This means that there is a constant formation and dissociation of aggregates and transfer of monomer units between aggregates. This exchange occurs faster than the acquisition of NMR data and the peaks appear at chemical shift which is an average of all the assemblies in the solution. Slower exchange would lead to a distribution of peaks relating to each of the aggregates sizes. The chemical shifts of the peaks change with concentration; as the concentration of the sample is increased the peaks shift to lower chemical shifts and become broader. Spectra acquired for the whole range of concentrations of sunset yellow in D_2O (10-700 mM) are shown in Figure 4.2. Higher concentrations of sunset yellow underwent a phase transition to liquid crystal evidenced by a highly viscous solution and broad ^{1}H peaks.

The observed change in chemical shift is due to additional shielding caused by the aromatic ring-current[82] from the neighbouring molecules in the stack. The broadening of the peaks is caused by the increased aggregate size leading to slow molecular tumbling and shorter spin-spin relaxation times (T_2).

At 50 mM all ^{1}H peaks are well resolved and can be assigned to the sunset yellow molecule, as shown in Figure 4.3. Peaks were assigned using chemical shift and J-coupling values as well

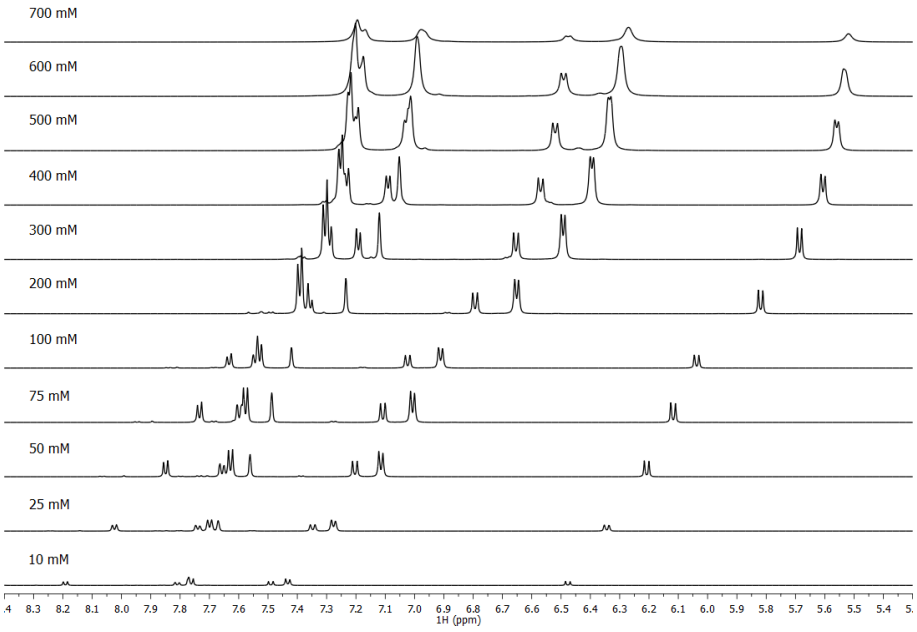

Figure 4.2: Extracts of ^{1}H NMR spectra for sunset yellow in D_2O at varying concentrations (10–700 mM as labelled)

as 2-dimensional NMR data (included in Appendix B) and comparison with reported literature values.[21,22] As the concentration is changed the magnitude of change in chemical shift ($\Delta\delta$) differs between peaks leading to peak overlap at other concentrations. For example, at 100 mM the peak at 7.63 ppm is resolved from all of the other peaks, however at 200 mM this peak is overlapping with another peak at 7.4 ppm. The difference in $\Delta\delta$ between peaks was used by Edwards et al.[21] to infer the organisation of the molecules within the aggregates, peaks with greater shift were said to be in the core of the $\pi - \pi$ stacking, this includes protons from both the naphthalene and the phenyl rings suggesting head-to-tail stacking of the molecules. Figure 4.4 shows the progression of the chemical shifts of the peaks assigned in Figure 4.3 over the range of concentrations used in this study.

The difference in chemical shift between the lowest concentration (10 mM) and the highest concentration (700 mM) for each peak is reported in Table 4.1, H_B on the phenyl ring and H_G on the naphthalene ring show the largest decrease in chemical shift, while those around the periphery of the molecule (H_A, H_C) and close to the sulphonate groups (H_D, H_E and H_F) show less change in chemical shift.

Table 4.1: Magnitude of Change in Chemical Shifts

Peak	A	B	C	D	E	F	G
δ_H(10 mM)−δ_H(700 mM)	0.96	1.16	1.01	0.56	0.79	0.64	1.21

The mechanism of aggregation of chromonic systems has previously been modelled as isodesmic; this model is based on equal energy requirements for the addition of a monomer to an aggregate, with no dependence on aggregate size.[14] This model has been successfully applied to several similar aggregate systems, such as Orange II[4] and Acid Red 266,[9] to obtain K_{eq} values for aggregation from the variations in chemical shift; however, Jones et al.[22] have recently shown that the isodesmic model is too simple for accurate modelling of sunset yellow aggregation. As knowledge of the equilibrium constant for sunset yellow was not required for the application of SEC-DOSY in this

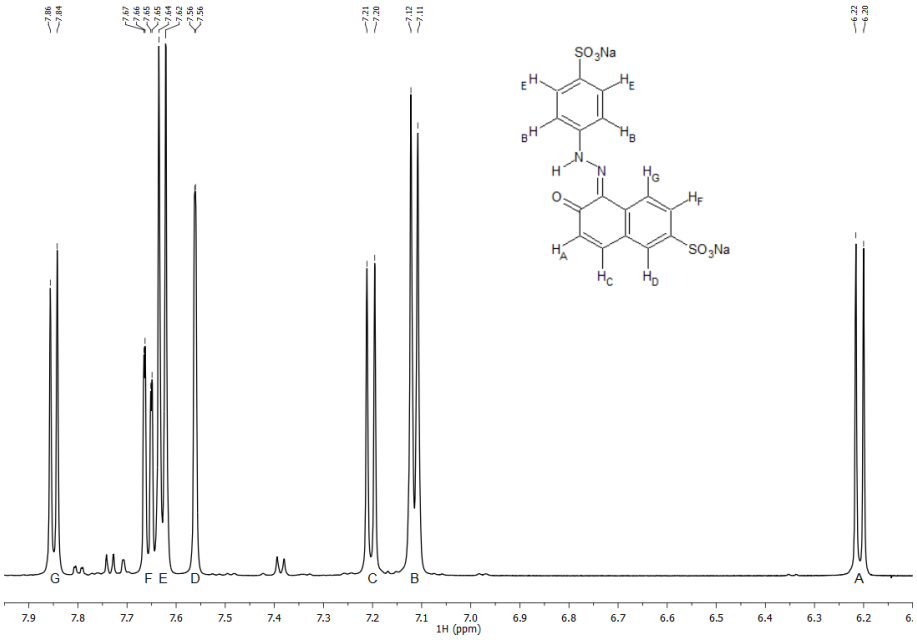

Figure 4.3: Extract of ^{1}H spectrum of 50 mM sunset yellow in D_2O with peak assignment. The additional small peaks are attributed to the presence of a small amount of the azo tautomer.

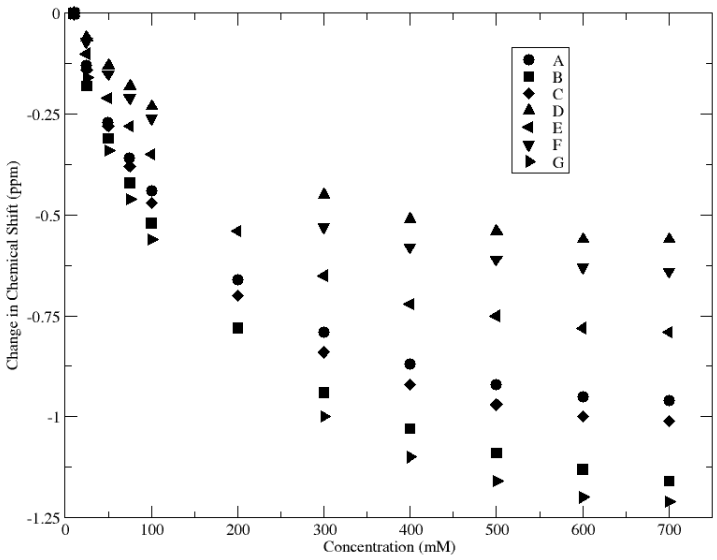

Figure 4.4: Change in chemical shift for each peak over a range of sunset yellow concentrations

work, no modelling of the system was attempted. The development and investigation of other aggregation models is currently in progress in the Day lab.

4.1.1.2 DOSY

Diffusion NMR data were acquired for a range of sunset yellow concentrations from 10 mM to 700 mM. At all concentrations a single diffusion coefficient is extracted for each peak, even when a bi-exponential fit is allowed in DOSY toolbox.[107] The diffusion coefficient decreases as the concentration increases consistent with an increase in number of larger aggregates (with smaller associated diffusion coefficients). Figure 4.5 shows the trend in diffusion coefficient with concentration.

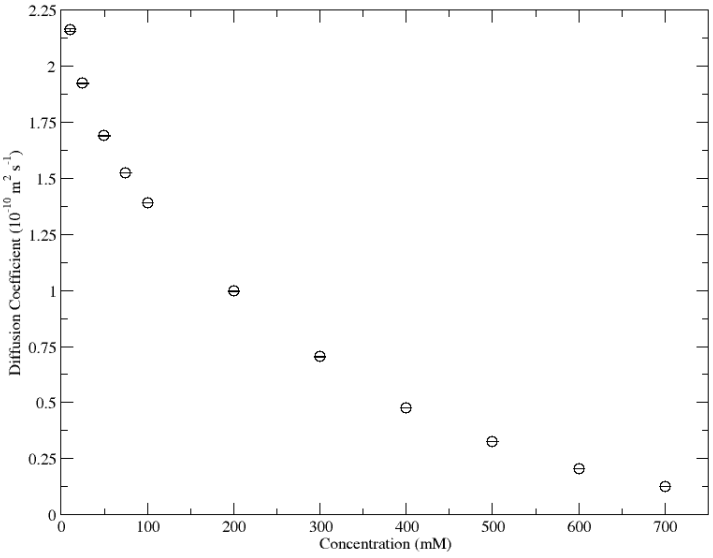

Figure 4.5: Change in diffusion coefficient over a range of sunset yellow concentrations

Previous diffusion NMR studies of sunset yellow also showed a single diffusion coefficient which decreased with increasing concentration as the size of the aggregates increased.[23] Due to the fast exchange between the monomeric and aggregated species (as indicated by the single set of peaks and diffusion coefficients), the diffusion coefficient can be considered as a population-weighted average of all aggregates in the solution (Equation 4.1).

$$D_{av} = \sum_i \frac{X_N^{(i)} D_i}{N} \tag{4.1}$$

In the study by Renshaw and Day the excellent fit of the signal decay to a single exponential was used to confirm the population-weighted average approach to diffusion coefficient analysis.[23] The distribution of aggregate sizes have been modelled using a simple thermodynamic theory of aggregation by Israelachvili[218] as demonstrated by Renshaw and Day[23] and Horowitz et al.[7]

4.1.2 Studies with Stationary Phase

Three Sephadex stationary phases were used for SEC-DOSY investigations of sunset yellow aggregation. The media differ in their fractionation ranges as detailed in Table 4.2. Samples were prepared by adding the dry Sephadex to sunset yellow solutions of varying concentration and allowing the

media to swell for ∼3 hours, as detailed in Chapter 2. The Superdex media used in Chapter 3 were not used in these experiments, as Superdex was supplied as a suspension, the only way to add analytes at sufficient concentration was to replace the supernatant volume with analyte solution. The volumes of sunset yellow stock solution required to prepare the desired concentrations were greater than the supernatant available (∼200 μl in 1 ml).

Table 4.2: Properties of Sephadex Stationary Phases[187,236–238]

Stationary Phase	Particle size (μm)	Bed Volume (ml g^{-1} dry Sephadex)	Fractionation Range (kDa)	
			Globular Proteins	Dextrans
Sephadex G-50	20–50	9–11	1.5–30	0.5–10
Sephadex G-75	20–50	12–15	3–70	1–50
Sephadex G-100	20–50	15–20	4–100	1–100

The three Sephadex stationary phases have the same composition of dextran cross-linked with epichlorohydrin, the different fractionation ranges are produced by varying amounts of cross-linking. With more cross-linking smaller pores are formed and therefore a lower fractionation range is achieved.[225] Another consequence of increasing the amount of cross-linking is a reduction in the number of polar hydroxyl groups which decreases the volume of solvent the stationary phase will absorb when swelling. The bed volumes for the three Sephadex stationary phases are included in Table 4.2. When the Sephadex stationary phases are swelled in excess solvent and allowed to settle, the settled volume increases across the series from G-50 to G-100, the increased cross-linking in Sephadex G-50 leads to a more densely packed stationary phase. In size-exclusion chromatography the packing of the stationary phase determines the maximum flow rate through the column, Sephadex G-50 behaves as rigid spheres so any increase in flow rate leads to an increase in pressure but does not affect the separation.[186] In contrast, Sephadex G-75 and G-100 are classed as 'soft' gels[225] and the pressure in the column must not exceed 0.16 and 0.096 bar for G-75 and G-100 respectively to avoid compressing the gel[239,240] which would affect the resolution. As no pressure is applied to the stationary phases in the NMR samples this should not be a problem.

4.1.2.1 ^{1}H NMR

Addition of Sephadex to all concentrations of sunset yellow results in additional peaks in the ^{1}H spectrum, these peaks appear upfield of the peaks originally seen in the absence of stationary phase. Figure 4.6 shows the ^{1}H spectra of 50 mM sunset yellow in D_2O and in each of the Sephadex phases. Peaks that are aligned with those without stationary phase are labelled •, the new peaks are marked with * and those belonging to overlapping peaks are marked ∘. The three multiplets between 7.5 and 7.7 ppm in D_2O are too broad to identify the individual peaks in the presence of stationary phase. It is likely that new peaks exist for each peak of the molecule, however broadening and peak overlap hinders the full assignment of the spectra with stationary phase. The Sephadex peaks are not visible in these spectra as the peaks occur at a lower chemical shift, however, the slight increase in baseline on the right side of the Sephadex G-50 spectrum is due to the broad peaks of the Sephadex G-50.

In the absence of the stationary phase it was shown that the chemical shift of the peaks decreased as the concentration (and therefore the size of the aggregates) increased (Figure 4.4); the large aggregates have lower chemical shifts due to increased shielding.[21] In the presence of stationary phase, the higher chemical shifts of the 'new' peaks are therefore indicative of smaller aggregates.

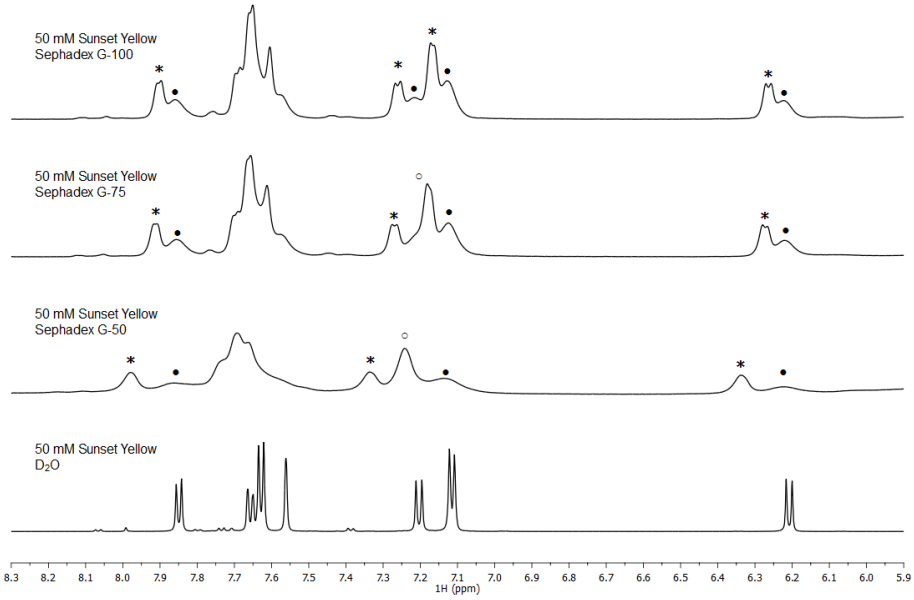

Figure 4.6: Extracts of ^{1}H spectra of 50 mM sunset yellow in D_2O, Sephadex G-50, Sephadex G-75 and Sephadex G-100. Labels: •, peaks aligned with D_2O sample; *, new peaks in presence of stationary phase; ∘, overlapping peaks.

These peaks are likely to be from the monomers and small aggregates which are able to access the pores of the stationary phase. The appearance of these new peaks indicates that there is no longer fast exchange between the small aggregates in the pores and the larger aggregates which do not fit in the pores of the stationary phase. This assignment is confirmed by the use of HR-MAS and the DOSY experiments, as discussed in the following sections. There are now two different exchange regimes within the sample. There is slow exchange between the 'free' and 'in pore' components, but each component is a distribution of aggregates in which the fast exchange between the monomers and aggregates is retained. For clarity, the new peaks in the presence of stationary phase will be referred to as 'in pore' and those with the same chemical shift as those without stationary phase will be referred to as 'free'. The chemical shift of all peaks decrease as the concentration of sunset yellow is increased. The trend is consistent with the data acquired in the absence of stationary phase and is due to the increased shielding in the aggregates.

All three stationary phases cause broadening of the sunset yellow signals due to the introduction of sample inhomogeneity, the magnitude of broadening decreases across the series of stationary phases from G-50 to G-100, this is a consequence of the decrease in density of the networks due to the decrease in cross-linking. In samples with Sephadex G-75 and G-100 some of the 'in pore' peaks retain some coupling patterns, this is possibly due to the larger pores allowing the small aggregates to tumble more freely than in Sephadex G-50.

Size of 'In Pore' Aggregates

At each concentration the difference in chemical shift between the 'in pore' and 'free' peaks decreases from G-50 to G-100, this is most clearly seen for the pair of peaks between 6.15 and 6.45 ppm in Figure 4.6 and is due to the increasing fractionation ranges of the stationary phases. In Sephadex G-50 the largest component which will fit in the pores is an aggregate of a similar size to a 30 kDa globular protein, in Sephadex G-100 the pores are accessible for aggregates up to the size of a 100 kDa globular protein. From this, it is clear that the average chemical shift of the 'in pore' component for Sephadex G-50 will be higher than that of Sephadex G-100 due to the smaller

aggregate sizes able to access the pore. The chemical shift of the 'free' component does not differ between the stationary phases, leading to the observed decrease in separation of the 'in pore' and 'free' peaks on change of stationary phase.

Using the molecular weight and corresponding values of Stokes radius (R_s) for a range of proteins taken from an article by Erickson[241] on the 'Size and Shape of Protein Molecules', a calibration curve was produced and used to estimate the size of the proteins excluded from the stationary phases and therefore the size of the pores of the stationary phases. The calibration curve with values for the proteins and the exclusion limits of the stationary phases is shown in Figure 4.7.

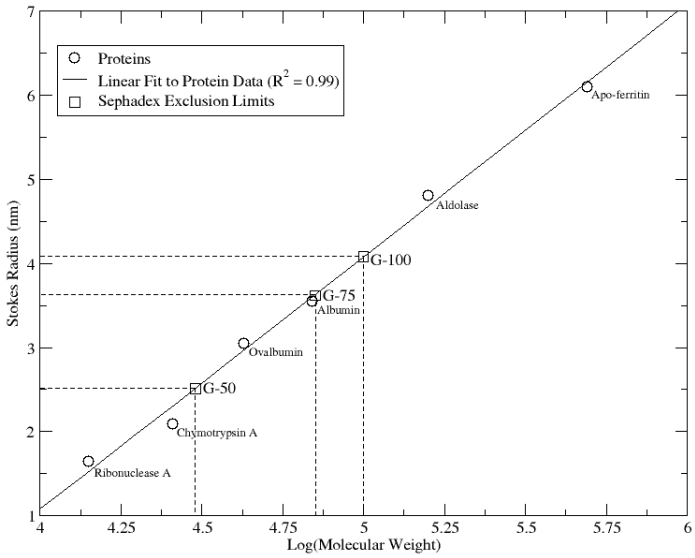

Figure 4.7: Calibration graph for the pore size of the Sephadex stationary phases. Circles represent proteins, the molecular weight and stokes radius data were taken from literature.[241] Linear regression of this data provides the equation $R_S = 3.004 \times \log(MW) + 10.939$. This equation was used to calculate the pore radius of each of the Sephadex phases, these values are plotted as squares.

An X-ray study of sunset yellow aggregates by Joshi et al. showed that the distance between molecules in the stacks is 3.32 Å and the diameter of the aggregate is 13.4 Å.[18] Each aggregate is therefore described by a cylinder with a radius of 6.7 Å and a length which is dependent on the number of monomers in the stack. Using these dimensions the number of molecules in the aggregates excluded from the pores of the stationary phase can be estimated by dividing the diameter of the pores by the intermolecular spacing of the stack, these values are rounded up to the nearest integer number of monomers and are included in Table 4.3. For example, Sephadex G-75 has an estimated pore diameter of 7.24 nm, an aggregate of this length would contain 21.8 monomers. This suggests that aggregates composed of more than 21 monomers are excluded from the pores of Sephadex G-75. Due to the cylindrical shape of the aggregates compared to the spherical nature of globular proteins, this can only be taken as an estimate of the size of aggregates excluded from the pores of the stationary phase.

Distribution of Aggregates

The distribution of aggregates between the pores and free solution can be determined using the relative peak areas of the individual peaks. The peak areas are determined by fitting the lineshape of the pair of peaks assigned to H_A, these peaks were used as they were well separated from the others at all concentrations, however because they appear closest to the solvent and stationary phase peaks the sunset yellow peaks can be obscured at low concentrations, as shown in Figure 4.8.

Table 4.3: Calculated Radii of Stationary Phase Pores

Stationary Phase	Exclusion Limit (Da)	Calculated Radius (nm)	Number of Monomers in Aggregate Excluded from Stationary Phase
Sephadex G-50	30000	2.52	16
Sephadex G-75	70000	3.62	22
Sephadex G-100	100000	4.09	25

The large stationary phase peaks can interfere with the peaks of the sunset yellow, as such these are included in the peak fitting in efforts to compensate for any additional area the stationary phase contributes to the sunset yellow peaks. The ability to compensate for the stationary phase peaks in linefitting makes it a preferable method of peak area analysis over integration where contributions from surrounding peaks are difficult to estimate and adjust for.

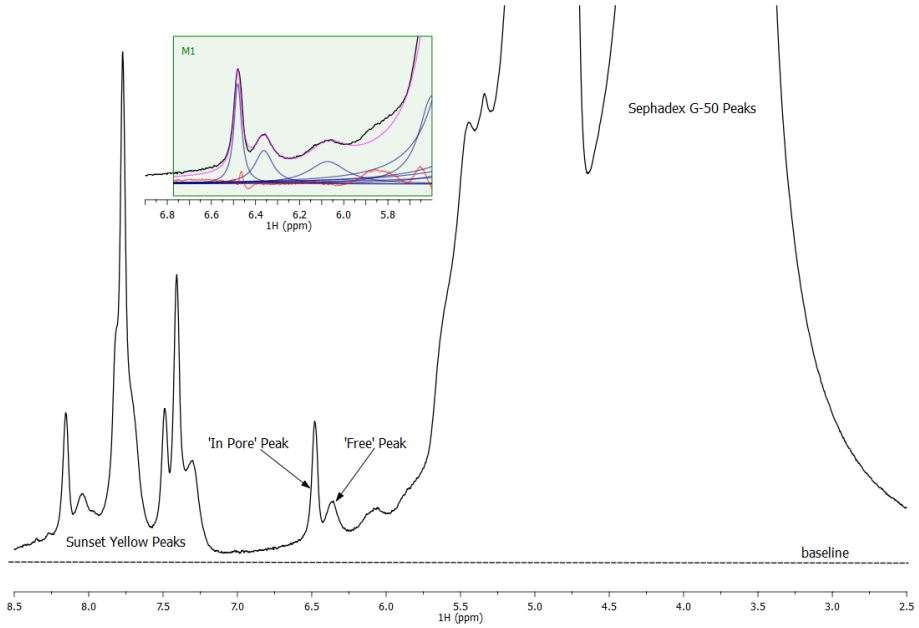

Figure 4.8: Extract of the ^{1}H spectrum of 25 mM sunset yellow in Sephadex G-50. The inset shows the peak fitting used in the peak area ratio analysis.

The peak area of each of the individual peaks is proportional to the number of nuclei in the two environments. The mole fraction of 'in pore' sunset yellow is determined by dividing the peak area of the 'in pore' peak by the total peak area (Equation 4.2, where x_p is the mole fraction of sunset yellow in pore and I_f and I_p are the peak areas of the 'free' and 'in pore' peaks respectively). The results for each of the stationary phases are shown in Figure 4.9.

$$x_p = \frac{I_p}{I_f + I_p} \tag{4.2}$$

The trend in mole fraction of 'in pore' sunset yellow with increasing concentration is similar for all three stationary phases, there is a rapid decrease between 10 mM and 100 mM, followed by a slower decrease from 100 mM to 700 mM. The decrease in the fraction of 'in pore' sunset yellow is consistent with the increasing aggregate size leading to a reduction in the fraction available which fit in the pores. There are two regimes apparent in this data, above and below 100 mM, these two

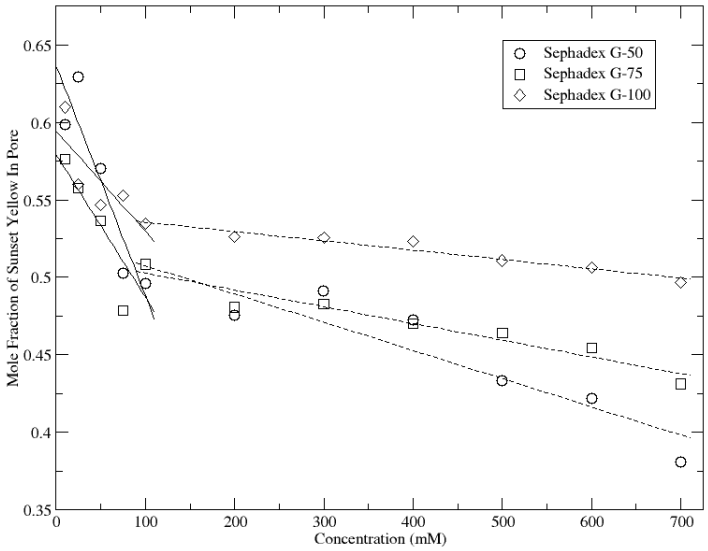

Figure 4.9: Trend in mole fraction of 'in pore' sunset yellow with concentration

regimes can be modelled with straight lines, as shown on Figure 4.9 with the fitted parameters detailed in Table 4.4.

Table 4.4: Parameters extracted from Linear Fits of the Fraction 'In-Pore' Data

Stationary Phase	[SSY] $\leq$ 100 mM			[SSY] $\geq$ 100 mM		
	Gradient ($\times 10^{-3}$ M^{-1})	Intercept	R^2	Gradient ($\times 10^{-3}$ M^{-1})	Intercept	R^2
Sephadex G-50	-1.48	0.64	0.85	-0.18	0.53	0.87
Sephadex G-75	-0.92	0.58	0.75	-0.11	0.52	0.93
Sephadex G-100	-0.64	0.59	0.67	-0.06	0.54	0.95

In both regimes the trend in the gradient of the fitted data follows the trend in fractionation range (and therefore pore size) of the stationary phases. This indicates that the differences between the stationary phases are caused by size-exclusion effects, i.e. the partitioning of the aggregates between the 'in-pore' and 'free' domains is determined by the size of the aggregates relative to the size of the pores of the stationary phase.

4.1.2.2 HR-MAS

Magic angle spinning can be used to reduce broadening caused by magnetic susceptibility broadening[230] as seen in the presence of Sephadex and has been used in other chromatographic NMR applications.[194,201,202] Application of MAS to the samples of sunset yellow in the presence of Sephadex reduces the linewidths of the peaks relating to aggregates in 'free' solution but those of the 'in pore' aggregates are not affected to the same extent. Figure 4.10 shows the ^{1}H spectra of 50 mM sunset yellow in the presence of Sephadex G-50 acquired in a standard liquids experiment and in an HR-MAS experiment.

The addition of the stationary phase causes broadening through two mechanisms; the dominant effect applied to all aggregates is the magnetic susceptibility broadening due to sample inhomogeneity, however, restricted motion of the aggregates can lead to additional dipolar broadening. The 'free' aggregates are affected only by the inhomogeneity broadening which is effectively reduced by the

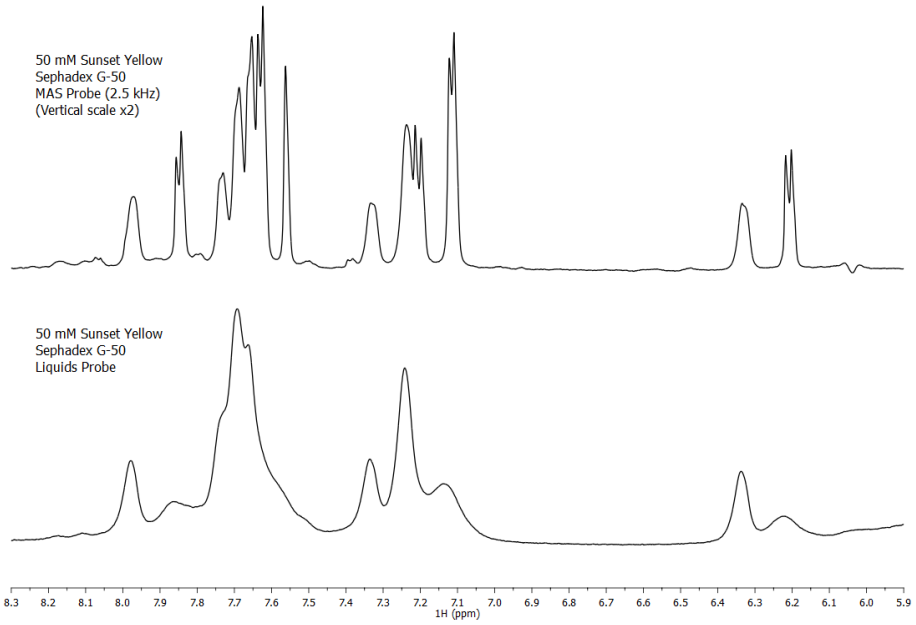

Figure 4.10: Extracts of ^{1}H spectra of 50 mM sunset yellow in Sephadex G-50, with and without Magic Angle Spinning.

application of MAS. The tumbling of the 'in pore' aggregates is reduced through coupling of the aggregate motion to that of the Sephadex particles, the additional broadening caused by this is not reduced by MAS as the low speed spinning does not effect the position of the aggregate relative to the particle. It is this difference in broadening effects that allows the assignment of the 'free' and 'in pore' components.

Use of MAS allows partial resolution of the separate peaks where an 'in pore' peak occurs at the same chemical shift as a 'free' peak, this is best seen with the peak at δ_{H} 7.24 ppm which is a broad peak without MAS but clearly appears as an overlapping doublet ('free' component) and broad peak ('in pore' component) with MAS. This application of MAS is useful for identifying the peaks belonging to a single component as these are the peaks that can be used most accurately for subsequent DOSY analysis.

4.1.2.3 DOSY

Diffusion-Ordered Spectroscopy data were acquired for each of the sunset yellow concentrations with each of the Sephadex stationary phases. The MAS data obtained previously was used to identify single component peaks for DOSY analysis, however, given the problems observed with the polymers, where the spinning induces vortexing and potentially disrupts the diffusion of the molecules, DOSY data for sunset yellow was not acquired using MAS. The representative DOSY plots for 400 mM sunset yellow in D_2O, Sephadex G-50, Sephadex G-75 and Sephadex G-100 are shown in Figure 4.11.

In D_2O the peaks of the multiplets appear at slightly different diffusion coefficients, this is due to a systematic phase change over the course of the experiment, possibly due to coherent motion caused by convection within the sample tube.[99,242] Applying phase correction to each increment spectrum of the data set improved the data and reduced the difference between the individual peaks of the multiplet, but did not completely solve the issue. The diffusion coefficients used in Figure 4.5 were

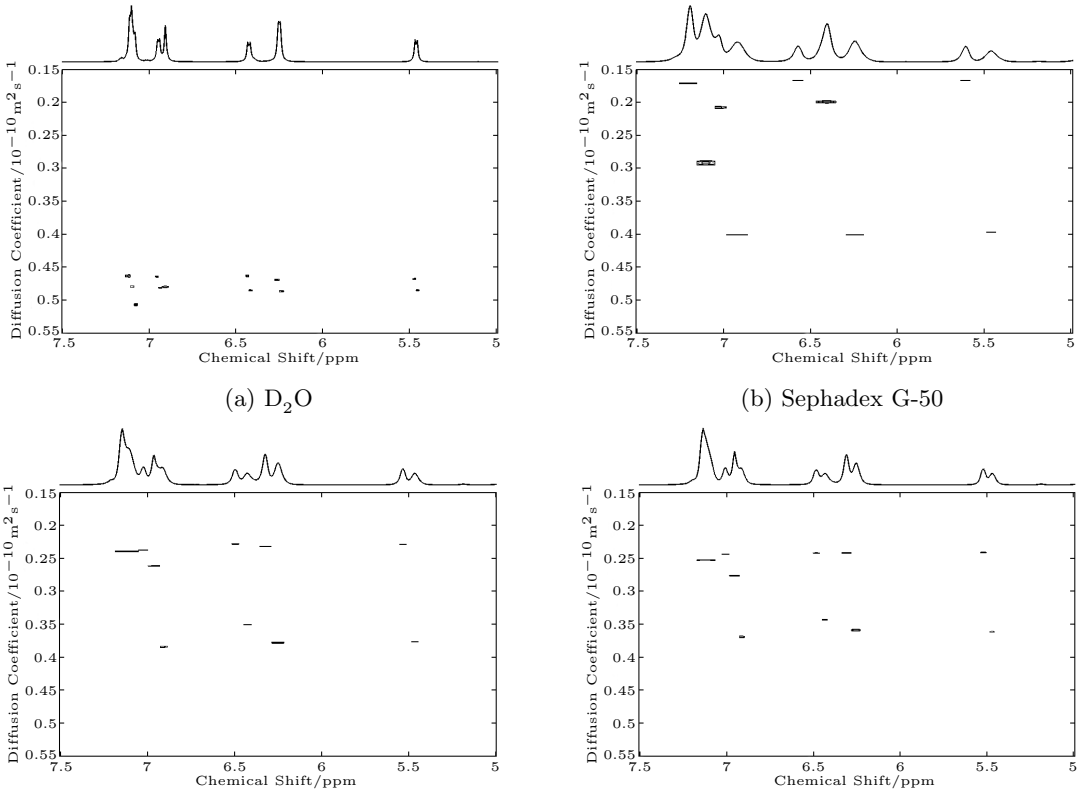

(a) D_2O (b) Sephadex G-50

(c) Sephadex G-75 (d) Sephadex G-100

Figure 4.11: DOSY plots of 400 mM sunset yellow in a) D2O, b) Sephadex G-50, c) Sephadex G-75 and d) Sephadex G-100. Data were acquired with a diffusion delay of 0.2 s, gradient pulse lengths of 4 ms and 32 gradient increments from 4.5 G cm^{-1} to 56.5 G cm^{-1} arrayed linearly in g^2.

average values across all of the peaks.

The diffusion coefficients extracted for signals relating to the 'free' component are slightly smaller than those observed in the absence of stationary phase. The slight decrease in diffusion coefficient is due to the effective increase in viscosity caused by addition of stationary phase. This similarity confirms the assignment of these peaks as aggregates in free solution, mostly those too large to fit in the pores of the stationary phase.

The 'in pore' component has a small diffusion coefficient in comparison to the 'free' component and the diffusion coefficient observed without stationary phase. This is indicative of molecules spending a significant amount of time in the pores of the stationary phase, where diffusion is restricted by the walls of the pore, these are most likely to be the monomers and small aggregates. The diffusion coefficient of aggregates in the pores of the Sephadex is characterised by the size of the pores. At each concentration the diffusion coefficient of the 'in pore' component increases across the stationary phase series of G-50, G-75, G-100. Sephadex G-50 has the smallest pores, this causes the most hindrance of the aggregates leading to the smallest apparent diffusion coefficient. The increase in the pore sizes for Sephadex G-75 and G-100 provides a higher 'in pore' volume for the aggregates, the diffusion is less hindered and the resulting diffusion coefficients are closer to the free component.

All diffusion coefficients decrease with increasing concentration as observed without stationary phase, and shown in Figure 4.12. The diffusion coefficient for 'free' sunset yellow at 10 mM in Sephadex G-50 appears larger than expected from the trend of the higher concentrations, this is

most likely an overestimation due to poor data quality, the peaks for this component decay within the first 12 increments (of a 32 increment experiment), fewer data points for the fitting of the signal decay leads to inaccurate diffusion coefficients, this is highlighted by the increased error associated with the data point as shown in Figure 4.12a. The data for 10 mM sunset yellow in Sephadex G-50 is excluded from further analysis.

There is a linear correlation between log(diffusion coefficient) and concentration for all sets of data of the form $\log D = c - mC$, where D is the diffusion coefficient ($\times 10^{-10}$ m^2 s^{-1}) and C is the concentration in mM, as shown in Figure 4.13. The parameters obtained from this fitting are summarised in Table 4.5.

Table 4.5: Parameters from Linear Regression of Log(Diffusion Coefficient) data

	Gradient ($\times 10^{-3}$)	Intercept	R^2
No Sephadex	1.70	0.333	0.997
G-50 'Free'	1.68	0.228	0.994
G-50 'In Pore'	1.57	-0.158	0.999
G-75 'Free'	1.72	0.231	0.996
G-75 'In Pore'	1.66	0.0133	1.000
G-100 'Free'	1.70	0.217	0.998
G-100 'In Pore'	1.72	0.0578	0.999

The difference in intercepts is due to the decrease in diffusion coefficient caused by the addition of the stationary phase. For the 'free' component it is the increase in viscosity that causes the slight reduction in diffusion coefficient at all concentrations. For the 'in pore' species it is the time spent occupying the pores and the size of the pore itself which determines the diffusion coefficient of the sunset yellow.

The gradient values for all of these data appear to be quite similar, indicating that the addition of stationary phase does not significantly perturb the formation of aggregates with increasing concentration or affect the distribution of aggregate sizes at each concentration. However, while there is no trend in the gradients of the 'free' data, all of which are reasonably close to that of the data with no Sephadex, the gradients of the 'in pore' data sets increase across the series of G-50, G-75, G-100. This is less noticeable from the comparison of Figures 4.13a-c, but is clear when directly comparing the G-50, G-75 and G-100 data on the same axis as shown in Figure 4.14a. The data for the 'free' component for each of the stationary phases on the same axis is shown in Figure 4.14b and these data are much more similar than the 'in pore' data.

The separation of the 'free' and 'in pore' components in the diffusion domain is greatest for Sephadex G-50, while the separation with Sephadex G-75 is only slightly greater than with Sephadex G-100. This trend is comparable to the separation of the peaks in the ^{1}H spectra and relates to the range of aggregates able to access the pores of the stationary phase i.e. the fractionation range. The fractionation range of the stationary phase is determined by the degree of cross-linking; more cross-linking forms smaller pores. Smaller pores lead to a greater reduction in the diffusion coefficient of the 'in pore' component through more restriction in displacement during the diffusion delay.

The appearance of separate peaks for the 'free' and 'in pore' components indicates that there is slow exchange between aggregates that can and can not fit in the pores, the exchange is likely hindered by the partitioning of the monomers and small aggregates into the pores of the stationary phase. As stated previously, the observed diffusion coefficient in the absence of stationary phase is a

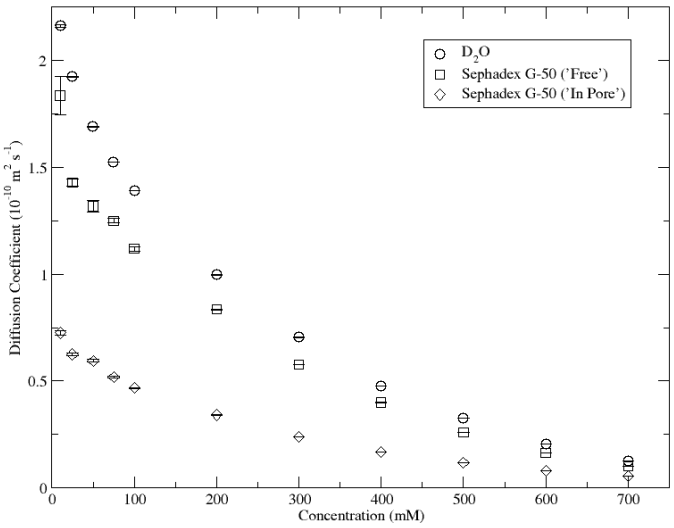

(a) Sephadex G-50

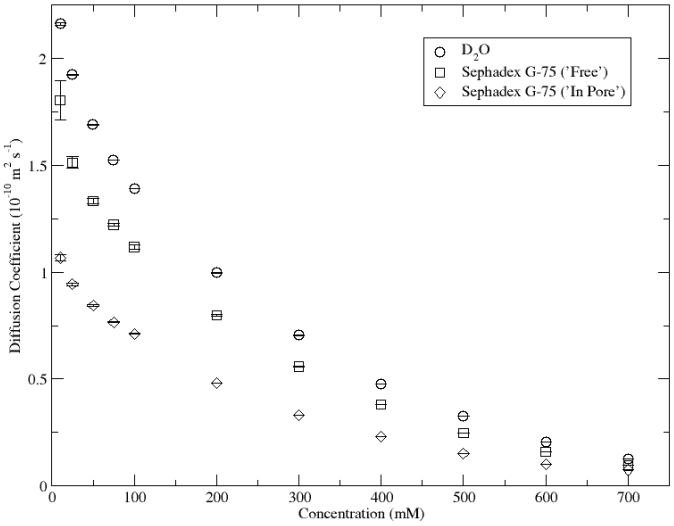

(b) Sephadex G-75

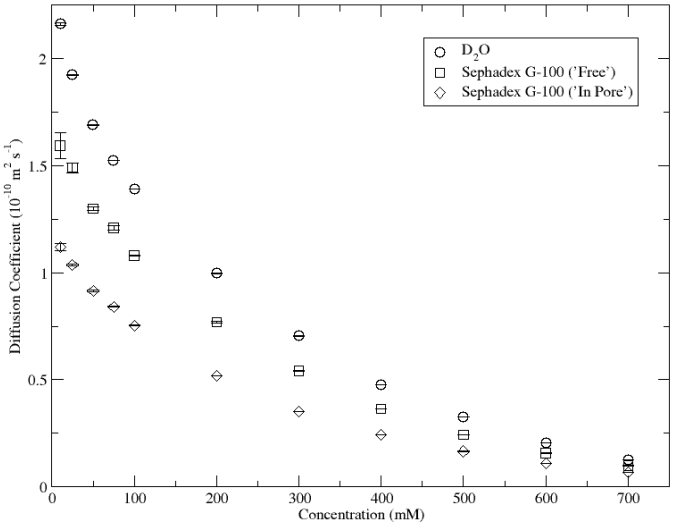

(c) Sephadex G-100

Figure 4.12: Graphs of diffusion coefficients of 10–700 mM sunset yellow with and without stationary phases

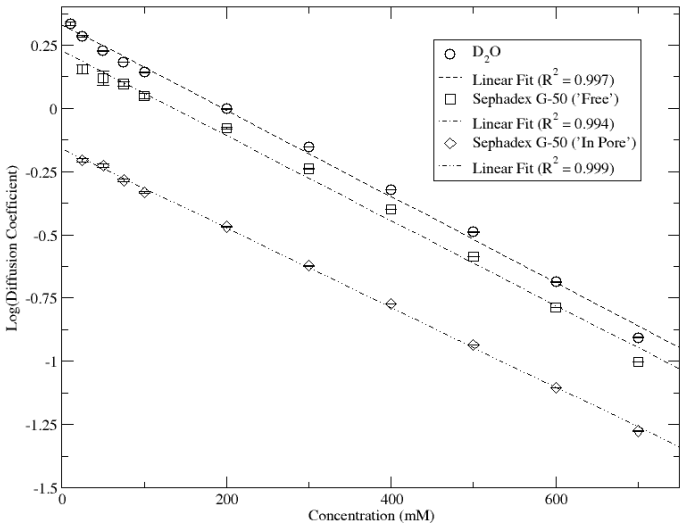

(a) Sephadex G-50

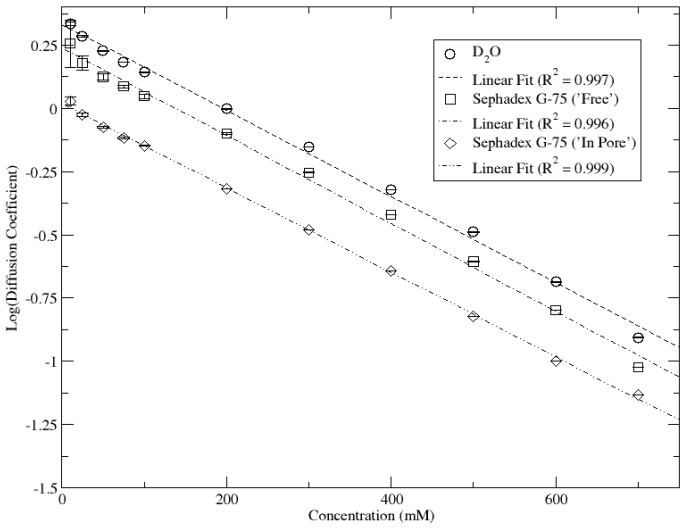

(b) Sephadex G-75

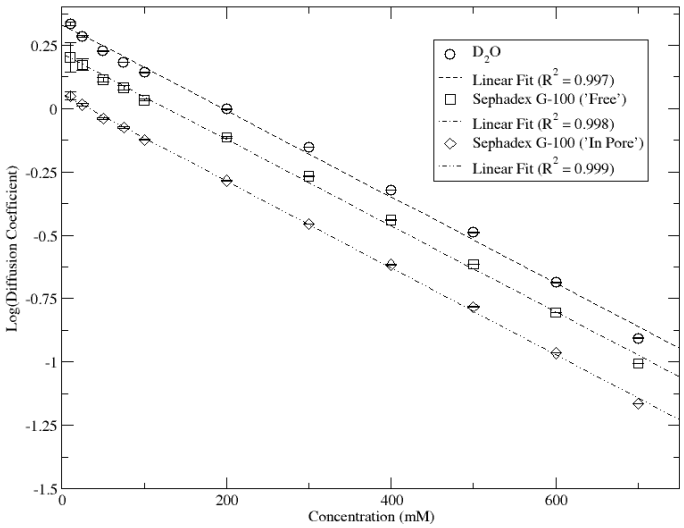

(c) Sephadex G-100

Figure 4.13: Graphs of log(diffusion coefficient)s of 10–700 mM sunset yellow with and without stationary phases

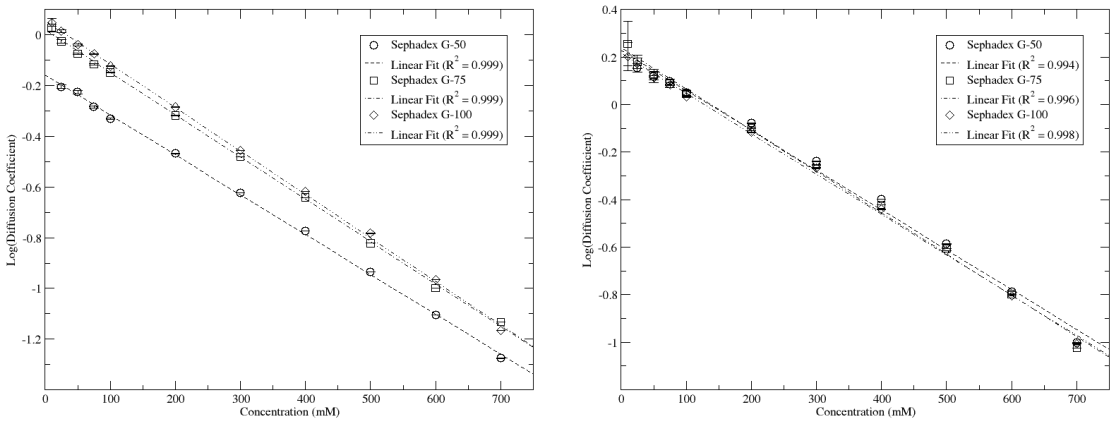

(a) 'In Pore' Component (b) 'Free' Component

Figure 4.14: Comparison of log(diffusion coefficient)s of a) 'in pore' and b) 'free' components for Sephadex G-50, G-75 and G-100

population weighted average of all the various aggregate sizes in solution. The same approximation can be applied to the 'free' component in the presence of stationary phase which is a distribution of aggregates of all sizes with fast exchange between monomers and aggregates. The analysis of the 'in pore' component is more complicated, there is still a distribution of aggregate sizes undergoing fast exchange between monomers and aggregates, however, the maximum aggregate size is smaller than in free solution, dictated by the pore size of the stationary phase. The observed diffusion coefficient for the 'in pore' component depends on both the average aggregate size and the restriction in diffusion applied by the pore which is related to the pore size of the stationary phase. Figure 4.15 shows a schematic of the exchange processes present in the stationary phase samples.

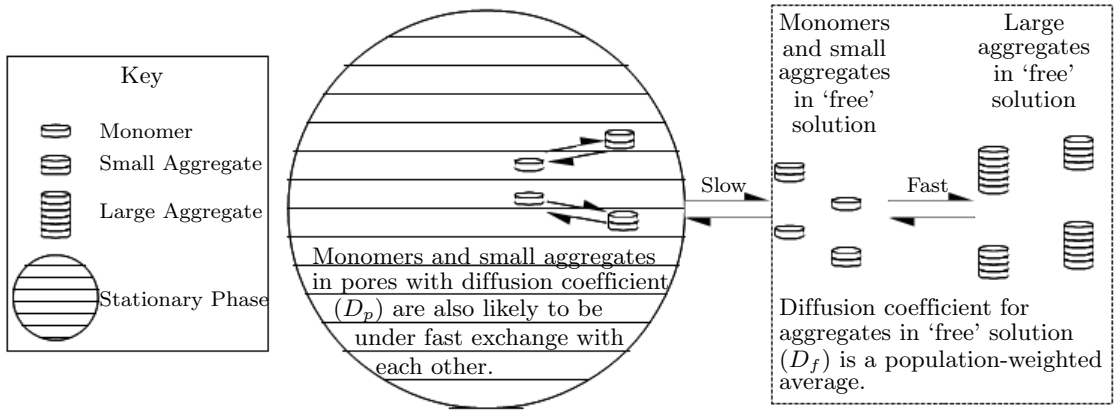

Figure 4.15: Schematic of sunset yellow exchange mechanism

The slow exchange between the 'free' and 'in pore' components on addition of stationary phase shown in these experiments is contradictory to the conclusions drawn from the polymer data in the previous chapter where the single peak and diffusion coefficient was taken as evidence for fast exchange. It is likely that in the polymer case the broad peaks of the 'free' and 'in pore' components are overlapped, a consequence of the width of the peaks and the absence of any size dependence of the chemical shift.

In the polymer experiments the low polydispersity of the polymer standards allows the assumption of a single size molecule with the molecular weight provided by the supplier. The broadness of the

peaks is attributed to the high number of repeat units within the molecule and the large size of the molecules. A single peak (for each proton environment) is observed in both the absence and presence of stationary phase with any differences in linewidths attributed to the increased viscosity on addition of stationary phase. In the absence of stationary phase the DOSY data of the single polymer peak is correctly analysed using a mono-exponential decay leading to the extraction of a single diffusion coefficient. On addition of stationary phase, the same analysis was applied with the justification that under fast exchange conditions between the 'free' and 'in pore' components, the observed diffusion coefficient is a weighted average. (Equation 4.3, where f_f and f_p are the fractions in free solution and in pores, D_f and D_p are the diffusion coefficients for these environments)

$$D_{obs} = f_f D_f + f_p D_p = (1 - f_p) D_f + f_p D_p \tag{4.3}$$

The separate peaks observed in the sunset yellow data indicate that the assumption of fast exchange in the polymer experiments was incorrect. The broad polymer peak observed in the presence of stationary phase is in fact two peaks with significant overlap, one peak relating to the polymer in 'free' solution and the other to polymer residing in the pores of the stationary phase. Each of these peaks has an associated fractional population (f_f for the 'free' component and f_p for the 'in pore' component) and a diffusion coefficient (D_f and D_p for 'free' and 'in pore' respectively). Similar to the 'free' and 'in pore' components of the sunset yellow samples, D_f is likely to be slightly lower than the diffusion coefficient in the absence of stationary phase, while D_p is determined by the size of the pores of the stationary phase.

The diffusion coefficients for the 'free' and 'in pore' components for sunset yellow can be extracted directly from the signal decay of the 'free' and 'in pore' peaks in the DOSY experiment due to the resolution of the separate peaks. In the polymer experiments the signal decays of the two overlapping peaks can not be extracted individually; the signal decay for the single observed peak is a combination of the two exponential decays for the two components as detailed in Equation 4.4 where f_f, D_f, f_p and D_f have already been defined, $E(q, \Delta)$ is the normalised intensity of the signal attenuation, Δ is the diffusion delay and $q = \gamma \delta g / 2\pi$, a measure of the gradient intensity applied.[92]

$$E(q, \Delta) = f_f \exp(-(2\pi q)^2 D_f \Delta) + f_p \exp(-(2\pi q)^2 D_p \Delta) \tag{4.4}$$

The diffusion coefficient of the polymers in absence of stationary phase are much smaller than those of sunset yellow aggregates, due to the large size of the polymers, there is therefore likely to be much less difference between D_f and D_p than observed in the sunset yellow experiments. The resolution in the diffusion domain of overlapping peaks is a known problem in diffusion-ordered spectroscopy, especially when the diffusion coefficients are similar.[195] Due to the overlap of the two components and their similar diffusion coefficient, the extracted diffusion coefficient in the polymer experiments is an approximate average of the diffusion coefficients for the individual components. In the sunset yellow experiments the separation of the peaks allows the diffusion coefficient to be extracted for each of the components which is useful for probing the aggregation mechanism of the molecule.

4.2 Insulin

Insulin aggregation occurs both *in vivo* and *in vitro*.[243] The aggregation of insulin can be a problem for diabetic patients; fibrils formed from insulin can occur at repeat injection sites.[244–246]

Aggregation also causes problems in long-term storage of monomeric insulin for pharmaceutical use.[55,247] The aggregation of insulin has been studied by a wide range of techniques including mass spectrometry,[248] atomic force microscopy[60] and Fourier transform infrared spectroscopy.[249] In the body the functional form of insulin is the monomer but it is stored in the β-cells of the pancreas as a Zn^{2+}-coordinated hexamer to protect against fibrillation.[250]

Aggregation of insulin is suggested to occur via three steps: nucleation, growth and precipitation.[41] Nucleation involves the partial unfolding of the monomer which exposes hydrophobic domains normally buried within the molecule.[247] This leads to non-covalent interactions to form a nucleus from which a fibril is grown by the addition of more molecules. Further flocculation of the fibrils into 'spherites'[251] leads to the formation of the 'heat precipitate' described by du Vigneaud et al.[252] Fibrillation of insulin can be initiated by heating at low pH or by using organic solvents and agitation.[65] Decreased pH leads to an increase in monomers and dimers compared to hexamers thus increasing the tendency for fibrillation.[247] Formation of the precipitate or 'spherites' is suggested to be favoured by shorter fibrils which experience less steric hindrance on addition to a growing 'spherite'.[251]

Insulin belongs to a class of proteins, sometimes called amyloid proteins, which undergo aggregation to form fibrils with a characteristic cross-β structure[253] called amyloid fibrils.[30] Insulin is frequently used as a model amyloid protein,[41,254] the fibrillation process has been well studied since the 'heat precipitate' was described by du Vigneaud et al.[252] in 1933 and the conditions for fibrillation fully investigated by Waugh from 1944.[251,255–258] Insulin is therefore a useful molecule to study as a precursor to other amyloid proteins such as Aβ, islet-amyloid polypeptide (IAPP) or α-synuclein.

4.2.1 DOSY and SEC-DOSY Experiments

Multiple diffusion NMR studies were performed to probe the mechanism of insulin aggregation. Samples of 2 mM insulin in pH 2 HCl (D_2O) were incubated in the spectrometer at 40°C and 60°C and DOSY data acquired every hour. The diffusion coefficient data obtained from these experiments are shown in Figure 4.16. The premise of these experiments was that as the insulin aggregated into fibrils the diffusion coefficient would decrease due to the increase in size, by acquiring diffusion data every hour the time dependence of the aggregation could be monitored. Application of the SEC-DOSY method to the aggregation of insulin was expected to allow further analysis of the distributions of aggregate size over time.

The 40°C experiment was carried out for 140 hours with DOSY experiments acquired every hour. The diffusion coefficients settle to an average value of $\sim 1.5 \times 10^{-10}$ m^2 s^{-1} within $\sim$3 hours and remain reasonably constant for the rest of the time. The data for the first 40 hours is included in Figure 4.16a and the full time range is shown separately in Figure 4.16b, for simplicity after $t = 30$ hours only data points for every 5 hours are included. The initial decrease in diffusion coefficient is most likely due to the increase in viscosity which occurs on formation of insulin oligomers.[255] After 140 hours there is minimal loss of signal, little change in diffusion coefficient and no visible evidence of fibrils; this suggests that although insulin oligomers may have formed causing an increase in viscosity and complementary decrease in diffusion coefficient, the additional association of the oligomers into extended fibrils has not occurred. This could be due to the temperature of the experiment, which may be too low for fibril formation, but not for oligomer formation. Sorci et al. showed using absorbance measurements that when insulin is heated to 65°C and then cooled to 25°C oligomers continue to form at the low temperature but fibril formation is halted compared to

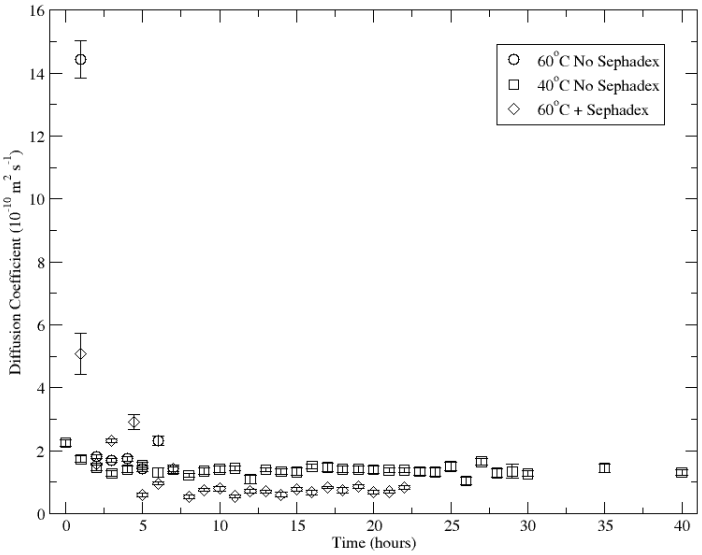

(a) Insulin diffusion of all three experiments (40°C, 60°C and 60°C + Sephadex G-50)

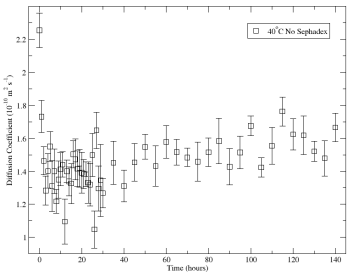

(b) Insulin diffusion at 40°C

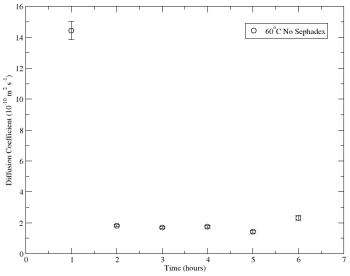

(c) Insulin diffusion at 60°C

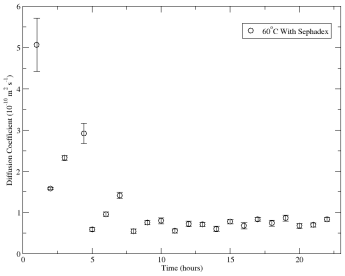

(d) Insulin diffusion at 60°C in the presence of Sephadex G-50

Figure 4.16: Diffusion coefficients for 2 mM insulin in pH 2 HCl at 40°C and 60°C and 2 mM insulin in Sephadex G-50 at 60°C. a) All conditions together, b) 40° without Sephadex, c) 60° without Sephadex, d) 60° with Sephadex.

the uncooled sample.[254] Studies by Waugh et al. also suggested that without seeding, precipitate is not formed at temperatures below 48°C.[257] A similar effect could be in action in this experiment, where the temperature allows formation of small oligomers but is not high enough for full fibril formation. Figure 4.17 shows the first increment of the DOSY experiments for $t = 2$–140 hrs in 10 hour steps, there is slight broadening of the peaks over time but no significant decrease in signal intensity. This indicates some increase in aggregate size but not enough for the aggregates to become so large as to be invisible in the NMR spectrum.

The 60°C experiment was run for 65 hours over a weekend with DOSY experiments acquired every hour. The peaks disappeared after only 8 hours indicating the formation of large, NMR-invisible aggregates, the diffusion coefficients extracted for these time points initially decreased but settled at a value of $\sim 2.0 \times 10^{-10}$ m^2 s^{-1}. After the 65 hour experiment there was visible evidence of precipitate in the NMR tube, it is likely that the formation of the precipitate occurred some time after the loss of signal through association of the fibrils. The slightly larger diffusion coefficient value at 60°C compared to the value obtained at 40°C can be attributed to faster diffusion as a result of the increased temperature. The first increment of the DOSY experiments obtained at $t = 1$–8 hrs displayed in Figure 4.18 show the broadening and decrease in signal intensity for these time points. The diffusion coefficients for this experiment are included in Figure 4.16a and shown

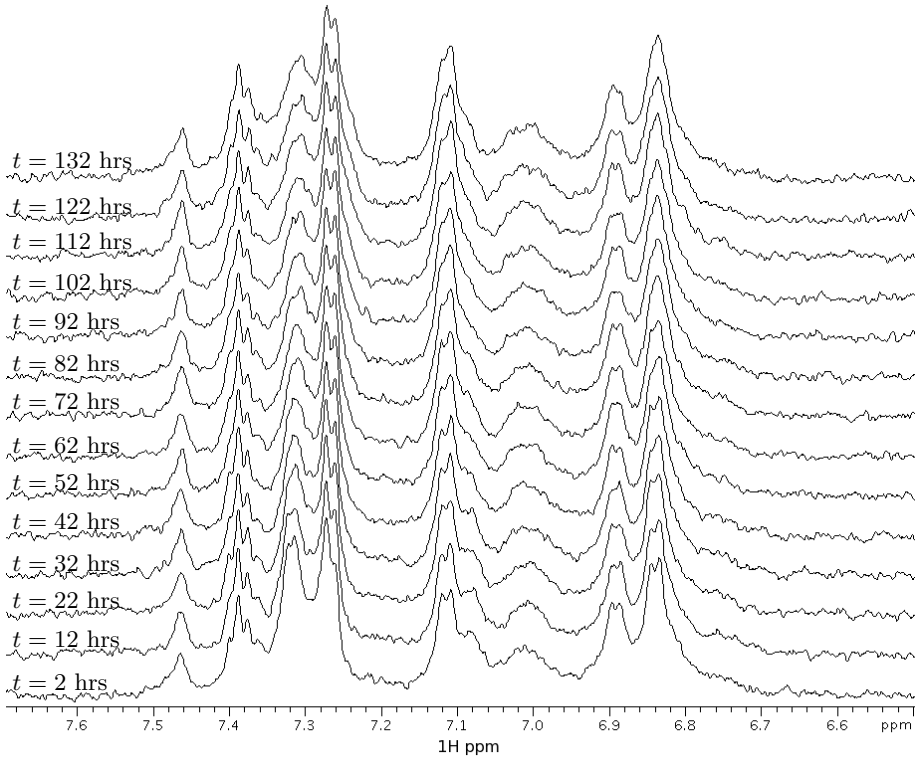

Figure 4.17: Extracts of first increment of DOSY experiment for 2 mM insulin in pH 2 HCl at t = 2–140 hrs in 10 hour steps and 40°C.

separately in Figure 4.16c.

In these two experiments in the absence of stationary phase, a single set of peaks is apparent at all time points, indicating a fast exchange between monomers and small aggregates in solution. The decrease in diffusion coefficient is due to the increased viscosity caused by the formation of oligomers and fibrils; in the 60°C experiment as the fibrils flocculate and then precipitate, more small aggregates form, maintaining the solution viscosity and leading to the constant value of the diffusion coefficient until complete fibril formation leads to loss of signal. The broadening of the peaks is an indication of the increase in aggregate size, larger aggregates tumble more slowly and have shorter T_2 relaxation times. The decrease in signal intensity seen at 60°C occurs as the size of aggregates increases. Large aggregates become too broad to be detected, with the remaining signals belonging only to the small aggregates and monomers, of which there are fewer and leads to reduction in peak size.

A time resolved diffusion study of 2 mM insulin in Sephadex G-50 incubated at 60°C in the spectrometer show a similar trend to previous experiments with a rapid decrease in diffusion coefficient in the first few hours followed by settling to $\sim 0.7 \times 10^{-10}$ m^2 s^{-1}. In contrast to the sunset yellow experiments, there is no separation in the chemical shift domain of the monomers and aggregates on addition of Sephadex G-50. The formation of aggregates from insulin does not alter the chemical shift because the orientation of the monomers does not lead to any stacking of the aromatic groups as seen in sunset yellow. This is not surprising given the small proportion of aromatic residues in insulin, only 9 of the 51 amino acids contain aromatic moieties.[259] Also, the assembly is driven by electrostatic and hydrophobic interactions[41] of the peptide charges so there is minimal interaction of the side chains. This leads to the lack of separation of the 'free' and 'in pore' components, similar to the situation observed in the case of polymer diffusion.

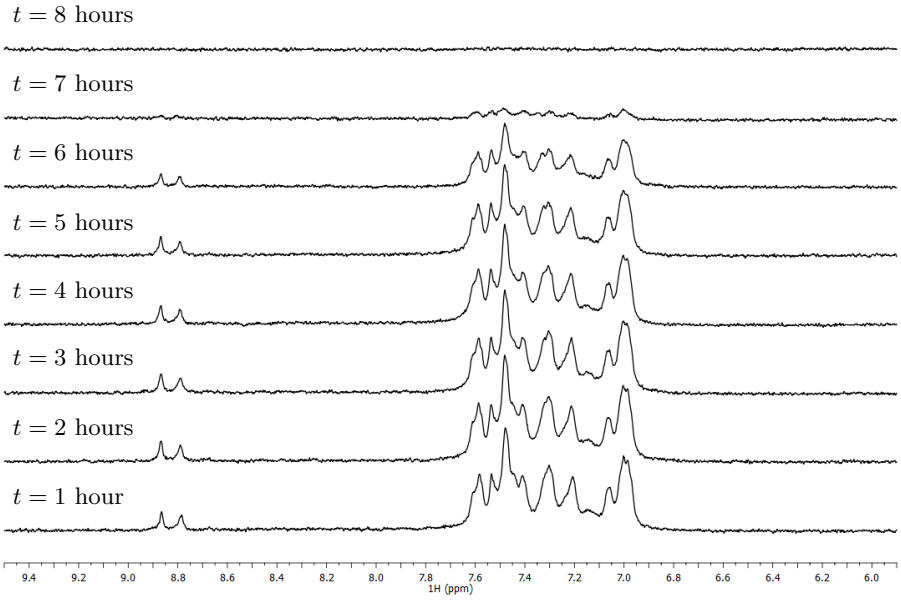

Figure 4.18: Extracts of first increment of DOSY experiment for 2 mM insulin in pH 2 HCl at $t = 1$–8 hrs and 60°C.

On addition of stationary phase the peaks are broadened, peaks belonging to the 'free' and 'in pore' components are most likely overlapping, as seen in the polymer experiments (Chapter 3). The 'free' solution outside of the pores may also contain some aggregates, such as elongated fibrils, which have become invisible to NMR due to reduced tumbling in solution, these will affect the viscosity of the sample but not contribute directly to the diffusion coefficient of the 'free' component. The diffusion coefficients in the presence of stationary phase settle to a smaller value than the previous experiments incubated without stationary phase, this is consistent with the addition of stationary phase and the associated hindering of motion that this causes. The data for this experiment is included in Figure 4.16. In this case there is no loss of signal over 22 hours although there was some visible evidence of precipitate in the supernatant volume above the stationary phase. The presence of the stationary phase may hinder the flocculation of the fibrils and therefore reduce the amount of precipitate observed.

In order to clarify any hindering effects of the stationary phase a 4 mM stock solution of insulin was incubated in a water bath at 40°C, 500 μl aliquots were removed every hour and split between two samples, one with solvent (pH2 HCl, D_2O) only and one with Sephadex G-50 (swelled in pH2 HCl, D_2O). The aliquots were cooled in ice for approximately 10 minutes in order to halt fibrillation before dividing the sample between the solvent and Sephadex samples. The DOSY experiments were acquired on 2 mM samples at 25°C. Using the same insulin stock solution for the samples with and without Sephadex allows direct comparison of the diffusion coefficients.

The samples without stationary phase show increased broadening and a decrease in peak size over time, the first increment of the DOSY experiments are shown in Figure 4.19a. The broadening is due to the increased aggregate size and the decrease in peak size indicates the formation of large NMR-invisible aggregates such as extended fibrils and flocculates. The peaks observed between 7.45 and 8.45 ppm and the peak at 8.72 ppm in the $t = 0$ hours spectrum disappear in the following spectra, these peaks are thought to belong to the amide protons which are exchanged with the ^2H of the D_2O within the first hour. The peak size decreases gradually over the first 8 hours and a large

difference in peak size is observed between the $t = 8$ hours and $t = 24$ hours spectra, indicating that most of the aggregation occurs during this time.

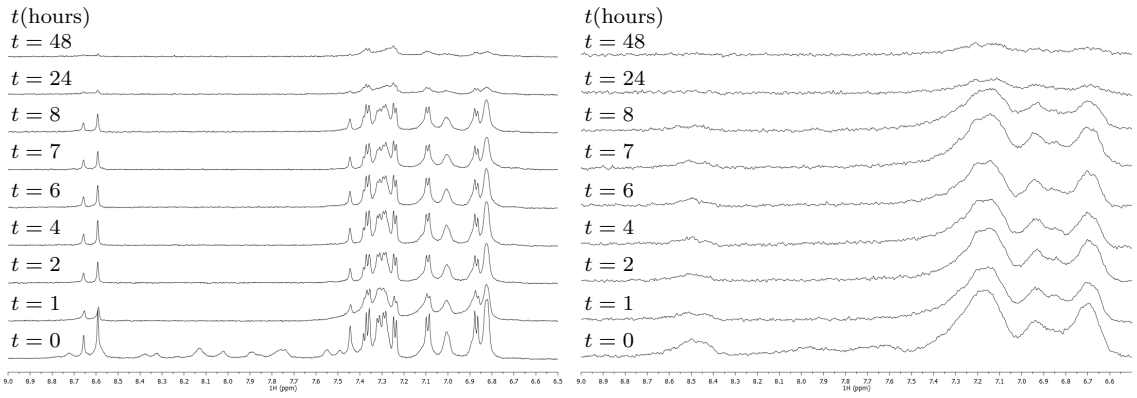

(a) Without Stationary Phase

(b) With Stationary Phase

Figure 4.19: Stacked extracts of ^{1}H spectra of 2 mM insulin incubated in pH 2 HCl at 40°C, then added to a) pH 2 HCl, D_2O, b) Sephadex G-50 swelled in pH 2 HCl, D_2O

In the presence of stationary phase the peaks are broadened by the sample inhomogeneity, this hides any additional broadening over time due to increase in aggregate size. The decrease in peak size is also seen in the presence of stationary phase, the first increment of these DOSY experiments are shown in Figure 4.19b. The decrease in peak size is similar to that observed in the absence of stationary phase, with the largest decrease occurring between the $t = 8$ hours and $t = 24$ hours spectra.

The diffusion data from this experiment is shown in Figure 4.20. The trends in diffusion coefficient for the samples with and without stationary phase are similar; in the presence of Sephadex G-50 the diffusion coefficients are smaller as seen previously on addition of stationary phase. The slight decrease in diffusion coefficient over time for both samples can be attributed to the increase in viscosity caused by the formation of fibrils, as seen in previous experiments. There is less of a sharp decrease in diffusion coefficient in these experiments in comparison to the previous experiments, this is most likely a consequence of incubating a 4 mM stock solution, the increase in concentration is known to increase the rate of insulin fibrillation.[247] Some fibrillation may have already occurred before the first DOSY experiments were acquired leading to a reduced diffusion coefficient for the first time point in comparison to previous experiments. The smaller diffusion coefficients for both of these sets of data, in comparison to the data for the samples incubated in the spectrometer, is due to the lower temperature used during acquisition of the DOSY data.

In the presence of stationary phase the observed diffusion coefficient is most likely an average of the 'free' and 'in pore' components, similar to the case of the polymer diffusion where the peaks for the individual components are significantly overlapping. The diffusion coefficients of the 'free' and 'in pore' components cannot be extracted from this data and due to the peak overlap there is also no indication of aggregate size distribution. The results of these experiments indicate that SEC-DOSY in this form is not a suitable technique for monitoring the aggregation of proteins. The uniform peak broadening and absence of chemical shift changes on aggregation suggests that the concentration of small aggregates such as dimers and trimers is low in comparison to the concentrations of the monomers and fibrils.[250] This in turn leads to the failure of SEC-DOSY as the only visible component is the monomer, from which no significant information can be extracted.

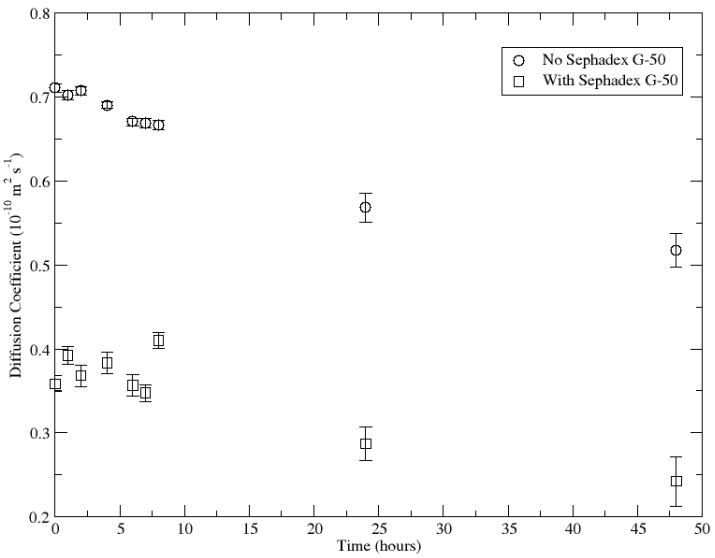

Figure 4.20: Diffusion coefficients for 2 mM insulin incubated in pH 2 HCl at 40°C, then added to a) pH 2 HCl and b) Sephadex G-50 in pH 2 HCl.

4.3 Comparison of Applications

The application of SEC-DOSY to the concentration dependent aggregation of sunset yellow is much more effective than the application to the time dependent aggregation of insulin. This stems from the different modes of aggregation in these two systems. The π-π stacking in sunset yellow[7] and the corresponding change in chemical shift on aggregation provide a mechanism for the separation of peaks belonging to the 'in pore' and 'free' components. In contrast, the aggregation of insulin occurs via hydrophobic interactions[41] which do not greatly affect the chemical shift of the aggregates. Insulin is also a much larger molecule than sunset yellow, the aggregation of insulin rapidly leads to large assemblies which do not fit in the pores of the stationary phase and eventually are too large for NMR analysis. The aggregation of sunset yellow is reversible; reducing the concentration will decrease the average aggregate size, the same can not be said of insulin fibrils. This could be a factor in the application of SEC-DOSY, the reversible aggregation allows exchange between aggregates and monomers which aids the resolution of peaks of the different components.

These experiments suggest that SEC-DOSY is a useful method to probe aggregation of molecules, such as sunset yellow, which aggregate into stacks with small increments in assembly size and defined changes in chemical shift. This applies to a whole range of chromonic liquid crystals with similar properties to sunset yellow such as other azo dyes (e.g. methyl orange[6] and C.I. Direct Blue 67[13]), antiasthmatic drugs (e.g. disodium cromoglycate)[17] and nucleic acids.[12]

Chapter 5

Studies of Phospholipid Vesicles

Aggregation of proteins is implicated in the cause of several diseases, such as Alzheimer's and Parkinson's.[2,260] An understanding of the interactions between aggregate species and cell membranes is an important part of the investigation into the cause of these diseases. There is evidence that some aggregating species associate with cell membranes and cause membrane permeation.[169,261]

Cell membranes are mainly composed of a range of phospholipids along with membrane proteins[124] and other functional additives such as sterols (e.g. cholesterol and derivatives),[122] sphingolipids[124] and glycolipids.[43] Vesicles prepared from a single phospholipid, although not as complex, form a useful model system with which to study cell membranes.

By producing biomimetic membranes from phospholipids the process of cell permeation induced by aggregates can be investigated. Many studies of membrane permeation caused by a variety of peptides have been performed using fluorescence spectroscopy to monitor the leakage of fluorescent molecules, which are encapsulated at self-quenching concentrations.[169,262–265] NMR studies of phospholipid vesicles, using paramagnetic shift reagents, have mainly focussed on determining distributions of different phospholipids across the bilayer[139,143,145,266] and monitoring transmembrane transport of small ions.[150,154,156] There are also a few examples of membrane permeability being monitored by changes in the peak intensity of shifted and unshifted peaks.[267,268] Combination of the fluorescence and NMR techniques has the potential to yield useful information regarding the mechanism of membrane permeation, however, first the phospholipid vesicle system needs to be optimised for NMR analysis.

This chapter details the optimisation of the preparation of phospholipid vesicles for NMR analysis, followed by an analysis of the stability of the vesicles and an investigation of the effect of solubilisation by detergent, an experiment which acts as a positive control for membrane permeation.

5.1 Optimisation of Phospholipid Vesicles for NMR

5.1.1 Requirements for NMR Analysis

Phospholipid vesicles have been used extensively in NMR studies of biomimetic membranes.[145,269,270] Some studies focussed on the ^{1}H spectra,[141,146,271] however, although ^{31}P has a lower gyromagnetic ratio and therefore a lower receptivity (ease of signal acquisition) relative to that of ^{1}H, ^{31}P is a

more useful nucleus for vesicle studies. Where the ^{1}H spectrum displays a large number of peaks, the ^{31}P spectrum of a single phospholipid appears as a single peak. On formation of vesicles the ^{1}H spectrum is broadened considerably due to the size of the vesicles and sample heterogeneity, further reducing the spectral resolution. In contrast, the ^{31}P spectrum of phospholipid vesicles has peaks from only two environments, the interior and exterior leaflets of the membrane bilayer, although the peaks are also broadened due to the size of the vesicles this is less of a problem with only two peaks. In theory, these peaks should have slightly different chemical shifts, due to the difference in curvature of the individual leaflets. There are several reports of peak separations of ~0.15 ppm,[269,272] however these studies were performed with a low magnetic field strength (2.11 T) which reduces the chemical shift anisotropy contribution to the linewidth. In practice, the two environments are generally not resolved and the spectrum appears as a single peak. Resolution of the interior and exterior peaks is achieved by addition of a paramagnetic shift reagent, such as Nd^{3+},[141] Eu^{3+} [139–141] or Pr^{3+},[140,145,146] to the solution surrounding one leaflet, i.e. either inside or outside the vesicles. Praseodymium(III) chloride ($PrCl_3$) is a useful paramagnetic shift reagent. A study by Andrews et al. showed that, compared to Eu^{3+} the peak shift was greater, but the line broadening was also greater. The same study showed that the line broadening effect of Pr^{3+} was much less than that of Tb^{3+} and Dy^{3+} which have greater shift effects.[140] Pr^{3+} therefore provides a compromise between extent of paramagnetic shift and line broadening.

For successful time-resolved studies of membrane permeation using NMR there are several requirements:

- Sharp ^{31}P peaks
  - for best resolution of separate peaks on addition of shift reagent
  - achieved by small vesicles (less broadening due to slow tumbling vesicles or chemical shift anisotropy (CSA) contributions)
- Stable vesicles
  - no disintegration occurring in the absence of permeating additives (e.g. detergent or cytotoxic aggregates)
- Rapid spectrum acquisition
  - for kinetic studies spectra will be acquired every 30 minutes, spectrum acquisition time should therefore be less than this
  - faster spectrum acquisition allows more spectra to be acquired in a given time period and therefore increases the resolution of kinetic studies.

Changes to the membrane composition and different preparation methods can affect the properties of the phospholipid vesicles, such as vesicle size, size distribution and membrane fluidity, all of which may affect the appearance of the NMR spectrum. Several phospholipids and preparation techniques were investigated in order to optimise the phospholipid vesicle system for NMR analysis following the criteria listed above.

5.1.2 Effect of Paramagnetic Shift Reagent

Addition of $PrCl_3$ to the vesicle solution causes a downfield shift to nuclei in contact with the shift reagent.[140,144] Phospholipid membranes are impermeable to ions without the assistance of

ion channels,[43] as such $PrCl_3$ added to the outside of vesicles cannot travel through the bilayer, only the lipids on the exterior leaflet are in contact with the $PrCl_3$ and are therefore affected by the paramagnetic shift reagent. The mechanism of peak shifting by paramagnetic lanthanide ions is dipolar rather than contact in nature,[85] as such, the phosphorus does not need to be directly bound to the paramagnetic ion. However, the magnitude of the shift will depend on the distance and orientation of the La^{3+}-^{31}P dipolar interaction. Figure 5.1 shows the ^{31}P spectra of 1-palmitoyl-2-oleoyl-sn-glycero-3-phosphocholine (POPC) vesicles, (a) without $PrCl_3$ and (b) with $PrCl_3$ on the outside of the vesicles.

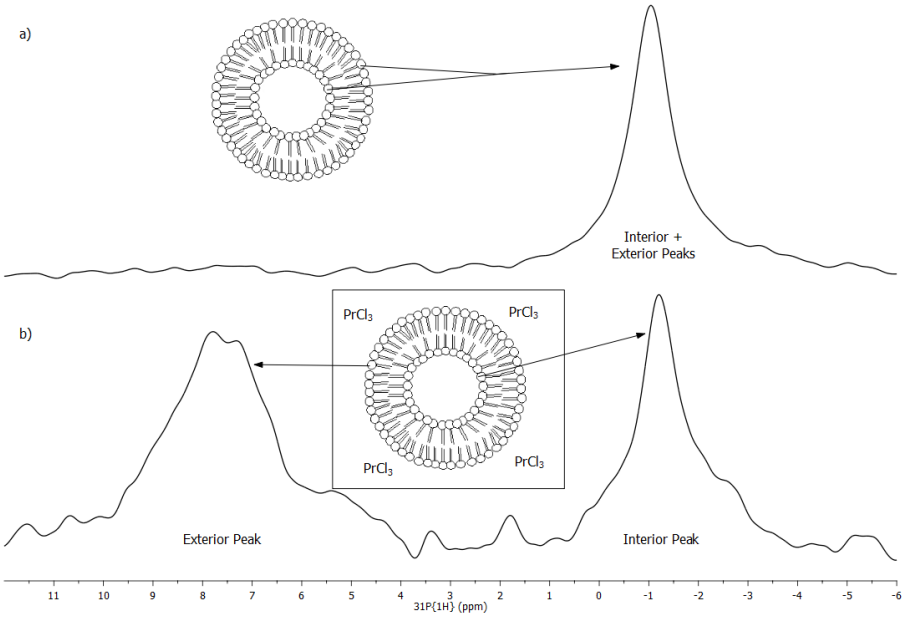

Figure 5.1: Labelled extracts of ^{31}P spectra of 1-palmitoyl-2-oleoyl-sn-glycero-3-phosphocholine (POPC) with and without $PrCl_3$ paramagnetic shift reagent. a) Before addition of 3 mM $PrCl_3$, b) After addition of 3 mM $PrCl_3$. POPC vesicles were prepared at 10 mg ml^{-1} in 10 mM HEPES + 100 mM NaCl by 3 hours of sonication at 35°C. Both spectra were acquired with 128 transients and processed with 100 Hz exponential apodisation. The vertical scale of spectrum b) is increased by a factor of 3 compared to the spectrum without $PrCl_3$.

In the absence of shift reagent there is a single peak belonging to the ^{31}P on both leaflets of the vesicles, the difference in curvature of the leaflets should cause a slight difference in chemical shift between two environments, however, because the difference in chemical shift is less than the linewidth of the peaks there is no resolution of the two peaks in these experiments. On addition of $PrCl_3$ to the outside of the vesicles the ^{31}P nuclei on the exterior leaflet of the vesicles are shifted to a higher chemical shift and are broadened.

There are several literature examples which show resolved peaks for the interior and exterior leaflets without the addition of shift reagent.[145,269] Kumar et al. show POPC/lysoPC vesicles with resolved peaks for the interior and exterior leaflets for both phospholipids with a separation of approximately 0.2 and 0.1 ppm for POPC and lysoPC respectively.[145] McLaughlin et al. also showed a peak separation of ∼0.15 ppm in sonicated dipalmitoyl lecithin (DPPC) vesicles but only at 50°C, above the gel-liquid crystalline transition temperature of the phospholipid.[269] Another study of the same DPPC system showed that the linewidth of the peak increases by a factor of five on changing the magnetic field strength from 36.4 MHz to 129 MHz, such that even above the transition temperature the two peaks are not resolved.[272] The dependence of the linewidth of the peaks on the magnetic field strength is a result of chemical shift anisotropy and it is this which is the likely cause of the

lack of peak resolution in the absence of the paramagnetic shift reagent in the POPC systems investigated in this work.

With the paramagnetic shift reagent providing resolution of the peaks of the interior and exterior leaflets, the ratio of the peak areas can be used to gain information regarding the vesicle structure. The interior:exterior ratio of the peak areas ($R_{i/e}$) in Figure 5.1 is 0.59. This value indicates that the number of lipid molecules on the interior leaflet is 0.59 times the number of lipid molecules in the exterior leaflet. This ratio, combined with a diameter from DLS measurements, can be used to estimate the thickness of the lipid bilayer, as detailed in Equation 5.1.

$$\begin{aligned}
\text{Surface area of a sphere} &= 4\pi r^2 \\
R_{i/e} = \frac{\text{Interior Peak Area}}{\text{Exterior Peak Area}} &\propto \frac{4\pi r_i^2}{4\pi r_e^2} \\
\text{From DLS, } r_e &= 16 \text{ nm} \\
R_{i/e} = 0.59 &= \frac{4\pi r_i^2}{4\pi 16^2} \\
r_i^2 &= 0.59 \times 16^2 = 151 \\
r_i &= 12.3 \text{ nm} \\
\text{Bilayer Thickness} = r_e - r_i &= 16 - 12.3 = 3.7 \text{ nm}
\end{aligned} \tag{5.1}$$

5.1.3 Preparation Method

Two methods of membrane preparation were tested: extrusion through polycarbonate membranes and sonication, as detailed in Chapter 2.

5.1.3.1 Extrusion

Extrusion through polycarbonate membranes is a common method for preparing large unilamellar vesicles with diameters in the range 100–200 nm.[273–275] Solutions prepared by extrusion are reasonably monodisperse with diameters slightly larger than the size of the pores in the membrane. Use of polycarbonate membranes of 50 nm pores produced small vesicles, however the membranes were damaged and/or easily broken during extrusion with lipid concentrations above 20 mg ml^{-1} and therefore did not form a reliable method for preparing the vesicles.

The NMR spectrum of 50 nm extruded POPC vesicles (10 mg ml^{-1} in 10 mM HEPES + 150 mM NaCl) appears as a single broad peak and on addition of $PrCl_3$ to the exterior volume the peak splits into two, these spectra are shown in Figure 5.2. The results of the DLS measurements for these vesicles suggest an average diameter of ∼93 nm, the traces for the DLS measurements are shown in Figure 5.3.

5.1.3.2 Sonication

Sonication is another frequently used technique for the preparation of unilamellar phospholipid vesicles,[129,130,276,277] the resulting vesicles are generally smaller than those prepared by extrusion, however the solutions tend to be more polydisperse.

The NMR spectrum of POPC vesicles formed following 2 hours bath sonication is a single sharp peak in the absence of $PrCl_3$. On addition of 3 mM $PrCl_3$ a second peak appears downfield of the

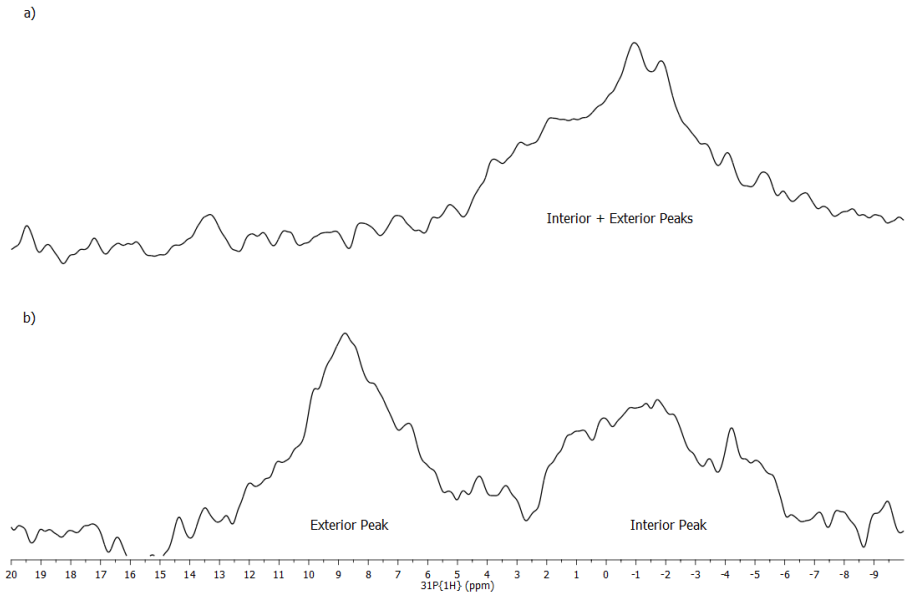

Figure 5.2: Extracts of ^{31}P spectra of extruded vesicles. POPC vesicles were prepared at 10 mg ml^{-1} in 10 mM HEPES + 100 mM NaCl by extrusion through 50 nm polycarbonate membranes. a) Before addition of 3 mM $PrCl_3$, b) After addition of 3 mM $PrCl_3$. Spectrum a) was acquired with 128 transients, spectrum b) was acquired with 256 transients, both spectra were processed with 100 Hz exponential apodisation.

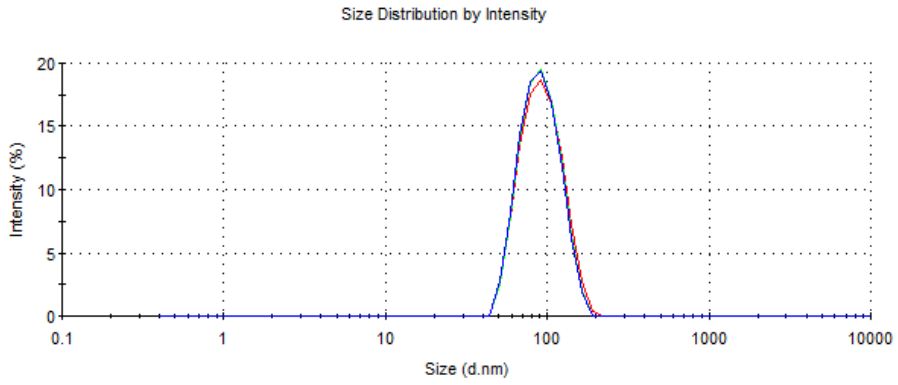

Figure 5.3: DLS traces of extruded POPC vesicles, measurements are acquired in triplicate, all three traces are shown (red, green and blue traces).

original peak, this peak belongs to the ^{31}P on the exterior leaflet of the vesicle which is in contact with the shift reagent. These spectra are shown in Figure 5.4.

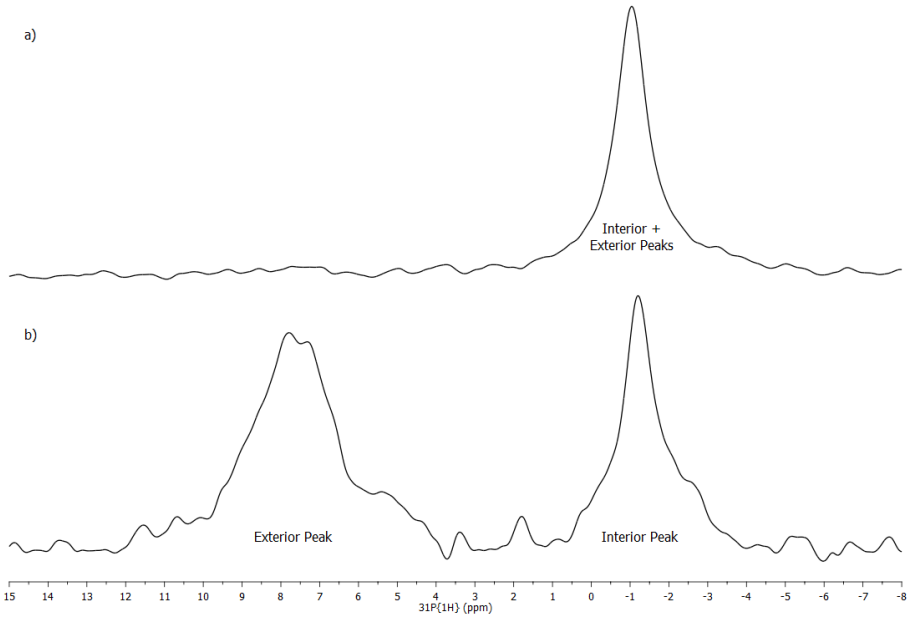

Figure 5.4: Extracts of ^{31}P spectra of sonicated vesicles. POPC vesicles were prepared at 10 mg ml^{-1} in 10 mM HEPES + 100 mM NaCl by sonication for 3 hours at 35°C. a) Before addition of 3 mM $PrCl_3$, b) After addition of 3 mM $PrCl_3$. Both spectra were acquired with 128 transients and processed with 100 Hz exponential apodisation. The vertical scale of spectrum b) is increased by a factor of 3 compared to the spectrum a).

The spectra obtained from sonicated vesicles are clearly superior to those obtained from extruded vesicles. In the absence of shift reagent the peak is much sharper for the sonicated vesicles, most likely due to the smaller average size of the vesicles.

DLS results show two components with average diameters of 32 nm and 116 nm (Figure 5.5). In dynamic light scattering the intensity of light scattered (I) is proportional to the particle diameter (d) to the power of 6, i.e. $I \propto d^6$. The larger vesicles therefore contribute more to the measured light scattering than the smaller vesicles. The intensity distribution can be converted to a volume distribution using Mie theory,[278] however this can be inaccurate and the results should be considered as an approximation. The volume distribution is shown in Figure 5.5b and indicates that a larger volume of the sample is composed of the small ~30 nm vesicles. The presence of the larger vesicles is a consequence of the sonication, however these should not interfere with the NMR stability investigation as they are too large to be visible.

On addition of $PrCl_3$, the peak of the interior leaflet which is unshifted remains sharp, while the shifted peak of the exterior leaflet is broadened. This is a consequence of the paramagnetic shift reagent also causing some line broadening.[144]

5.1.4 Choice of Phospholipid

The structure of the phospholipid used changes the rigidity of the membrane formed. 1,2-dimyristoyl-sn-glycero-3-phosphocholine (DMPC) is a saturated phospholipid with two hydrocarbon chains each composed of 14 carbon atoms (Figure 5.6a). This phospholipid is sometimes described as 14:0 PC, where 14 refers to the length of the hydrocarbon chain and the 0 indicates the chains are fully

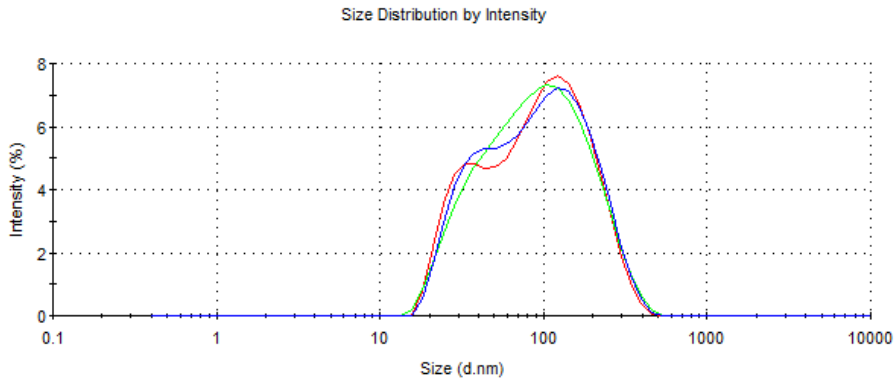

(a) Intensity distribution

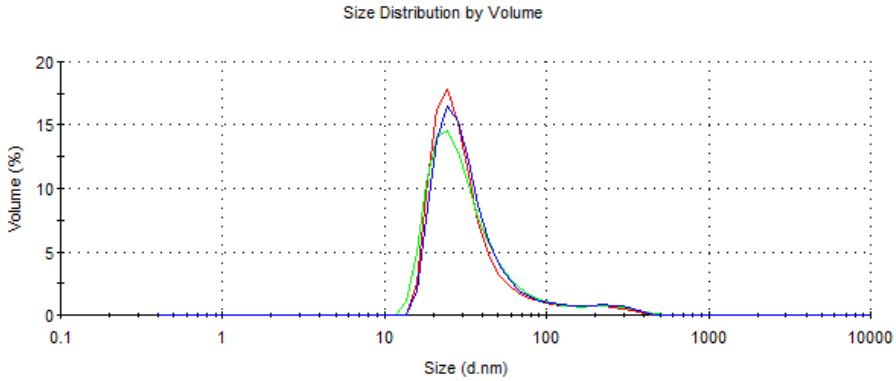

(b) Volume distribution

Figure 5.5: DLS traces of sonicated POPC vesicles, measurements are acquired in triplicate, all three traces are shown (red, green and blue traces).

saturated. 1-palmitoyl-2-oleoyl-sn-glycero-3-phosphocholine (POPC) is composed of one 16 carbon saturated chain and one 18 carbon chain with a cis double bond between the 9th and 10th carbon atoms (Figure 5.6b). This phospholipid is described as 16:0–18:1cΔ^9,[279] where 16:0 denotes the 16 carbon saturated chain and 18:1cΔ^9 indicates a chain with 18 carbons with 1 double bond in the cis confirmation(c) at the 9th position(Δ^9). Both of these phospholipids have been used frequently in membrane studies in the literature.[145,280–284] Unsaturated phospholipids are known to form less rigid membranes than saturated phospholipids,[43] the double bonds in unsaturated phospholipids disrupt the ordered packing of the chains making the membrane more fluid, this is advantageous for NMR analysis as increased rigidity will lead to broadening of peaks.

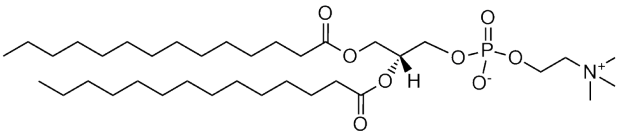

(a) 1,2-dimyristoyl-sn-glycero-3-phosphocholine (DMPC)

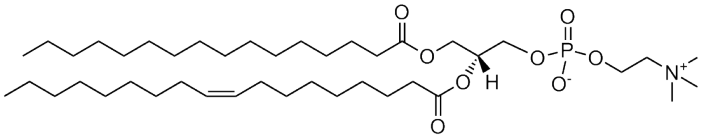

(b) 1-palmitoyl-2-oleoyl-sn-glycero-3-phosphocholine (POPC)

Figure 5.6: Structure of phospholipids used in vesicles, a) DMPC, b)POPC.

Another consideration when selecting the most suitable phospholipid is the gel-liquid crystalline transition temperature. In the gel phase the chains lie parallel with a hexagonal packing order,[132] this phase is sometimes referred to as an ordered, rigid state and characterised by hydrocarbon chains all in trans conformation.[43] The liquid crystalline phase is characterised by the introduction of gauche conformations in the hydrocarbon chains forming a more fluid, disordered state.[43] Above the gel-liquid crystalline transition temperature the phospholipid molecules are able to diffuse laterally across the membrane leaflet more freely. Transverse diffusion between the leaflets is rare above or below the gel-liquid crystalline transition temperature due to the high energy barrier associated with the polar phosphatidylcholine head group passing through the hydrophobic region of the membrane.[285] The transition temperature is affected by the acyl chain length and the number of double bonds in the chains;[128] the transition temperatures for DMPC and POPC are 23°C and -2°C respectively.[279,286] Optimum NMR spectra will be acquired when the lipids are in the liquid-crystalline phase where the lateral motion of the molecules is not restricted, this suggests the use of POPC due to its lower transition temperature.

Sonicated vesicles formed of DMPC and POPC were prepared at a concentration of 10 mg ml^{-1} in 20 mM Tris-HCl + 150 mM NaCl (pH 7.4). The spectra of these vesicles with and without $PrCl_3$ are shown in Figure 5.7

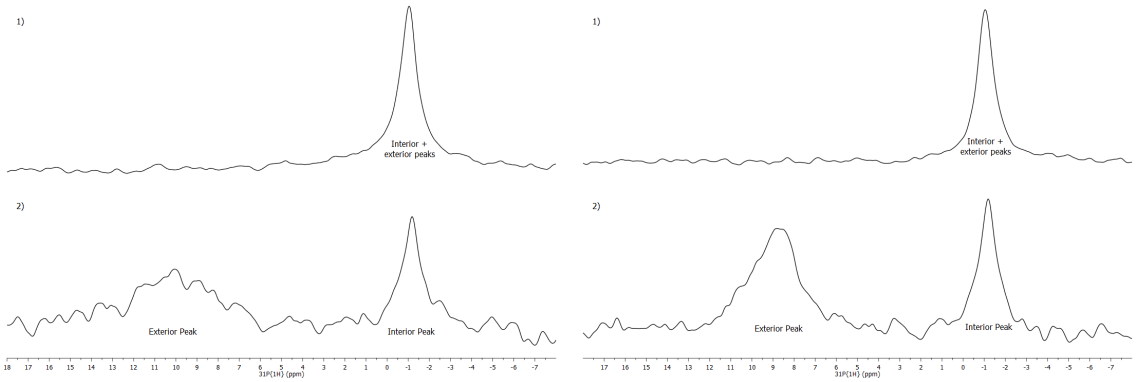

(a) DMPC vesicles (b) POPC vesicles

Figure 5.7: Extracts of ^{31}P spectra of DMPC and POPC vesicles before and after addition of $PrCl_3$ to exterior. a)DMPC vesicles, prepared at 10 mg ml^{-1} in 20 mM Tris + 150 mM NaCl by sonication for 2.5 hours at 35°C, spectra acquired with 128 transients. b)POPC vesicles, prepared at 10 mg ml^{-1} in 20 mM Tris + 150 mM NaCl by sonication for 2 hours at 35°C, spectra acquired with 64 transients. In both cases the spectra before addition of $PrCl_3$ are labelled 1) and those acquired after the addition of $PrCl_3$ are labelled 2). All spectra were processed with 100 Hz exponential apodisation. The vertical scale of the spectra labelled 2) are increased by a factor of 3 compared to the spectra labelled 1).

The spectra without $PrCl_3$ appear similar for both DMPC and POPC, although the DMPC peak is slightly broader with a linewidth of 273 Hz, compared to 218 Hz for the POPC vesicles. On addition of the shift reagent the DMPC peaks are twice as broad as the POPC peaks. The DMPC spectra were acquired with double the number of scans in efforts to improve the sensitivity of the shifted peak. The chemical shift of the exterior peak is slightly higher for the DMPC vesicles than the POPC vesicles, occurring at 10.14 and 8.86 ppm for DMPC and POPC respectively. The magnitude of peak shifting and line broadening caused by paramagnetic reagents is related to the distance between the paramagnetic ion and the observed nucleus.[85] The greater peak shift and line broadening observed in the DMPC spectrum is therefore indicative of a closer interaction between the ^{31}P nuclei of the DMPC and the paramagnetic Pr^{3+} ions. The spectra were acquired at 25°C,

only slightly above the transition temperature of DMPC, this could cause restriction of the motion of the molecules within the membrane leaflets which would cause additional broadening compared to POPC which has a much lower transition temperature.

5.1.5 Effect of Additives

Cholesterol is frequently included in studies of biomimetic membranes to make the vesicles more physiologically relevant. Cholesterol is found in eukaryotic cells, typically with a phospholipid:cholesterol ratio of 2:1.[287,288] Cholesterol (Figure 5.8) inserts into the lipid bilayer parallel to the lipid molecules with the hydroxyl group hydrogen bonded to a carbonyl oxygen of the ester groups of the phospholipid.[289] The presence of cholesterol in a bilayer is known to modify the fluidity of the membrane[290] and increase vesicle size.[147]

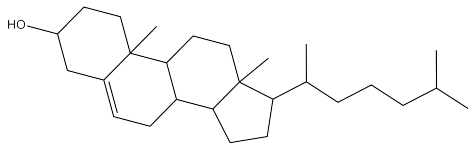

Figure 5.8: Structure of cholesterol

In order to test the effect of the addition of cholesterol to the phospholipid vesicles, a sample of DMPC/Cholesterol vesicles was prepared with a cholesterol content of 30 w/w%. The cholesterol was added by co-solubilisation in chloroform/methanol before lipid film preparation and vesicles were prepared by sonication as described in Chapter 2. The spectra acquired for this sample before and after addition of $PrCl_3$ are shown in Figure 5.9.

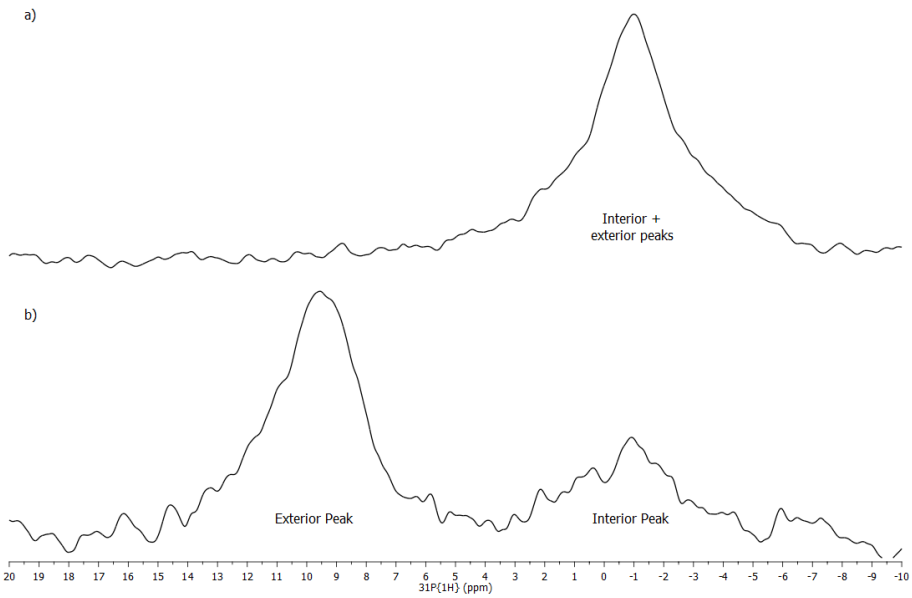

Figure 5.9: Extracts of ^{31}P spectra of 70/30 DMPC/cholesterol vesicles. Vesicles were prepared by sonication for 3 hours at 40°C of a 70/30 w/w mixture of DMPC and cholesterol in 20 mM Tris-HCl + 150 mM NaCl. a) Before addition of $PrCl_3$, b) After addition of $PrCl_3$. Both spectra were acquired with 1024 transients and processed with 100 Hz exponential apodisation. The vertical scale of the spectrum b) is increased by a factor of 2 compared to spectrum a).

The spectra display broader peaks compared to vesicles without cholesterol. Without the shift

reagent the linewidth is 790 Hz, 4 times greater than that of the DMPC vesicles formed without cholesterol, shown in Figure 5.7a. This broadening is a consequence of restriction in lateral diffusion of the phospholipid molecules within each leaflet caused by the cholesterol as well as the potential increase in vesicle size, which the addition of cholesterol is known to cause.[147] On addition of $PrCl_3$ both peaks are broad, especially the interior (unshifted) peak which is almost too broad to be visible. The additional broadening of the interior peak, combined with a decrease in the interior/exterior peak area ratio suggests that the cholesterol preferentially occupies the inner leaflet, this bilayer asymmetry has been reported in the literature.[147,291,292]

In this experiment 6 mM $PrCl_3$ was used instead of 3 mM because the peaks were not resolved with 3 mM $PrCl_3$ in a previous experiment. The effect of the change in $PrCl_3$ concentration will be discussed further in Section 5.3.1.3.

Although the addition of cholesterol to the vesicles would make the system more comparable to biological cells, the poor peak resolution and sensitivity of the interior peak makes it unsuitable for membrane permeation studies in this situation. The addition of cholesterol was therefore not implemented in ongoing studies.

5.2 Time-Resolved Stability Studies of Vesicles

To study the membrane permeating ability of potentially cytotoxic aggregates the vesicles should remain intact and stable for a reasonable period of time in the absence of any permeating species. In order to monitor the stability of the phospholipid vesicles over time ^{31}P spectra were acquired every 30-60 minutes over the course of a weekend (typically ∼65–70 hours).

Experiments were conducted with either $PrCl_3$ on the outside of the vesicles or with $PrCl_3$ encapsulated within vesicles. Changes in the ratio of the area of the interior and exterior peaks ($R_{i/e}$) provide a measurement of stability of the vesicles. With $PrCl_3$ on the outside of the vesicles any disintegration of the vesicle bilayer would allow the $PrCl_3$ to come into contact with the interior leaflet and lead to a decrease in $R_{i/e}$. Similarly, with $PrCl_3$ on the inside, any breakage of the membrane would allow $PrCl_3$ to leak out and cause shifting of the exterior peak and a corresponding increase in $R_{i/e}$.

5.2.1 DMPC

To test the stability of DMPC vesicles, a 20 mg ml^{-1} sample was prepared by sonication with 3 mM $PrCl_3$ added to the outside of the vesicles. ^{31}P spectra were acquired every 30 minutes over a period of 48 hours beginning at approximately 30 minutes after the end of the sonication period. Figure 5.10 shows the arrayed ^{31}P spectra for $t = 0.5$–35 hours, after this time the peaks merged and decreased in intensity.

Peak fitting analysis was performed on the region of -6 to 20 ppm of each spectrum. Figure 5.11 shows the chemical shift, peak height, peak width and peak area data for the two peaks over the 35 hours. Over time the interior peak, which is initially not affected by the addition of $PrCl_3$, shifts downfield towards the exterior peak, this shift is combined with a decrease in peak height and an increase in peak width. By $t = 33.5$ hours the interior peak cannot be resolved from the exterior peak. The decrease in exterior chemical shift of ∼2 ppm over the course of the experiment is small

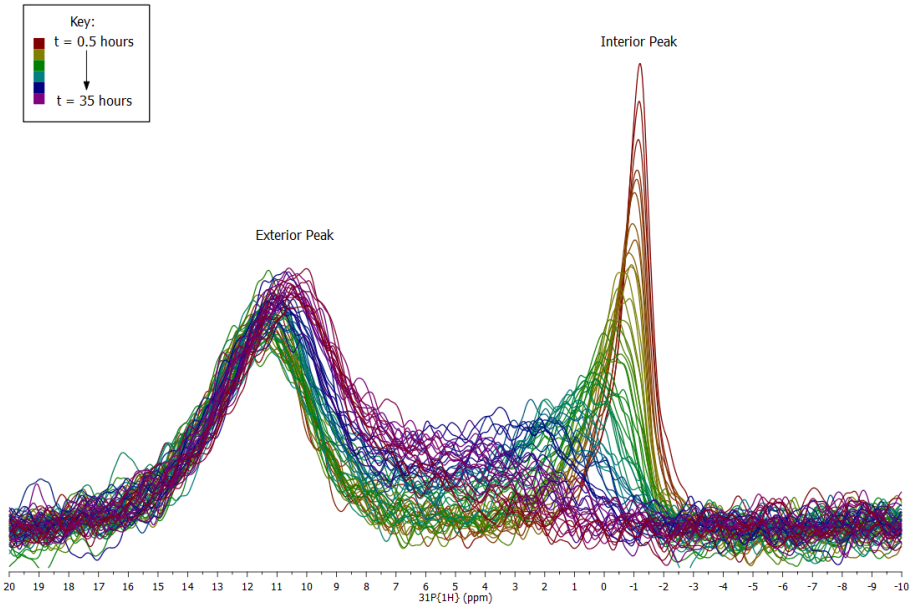

Figure 5.10: Extracts of arrayed ^{31}P spectra of DMPC vesicles with $PrCl_3$ outside. Vesicles were prepared at 20 mg ml^{-1} in 20 mM Tris-HCl + 150 mM NaCl by sonication for 2 hours at 35°C, 3 mM $PrCl_3$ was added to the exterior volume after sonication. Spectra were acquired with 128 transients every 30 minutes for 48 hours and processed with 100 Hz exponential apodisation, only spectra for t = 0.5–35 hours are included in this figure.

compared to change in chemical shift of the interior peak, it is most likely due to the decrease in effective concentration of the $PrCl_3$ on permeation of the vesicles.

The changes to the peak areas, shown in Figure 5.11d, lead to an overall decrease in the peak area ratio ($R_{i/e}$) as shown in Figure 5.12. The decrease in peak area ratio is caused by disintegration of the vesicles, as the membrane is broken the interior leaflet comes into contact with the $PrCl_3$ and this results in a paramagnetic shift of the interior peak. As this happens the nuclei in contact with the shift reagent end up with the same chemical shift leading to an increase in peak area of the shifted peak and corresponding decrease in unshifted peak area.

The peak area ratio decreases from the first time point, indicating that the vesicles begin to break down almost immediately. This vesicle system is therefore only suitable for use with cytotoxic aggregates which cause rapid membrane permeation on a timescale of less than 1 hour, although this may be the case for Aβ,[169] a more stable system is preferable to allow for slower permeation to be investigated.

5.2.2 POPC

POPC may be a more suitable phospholipid for use in vesicles for permeation studies, as discussed in Section 5.1.4, the incorporation of a double bond in one of the acyl chains leads to a decrease in the gel-liquid crystalline transition temperature and sharper peaks in the ^{31}P spectra. Figure 5.13 shows the ^{31}P spectra of 10 mg ml^{-1} POPC vesicles with 3 mM $PrCl_3$ added to the outside of the vesicles over a period of 68 hours.

Compared to the spectra from the DMPC vesicles, the interior peak in this experiment does not change significantly over the course of the experiment. There is however a clear change in the

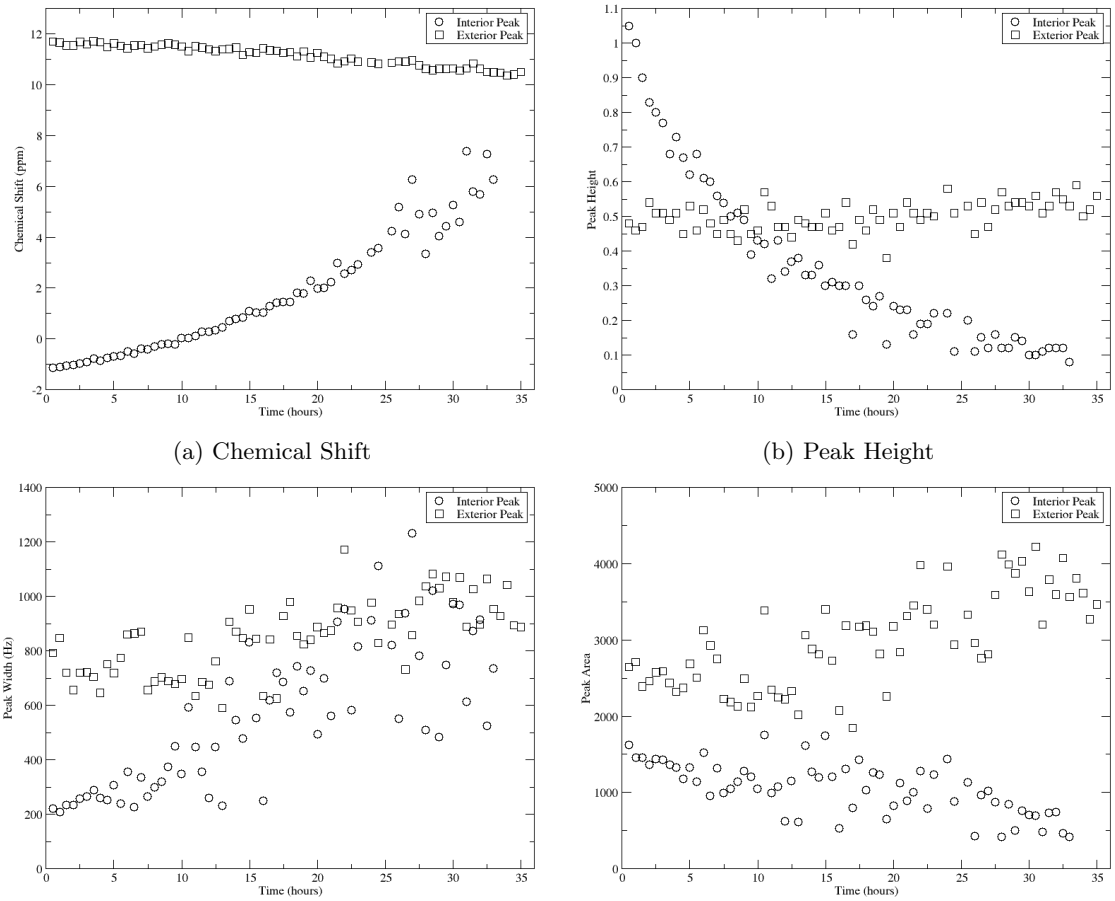

(a) Chemical Shift

(b) Peak Height

(c) Peak Width

(d) Peak Area

Figure 5.11: Graphs showing the progression of peak parameters over 35 hours for 20 mg ml^{-1} DMPC vesicles with $PrCl_3$ outside. All graphs show data for both interior and exterior peaks.

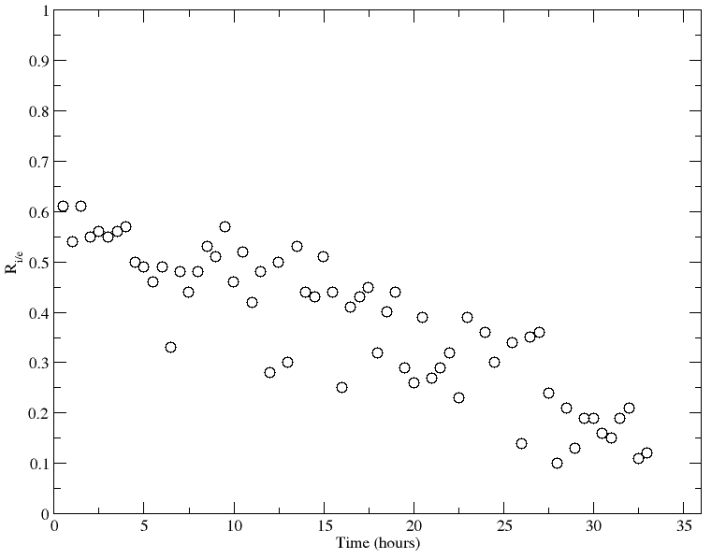

Figure 5.12: Peak area ratio ($R_{i/e}$) for DMPC vesicles

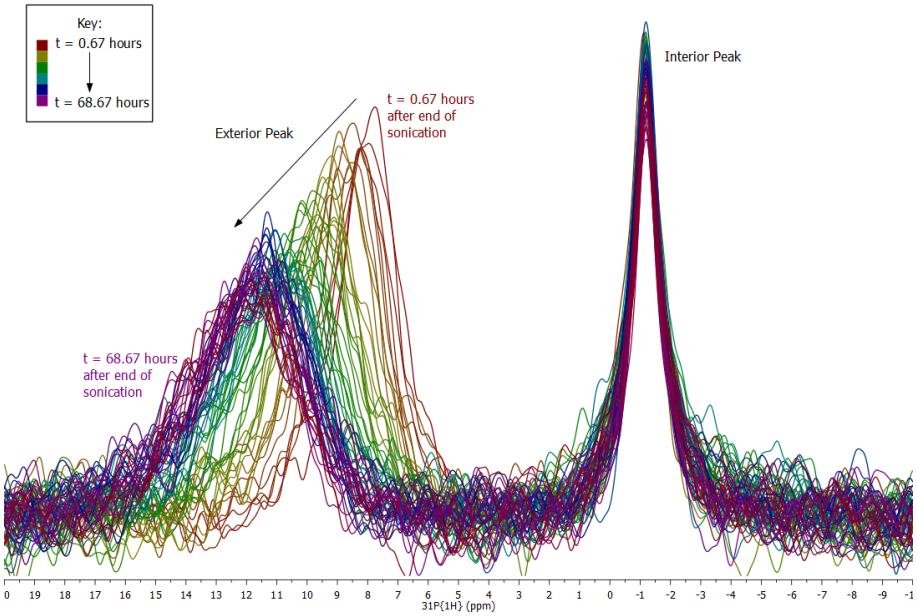

Figure 5.13: Extracts of arrayed ^{31}P spectra of POPC vesicles with $PrCl_3$ outside. Vesicles were prepared at 10 mg ml^{-1} in 10 mM HEPES + 100 mM NaCl by sonication for 3 hours at 35°C, 3 mM $PrCl_3$ was added to the exterior volume after sonication. Spectra were acquired with 128 transients every hour for 68 hours and processed with 100 Hz exponential apodisation.

exterior peak over time, the peak shifts downfield, decreases in height and increases in width. The parameters obtained from peak fitting of the interior and exterior peak for each time point are shown in Figure 5.14.

Despite the changes in chemical shift, peak height and peak width of the exterior peak, the peak areas of both peaks remain constant (Figure 5.14d) and therefore the ratio of the peak areas is also reasonably constant, as shown in Figure 5.15.

These results suggest that the vesicles are stable and there is no membrane disintegration over the course of the experiment, these vesicles are therefore suitable for permeation studies, however, further investigation into the cause of the time dependent shift in the exterior peak is required.

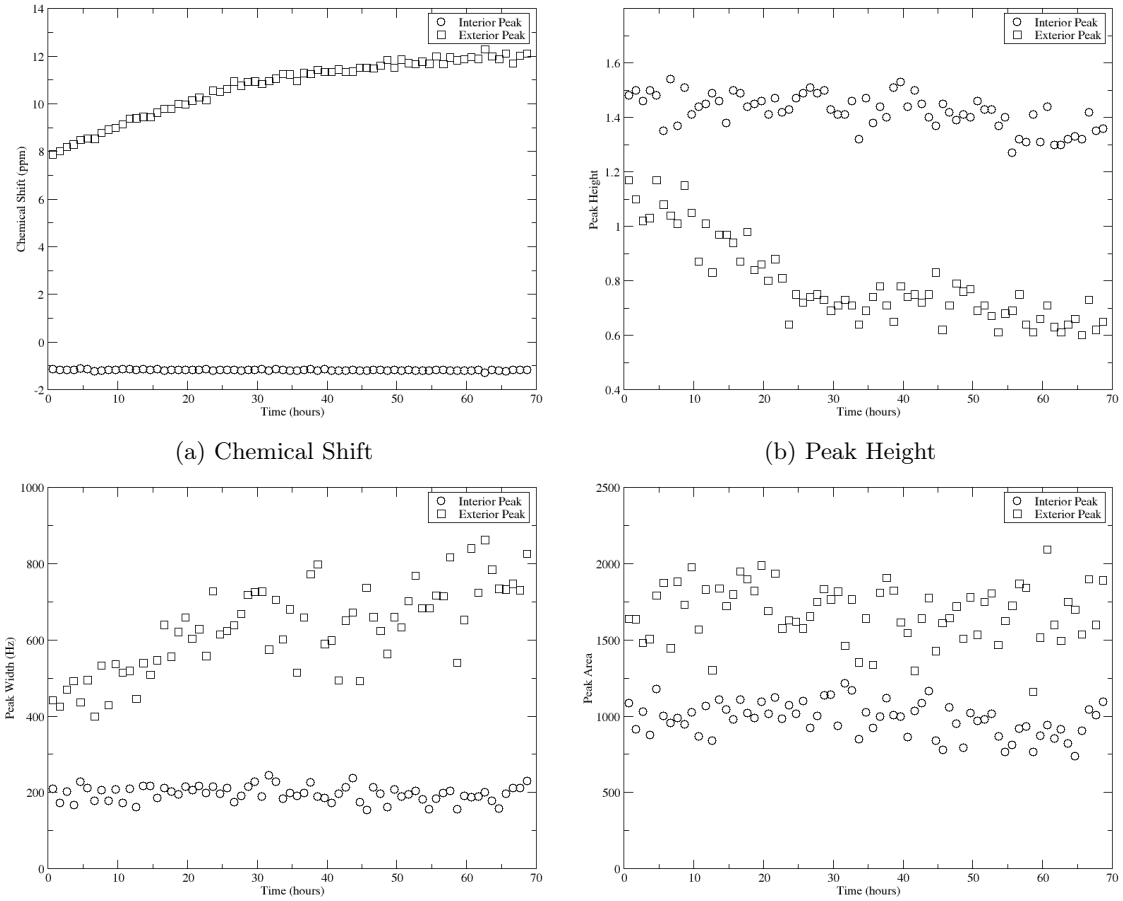

(a) Chemical Shift

(b) Peak Height

(c) Peak Width

(d) Peak Area

Figure 5.14: Graphs showing the progression of peak parameters of POPC vesicles over the course of the 68 hour experiment. All graphs show data for both interior and exterior peaks.

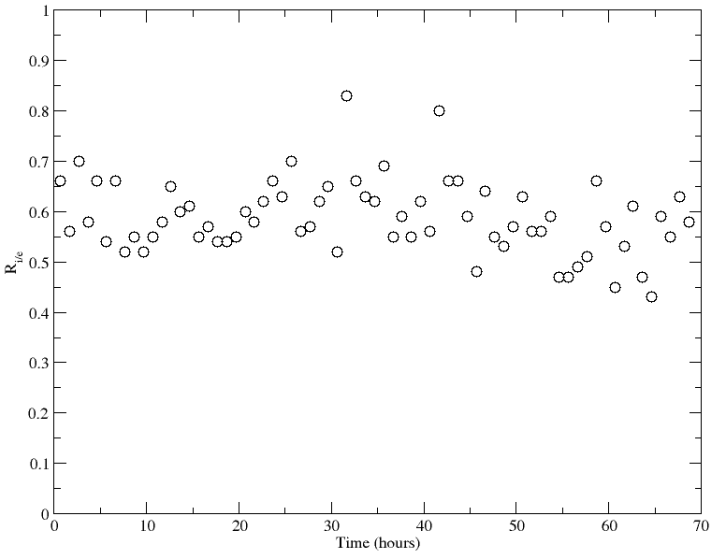

Figure 5.15: Peak area ratio ($R_{i/e}$) for POPC vesicles

5.3 Studies of Time-Resolved Peak Shifting in Vesicles

The downfield shift of the exterior peak observed in Figure 5.13 was not anticipated as there is no literature precedent for the shift, for example Kumar et al. state that "there was no change in chemical shift, signal intensity or line shape for several weeks".[145] Although the shift does not affect the stability of the vesicles, as shown by the constant peak area ratio (Figure 5.15), the cause of the observed downfield shift required investigation. Several experiments were performed in efforts to understand the cause of the downfield shift of the exterior peak over time. These experiments are summarised in Table 5.1.

5.3.1 Downfield Shift

Where the $PrCl_3$ is on the outside of the vesicles there is a downfield shift in the exterior peak over time, as seen in Figure 5.13. The change in chemical shift over time only occurs when a buffer such as Tris-HCl or HEPES is also in the solution (see Table 5.1).

The change in chemical shift of the exterior peak can be modelled as a single exponential of the form shown in Equation 5.2.

$$\delta_{ext} = A(1 - \exp(-t/T)) + \delta^0_{ext} \tag{5.2}$$

Where δ_{ext} is the chemical shift of the exterior peak in ppm, t is the time of spectrum acquisition relative to the end of the sonication process in hours, A is a measure of the magnitude of peak shifting, T is the time it takes for the peak to shift by half of the maximum shifting and δ^0_{ext} is the chemical shift of the exterior peak at $t = 0$.

The exterior chemical shift data from the spectra shown in Figure 5.13 are plotted in Figure 5.16 along with the model fitted to the data with the equation. The parameters of the model are included in Table 5.2 (entry 1).

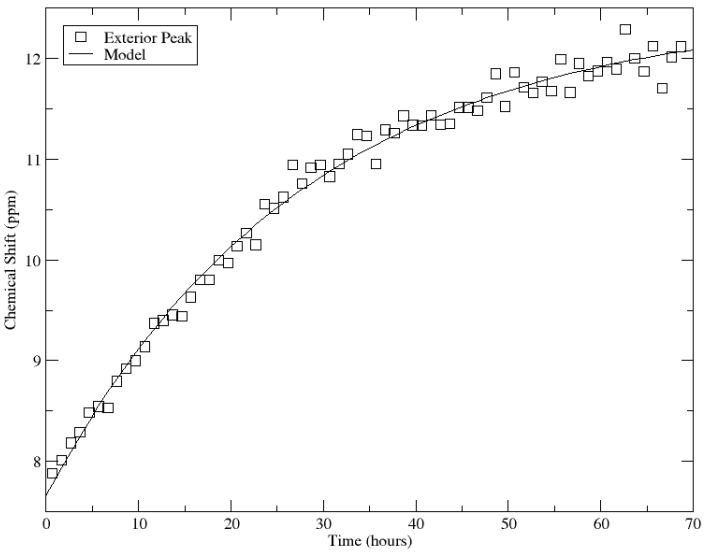

Figure 5.16: Graph of exterior chemical shift over 69 hour experiment and the result of fitting the data to Equation 5.2.

Table 5.1: Details of POPC Vesicle Experiments

Direction of Shift	$PrCl_3$ Location	$[PrCl_3]$ (mM)	Interior Conditions	Exterior Conditions	Additional Information
Downfield	Outside	3	20 mM Tris + 150 mM NaCl	18 mM Tris + 135 mM NaCl + 3 mM $PrCl_3$	
		6	20 mM Tris + 150 mM NaCl	16 mM Tris + 120 mM NaCl + 6 mM $PrCl_3$	
		3	10 mM HEPES + 100 mM NaCl	9 mM HEPES + 90 mM NaCl + 3 mM $PrCl_3$	
		3	10 mM HEPES + 100 mM NaCl	9 mM HEPES + 90 mM NaCl + 3 mM $PrCl_3$	
		3	10 mM HEPES + 100 mM NaCl	9 mM HEPES + 90 mM NaCl + 3 mM $PrCl_3$	
		6	10 mM HEPES + 100 mM NaCl	8 mM HEPES + 80 mM NaCl + 6 mM $PrCl_3$	
		6	10 mM HEPES + 100 mM NaCl	10 mM HEPES + 100 mM NaCl + 6 mM $PrCl_3$ (in 10 mM HEPES + 100 mM NaCl)	
None	Outside	3	20 mM Tris + 150 mM NaCl + Calcein	∼139 mM NaCl (0.9% from wash) + 3 mM $PrCl_3$	Washed (0.9% NaCl)
		3	20 mM Tris + 150 mM NaCl + Calcein	∼139 mM NaCl (0.9% from wash) + 3 mM $PrCl_3$	Washed (0.9% NaCl)
		3	20 mM Tris + 150 mM NaCl + Calcein	∼139 mM NaCl (0.9% from wash) + 3 mM $PrCl_3$	Washed (0.9% NaCl)
		3	20 mM Tris + 150 mM NaCl	∼139 mM NaCl (0.9% from wash) + 3 mM $PrCl_3$	Washed (0.9% NaCl)
		3	20 mM Tris + 150 mM NaCl	∼139 mM NaCl (0.9% from wash) + 3 mM $PrCl_3$	Washed (0.9% NaCl)
		3	10 mM HEPES + 100 mM NaCl	∼139 mM NaCl (0.9% from wash) + 3 mM $PrCl_3$	Washed (0.9% NaCl)
		3	150 mM NaCl, D2O	135 mM NaCl + 3 mM $PrCl_3$	
	Inside	3	135 mM NaCl + 3 mM $PrCl_3$	150 mM NaCl	Washed (150 mM NaCl)
	Inside and Outside	6	8 mM HEPES + 80 mM NaCl + 6 mM $PrCl_3$	8 mM HEPES + 80 mM NaCl + 6 mM $PrCl_3$	
Upfield	Inside	3	9 mM HEPES + 90 mM NaCl + 3 mM $PrCl_3$	10 mM HEPES + 100 mM NaCl (+10% D2O) = 9 mM HEPES + 90 mM NaCl	Washed (HEPES)
		6	8 mM HEPES + 80 mM NaCl + 6 mM $PrCl_3$	10 mM HEPES + 100 mM NaCl	Washed (HEPES)
		6	8 mM HEPES + 80 mM NaCl + 6 mM $PrCl_3$	10 mM HEPES + 100 mM NaCl	Washed (HEPES)
		6	8 mM HEPES + 80 mM NaCl + 6 mM $PrCl_3$	10 mM HEPES + 100 mM NaCl	POPC rehydrated in HEPES and then $PrCl_3$

Table 5.2: Downfield Shift Model Fitting Parameters

	Buffer	[$PrCl_3$]	Figure	A (ppm)	T (hours)	δ^0_{ext} (ppm)
1	HEPES	3 mM	5.13	4.82	27.69	7.66
2	Tris-HCl	3 mM	5.18a	4.91	25.52	8.65
3	HEPES	6 mM	5.20a	5.39	25.33	9.32

5.3.1.1 Effect of Buffer Selection

The change in chemical shift over time of the peak in contact with the $PrCl_3$ only occurs when a buffer such as Tris or HEPES is also in the solution (see Table 5.1). This indicates that the $PrCl_3$ could be competitively binding to the buffer molecules. The structures for Tris and HEPES are shown in Figure 5.17, which shows that it is likely that binding of the Pr^{3+} ions occurs through the nitrogen lone pairs of the molecules and the hydroxyl groups.

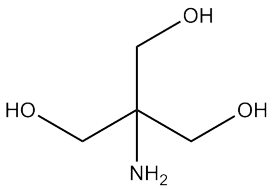

(a) Tris(hydroxymethyl)aminomethane (Tris)

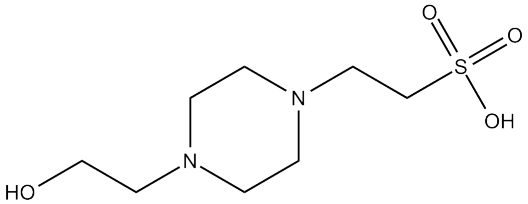

(b) 4-(2-Hydroxyethyl)piperazine-1-ethanesulfonic acid (HEPES)

Figure 5.17: Structure of buffer molecules used in vesicle studies

There are several literature examples of HEPES, Tris and similar molecules binding to lanthanide metals, with stability constants determined by potentiometric measurements and quoted as $\log K$ values. The stability constants of some lanthanide ions with HEPES were presented by Anwar and Azab,[293] for praseodymium(III) the stability constant was given as 3.44. A study of HEPES binding to copper(II) suggested a bidentate chelation through the nitrogen of the piperazine ring and the oxygen of the hydroxyl group, with no binding at the opposite end of the molecule due to steric hindrance around the sulfonate group.[294] The same study showed comparable Cu^{2+} binding properties for HEPES and Tris, with stability constants of 3.22 and 4.05 respectively. Binding of copper ions is likely to be more favourable than binding of lanthanide ions, due in part to the smaller ionic radius, this is confirmed by a study of bis(2-hydroxyethyl)piperazine (a molecule with similar structure to HEPES except the CH_2SO_3H moiety is replaced by CH_2OH), the stability constants for the complex of monohydrated bis(2-hydroxyethyl)piperazine with Cu^{2+} and Pr^{3+} are given as 10.18 and 9.18 respectively.[295] The binding of lanthanide metals by HEPES or Tris is weak in comparison to the hexadentate chelating agent EDTA, which binds through two nitrogen atoms and four oxygen atoms in an octahedral arrangement, the stability constants for EDTA complexes with the lanthanides Ce^{3+}, Eu^{3+}, Gd^{3+} and Yb^{3+} range from 15.94 to 19.51 across the series.[296]

There is little difference in the extent of peak movement when changing buffers between Tris and HEPES, Figure 5.18 shows the spectra acquired for vesicles prepared in Tris (a) and HEPES (b). The interior peaks have the same chemical shift in both buffers, however the exterior peak at $t = 0$ hours is shifted slightly more in Tris than HEPES, occuring at 8.81 ppm and 7.88 ppm in Tris and HEPES respectively. Despite the initial difference in chemical shift of the exterior peak, the trend in downfield shift over time is similar for both sets of vesicles, the change in chemical shift, relative

to the initial spectrum, are shown in Figure 5.19.

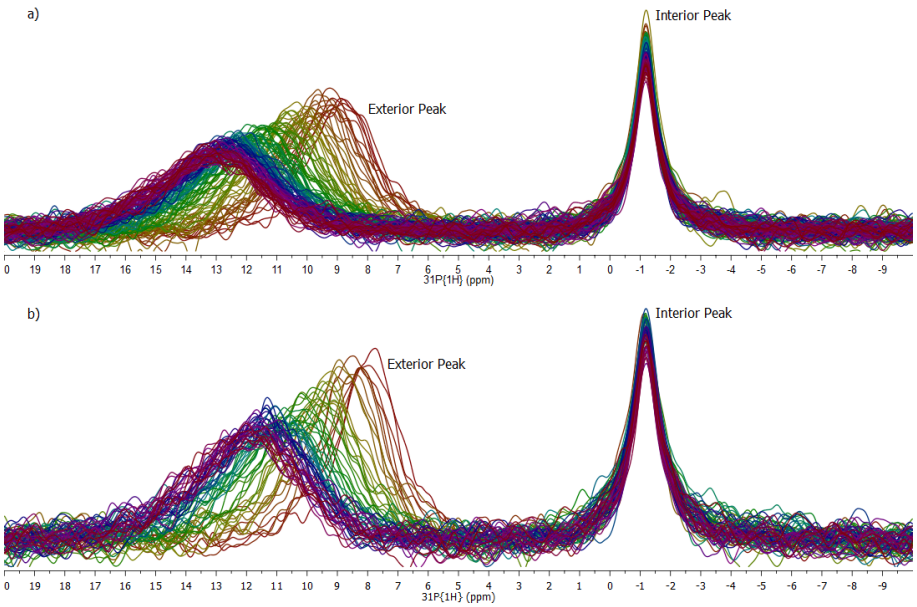

Figure 5.18: Arrayed extracts of ^{31}P spectra for 10 mg ml^{-1} POPC vesicles with 3 mM $PrCl_3$ outside. a) Vesicles prepared in 20 mM Tris + 150 mM NaCl by sonication for 2 hours at 35°C, spectra acquired every 30 minutes for 69 hours. b) Vesicles prepared in 10 mM HEPES + 100 mM NaCl by sonication for 3 hours at 35°C, spectra acquired every hour for 68 hours. All spectra were acquired with 128 transients and processed with 100 Hz exponential apodisation.

The parameters obtained from fitting Equation 5.2 to the exterior chemical shift of both sets of data are included in Table 5.2 (entries 1 and 2 for HEPES and Tris respectively). The slightly larger value of A for the vesicles in Tris reflects the greater range of chemical shift values covered over the experiment time, as observed in Figure 5.18. The difference in δ^0_{ext} is due to the difference in initial chemical shift of the exterior peak in Tris compared to HEPES. The lower value of T for vesicles in Tris indicates that the peak shifts more rapidly and as a consequence reaches a maximum value in less time then the vesicles in HEPES.

The slight difference in magnitude of peak shift could be due to different binding affinities of the buffers for the $PrCl_3$. A study by Sokolowska et al.[294] suggests that HEPES and Tris have similar affinities for binding Cu^{2+}, however the stability constant value given for Tris is slightly higher than that of HEPES. Binding to the Pr^{3+} ions via the nitrogen lone pairs is only available in the basic form of the buffer molecules; at pH 7.4 the base:acid ratio is 0.2 for Tris and 0.8 for HEPES (calculated using the Henderson-Hasselbalch equation[297] with pKa values of 8.1 and 7.5 for Tris[298] and HEPES[299] respectively). The concentration of buffer molecules available for binding to the Pr^{3+} ions can be calculated using these ratios and the concentration of the buffer solutions (20 mM for Tris and 10 mM HEPES), this results in concentrations of 3.4 mM Tris (base form) and 4.4 mM HEPES (base form). These buffer concentrations were selected to mimic the conditions used in literature studies of phospholipid vesicles (20 mM Tris-HCl, 150 mM NaCl, pH 7.4)[145] and membrane permeation (10 mM HEPES, 100 mM NaCl, pH 7.4).[169] A more in depth understanding of the effect of buffer choice using buffers with the same concentration and NaCl content is required.

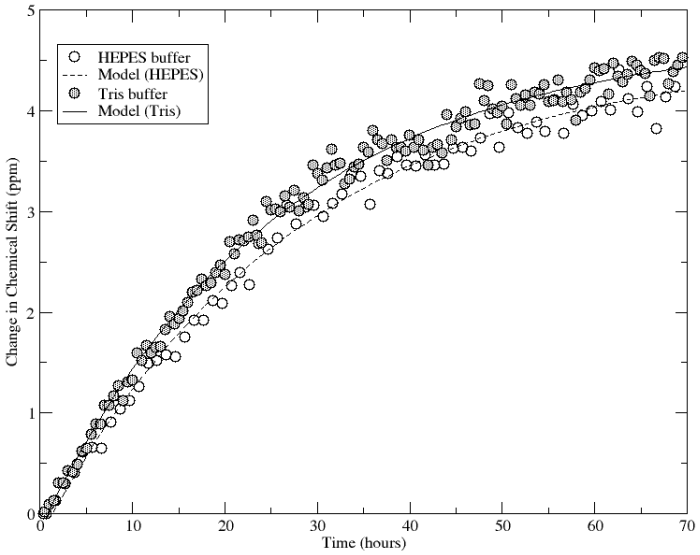

Figure 5.19: Graph showing the change in exterior chemical shift over time relative to the first time point for vesicles in Tris and HEPES.

5.3.1.2 Effect of Differences in Buffer Concentration Across the Membrane

The addition of $PrCl_3$ to the vesicle sample was achieved through the addition of a small aliquot of $PrCl_3$ stock solution in D_2O. This lead to a slight decrease in buffer and salt concentrations on the outside compared to the interior concentrations, the buffer concentrations for each experiment are included in Table 5.1. For example addition of 3 mM $PrCl_3$ reduces the exterior concentration of HEPES buffer from 10 mM to 9 mM and NaCl from 100 mM to 90 mM. To investigate whether the buffer concentration gradient was a cause of the peak movement a stock solution of $PrCl_3$ was prepared in 10 mM HEPES + 100 mM NaCl ($PrCl_{3(\mathrm{HEPES})}$), addition of this solution to vesicles in the same buffer maintained the same concentration inside and outside the vesicles. Figure 5.20a shows the 66 hour time study for these vesicles, the spectra show a downfield shift of the exterior peak, as seen in previous experiments. Another aliquot of the same vesicle solution was used with $PrCl_{3(D_2O)}$, Figure 5.20b shows the spectra at $t \approx 0$ hours and $t \approx 66$ hours for both samples. There is no significant difference between the spectra, indicating that a difference in buffer concentration between the interior and exterior volumes does not affect the peak shifting over time.

5.3.1.3 Concentration of Paramagnetic Shift Reagent

The magnitude of initial peak shift is related to the concentration of $PrCl_3$. Experiments were run with two concentrations of $PrCl_3$, 3 mM and 6 mM. Comparison of the magnitude of downfield shift of the exterior peak with the different concentrations of $PrCl_3$ should provide additional information regarding the cause of peak shifting. Figure 5.21 shows the 1st spectrum of the array for the vesicles with 3 mM and 6 mM $PrCl_3$, the arrayed time studies have been shown previously in Figure 5.13 and Figure 5.20a for 3 mM and 6 mM $PrCl_3$ respectively. These vesicles were prepared at the same concentration, with the same length of sonication time, only differing in the amount of $PrCl_3$ added. The graphs in Figure 5.22 show the exterior chemical shift data obtained from peak fitting for both of these samples. Figure 5.22a shows the actual chemical shift values and clearly shows the higher chemical shift in the presence of 6 mM $PrCl_3$. Figure 5.22b presents the chemical shift values relative to the initial value and shows that with 6 mM $PrCl_3$ the magnitude and rate of

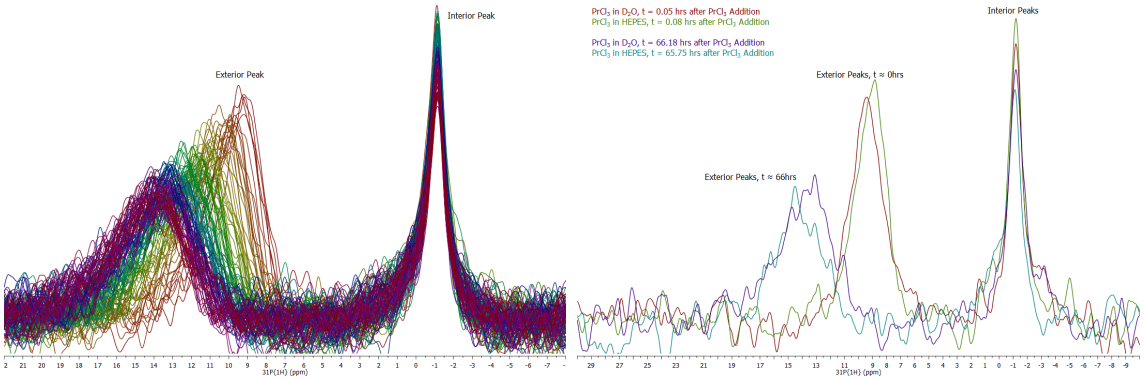

(a) $PrCl_{3(HEPES)}$ added to POPC vesicles (b) Comparison of $PrCl_{3(HEPES)}$ and $PrCl_{3(D_2O)}$

Figure 5.20: Extracts of ^{31}P spectra of POPC vesicles with $PrCl_{3(HEPES)}$ outside. POPC vesicles were prepared at 10 mg ml^{-1} in 10 mM HEPES + 100 mM NaCl by sonication for 3 hours at 35°C, 6 mM $PrCl_{3(HEPES)}$ was added to the exterior volume after sonication. a) Array of 66 hour experiment with $PrCl_{3(HEPES)}$, spectra acquired with 256 transients every 30 minutes, b)Overlay of $t \approx 0$ hours and $t \approx 66$ hours for POPC vesicles with $PrCl_{3(HEPES)}$ and $PrCl_{3(D_2O)}$. Colour coding: $PrCl_{3(D_2O)}$, $t = 0.05$ hours after $PrCl_3$addition, $PrCl_{3(HEPES)}$, $t = 0.08$ hours after $PrCl_3$addition, $PrCl_{3(D_2O)}$, $t = 66.18$ hours after $PrCl_3$addition, $PrCl_{3(HEPES)}$, $t = 65.75$ hours after $PrCl_3$addition.

peak shifting is greater than with 3 mM $PrCl_3$. The parameters obtained from modelling the 6 mM $PrCl_3$ data with Equation 5.2 are included in Table 5.2 (entry 3), the greater value for A and smaller T confirms the observation from Figure 5.22b that the peak moves by a greater distance and at a faster rate, the higher value for δ^0_{ext} is due to the higher initial shifting of the peak by the higher concentration of $PrCl_3$.

The magnitude of initial peak shift is known to be related to the concentration of shift reagent, this has been demonstrated for several paramagnetic shift ions, such as Pr^{3+} and Eu^{3+}.[140,142] The comparison above shows that peak shifting over time is also clearly affected by the $PrCl_3$ concentration, this warrants further investigation of data with other concentrations of $PrCl_3$.

5.3.2 Upfield Shift

For investigations of the membrane permeating ability of potentially cytotoxic aggregates it is advantageous to minimise competing interactions with the membrane. The presence of $PrCl_3$ on the outside of vesicles would complicate the analysis of experiments with Aβ added to the outside of vesicles as there is the potential for binding between the Aβ and $PrCl_3$ as well as the $PrCl_3$ obstructing access to the vesicle. To avoid these complications, the $PrCl_3$ could be encapsulated within the vesicles. Separating the shift reagent from the Aβ ensures unobstructed observation of membrane permeation.

Given the downfield shift observed in the exterior peak when $PrCl_3$ was outside the vesicles, it was necessary to confirm the effect of $PrCl_3$ when on the inside of vesicles. With $PrCl_3$ encapsulated within the vesicles the peak shifted by the $PrCl_3$ is that of the interior leaflet. This peak undergoes an upfield shift over time, as shown in Figure 5.23, for clarity the spectra of the first and last time points are shown in the insert of this figure. In this experiment 6 mM $PrCl_3$ was used in order to improve the initial resolution of the two peaks.

The data obtained from peak fitting each of the spectra is shown in Figure 5.24. As with the vesicles with $PrCl_3$ on the outside, the peak areas of both peaks remain reasonably constant (Figure 5.24d)

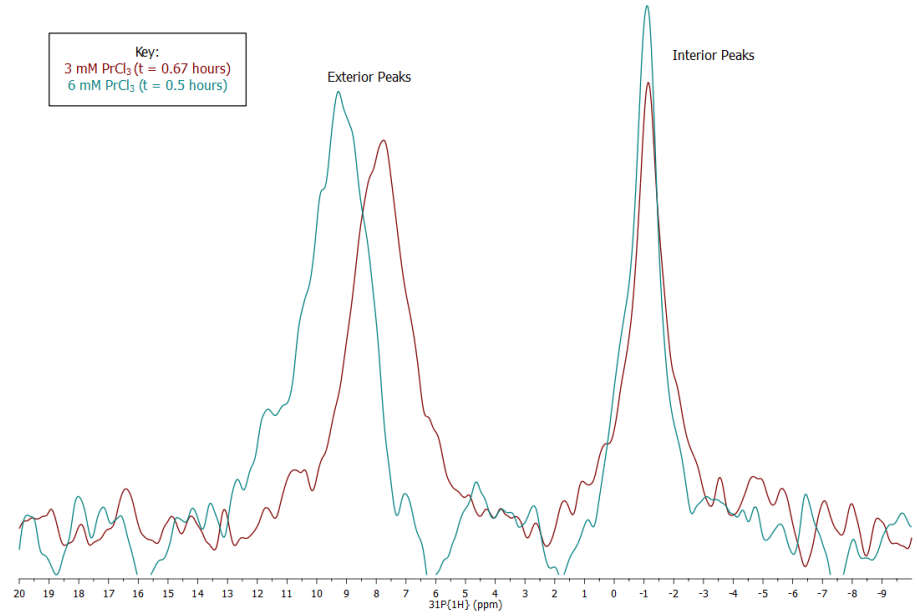

Figure 5.21: Extracts of ^{31}P spectra of POPC vesicles with 3 mM and 6 mM $PrCl_3$ outside. 1st spectrum of arrayed experiments ($t \approx 0.5$ hours), spectra are colour coded: 3 mM $PrCl_3$ ($t = 0.67$ hours after end of sonication), 6 mM $PrCl_3$ ($t = 0.5$ hours after end of sonication). POPC vesicles were prepared at 10 mg ml^{-1} in 10 mM HEPES + 100 mM NaCl by sonication for 3 hours at 35°C.

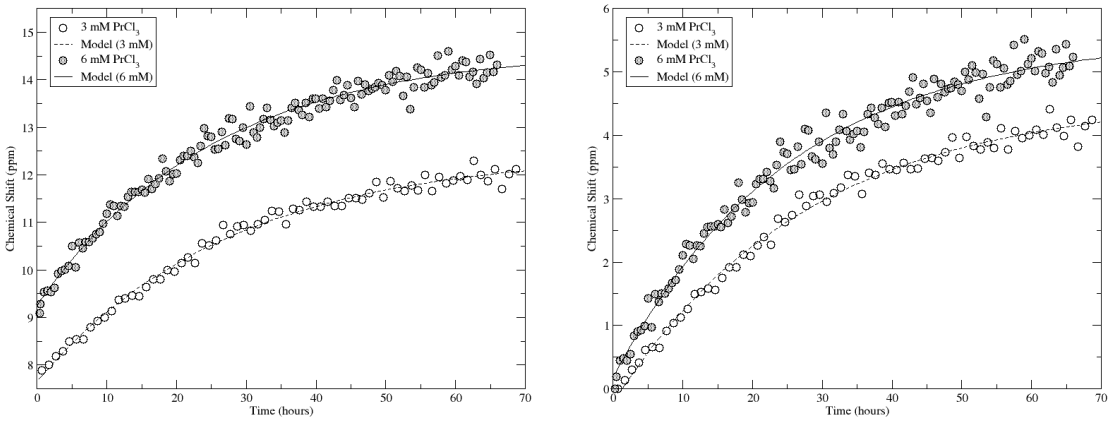

(a) Exterior Chemical Shifts

(b) Change in Exterior Chemical Shift

Figure 5.22: Graphs of exterior chemical shift over time for vesicles with 3 mM and 6 mM $PrCl_3$. a) Chemical shift values from spectra. b) Chemical shift values relative to first time point.

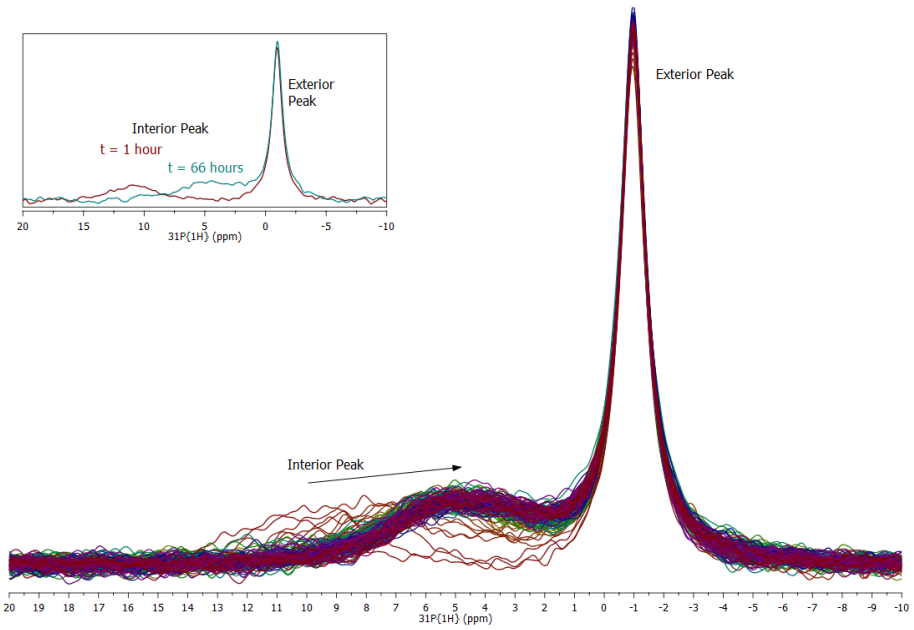

Figure 5.23: Extracts of arrayed ^{31}P spectra of POPC vesicles with 6 mM $PrCl_3$ encapsulated inside. Vesicles were prepared by sonication of 20 mg ml^{-1} POPC in 6 mM $PrCl_3$ + 10 mM HEPES + 100 mM NaCl for 3.5 hours at 35°C, exterior $PrCl_3$ was removed by washing with Sephadex columns in 10 mM HEPES + 100 mM NaCl. Spectra were acquired with 512 transients every 30 minutes for 66 hours and processed with 100 Hz exponential apodisation. Insert shows only $t = 1$ hour and $t = 66$ hours.

despite the change in the chemical shift of the interior peak, the stability of the peak area ratio (Figure 5.24f) indicates that no membrane disintegration occurs during the 66 hour experiment.

Figure 5.24a clearly shows the decrease in chemical shift of the interior peak, this trend can be modelled with an exponential function of the form shown in Equation 5.3.

$$\delta_{int} = A(\exp(-t/T)) + \delta^{\infty}_{int} \tag{5.3}$$

Where δ_{int} is the chemical shift of the interior peak, t is the time of spectrum acquisition, A is the magnitude of peak shifting, T is the time for the peak to shift by half of the maximum shift and δ^{∞}_{int} is the chemical shift to which the peak settles. Table 5.3 shows the parameters obtained from fitting Equation 5.3 to the interior chemical shift data and Figure 5.24e shows the graph of the interior chemical shift data with the fitted model.

Table 5.3: Upfield Shift Model Fitting Parameters

	Buffer	[$PrCl_3$]	Figure	A (ppm)	T (hours)	δ^{∞}_{int} (ppm)
1	HEPES	6 mM	5.23	7.41	3.66	4.65

The initial separation of the interior and exterior peaks is dependent on the location of the $PrCl_3$; with 6 mM $PrCl_3$ inside the vesicles the peak separation in the first spectrum acquired ($t = 1$ hour after sonication end) is 11.8 ppm, in comparison with 6 mM $PrCl_3$ outside the vesicles the initial peak separation is 10.3 ppm in the spectrum acquired at $t = 0.33$ hours after the end of sonication. The difference in time of spectrum acquisition is a consequence of the wash process required when $PrCl_3$ is encapsulated within the vesicle. Extrapolation of the modelled data to $t = 0$ hours and

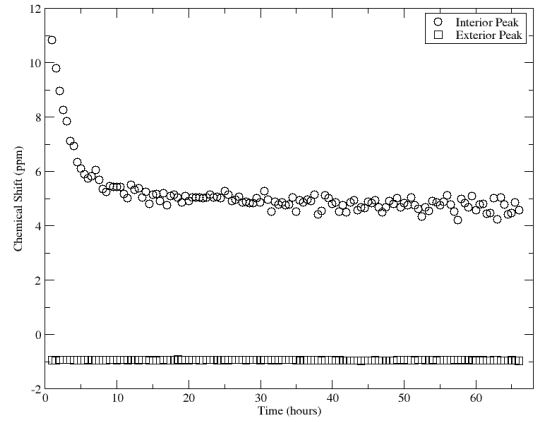

(a) Chemical Shift

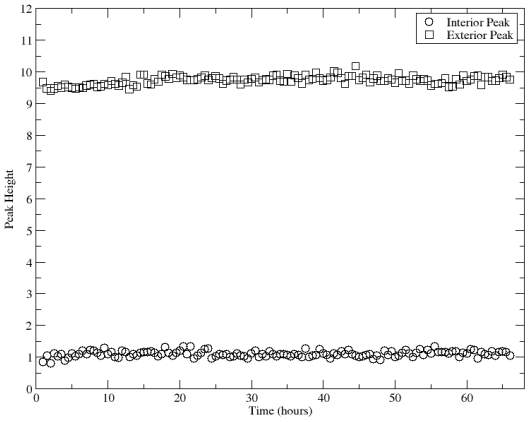

(b) Peak Height

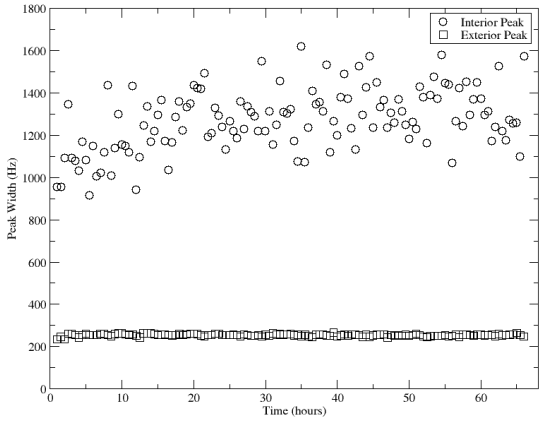

(c) Peak Width

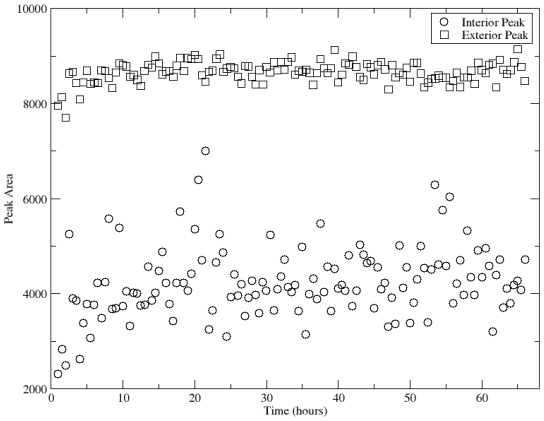

(d) Peak Area

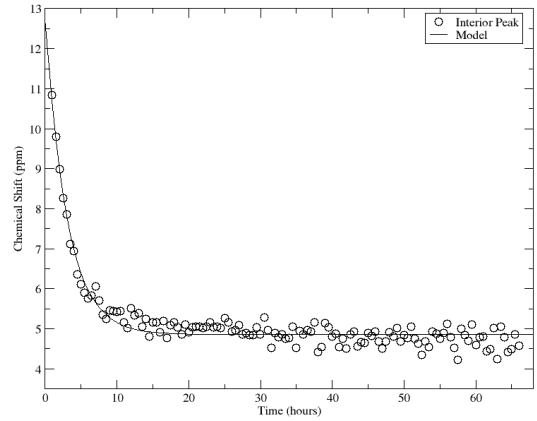

(e) Interior Peak Chemical Shift with Modelling

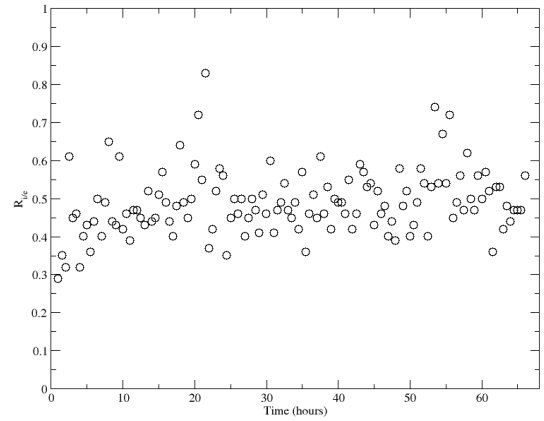

(f) Peak Area Ratio

Figure 5.24: Graphs showing the progression of peak parameters over 66 hours. All graphs show data for both interior and exterior peaks except the graph of peak area ratio(f).

subtraction of the average chemical shift of the unshifted peak gives peak separations of 13.01 ppm and 10.39 ppm for $PrCl_3$ inside and outside respectively. It is clear from this that $PrCl_3$ inside the vesicles causes greater initial peak separation than $PrCl_3$ outside the vesicles.

The peak shifting of the interior peak when $PrCl_3$ is inside the vesicles is much faster than that of the exterior peak when $PrCl_3$ is outside the vesicles. This peak settles to a minimum value within ∼20 hours and shifts by approximately 6 ppm in this time. In comparison, the exterior peak shifting with 6 mM $PrCl_3$ occurs over a range of ∼5 ppm and does not reach the maximum value until ∼150 hours. The difference in peak shifting and the initial peak separation is probably due to differences in effective $PrCl_3$ concentration. The peak area ratio of 0.5 indicates that there are twice as many phospholipid molecules in the exterior leaflet compared to the interior leaflet. With equal concentrations of $PrCl_3$(6 mM) the effective concentration of $PrCl_3$ per mole of POPC for the interior leaflet is double that for the exterior leaflet.

5.3.3 No Shift

Encapsulation of probe molecules, either $PrCl_3$ for NMR studies or calcein for fluorescence studies (to be discussed in Chapter 6), requires removal of excess material from the exterior volume after sonication, as described in Chapter 2. The wash process exchanges the solution outside the vesicles for the solution of the mini-column, in initial experiments the mini-columns were prepared in 0.9 w/v% NaCl (∼154 mM).

Time-resolved studies of these vesicles with buffer inside and NaCl outside were acquired to confirm the stability of 'washed' vesicles. In contrast to the vesicles with buffer both inside and outside, there is no visible shift of the exterior peak. Figure 5.25 shows the spectra of POPC vesicles sonicated in Tris and washed with 150 mM NaCl columns before addition of 3 mM $PrCl_3$ to the exterior volume, acquired over 64 hours. The spectra show no significant shifting of either peak over the course of the experiment, however, peak fitting analysis shows that the exterior peak shifts downfield by about 0.5 ppm over 64 hours, the data from the peak fitting is shown in Figure 5.26. All parameters apart from the chemical shift of the exterior peak remain constant over the course of the experiment, the constant peak area ratio again confirms the stability of these vesicles.

This experiment was repeated several times with either Tris or HEPES buffers in the interior of the vesicles, all experiments showed no significant shift in the exterior or interior peaks when the vesicles contained buffer on the inside and NaCl only on the outside. These experiments are summarised in Table 5.1.

There is also no significant shift of either peak when the vesicles are prepared in 150 mM NaCl only solution, with the $PrCl_3$ on the inside or the outside of the vesicles. Figure 5.27 shows the arrayed spectra of vesicles prepared in 150 mM NaCl with $PrCl_3$ on the outside (a) and inside (b).

Another case where there is no significant shifting of the peaks is when there is $PrCl_3$ both inside and outside the vesicles in the presence of HEPES, the spectra for these vesicles are shown in Figure 5.28. These vesicles were prepared by sonication of POPC in 6 mM $PrCl_3$ + 8 mM HEPES + 80 mM NaCl (the HEPES and NaCl concentrations were reduced by the addition of $PrCl_3$) and acquiring spectra without washing. Results from earlier experiments where $PrCl_3$ was either inside or outside the vesicles suggest that the peaks should shift in opposite directions over time. This shifting does not occur when $PrCl_3$ is both inside and outside the vesicles, suggesting that the peak shifting may be partly caused by the $PrCl_3$ concentration difference between the interior and

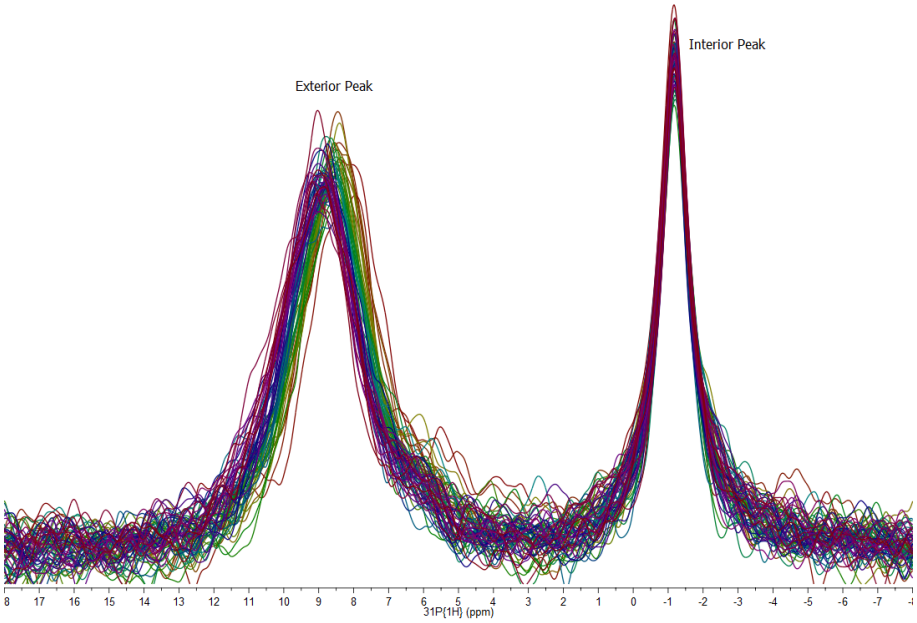

Figure 5.25: Extracts of arrayed ^{31}P spectra of washed POPC vesicles. Vesicles were prepared at 10 mg ml^{-1} in 20 mM Tris-HCl + 150 mM NaCl by sonication for 3 hours at 35°C, vesicles were then washed with Sephadex columns in ∼150 mM NaCl, 3 mM $PrCl_3$ was added to the exterior volume after washing. Spectra were acquired with 256 transients every hour for 64 hours and processed with 100 Hz exponential apodisation.

exterior volumes.

There is a slight difference in the effect of the $PrCl_3$ on the inside and outside of the vesicles, as evidenced by the peak shape in Figure 5.28. Fitting of this peak with two peaks is shown in Figure 5.29, the smaller peak at a higher chemical shift is tentatively assigned to the interior due to its lower peak area. There is also evidence of an additional small peak between the two shown in Figure 5.29, possibly due to another environment for the lipid molecules such as a small micelle or surrounded by the buffer molecules. The parameters from the peak fitting are summarised in Table 5.4, the interior peak has a higher chemical shift and lower peak height, but the peak widths are similar for both peaks. The interior/exterior peak area ratio for the peaks is 0.46, this is comparable to previous samples and confirms the assignment of the peaks shown in Figure 5.29.

Table 5.4: Peak Fitting Parameters for POPC Vesicles with $PrCl_3$ Inside and Outside

Peak	Chemical Shift (ppm)	Peak Height	Peak Width (Hz)	Peak Area	Peak Area Ratio
Interior	14.31	1.54	1009	5439	0.46
Exterior	10.01	3.23	1100	11830	

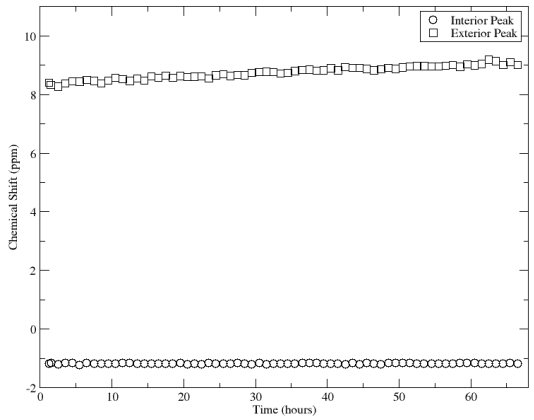

(a) Chemical Shift

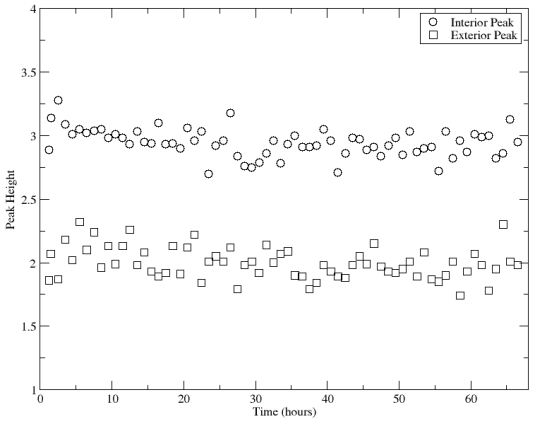

(b) Peak Height

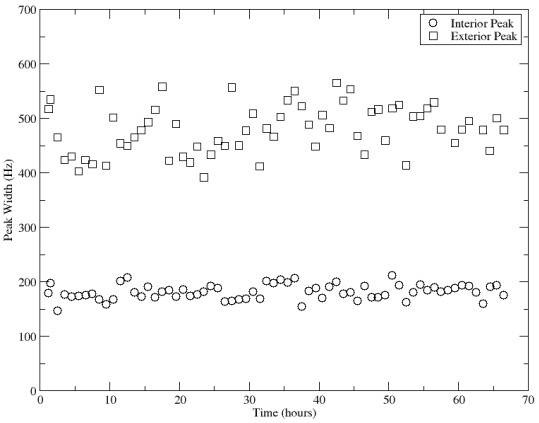

(c) Peak Width

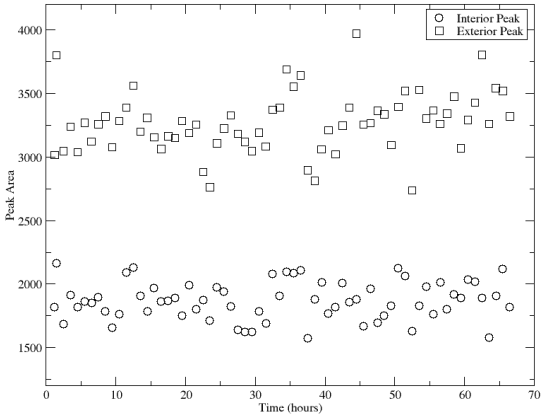

(d) Peak Area

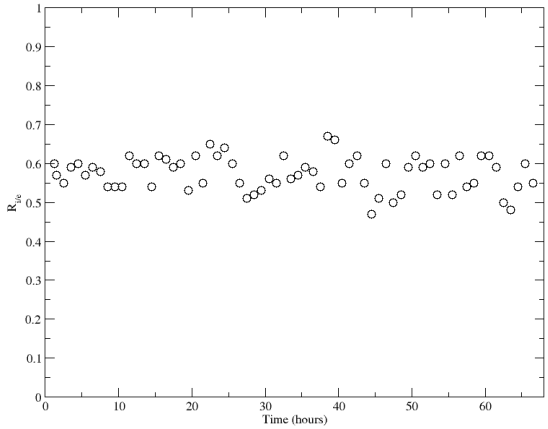

(e) Peak Area Ratio

Figure 5.26: Graphs showing the progression of peak parameters for washed POPC vesicles over 66.5 hours. All graphs show data for both interior and exterior peaks, except the graph of peak area ratio(e).

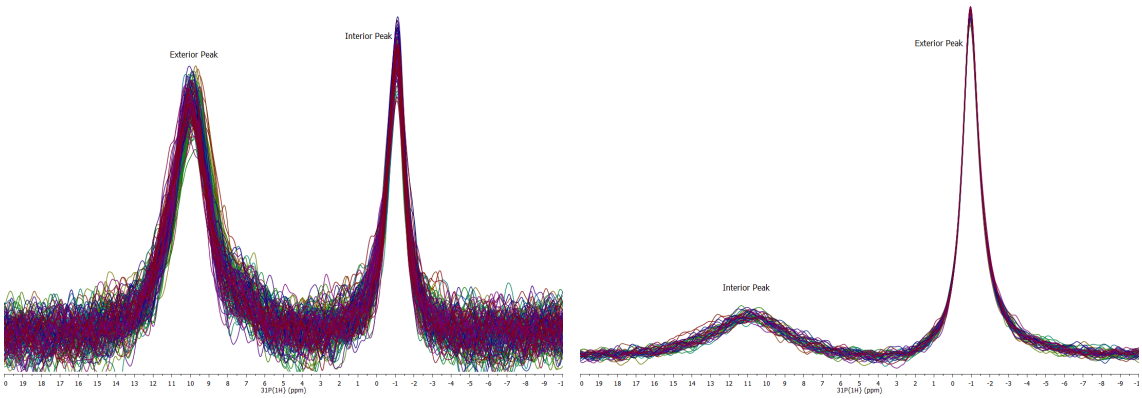

(a) $PrCl_3$ Outside (b) $PrCl_3$ Inside

Figure 5.27: Extracts of arrayed ^{31}P spectra of vesicles prepared in 150 mM NaCl which show no peak shifting. a) 10 mg ml^{-1} POPC vesicles sonicated in 150 mM NaCl (3 hours at 35°C), 3mM $PrCl_3$ added to exterior volume after sonication. Spectra acquired with 128 transients every 30 minutes for 67 hours. b) 20 mg ml^{-1} POPC vesicles sonicated in 3 mM $PrCl_3$ + 150 mM NaCl (3 hours at 35°C), exterior $PrCl_3$ removed by washing with Sephadex columns in 150 mM NaCl. Spectra acquired with 512 transients every 30 minutes for 19 hours.

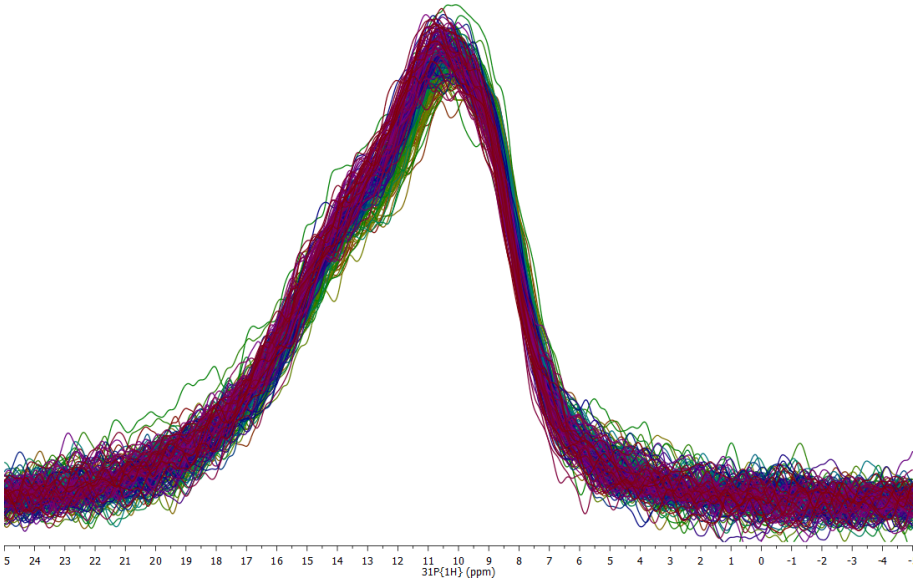

Figure 5.28: Extracts of arrayed ^{31}P spectra of POPC vesicles with $PrCl_3$ both inside and outside the vesicles. Vesicles were prepared by sonication of 20 mg ml^{-1} POPC in 6 mM $PrCl_3$, 10 mM HEPES + 150 mM NaCl for 3 hours at 35°C. Spectra were acquired with 512 transients every 30 minutes for 88 hours and processed with 100 Hz exponential apodisation.

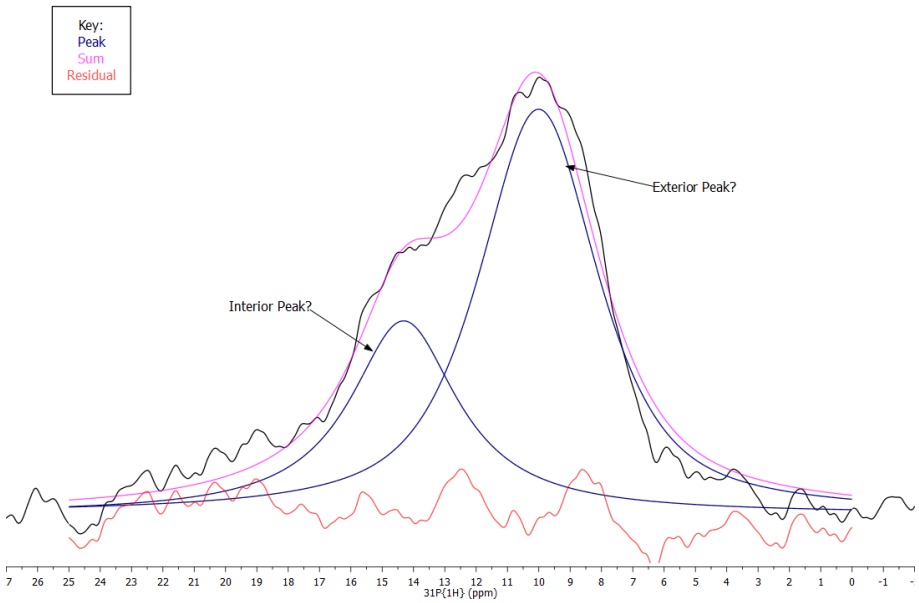

Figure 5.29: Peak fitting of 1st spectrum of POPC vesicles with $PrCl_3$ inside and outside. The peak fitting has three components shown on the spectrum with the following colour coding: Fitted Peaks, Sum of Peaks, Residual of Fit.

5.3.4 Conclusions

Several conclusions can be drawn regarding the cause of the shifting of the ^{31}P peak.

Firstly, significant peak shifting only occurs when the $PrCl_3$ is in contact with buffer molecules. No significant shifting is observed when the buffer is replaced with NaCl solutions. This indicates that the buffer is part of the cause of the shifting, however, the magnitude of peak shifting is not significantly affected by the choice of buffer.

Secondly, the direction of peak shifting depends on the location of the $PrCl_3$. When $PrCl_3$ is outside the vesicles the exterior peak shifts downfield. When $PrCl_3$ is inside the vesicles the interior peak shifts upfield. This difference could be a consequence of the different curvatures of the leaflets.

The magnitude of the peak shifting is affected by the concentration of the $PrCl_3$, higher concentrations of $PrCl_3$ cause greater initial peak separation and greater peak shifting.

Finally, no shifting of the peaks occurs when $PrCl_3$ is both inside and outside the vesicles, suggesting that the shifting is caused in part by the difference in $PrCl_3$ concentration between the interior and exterior volumes.

From this it is clear that several factors contribute to causing the peak shift, further investigation is therefore warranted.

5.4 Solubilisation with Detergent

Detergents such as Triton X-100[i] and SDS[ii] are known to cause the lysing of vesicles through insertion of detergent molecules into the bilayer followed by formation of mixed micelles.[300,301] Solubilisation of vesicles by detergent is a useful model for membrane permeation (positive control) and has been studied extensively.[302–304]

A sample of POPC vesicles (10 mg ml^{-1} in Tris) were prepared with 3 mM $PrCl_3$ outside as described previously. Aliquots of 50 mM Triton X-100 were added to the vesicles and several ^{31}P spectra were acquired over a period of 30–40 minutes to monitor changes in the spectra before addition of the next aliquot of Triton. Figure 5.30a shows the spectra acquired for the POPC vesicles with a range of Triton concentrations. The spectra were not significantly affected by the addition of up to 0.88 mM Triton, but increasing Triton concentration from 0.88 mM to 1.46 mM lead to a decrease in interior peak size and slight reduction in peak area ratio (Figure 5.30b). Addition of a further aliquot of Triton to a total concentration of 1.69 mM lead to a further reduction to the interior peak within 10 minutes of addition and a decrease in peak area ratio, these decreasing trends continue over time, the interior peak has completely disappeared after 90 minutes.

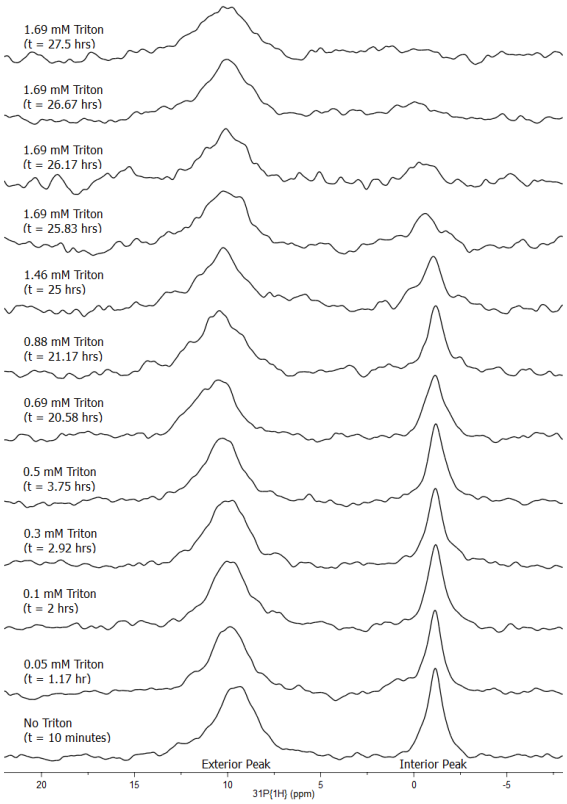

(a) ^{31}P Spectra

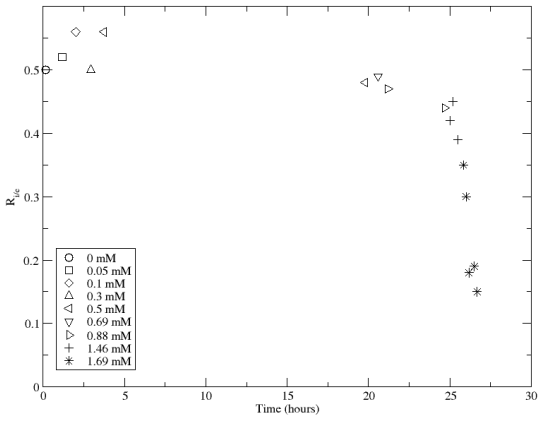

(b) Peak Area Ratio

Figure 5.30: ^{31}P spectra and peak area ratio data for POPC vesicles with 0–1.69 mM Triton. a)Stacked ^{31}P spectra of POPC vesicles with 0–1.69 mM Triton over time. Each spectrum is labelled with the time the spectrum was acquired relative to the end of sonication time. b)Peak Area Ratio from peak fitting of each spectrum.

On further analysis of the peak area ratio, there is a linear decrease after the increase in Triton

[i]Triton X-100 = polyethylene glycol *p*-(1,1,3,3-tetramethylbutyl)-phenyl ether with an average of 9.5 ethylene oxide repeat units

[ii]SDS = Sodium dodecyl sulfate

concentration to 1.46 mM, this is shown in Figure 5.31b. Figure 5.31a shows the spectra acquired for the vesicles with 1.46 and 1.69 mM Triton over the course of time.

The decrease in peak area ratio is an indicator of membrane permeation, as the Triton breaks the bilayer, the $PrCl_3$ on the outside of the vesicles is able to come into contact with some of the interior phospholipids. Linear regression of the peak area data in Figure 5.31b gives the equation $R_{i/e} = -0.19t + 5.2$, where $R_{i/e}$ is the peak area ratio and t is the time of spectrum acquisition measured from the end of sonication. This indicates that once the Triton reaches a suitable concentration, in this case 1.46 mM, the peak area ratio decreases by approximately 0.19 every hour. With a starting value of ~0.5, the vesicles are completely broken apart within 2 hours 40 minutes.

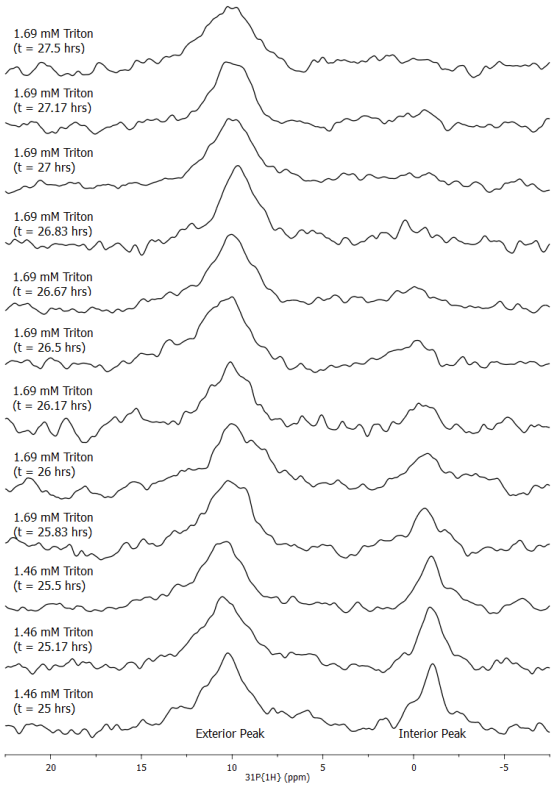

(a) ^{31}P Spectra

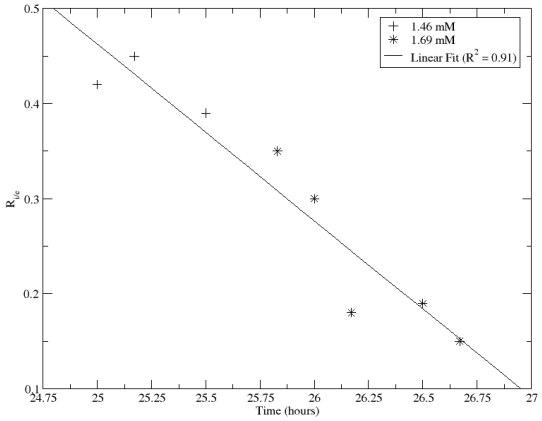

(b) Peak Area Ratio

Figure 5.31: ^{31}P spectra and peak area ratio data for POPC vesicles with 1.46 and 1.69 mM Triton. a)Stacked ^{31}P spectra of POPC vesicles with 1.46 and 1.69 mM Triton over time. Each spectrum is labelled with the concentration of Triton and the time the spectrum was acquired relative to the end of sonication time. b)Peak Area Ratio from peak fitting of each spectrum, this graph is an expansion of Figure 5.30b.

A Triton concentration of 1.46 mM for membrane permeation is consistent with turbidity measurements by Memoli et al.,[305] for sonicated egg PC vesicles they showed that a Triton X-100 concentration of ~1.2 mM was required to form detergent-saturated vesicles with PC concentration of ~13 mM (comparable to 10 mg/ml POPC). From this it can be inferred that the permeation of the membrane, to allow the $PrCl_3$ to come into contact with the interior ^{31}P, occurs once the vesicles are fully saturated with Triton molecules.

A similar study was performed with the $PrCl_3$ on the interior of the vesicles, the spectra acquired with 0–3.70 mM Triton are shown in Figure 5.32. These vesicles were stored for 190 hours after sonication to allow the interior peak to shift to its final position so that the effect of the detergent

was not obscured by the peak shifting caused by the paramagnetic shift reagent.

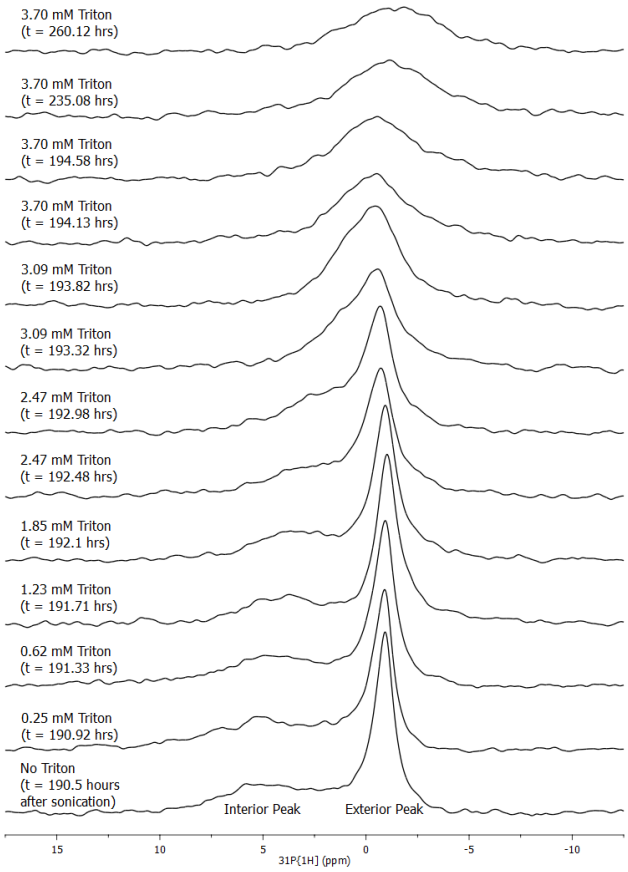

Figure 5.32: Stacked ^{31}P spectra of POPC vesicles with 6 mM $PrCl_3$ inside and 0–3.70 mM Triton. Each spectrum is labelled with the concentration of Triton and the time the spectrum was acquired relative to the end of sonication time.

As permeation occurs the chemical shift of the shifted interior peak decreases and on complete permeation the single observable peak is slightly lower than the exterior peak in the absence of Triton. This is the opposite effect to that observed when the $PrCl_3$ is on the outside where the unshifted interior peak moves towards the shifted exterior peak on membrane permeation and the peak on complete permeation is at the same position as the shifted exterior peak. The differences in these experiments are due to the small encapsulation volume of the vesicles compared to the exterior volume. When $PrCl_3$ is encapsulated inside the vesicles the concentration of the $PrCl_3$ is significantly reduced on membrane permeation such that there is no visible paramagnetic shift effect. In contrast, when $PrCl_3$ is outside the membrane, permeation only decreases the concentration of the shift reagent slightly and therefore causes minimal change to the shifted exterior peak.

Addition of excess Triton (6.52 mM) to the vesicles 66 hours after the concentration was increased to 3.70 mM yielded a sharp peak relating to POPC in lipid-detergent mixed micelles. The small radius of the micelles allows the assembly to tumble more rapidly than the vesicles thus decreasing the linewidth of the peak.[306] This peak occurs at roughly the same chemical shift as the single peak with 3.70 mM, which is also the same chemical shift as exterior peak for the vesicles without Triton. The spectra of POPC vesicles, a) without Triton, b) with 3.70 mM Triton (65 hours after Triton addition) and c) with excess Triton are shown in Figure 5.33

These studies demonstrate the potential utility of this method for monitoring membrane permeation

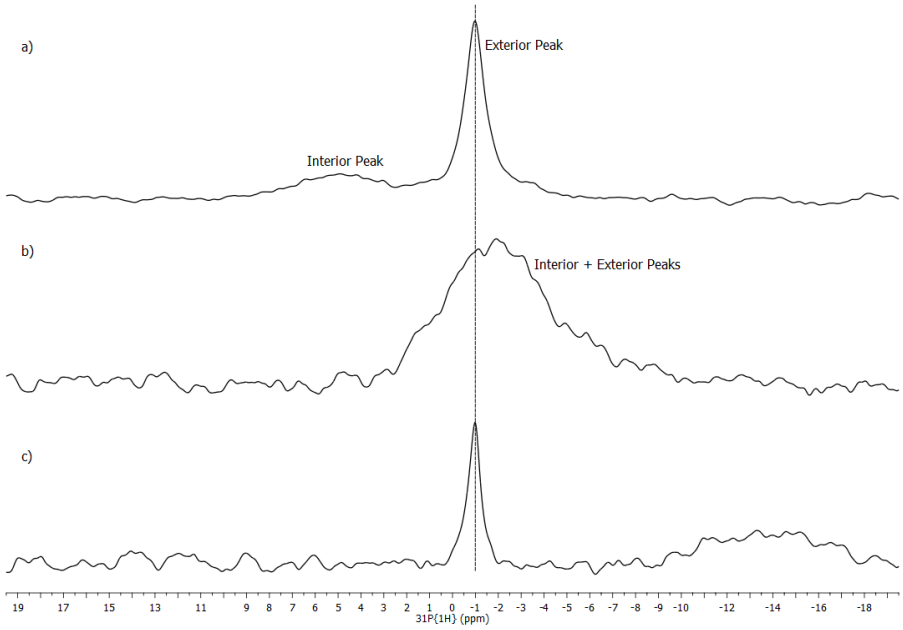

Figure 5.33: Extracts of ^{31}P spectra of POPC vesicles with $PrCl_3$ inside with 0 mM, 3.70 mM and 6.52 mM Triton, a) No Triton, $t = 274.22$ hrs after sonication, b) 3.70 mM Triton, $t = 235.08$ hrs after sonication (65.72 hrs after Triton addition), c) 6.52 mM Triton, $t = 260.12$ hrs after sonication. All spectra were acquired with 512 transients and processed with 100 Hz exponential apodisation, the vertical scales of spectra b) and c) are increased by a factor of three compared to spectrum a). The vertical dashed line shows the alignment of the peaks.

in a time-resolved manner. Lysing the vesicles with the detergent provides a positive control of membrane permeation and shows the effect of membrane permeation on the NMR spectra.

5.5 Conclusions

In this chapter the ideal conditions for phospholipid vesicle experiments have been identified for use in membrane permeation studies. The ideal vesicle system was described in Section 5.1.1; briefly, for optimum results the vesicles should be small, to give best resolution of the separate peaks on addition of paramagnetic shift reagent, the vesicles should also be stable in the absence of permeating additives. Sonicated vesicles are smaller than those formed by extrusion and therefore produce sharper peaks with better resolution on addition of $PrCl_3$. Vesicles formed of POPC demonstrate better stability than DMPC vesicles and are therefore the preferred system for ongoing studies. It was also shown that the peak area ratio can be used to gain an estimate of the membrane thickness and therefore an indication of the size and structure of the vesicle.

Time-resolved stability studies of POPC vesicles showed an unexpected movement of the paramagnetically shifted peak over time. The direction of movement depends on the environment of the shift reagent. When $PrCl_3$ is added to the exterior volume the shifted peak belongs to phospholipids on the exterior leaflet, this peak moves downfield over time with an exponential trend described by a single exponential. When $PrCl_3$ is encapsulated within the vesicles the shifted peak belongs to the interior leaflet, this peak undergoes an upfield shift. The peak movement occurs when the vesicles are prepared in buffer solutions (either Tris or HEPES), it does not occur when the vesicles are prepared in 150 mM NaCl solutions or when the buffer is removed from the exterior volume of the vesicles (before $PrCl_3$ addition), this suggests that the peak movement is caused by the presence

of the buffer molecules, possibly through competing interactions between the shift reagent and the buffer molecules. No peak movement happens when the $PrCl_3$ is both inside and outside the vesicles, suggesting that a concentration difference between the interior and exterior volumes is a partial cause of the peak movement.

Although a full explanation of the cause of the peak movement has not been found, the shift has been sufficiently characterised such that these vesicles can be utilised in membrane permeation studies with potentially cytotoxic additives. A study of vesicle permeation in the presence of Aβ will be discussed in Chapter 6.

Chapter 6

Interaction of Amyloid Aggregates with Phospholipid Vesicles

Membrane permeation studies have frequently been carried out using fluorescence spectroscopy to monitor leakage of a fluorescent molecule such as calcein.[262,263,307] In these studies the fluorescent dye is encapsulated within the vesicles at a self-quenching concentration, the molecules are too large to traverse the membrane so there is minimal change in fluorescence as long as the vesicles are stable. When membrane permeation occurs, either through instability or the effect of additives, the fluorescent molecules leak out and the effective concentration is reduced leading to an increase in fluorescence.

A study by Williams et al. used the fluorescence experiment to show that the oligomeric species of Aβ cause membrane permeation.[169] Several other *in vitro* studies have demonstrated the membrane disrupting properties of Aβ oligomers[308,309] using several methods, including monitoring membrane conductivity[310] and Ca^{2+}-dependent fluorescence.[311] There have also been several *in vivo* studies indicating that Aβ oligomers inhibit hippocampal long-term potentiation,[312,313] which is linked to learning and memory.[314]

The aim of the experiments in this work was to replicate the results shown by Williams et al. using NMR, which has the potential to yield additional structural information about the membrane permeation process. This is achieved through direct observation of the membrane rather than using a probe molecule like the fluorescent dye.

Chapter 5 detailed the optimisation of a phospholipid system for use in NMR analysis. There are several differences between this system and the one used for fluorescence experiments by Williams et al. The first alteration to the system was the size of the vesicles. The fluorescence measurements used large unilamellar vesicles (~100 nm diameter) formed by extrusion, these vesicles have the advantage of a large encapsulation volume for the fluorescent probe molecule. Smaller vesicles were required for NMR in order to obtain sharp peaks. Extrusion was shown to be an unsuitable method for the formation of small unilamellar vesicles (SUVs), vesicles prepared by extrusion through 50 nm polycarbonate membranes had an average diameter of ~81 nm by DLS and the NMR spectra appeared as broad peaks both with and without $PrCl_3$. Sonication was found to be the preferable method for the formation of SUVs, producing vesicles with an average diameter of 35 nm with ^{31}P NMR spectra appearing as a single sharp peak in the absence of $PrCl_3$ and two well resolved peaks on addition of $PrCl_3$ to the exterior volume of the vesicles. Another alteration to the vesicle system

was the composition of the vesicles, Williams et al. used vesicles composed of DMPC, cholesterol and GM1 (a monosialoganglioside) in a ratio of 68:30:2. In Chapter 5 it was demonstrated that 100% DMPC vesicles were unstable, the separation of the interior and exterior peaks facilitated by the $PrCl_3$ shift decreased over ∼33 hours such that the peaks had similar chemical shifts indicating membrane disintegration and re-distribution of the shift reagent throughout the sample. Vesicles formed of POPC were shown to be more stable than DMPC vesicles, with a constant peak area ratio indicating no membrane disintegration. The incorporation of cholesterol in the vesicles was also found to be a problem due to increased line broadening which lead to reduced sensitivity of the peaks. The optimised system for NMR was therefore found to be POPC vesicles in 10 mM HEPES + 100 mM NaCl, sonicated at concentrations of 10–20 mg ml^{-1}.

In this chapter the results of fluorescence experiments performed on POPC vesicles are discussed and compared to literature studies and an NMR experiment to monitor membrane permeation caused by Aβ is developed and tested.

6.1 Calcein Leakage Experiments

Fluorescence experiments to monitor membrane permeation were established in 1977 by Weinstein et al.,[315] by encapsulating 6-carboxyfluorescein within small unilamellar lipid vesicles at a self-quenching concentration (200 mM). They demonstrated that when incubated with lympocytes, the vesicles were transferred into the intracellular volume and the fluorescent marker released causing an increase in fluorescence signal due to dequenching. Allen and Cleland[307] replaced the 6-carboxyfluorescein with calcein in studies of liposome leakage induced by serum. Calcein (Figure 6.1) is a preferable fluorescent probe molecule because the fluorescence is less pH dependent than 6-carboxyfluorescein.[307] Studies of the release of fluorescent probe molecules have since been prevalent in many aspects of liposome permeability,[128] such as membrane fusion,[316] liposome stability[317] and membrane destabilisation by proteins.[318]

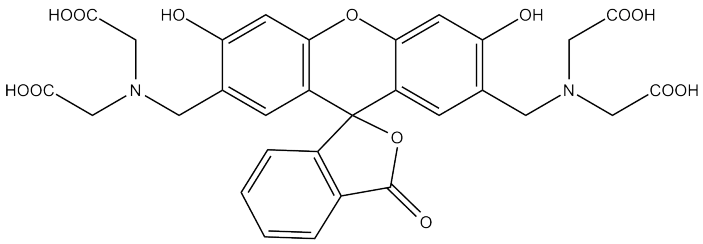

Figure 6.1: Structure of calcein

Membrane permeation can be quantified by comparing the fluorescence at a given time with that of vesicles lysed with excess Triton X-100, the equation for this calculation is given in Equation 6.1.[128]

$$\%\ Calcein\ Release = \frac{(I_t - I_0)}{(I_\infty - I_0)} \times 100 \tag{6.1}$$

Where I_t is the intensity of the fluorescence at time t, I_0 is the fluorescence intensity at $t = 0$ and I_∞ is the maximum fluorescence, observed when the vesicles are lysed with Triton X-100.

Vesicles for fluorescence experiments were prepared by sonication of POPC rehydrated with a solution containing 50–200 mM calcein, after sonication the exterior calcein was removed by mini-column washing and the vesicles were diluted with buffer to 0.5 mg ml^{-1} before fluorescence measurements.

Fluorescence experiments were performed with and without Aβ and the % *Calcein Release* calculated for time points up to 100 hours, the data for these experiments are shown in Figure 6.2. The Aβ begins fibrilising whenever it is in solution, the Aβ is therefore added to the vesicles as soon as possible after preparation in order to maintain maximum monomer concentration with minimal initial fibrillisation, on addition of the Aβ to the vesicles the Aβ continues to aggregate into fibrils. For the sample with Aβ the $t = 0$ measurement was acquired before the addition of Aβ, the first measurement shown in Figure 6.2 relates to $t_{A\beta} = 0$ and shows an immediate increase in fluorescence (and therefore calcein release) compared to the vesicles without Aβ.

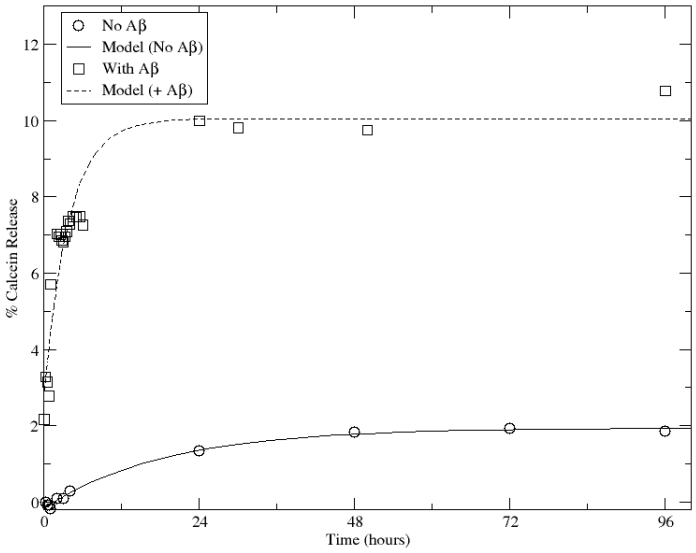

Figure 6.2: Results of fluorescence experiments of POPC vesicles with and without Aβ.

The fluorescence data was modelled with a single exponential function (Equation 6.2), the models are included in Figure 6.2 and the parameters obtained are detailed in Table 6.1.

$$\%\ Calcein\ Release = A(1 - \exp(-t/T)) + \%C_0 \tag{6.2}$$

Where A is the magnitude of the increase in % *Calcein Release*, T is the time constant which is the time for % *Calcein Release* to reach half of the maximum value and $\%C_0$ is the % *Calcein Release* at $t = 0$ (or $t_{A\beta} = 0$ for the sample with Aβ).

Table 6.1: Parameter of Exponential Fitting of Fluorescence Data

Sample	A	T (hours)	$\%C_0$
No Aβ	2.10	18.8	-0.154
+ Aβ	7.28	3.82	2.77

The higher A value for the sample with Aβ shows that more calcein leakage occurs in the presence of Aβ, this can only be caused by permeation of the membrane allowing additional calcein to be released. The low T value indicates that calcein release is much faster in the presence of Aβ, this is consistent with the small oligomers causing the most membrane permeation. The negative $\%C_0$ value for the sample without Aβ is due to slightly decreased fluorescence in the first few time points compared to the $t = 0$ measurement. These results clearly show, both qualitatively and

quantitatively, that significantly more leakage occurs in the presence of Aβ and that most of the membrane permeation occurs within the first 24 hours, this is consistent with the results shown by Williams et al. for 100 nm DMPC vesicles.

Pre-incubation of the Aβ before addition to the vesicles resulted in a reduction in membrane permeation of these vesicles, as shown in Figure 6.3. These experiments were performed by Dr Tom Williams at Drexel University, Philadelphia with sonicated POPC vesicles containing 200 mM calcein diluted to 0.5 mg ml^{-1} before addition of 10 μM Aβ. The Aβ was incubated for 0–52 hours before addition to the vesicles; during incubation aggregation of the Aβ occurs, the decrease in normalised fluorescence for longer incubation times indicates a reduction in membrane permeation caused by the addition of Aβ. The explanation for this decrease in membrane permeation is that the oligomers cause more membrane permeation than the Aβ fibrils. These results are also consistent with those of 100 nm DMPC vesicles presented in the literature.[169]

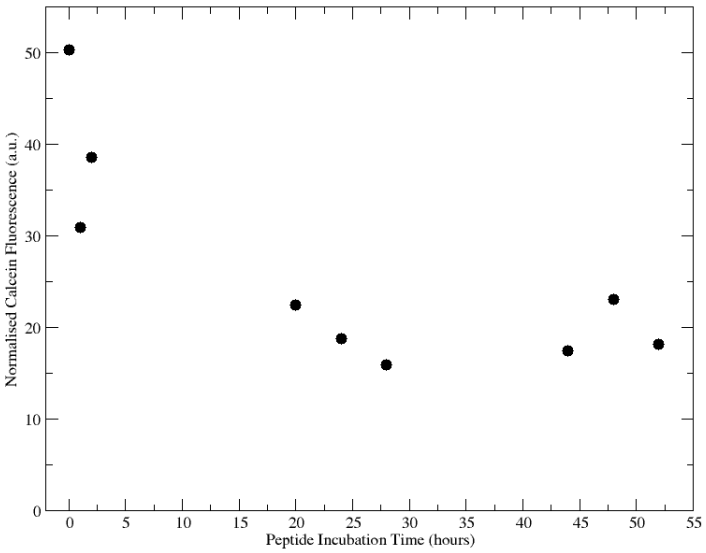

Figure 6.3: Normalised calcein fluorescence from POPC vesicles on addition of Aβ incubated for 0–52 hours. Data from Dr Tom Williams, Drexel University.

All of the fluorescence results shown here are comparable to those presented by Williams et al.[169] The normalised fluorescence data for POPC vesicles without Aβ over 100 hours are similar to those shown for DMPC vesicles, while the data for POPC vesicles with Aβ are slightly lower than those shown by Williams et al., this is probably due to the presence of GM1 in the DMPC vesicles which was shown to increase Aβ membrane permeation compared to DMPC vesicles with cholesterol only.[169] The general trend in normalised fluorescence for POPC vesicles with increasing Aβ incubation times is also comparable to that shown by Williams et al., although differences in actual normalised fluorescence values are likely due to the differences in vesicle composition. The general similarity of these fluorescence results with literature data using DMPC vesicles[169] suggests that the decrease in vesicle size and change of phospholipid do not significantly alter the membrane permeation of the vesicles caused by Aβ. These fluorescence results clearly demonstrate the validity of using small unilamellar POPC vesicles in membrane permeation studies with Aβ.

6.2 ^{31}P NMR Shift Experiments

The fluorescence experiment in the presence of Aβ, shown in Figure 6.2, was acquired in parallel with an NMR study. The amount of Aβ added to the vesicles was calculated such that the Aβ:POPC ratio was comparable in the NMR and fluorescence experiments. In the case of the fluorescence experiments, 6.32 μl of Aβ (192 μM) was added to 120 μl of POPC vesicles (0.5 mg ml^{-1}) in the cuvette, to give a final ratio of 20.2 μM Aβ per mg ml^{-1} of POPC. For the NMR experiments higher POPC concentrations were required in order to provide sufficient sensitivity of the two ^{31}P signals, for this experiment 200 μl of 192 μM Aβ was added to 200 of μl POPC vesicles (10 mg ml^{-1}), after addition of $PrCl_3$ the Aβ:POPC ratio was 19.2μM Aβ per mg ml^{-1} POPC.

^{31}P NMR spectra acquired after the addition of Aβ are shown in Figure 6.4. These vesicles were washed with Sephadex columns prepared in 150 mM NaCl solution in order to remove the calcein not encapsulated within the vesicles, this process also replaced the exterior HEPES buffer with 150 mM NaCl. As shown in chapter 5, vesicles with buffer inside but 150 mM NaCl and $PrCl_3$ outside show minimal downfield shift of the exterior peak, this was observed for the control sample without Aβ, as shown in Figure 6.5. However, the Aβ was prepared in HEPES buffer and addition of this lead to a downfield shift of the exterior peak, as shown in Figure 6.4 and Figure 6.5.

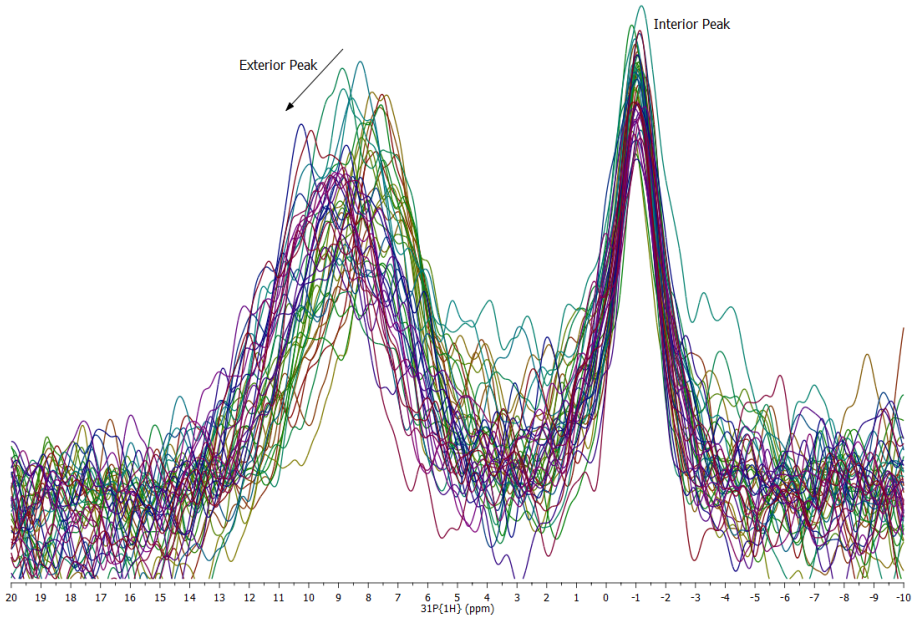

Figure 6.4: Extracts of arrayed ^{31}P spectra of POPC vesicles with calcein inside, Aβ and $PrCl_3$ outside. Spectra were acquired every 15 minutes for the first hour, followed by every half hour up to 21 hours. Spectra were processed with 150 Hz exponential apodisation.

The exterior chemical shift data for the sample with Aβ over an extended time period was modelled with Equation 6.3, as in Chapter 5, the model is included on Figure 6.5 and the parameters obtained are detailed in Table 6.2 along with the parameters for the initial stability study of POPC vesicles with $PrCl_3$ outside.

$$\delta_{ext} = A(1 - \exp(-t/T)) + \delta^0_{ext} \tag{6.3}$$

The values of A and δ^0_{ext} for the vesicles in the presence of Aβ are similar to those obtained for vesicles prepared in HEPES buffer with $PrCl_3$ outside (Chapter 5). The higher T value for the vesicles with Aβ indicates that the downfield shift of the exterior peak occurs more slowly in

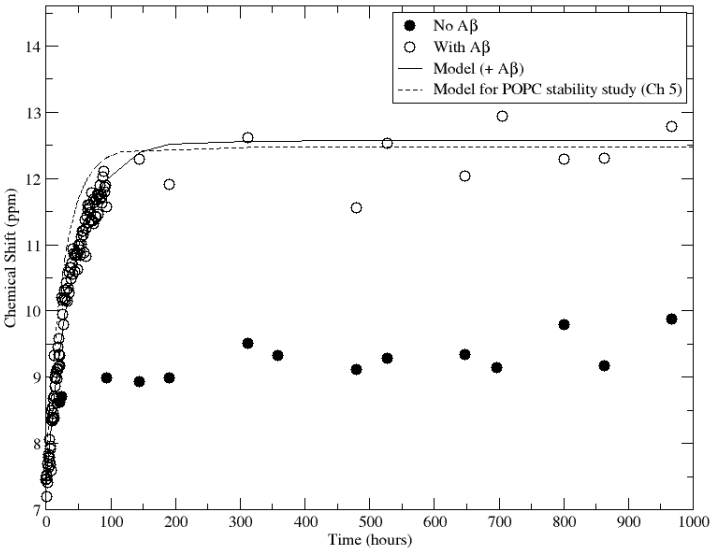

Figure 6.5: Chemical shift of the exterior peak for POPC vesicles with calcein inside and Aβ + $PrCl_3$ outside.

Table 6.2: Upfield Shift Model Fitting Parameters for Samples with and without Aβ

Sample	A (ppm)	T (hours)	δ^0_{ext} (ppm)
+ Aβ	5.20	42.6	7.37
Stability Study (Ch 5)	4.82	27.7	7.66

the presence of Aβ, this could be due to interactions of the $PrCl_3$ with the Aβ, possibly through chelation of the Pr^{3+} through the histidine groups of the Aβ in a similar binding mode to that of Cu^{2+}.[319,320]

Membrane permeation should lead to a decrease in the interior:exterior peak area ratio, however this is not observed in the analysis of this data, the peak area ratio for the first 100 hours of the experiment is shown in Figure 6.6, the data from the control sample is included in this figure to show that there is no significant difference between the sample with and without Aβ. The constant peak area ratio for the vesicles with Aβ indicates that no membrane permeation occurs over the course of this experiment, it also confirms that the downfield shift of the exterior peak is a consequence of the presence of HEPES buffer in the sample, as observed in Chapter 5, rather than membrane permeation.

It is possible that there are interactions between the Aβ and the $PrCl_3$ which reduces the membrane permeating ability of the Aβ. In order to counteract this complication the $PrCl_3$ was encapsulated within the vesicles; studies of these vesicles without the addition of Aβ, detailed in Chapter 5, showed an upfield shift of the interior peak over time but no change in peak area ratio indicating stability of the vesicles.

Considering the structure of calcein (Figure 6.1) it is likely that it will chelate to $PrCl_3$. There are several examples in the literature of calcein acting as a chelating agent for Fe^{3+} [321] and Al^{3+} [322] and the $N(CH_2COOH)_2$ moieties are also seen in EDTA which is known to chelate Pr^{3+}.[267] The presence of calcein with $PrCl_3$ would therefore hinder the paramagnetic shifting effect of the Pr^{3+} on the phosphorus signals of the vesicles. This was confirmed with vesicles prepared in calcein without

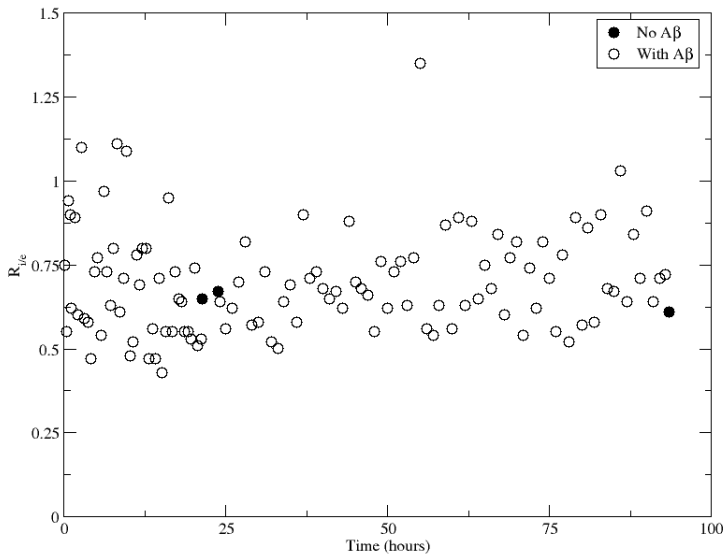

Figure 6.6: Peak area ratio data for POPC vesicles with calcein inside and Aβ + $PrCl_3$ outside

washing, addition of $PrCl_3$ to vesicles with calcein both inside and outside shows no separation of the interior and exterior peaks, as shown in Figure 6.7.

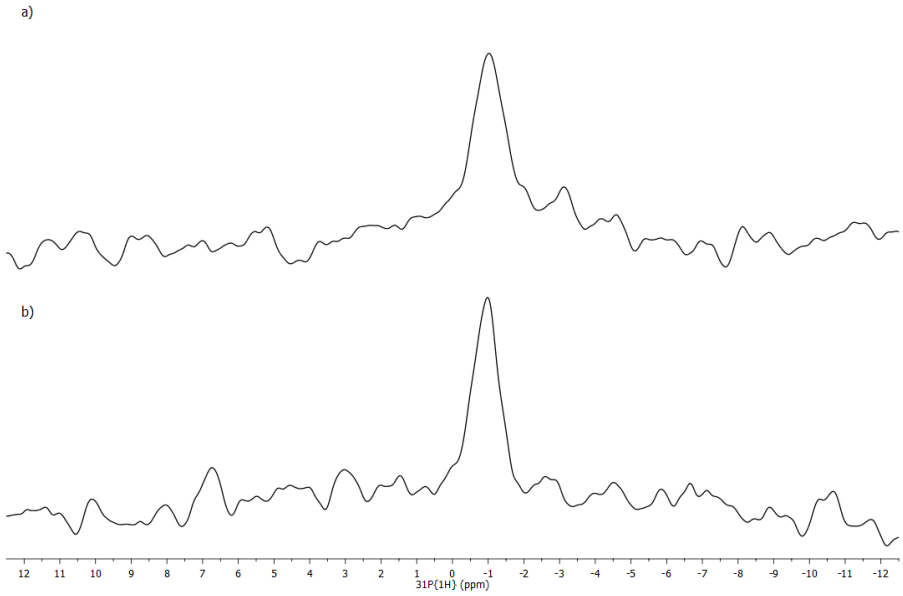

Figure 6.7: Extracts of ^{31}P spectra of POPC vesicles with calcein inside and outside, a) without $PrCl_3$, b) with 3 mM $PrCl_3$.

Ongoing experiments were performed only using NMR without a parallel fluorescence study, the fluorescence experiments showed that the vesicle system is permeated by Aβ, the removal of calcein from the vesicle interior should not affect this so the NMR study should provide similar results to the fluorescence.

An NMR study of membrane permeation by Aβ was performed using vesicles with $PrCl_3$ encapsulated inside (no calcein) and Aβ added to the outside. It was shown in Chapter 5 that when $PrCl_3$ is encapsulated within the vesicles the interior peak undergoes a fast upfield shift before settling within 20 hours, in order to compensate for this vesicles were prepared 24 hours before

Aβ addition. After sonication and washing of 40 mg ml^{-1} POPC vesicles with $PrCl_3$, two 200 μl aliquots were removed from the stock preparation sample, the first aliquot was diluted to 20 mg ml^{-1} with HEPES buffer and NMR spectra were acquired over 24 hours to confirm settling of the interior peak, these spectra are shown in Figure 6.8a. The second aliquot was stored at room temperature for ~24 hours, after which time 200 μl of Aβ (113 μM) was added, giving final concentrations of 20 mg ml^{-1} POPC and 56.5 μM Aβ (Aβ:POPC ratio 2.83 μM per mg ml^{-1}). The Aβ:POPC ratio is lower in this experiment compared to the fluorescence experiment due to concentration restrictions, the concentration of the Aβ was determined by the efficiency of the preparation and a vesicle concentration of 20 mg ml^{-1} was required for sufficient sensitivity of the interior peak. NMR spectra of this sample were acquired every 30 minutes for 66 hours, these spectra are shown in Figure 6.8b.

There appears to be no significant change in the spectra over 66 hours in the presence of Aβ, however, direct comparison of spectra of the two samples indicates that some permeation has occurred. Figure 6.9 shows overlayed spectra of the vesicles with and without Aβ at similar time points, straight after addition of Aβ and after 66 hours with Aβ. These spectra show that after 66 hours in the presence of Aβ the chemical shift of the interior peak is lower, as is the height of the exterior peak.

In stable, intact vesicles the interior volume of the vesicles containing the $PrCl_3$ is isolated from the exterior volume, due to the inability of large molecules, such as Aβ and $PrCl_3$, to traverse the membrane. As a consequence changes to the exterior volume, such as addition of Aβ, should not affect the interior volume unless membrane permeation occurs. In the absence of membrane permeation, the interior ^{31}P peak would be expected to be unaffected by the addition of Aβ. The decrease in chemical shift of the interior peak is therefore indicative of membrane permeation; disruption of the membrane allows $PrCl_3$ to leak out which leads to a decrease in effective concentration of the $PrCl_3$ and therefore a decrease in the chemical shift of the interior peak. This decrease in interior peak chemical shift is similar to that observed when vesicles with $PrCl_3$ inside were lysed with Triton X-100 as shown in Figure 5.32 in Chapter 5.

The peak fitting data, shown in Figure 6.10, includes the data for the vesicle sample without Aβ acquired in the first 24 hours (open circles) and the data for the vesicle sample with Aβ from $t = 24.5$ to $t = 90.55$ (closed circles) as well as data for both samples at extended time points. The peak fitting data show that on addition of Aβ the interior peak shifts upfield by approximately 1.5 ppm and the height of the exterior peak decreases by approximately 2 over 100 hours.

The upfield shift of the interior peaks in both samples can be modelled using the exponential function used in Chapter 5 (Equation 6.4). The parameters obtained from modelling the interior peak chemical shift with Equation 6.4 are shown in Table 6.3, the parameters obtained from the stability study of vesicles with $PrCl_3$ inside are included for comparison.

$$\delta_{int} = A(\exp(-t/T)) + \delta_{int}^{\infty} \tag{6.4}$$

The parameters for the sample without Aβ are comparable to those obtained for vesicles with $PrCl_3$ inside in the previous chapter, as expected for vesicles prepared using the same method. The data for the sample with Aβ was modelled with t replaced by $t_{A\beta}$ (time after Aβ addition) in order to observe the effect of Aβ addition. Comparison of the data for the samples with and without Aβ shows that the upfield shift caused by the addition of Aβ has a smaller magnitude of shift (lower A) and occurs over a longer time period (higher T) than the upfield shift observed in the presence

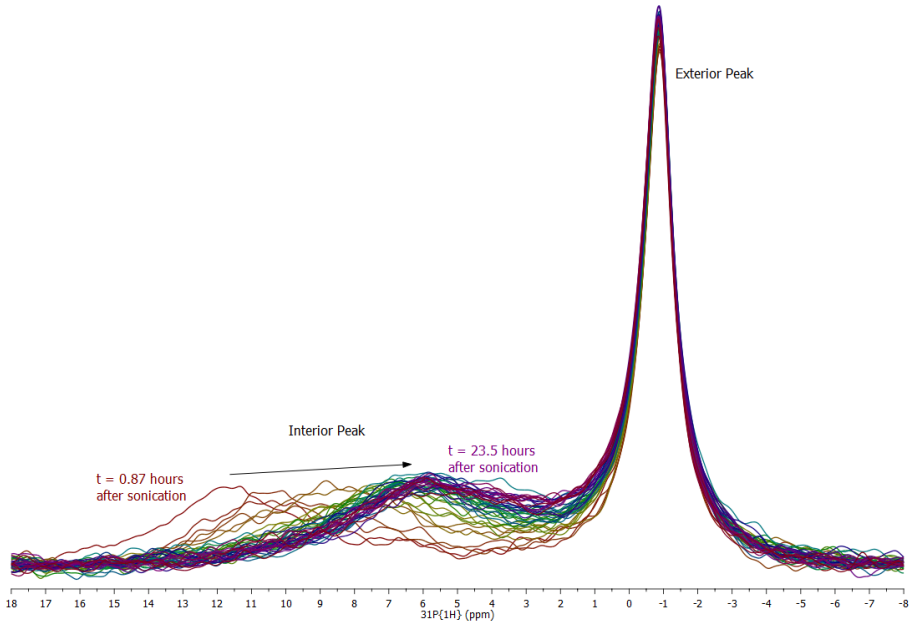

(a) Without Aβ

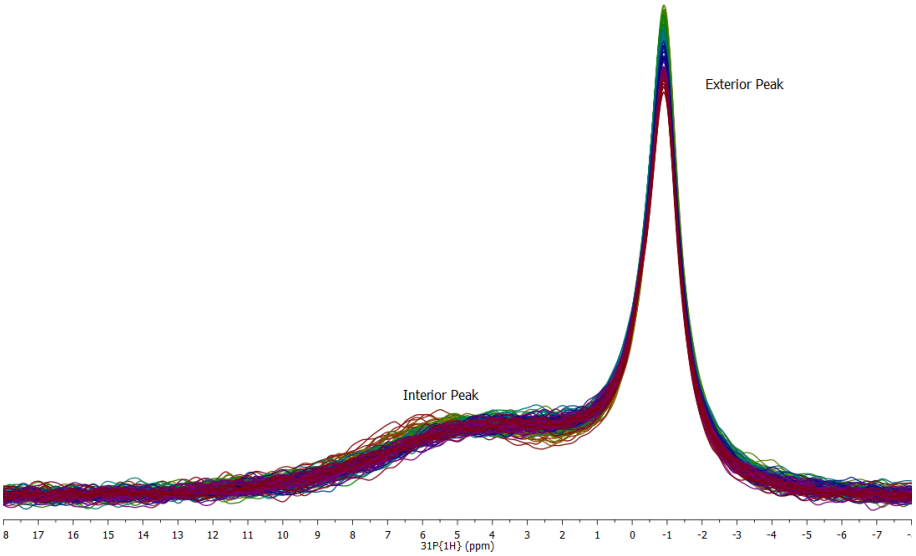

(b) With Aβ

Figure 6.8: Extracts of arrayed ^{31}P spectra of POPC vesicles with $PrCl_3$ inside, a) Vesicles before addition of Aβ, spectra acquired every 30 minutes from $t = 0.87$ hours to $t = 17.87$ and from $t = 19$ to $t = 23.5$ hours after sonication, b) Vesicles with Aβ, spectra acquired every 30 minutes from $t = 24.55$ to $t = 90.55$ hours after sonication ($t_{A\beta} = 0.18 - 66.18$ hours).

Table 6.3: Upfield Shift Model Fitting Parameters for Samples with and without Aβ

Sample	A (ppm)	T (hours)	δ_{int}^{∞} (ppm)
No Aβ	7.38	4.21	5.07
+ Aβ	1.51	10.2	3.71
$PrCl_3$ Inside (Ch 5)	7.41	3.66	4.65

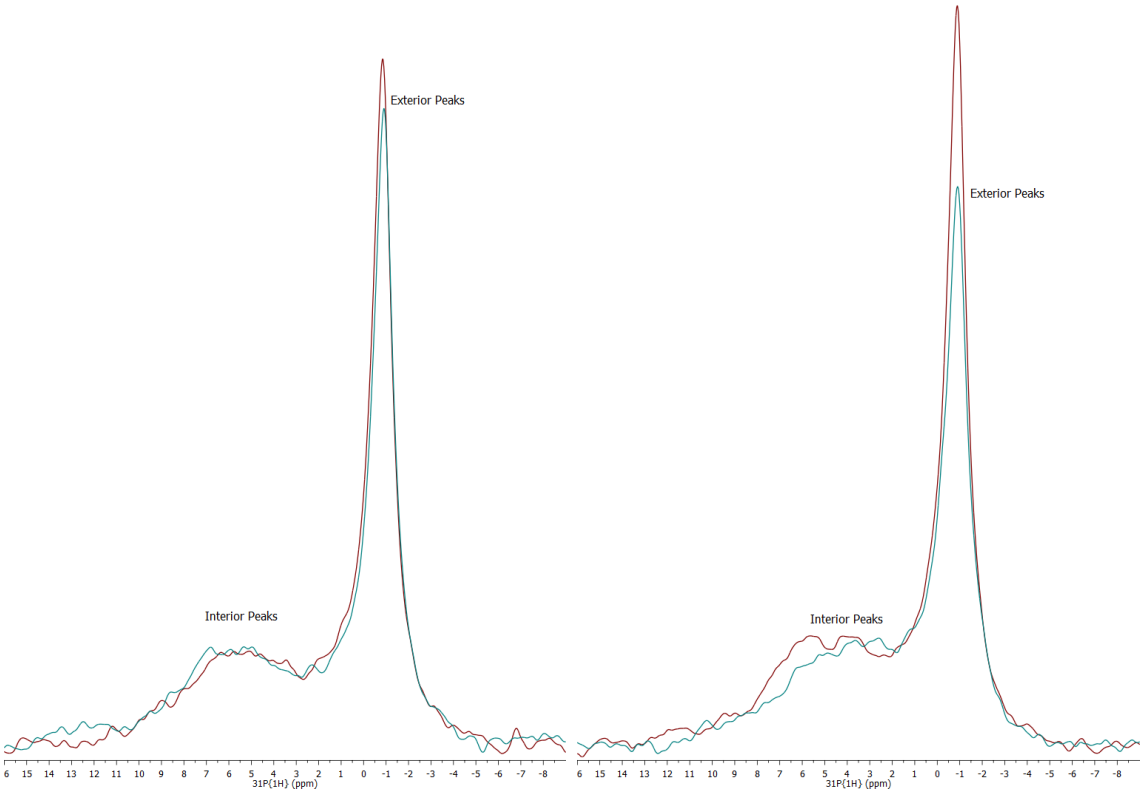

(a) $t \approx 24$ hours ($t_{A\beta} = 0.18$ hours) (b) $t \approx 91$ hours ($t_{A\beta} = 66.18$ hours)

Figure 6.9: Overlayed extracts of ^{31}P spectra of POPC vesicles with $PrCl_3$ inside, with and without Aβ a)Vesicles without Aβ acquired at $t = 23.5$ hours and vesicles with Aβ acquired at $t = 24.55$ hours ($t_{A\beta} = 0.18$ hours) b) Vesicles without Aβ acquired at $t = 91.1$ hours and vesicles with Aβ acquired at $t = 90.55$ hours ($t_{A\beta} = 66.18$ hours)

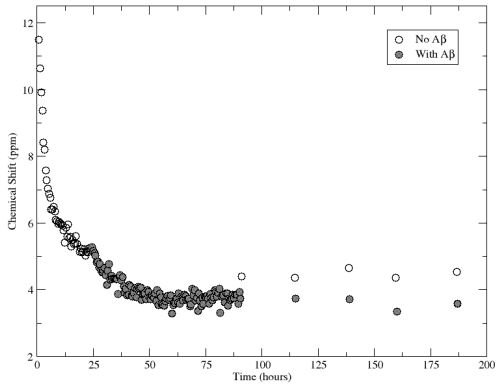

(a) Interior Peak Chemical Shift

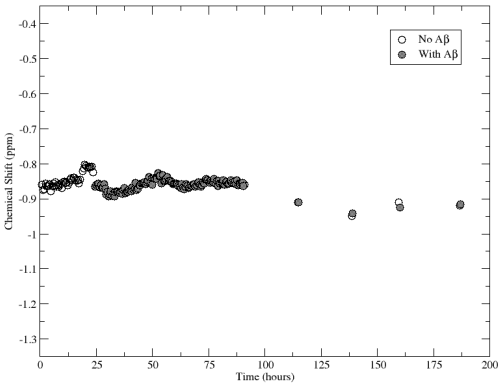

(b) Exterior Peak Chemical Shift

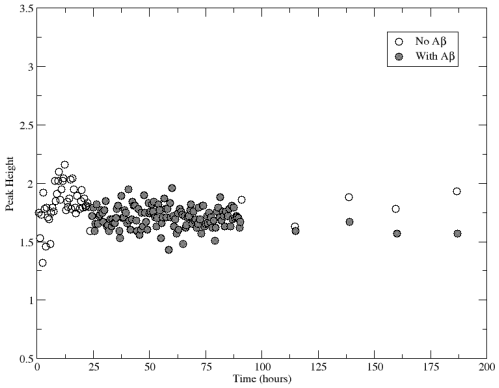

(c) Interior Peak Height

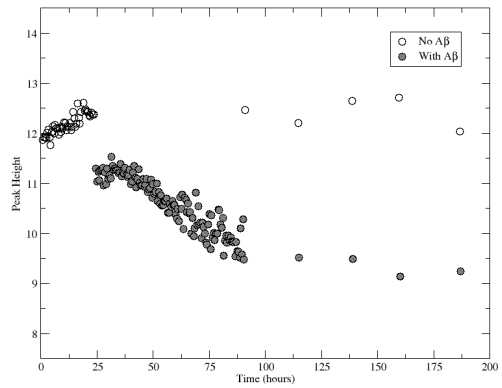

(d) Exterior Peak Height

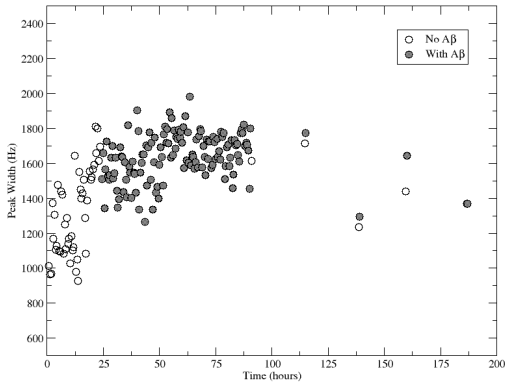

(e) Interior Peak Width

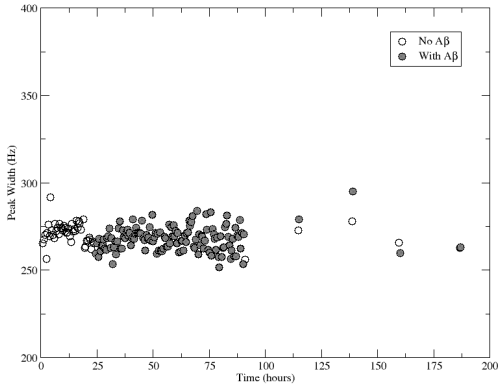

(f) Exterior Peak Width

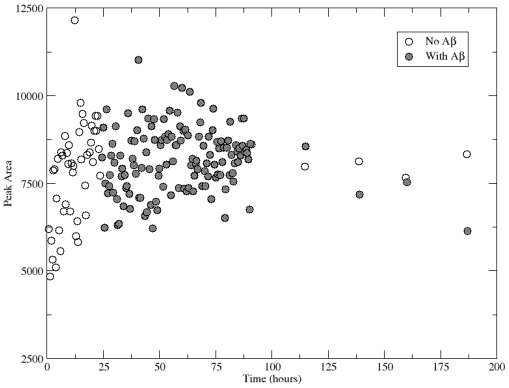

(g) Interior Peak Area

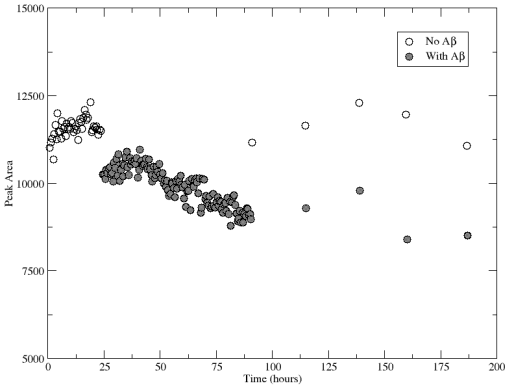

(h) Exterior Peak Area

Figure 6.10: Graphs showing the progression of peak parameters over 300 hours for POPC vesicles with $PrCl_3$ inside, with and without Aβ.

of buffer. The slower upfield shift in the presence of Aβ is most likely due to the additional time taken for membrane permeation to occur and the Pr^{3+} to leak out compared to the changes in Pr^{3+} binding between the buffer and phospholipids involved in the upfield shift observed previously. The lower magnitude of upfield shift with Aβ is indicative of the small amount of membrane permeation caused.

The peak area ratio ($R_{i/e}$) data for the two samples is shown in Figure 6.11. There is an increase in peak area ratio for the sample with Aβ which indicates some change in the distribution of the lipids in the membrane, possibly some membrane permeation. This is consistent with the additional shifting of the interior peak in the presence of Aβ compared to the sample without Aβ. The decrease in chemical shift of the interior peak on addition of Aβ indicates a decrease in effective $PrCl_3$ concentration which occurs when the Pr^{3+} leaks out of the vesicles. The peak area ratio ($R_{i/e}$) values for the spectra shown in Figure 6.9 are given in Table 6.4.

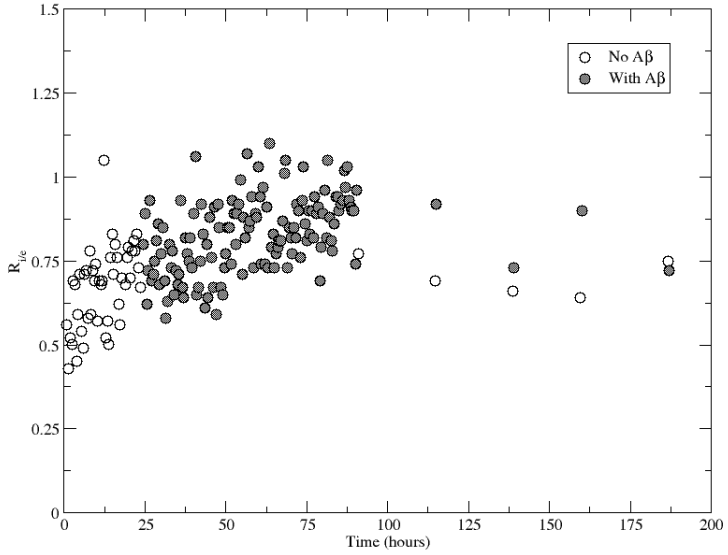

Figure 6.11: Peak area ratios for POPC vesicles with $PrCl_3$ inside, with and without Aβ.

Table 6.4: Peak Area Ratios of Vesicles with and without Aβ

	t (hours)	$t_{A\beta}$ (hours)	$R_{i/e}$
Vesicles without Aβ	23.5	-	0.67
	91.03	-	0.77
Vesicles with Aβ	24.55	0.18	0.80
	90.55	66.18	0.96

The peak area ratio is higher for the vesicles with Aβ at both time points indicating some membrane permeation may have occurred before the acquisition of the first spectrum with Aβ. The increase in $R_{i/e}$ for the vesicles without Aβ suggests some instability of these vesicles, however the increase in $R_{i/e}$ is greater for the vesicles with Aβ over a slightly shorter time period suggesting that the Aβ is the cause of some membrane permeation.

The detergent solubilisation experiments, discussed in Chapter 5.4, showed that when $PrCl_3$ is released from the inside of the vesicles, the decrease in effective $PrCl_3$ concentration leads to a decrease in interior peak chemical shift and peak area and consequently a decrease in $R_{i/e}$. The

increase in peak area ratio in the Aβ experiment suggests that the addition of Aβ caused a change in the distribution of lipids between the interior and exterior leaflets, but not complete disintegration of all of the vesicles. This is consistent with the fluorescence results showing only 10% calcein release on addition of Aβ with a higher Aβ:POPC ratio.

The increase in peak area ratio for the vesicles with Aβ is a consequence of the decrease in exterior peak area (Figure 6.10h), which is mainly caused by the decreased peak height of the exterior peak (Figure 6.10d) as the exterior peak width remains reasonably constant (Figure 6.10f). The corresponding increase in the interior peak area which would be expected if the $PrCl_3$ is released from the vesicles is only slight compared to the decrease in exterior peak area.

The decrease in exterior peak area and the small increase in interior peak area leads to an overall decrease in total peak area. This is most likely due to some precipitation of vesicles, possibly through interactions with the Aβ fibrils. A precipitate was observed in the sample after the 66 hour experiment, the precipitate was removed from the sample by centrifugation at 7000 g. There was little difference in the spectra before and after centrifugation, as shown in Figure 6.12, this indicates that any lipid material involved in the precipitate did not contribute to the spectra.

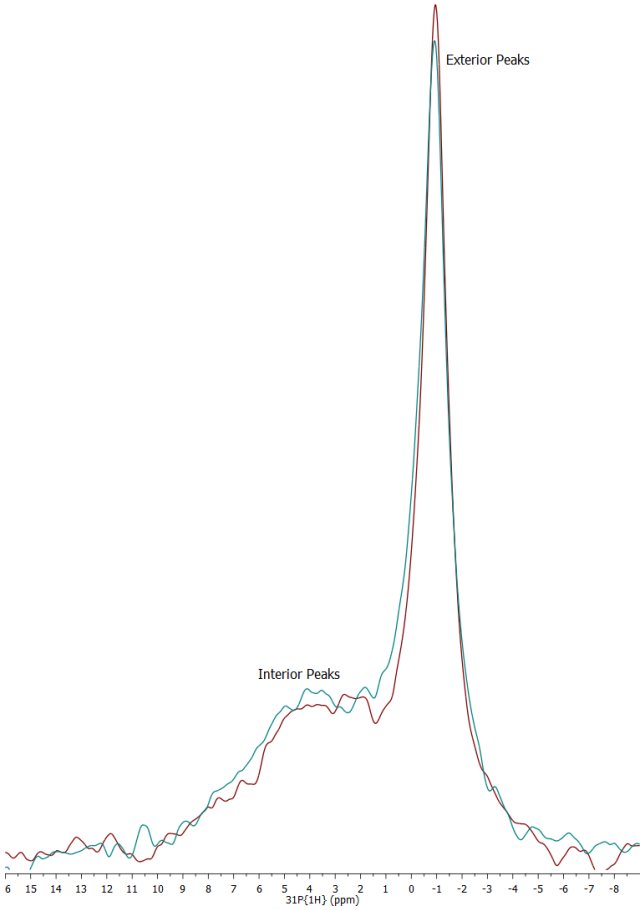

Figure 6.12: Overlayed extracts of ^{31}P of POPC vesicles with $PrCl_3$ inside and Aβ outside, before and after removal of precipitate.

6.2.1 TEM

TEM images of the precipitate were acquired, using uranyl acetate as a negative stain. Transmission electron microscopy utilises an electron beam to produce images with better resolution than light

microscopy. The shorter wavelength of the electron beam compared to light allows smaller objects to be observed. A sample is prepared as a thin layer on a formvar/copper grid as described in Chapter 2.4.4. The electrons are transmitted through the sample and focussed onto a fluorescent screen. Fluorescence occurs when an electron hits the screen, allowing an image of the sample to be viewed. Uranyl acetate is used as a negative stain to provide contrast in the TEM images, uranium is a heavy metal which absorbs electrons better than the carbon, oxygen, hydrogen and nitrogen atoms that make up the sample. Dark areas in the images are stained and light areas typically belong to the sample.

A selection of the images of the precipitate are shown in Figure 6.13, they all show the presence of some aggregation. The images do not look like images in literature of Aβ fibrils, this could be due to the extended period of time before removal of the precipitate from the solution ($\sim$ 11 days) allowing more aggregation to occur. Figures 6.13a, 6.13b and 6.13d show large tangled areas, most likely a mixture of broken vesicles and some amyloid fibrils. Figure 6.13c shows both fibrillar material and spherical components which could be amyloid fibrils interacting with intact vesicles, this image appears similar to images presented by Williams et al. of LUVs with Aβ after 72 hours.[169]

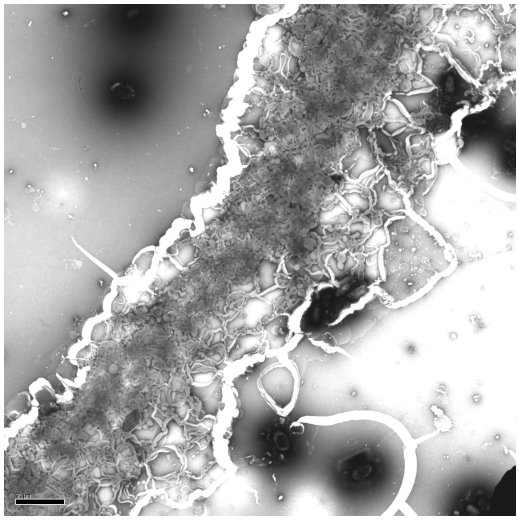

(a) 1000×magnification (bar = 2 μm)

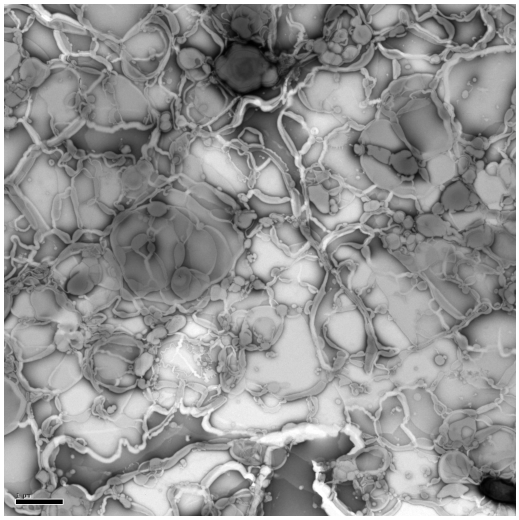

(b) 2000×magnification (bar = 1 μm)

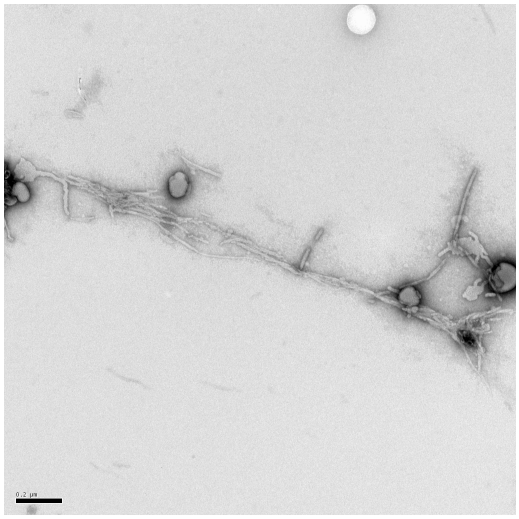

(c) 10000×magnification (bar = 0.2 μm)

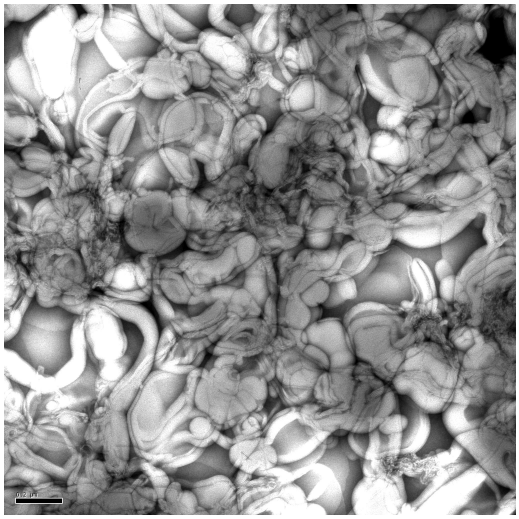

(d) 10000×magnification (bar = 0.2 μm)

Figure 6.13: TEM images of precipitate from POPC vesicles with Aβ

6.2.2 Summary of ^{31}P NMR Results

These results suggest that some membrane permeation of POPC vesicles occurred in the presence of Aβ and it can be monitored through the change in interior peak chemical shift and the increase in peak area ratio. The minimal effect is possibly due to the low Aβ concentration compared to the POPC concentration. Additionally, the fluorescence measurements showed only 10% calcein release with an Aβ:POPC ratio of $\sim$20, with only $\sim$3 μM Aβ per mg ml^{-1} of POPC less membrane permeation is perhaps not surprising.

Further optimisation of this experiment could yield improved results. For example, an increased $PrCl_3$ concentration would increase the separation of the interior and exterior peaks, better resolution of these peaks may improve the peak fitting analysis and therefore give a more accurate peak area ratio with which to observe membrane permeation. An increased Aβ concentration relative to the POPC concentration would cause more significant membrane permeation which would make the observed differences between the samples with and without Aβ more pronounced.

6.3 Conclusions

In this chapter fluorescence and NMR experiments were performed to monitor membrane permeation caused by Aβ on POPC vesicles. The fluorescence results confirmed the compatibility of small POPC vesicles ($\sim$30 nm) for use in membrane permeation studies, with results obtained in agreement with published results of 100 nm DMPC vesicles.[169]

Transferring the studies to NMR, it was hoped they would provide additional structural information about the mechanism of membrane permeation. Several complications arose in the implementation of the NMR method, firstly potential interactions between the Aβ and the paramagnetic shift reagent required the separation of these components. Parallel studies using fluorescence and NMR were not possible due to the chelation of the Pr^{3+} ions by the calcein which prevented the paramagnetic shift of the phosphorus signals. Finally, a compromise of the relative concentrations of the Aβ and POPC was required for observable membrane permeation and sufficient ^{31}P signal sensitivity.

These experiments showed some membrane permeation through changes to the interior peak chemical shift and the peak area ratio, however the effect was small and no significant conclusions could be drawn regarding the mechanism of permeation. Further optimisation of the experimental conditions may improve the results, and could provide the basis for ongoing research.

Chapter 7

Conclusions and Future Work

In this final chapter I will briefly summarise the conclusions drawn from the experiments presented in this thesis and discuss the potential future work.

7.1 Diffusion NMR Experiments

In Chapter 3 it was shown that the addition of a size-exclusion chromatographic stationary phase altered the diffusion profiles of a series of polymers, including a range of low polydispersity molecular weight standards. The change in the observed diffusion coefficient was dependent on the size of the polymer, consistent with size-exclusion effects.

On addition of the stationary phase the polymer equilibrates between the free solution and the interior volume of pores. The volume inside the pores accessible to the polymer is dependent on the size of the polymer and the fractionation range (and pore size) of the stationary phase. The observed diffusion coefficient in the presence of the stationary phase is a weighted average of the 'free' and 'in pore' polymers. The diffusion coefficients of the individual components cannot be resolved due to the significant peak overlap. The comparison of stationary phases indicated that, as with size-exclusion chromatography, the selection of the most suitable stationary phase is an important consideration in SEC-DOSY. The fractionation range of the stationary phase should cover the range of molecular sizes under investigation without greatly exceeding the size of the largest molecule.

Further work on the SEC-DOSY development should involve a thorough investigation of the polymer mixture studies. The possible presence of interactions between the charged polymers and the stationary phase were a complicating factor in this study. The selection of a more suitable solvent may solve this issue, for example a solvent with a higher ionic strength may improve the results by screening the polymer-stationary phase interactions and completely remove any chain expansion effects on the size of the polyelectrolytes. Improving the understanding of the nature of the interactions between the polymers and the stationary phase is another important aspect in these studies. Additional improvements to the research could also be gained by the use of higher gradient strengths which would provide access to smaller diffusion coefficients.

In Chapter 4 the SEC-DOSY method developed in Chapter 3 was applied to two aggregate systems, the small $\pi - \pi$ stacking dye molecule, sunset yellow and insulin, an amyloid fibril forming protein.

The addition of a stationary phase to isotropic solutions of sunset yellow allowed the observation of separate peaks for the 'in pore' and 'free' environments. The resolution of these peaks in both the ^{1}H and diffusion domain was dependent on the fractionation range of the stationary phase. The pore size of the stationary phase governs the maximum aggregate size with access to the 'in pore' volume and therefore the difference in chemical shift and diffusion coefficient between the 'in pore' and 'free' aggregates. This investigation provided useful information about the concentration dependent distribution of aggregates in isotropic solutions of sunset yellow. Ongoing work on the aggregation of sunset yellow within the Day group involves the insertion of small molecule probes within the aggregates to improve modelling of the aggregation process. Further investigation of the application of SEC-DOSY to sunset yellow solutions should focus on the lower end of the concentration range and the possible change over in mode of aggregation around 100 mM.

The application of SEC-DOSY to studies of the time dependent aggregation of insulin showed a decrease in diffusion coefficient on addition of the stationary phase, but no separation of monomeric and aggregate species, most likely due to overlapping peaks. The absence of a partitioning effect in this case may be due to the large size of the insulin molecule in comparison to the pore size of the Sephadex G-50 stationary phase. Stationary phases with larger pores may provide more useful data on the aggregation of insulin and other aggregating proteins.

7.2 Phospholipid Vesicle Experiments

In Chapter 5 the optimum conditions were found for the preparation of phospholipid vesicles for use in membrane permeation studies. These conditions were identified as small unilamellar vesicles prepared by sonication of POPC in a buffered or high ionic strength solvent. Samples prepared using these conditions were used in Chapter 6 to investigate membrane permeation by the amyloid protein Aβ.

Time-resolved studies of the POPC vesicles were used to investigate the stability of the vesicles in the absence of permeating additives. These studies showed an unexpected movement of one of the peaks over time, in addition to the paramagnetic shift produced on addition of the paramagnetic shift reagent, $PrCl_3$. This additional time-dependent peak shifting was investigated through changes in several parameters, such as location of shift reagent, concentration of shift reagent and the solvent inside and outside the vesicles. Several conclusions were drawn from these experiments. For instance, the presence of buffer molecules in the solution with the $PrCl_3$ is required for the peak shifting to occur, suggesting that competing interactions between the buffer and the phospholipid for the shift reagent is part of the cause of the peak shifting. A study with $PrCl_3$ both inside and outside the vesicles showed no peak shifting over time, suggesting that a difference in $PrCl_3$ concentration between the interior and exterior volumes is also a cause of the peak shifting. A full explanation of the time dependent peak shifting was not found during this investigation, future work should involve additional studies into this. Possible aspects to study include the role of the buffer molecules in the cause of the peak shifting. For example, the position of the buffer molecules within the sample could be a factor; the structure of the HEPES molecule shows potential for insertion into the phospholipid membrane, this could be determined using a NOESY experiment which shows correlations between nuclei which are close in space ($\leq$5 Å).

Further NMR studies into membrane permeation by Aβ would require more optimisation of the experimental conditions, such as increasing the Aβ:POPC ratio to increase the amount of membrane permeation and therefore improve observation of the changes caused by addition of Aβ.

Bibliography

[1] G. M. Whitesides, J. P. Mathias and C. T. Seto, *Science*, 1991, **254**, 1312–1319.

[2] M. Stefani and C. M. Dobson, *J. Mol. Med.*, 2003, **81**, 678–699.

[3] D. B. Davies, L. N. Djimant and A. N. Veselkovb, *J. Chem. Soc. Faraday Trans.*, 1996, **92**, 383–390.

[4] T. Asakura and M. Ishida, *J. Colloid Interface Sci.*, 1989, **130**, 184–189.

[5] T. R. Hoare and D. S. Kohane, *Polymer*, 2008, **49**, 1993–2007.

[6] J. Lydon, *Curr. Opin. Colloid Interface Sci.*, 1998, **3**, 458–466.

[7] V. Horowitz, L. Janowitz, A. Modic, P. Heiney and P. Collings, *Phys. Rev. E*, 2005, **72**, 1–10.

[8] M. R. Tomasik and P. J. Collings, *J. Phys. Chem. B*, 2008, **112**, 9883–9889.

[9] B. Neumann, K. Huber and P. Pollmann, *Phys. Chem. Chem. Phys.*, 2000, **2**, 3687–3695.

[10] J. Lydon, in *Handbook of Liquid Crystals*, ed. D. Demus, J. W. Goodby, G. W. Gray, H. W. Spiess and V. Vill, Wiley, e-book edn.

[11] C. A. Hunter and J. K. M. Sanders, *J. Am. Chem. Soc.*, 1990, **112**, 5525–5534.

[12] J. Lydon, *J. Mater. Chem.*, 2010, **20**, 10071–10099.

[13] J. Lydon, *Curr. Opin. Colloid Interface Sci.*, 2004, **8**, 480–490.

[14] Z. Chen, A. Lohr, C. R. Saha-Möller and F. Würthner, *Chem. Soc. Rev.*, 2009, **38**, 564–584.

[15] L. Schmidt-Mende, A. Fechtenkötter, K. Müllen, E. Moons, R. H. Friend and J. D. MacKenzie, *Science*, 2001, **293**, 1119–1122.

[16] J. P. Hill, W. Jin, A. Kosaka, T. Fukushima, H. Ichihara, T. Shimomura, K. Ito, T. Hashizume, N. Ishii and T. Aida, *Science*, 2004, **304**, 1481–1484.

[17] P. J. Collings, A. J. Dickinson and E. C. Smith, *Liq. Cryst.*, 2010, **37**, 701–710.

[18] L. Joshi, S.-W. Kang, D. M. Agra-Kooijman and S. Kumar, *Phys. Rev. E*, 2009, **80**, 1–8.

[19] A. J. Dickinson, N. D. LaRacuente, C. B. McKitterick and P. J. Collings, *Mol. Cryst. Liq. Cryst.*, 2009, **509**, 751–762.

[20] B. Neumann, *Langmuir*, 2001, **17**, 2675–2682.

[21] D. J. Edwards, J. W. Jones, O. Lozman, A. P. Ormerod, M. Sintyureva and G. J. T. Tiddy, *J. Phys. Chem. B*, 2008, **112**, 14628–14636.

[22] J. Jones, L. Lue, A. Ormerod and G. Tiddy, *Liq. Cryst.*, 2010, **37**, 711–722.

[23] M. P. Renshaw and I. J. Day, *J. Phys. Chem. B*, 2010, **114**, 10032–10038.

[24] S. Schreier, S. V. Malheiros and E. de Paula, *Biochim. Biophys. Acta*, 2000, **1508**, 210–234.

[25] Y. V. Frenkel, A. D. Clark, K. Das, Y.-H. Wang, P. J. Lewi, P. A. J. Janssen and E. Arnold, *J. Med. Chem.*, 2005, **48**, 1974–1983.

[26] S. J. Wallace, J. Li, C. R. Rayner, K. Coulthard and R. L. Nation, *Antimicrob. Agents Chemother.*, 2008, **52**, 3047–3051.

[27] S. J. Wallace, J. Li, R. L. Nation, R. J. Prankerd, T. Velkov and B. J. Boyd, *J. Phys. Chem. B*, 2010, **114**, 4836–4840.

[28] B. K. Shoichet, *Drug Discovery Today*, 2006, **11**, 607–615.

[29] C. A. Ross and M. A. Poirier, *Nat. Med.*, 2004, **10**, S10–S17.

[30] M. Sunde, L. C. Serpell, M. Bartlam, P. E. Fraser, M. B. Pepys and C. C. Blake, *J. Mol. Biol.*, 1997, **273**, 729–739.

[31] S. M. Butterfield and H. A. Lashuel, *Angew. Chem., Int. Ed.*, 2010, **49**, 5628–5654.

[32] B. Caughey and P. T. Lansbury, *Annu. Rev. Neurosci.*, 2003, **26**, 267–298.

[33] D. M. Fowler, A. V. Koulov, W. E. Balch and J. W. Kelly, *Trends Biochem. Sci.*, 2007, **32**, 217–224.

[34] W. Pulawski, U. Ghoshdastider, V. Andrisano and S. Filipek, *Appl. Biochem. Biotechnol.*, 2012, **166**, 1626–1643.

[35] V. A. Iconomidou, G. Vriend and S. J. Hamodrakas, *FEBS Lett.*, 2000, **479**, 141–145.

[36] J. M. Kenney, D. Knight, M. J. Wise and F. Vollrath, *Eur. J. Biochem.*, 2002, **269**, 4159–4163.

[37] D. M. Fowler, A. V. Koulov, C. Alory-Jost, M. S. Marks, W. E. Balch and J. W. Kelly, *PLoS Biol.*, 2006, **4**, e6.

[38] I. Cherny and E. Gazit, *Angew. Chem., Int. Ed.*, 2008, **47**, 4062–4069.

[39] M. E. M. Cromwell, E. Hilario and F. Jacobson, *AAPS J.*, 2006, **8**, E572–E579.

[40] E. D. B. Clark, *Curr. Opin. Biotechnol.*, 1998, **9**, 157–163.

[41] L. Nielsen, R. Khurana, A. Coats, S. Frokjaer, J. Brange, S. Vyas, V. N. Uversky and A. L. Fink, *Biochem.*, 2001, **40**, 6036–6046.

[42] J. Khoshnoodi, J.-P. Cartailler, K. Alvares, A. Veis and B. G. Hudson, *J. Biol. Chem.*, 2006, **281**, 38117–38121.

[43] L. Stryer, *Biochemistry*, W. H. Freeman and Company, New York, 4th edn., 1995.

[44] Z. Gaygadzhiev, V. Massel, M. Alexander and M. Corredig, *Food Hydrocolloids*, 2012, **26**, 405–411.

[45] A. Hill, *Cheese Making Technology*, http://www.uoguelph.ca/foodscience/cheese-making-technology, Accessed 4th March 2013.

[46] M. I. Ivanova, S. A. Sievers, M. R. Sawaya, J. S. Wall and D. Eisenberg, *Proc. Natl. Acad. Sci. U. S. A.*, 2009, **106**, 18990–18995.

[47] D. A. Kirschner, C. Abraham and D. J. Selkoe, *Proc. Natl. Acad. Sci. U. S. A.*, 1986, **83**, 503–507.

[48] L. C. Serpell, J. Berriman, R. Jakes, M. Goedert and R. A. Crowther, *Proc. Natl. Acad. Sci. U. S. A.*, 2000, **97**, 4897–4902.

[49] O. N. Antzutkin, J. J. Balbach, R. D. Leapman, N. W. Rizzo, J. Reed and R. Tycko, *Proc. Natl. Acad. Sci. U. S. A.*, 2000, **97**, 13045–13050.

[50] O. Antzutkin, R. Leapman, J. Balbach and R. Tycko, *Biochem.*, 2002, **41**, 15436–15450.

[51] A. T. Petkova, Y. Ishii, J. J. Balbach, O. N. Antzutkin, R. D. Leapman, F. Delaglio and R. Tycko, *Proc. Natl. Acad. Sci. U. S. A.*, 2002, **99**, 16742–16747.

[52] H. Li, F. Rahimi, S. Sinha, P. Maiti, G. Bitan and K. Murakami, in *Encyclopedia of Analytical Chemistry*, John Wiley & Sons, 2009, ch. Amyloids and Protein Aggregation - Analytical Methods.

[53] B. Ranjbar and P. Gill, *Chem. Biol. Drug Des.*, 2009, **74**, 101–120.

[54] C. J. Barrow, A. Yasuda, P. T. M. Kenny and M. G. Zagorski, *J. Mol. Biol.*, 1992, **225**, 1075–1093.

[55] M. Bouchard, J. Zurdo, E. J. Nettleton, C. M. Dobson and C. V. Robinson, *Protein Sci.*, 2000, **9**, 1960–1967.

[56] O. S. Makin and L. C. Serpell, *Biochem. Soc. Trans.*, 2002, 521–525.

[57] C. Goldsbury, J. Kistler, U. Aebi, T. Arvinte and G. J. S. Cooper, *J. Mol. Biol.*, 1999, **285**, 33–39.

[58] H. K. L. Blackley, G. H. W. Sanders, M. C. Davies, C. J. Roberts, S. J. B. Tendler and M. J. Wilkinson, *J. Mol. Biol.*, 2000, **298**, 833–840.

[59] O. N. Antzutkin, *Magn. Reson. Chem.*, 2004, **42**, 231–246.

[60] R. Jansen, W. Dzwolak and R. Winter, *Biophys. J.*, 2005, **88**, 1344–1353.

[61] H. Naiki, K. Higuchi, M. Hosokawa and T. Takeda, *Anal. Biochem.*, 1989, **177**, 244–249.

[62] R. Khurana, C. Coleman, C. Ionescu-Zanetti, S. A. Carter, V. Krishna, R. K. Grover, R. Roy and S. Singh, *J. Struct. Biol.*, 2005, **151**, 229–238.

[63] M. R. H. Krebs, E. H. C. Bromley and A. M. Donald, *J. Struct. Biol.*, 2005, **149**, 30–37.

[64] M. Biancalana and S. Koide, *Biochim. Biophys. Acta*, 2010, **1804**, 1405–1412.

[65] L. Nielsen, S. Frokjaer, J. Brange, V. N. Uversky and A. L. Fink, *Biochem.*, 2001, **40**, 8397–8409.

[66] I. Horvath, C. F. Weise, E. K. Andersson, E. Chorell, M. Sellstedt, C. Bengtsson, A. Olofsson, S. J. Hultgren, M. Chapman, M. Wolf-Watz, F. Almqvist and P. Wittung-Stafshede, *J. Am. Chem. Soc.*, 2012, **134**, 3439–3444.

[67] S. Loveday, X. Wang, M. Rao, S. Anema, L. Creamer and H. Singh, *International Dairy Journal*, 2010, **20**, 571–579.

[68] S. Loveday, X. Wang, M. Rao, S. Anema and H. Singh, *Food Hydrocolloids*, 2012, **27**, 242–249.

[69] F. Chiti and C. M. Dobson, *Annu. Rev. Biochem.*, 2006, **75**, 333–366.

[70] T. Okada, K. Ikeda, M. Wakabayashi, M. Ogawa and K. Matsuzaki, *J. Mol. Biol.*, 2008, **382**, 1066–1074.

[71] E. H. Schacht, *J. Phys. Conf. Ser.*, 2004, **3**, 22–28.

[72] D. Schmaljohann, *Adv. Drug Delivery Rev.*, 2006, **58**, 1655–1670.

[73] D. Buenger, F. Topuz and J. Groll, *Prog. Polym. Sci.*, 2012, **37**, 1678–1719.

[74] C. Yan and D. J. Pochan, *Chem. Soc. Rev.*, 2010, **39**, 3528–3540.

[75] K. Pal, A. K. Banthia and D. K. Majumdar, *Des. Monomers Polym.*, 2009, **12**, 197–220.

[76] B. Rangarajan, L. S. Coons and A. B. Scranton, *Biomaterials*, 1996, **17**, 649–661.

[77] A. M. Mathur and A. B. Scranton, *Biomaterials*, 1996, **17**, 547–557.

[78] E. A. El-hefian and A. H. Yahaya, *Maejo Int. J. Sci. Technol.*, 2010, **4**, 210–220.

[79] K. S. Anseth, C. N. Bowman and L. Brannon-Peppas, *Biomaterials*, 1996, **17**, 1647–1657.

[80] IUPAC, *Compendium of Chemical Terminology*, Blackwell Scientific Publications, 1997, vol. 2.

[81] Y. E. Shapiro, *Prog. Polym. Sci.*, 2011, **36**, 1184–1253.

[82] P. J. Hore, *Nuclear Magnetic Resonance*, Oxford University Press, Oxford, 1995.

[83] M. H. Levitt, *Spin dynamics*, John Wiley & Sons, New York, 2001.

[84] J. Keeler, *Understanding NMR Spectroscopy*, John Wiley & Sons, Chichester, 2005.

[85] I. Bertini, C. Luchinat and G. Parigi, *Solution NMR of Paramagnetic Molecules*, Elsevier, Amsterdam, 2001.

[86] P. J. Hore, J. A. Jones and S. Wimperis, *NMR: The Toolkit*, Oxford University Press, Oxford, 2000.

[87] I. J. Day, *eMagRes*, 2013, **2**, 253–266.

[88] E. L. Hahn, *Phys. Rev.*, 1950, **80**, 580–594.

[89] H. Y. Carr and E. M. Purcell, *Physical Review*, 1954, **94**, 630–638.

[90] E. Stejskal, *J. Chem. Phys.*, 1965, **43**, 3597–3603.

[91] W. S. Price, *Conc. Magn. Res.*, 1997, **9**, 299–336.

[92] W. S. Price, *NMR Studies of Translational Motion*, Cambridge University Press, Cambridge, 2009.

[93] C. S. Johnson Jr., *Prog. Nucl. Magn. Reson. Spectrosc.*, 1999, **34**, 203–256.

[94] D. Burstein, *Conc. Magn. Res.*, 1996, **8**, 269–278.

[95] W. S. Price, *Conc. Magn. Res.*, 1998, **10**, 197–237.

[96] G. Wider, V. Dötsch and K. Wüthrich, *J. Magn. Reson. A*, 1994, **108**, 255–258.

[97] D. Wu, A. Chen and C. S. Johnson Jr., *J. Magn. Reson. A*, 1995, **115**, 260–264.

[98] A. Botana, J. A. Aguilar, M. Nilsson and G. A. Morris, *J. Magn. Reson.*, 2011, **208**, 270–278.

[99] A. Jerschow and N. Müller, *J. Magn. Reson.*, 1997, **125**, 372–375.

[100] M. Nilsson, M. A. Connell, A. L. Davis and G. A. Morris, *Anal. Chem.*, 2006, **78**, 3040–3045.

[101] K. F. Morris and C. S. Johnson Jr., *J. Am. Chem. Soc.*, 1993, **115**, 4291–4299.

[102] P. Stilbs, K. Paulsen and P. C. Griffiths, *J. Phys. Chem.*, 1996, **3654**, 8180–8189.

[103] M. Nilsson and G. A. Morris, *Anal. Chem.*, 2008, **80**, 3777–3782.

[104] W. Windig, *Chemom. Intell. Lab. Syst.*, 1997, **37**, 241–254.

[105] K. Morris and C. S. Johnson Jr., *J. Am. Chem. Soc.*, 1992, **114**, 3139–3141.

[106] H. Barjat, G. A. Morris, S. Smart and A. G. Swanson, *J. Magn. Reson.*, 1995, **108**, 170–172.

[107] M. Nilsson, *J. Magn. Reson.*, 2009, **200**, 296–302.

[108] I. Bertini, M. B. Janik, Y. M. Lee, C. Luchinat and a. Rosato, *J. Am. Chem. Soc.*, 2001, **123**, 4181–8.

[109] I. Bertini, C. Luchinat and G. Parigi, *Prog. Nucl. Magn. Reson. Spectrosc.*, 2002, **40**, 249–273.

[110] G. Otting, *Annu. Rev. Biophys.*, 2010, **39**, 387–405.

[111] R. B. Martin, *Chem. Rev.*, 1996, **96**, 3043–3064.

[112] G. Comellas, L. R. Lemkau, D. H. Zhou, J. M. George and C. M. Rienstra, *J. Am. Chem. Soc.*, 2012, **134**, 5090–5099.

[113] A. S. Altieri, D. P. Hinton and R. A. Byrd, *J. Am. Chem. Soc.*, 1995, **117**, 7566–7567.

[114] A. J. Dingley, J. P. Mackay, B. E. Chapman, M. B. Morris, P. W. Kuchel, B. D. Hambly and G. F. King, *J. Biomol. NMR*, 1995, **6**, 321–328.

[115] W. S. Price, F. Tsuchiya and Y. Arata, *J. Am. Chem. Soc.*, 1999, **121**, 11503–11512.

[116] A. J. Baldwin, S. J. Anthony-Cahill, T. P. J. Knowles, G. Lippens, J. Christodoulou, P. D. Barker and C. M. Dobson, *Angew. Chem., Int. Ed.*, 2008, **47**, 3385–3387.

[117] A. J. Baldwin, R. Bader, J. Christodoulou, C. E. MacPhee, C. M. Dobson and P. D. Barker, *J. Am. Chem. Soc.*, 2006, **128**, 2162–2163.

[118] A. J. Baldwin, J. Christodoulou, P. D. Barker, C. M. Dobson and G. Lippens, *J. Chem. Phys.*, 2007, **127**, 114505.

[119] S. Viel, L. Mannina and A. Segre, *Tetrahedron Lett.*, 2002, **43**, 2515–2519.

[120] C. Sanna, C. La Mesa, L. Mannina, P. Stano, S. Viel and A. Segre, *Langmuir*, 2006, **22**, 6031–6041.

[121] A. Relini, O. Cavalleri, R. Rolandi and A. Gliozzi, *Chem. Phys. Lipids*, 2009, **158**, 1–9.

[122] E. J. Dufourc, *J. Chem. Biol.*, 2008, **1**, 63–77.

[123] S. Singer and G. Nicolson, *Science*, 1972, **175**, 720–731.

[124] W. Downham and M. Bogdanov, in *Biochemistry of Lipids, Lipoproteins and Membranes*, ed. D. E. Vance and J. E. Vance, Elsevier, Amsterdam, 4th edn., 2002, ch. Functional roles of lipids in membranes.

[125] *Textbook of Biochemistry with Clinical Correlations*, ed. T. M. Devlin, Wiley-Liss, New York, 5th edn., 2002.

[126] P. Walde, K. Cosentino, H. Engel and P. Stano, *Chembiochem*, 2010, **11**, 848–865.

[127] B. A. Cornell, G. C. Fletcher, J. Middlehurst and F. Separovic, *Biochim. Biophys. Acta*, 1982, **690**, 15–19.

[128] V. P. Torchilin and V. Weissig, *Liposomes*, Oxford University Press, Oxford, 2nd edn., 2003.

[129] C. Huang, *Biochem.*, 1969, **8**, 344–352.

[130] D. Papahadjopoulos and N. Miller, *Biochim. Biophys. Acta*, 1967, **135**, 624–638.

[131] B. Ladbrooke and D. Chapman, *Chem. Phys. Lipids*, 1969, **3**, 304–367.

[132] Y. K. Levine, *Prog. Surf. Sci.*, 1973, **3**, 279–352.

[133] J. A. Killian, *Biochim. Biophys. Acta*, 1998, **1376**, 401–415.

[134] N. Kučerka, M. A. Kiselev and P. Balgavý, *Eur. Biophys. J.*, 2004, **33**, 328–334.

[135] J. Pencer, M.-P. Nieh, T. A. Harroun, S. Krueger, C. Adams and J. Katsaras, *Biochim. Biophys. Acta*, 2005, **1720**, 84–91.

[136] J.-P. Douliez, A. Léonard and E. J. Dufourc, *J. Phys. Chem.*, 1996, **100**, 18450–18457.

[137] B. A. Lewis and D. M. Engelman, *J. Mol. Biol.*, 1983, **166**, 211–217.

[138] R. M. C. Dawson, *Biochem. J.*, 1963, **88**, 414–423.

[139] V. Bystrov, N. Dubrovina, L. Barsukov and L. Bergelson, *Chem. Phys. Lipids*, 1971, **6**, 343–350.

[140] S. B. Andrews, J. W. Faller, J. M. Gilliam and R. J. Barrnett, *Proc. Natl. Acad. Sci. U. S. A.*, 1973, **70**, 1814–1818.

[141] Y. K. Levine, A. G. Lee, N. J. Birdsall, J. C. Metcalfe and J. D. Robinson, *Biochim. Biophys. Acta*, 1973, **291**, 592–607.

[142] W. Hutton, P. Yeagle and R. Martin, *Chem. Phys. Lipids*, 1977, **19**, 255–265.

[143] J. Berden, R. Barker and G. Radda, *Biochim. Biophys. Acta*, 1975, **375**, 186–208.

[144] P. Nolden and T. Ackermann, *Biophys. Chem.*, 1976, **4**, 297–304.

[145] V. V. Kumar, B. Malewicz and W. J. Baumann, *Biophys. J.*, 1989, **55**, 789–792.

[146] C. Huang, J. P. Sipe, S. T. Chow and R. B. Martin, *Proc. Natl. Acad. Sci. U. S. A.*, 1974, **71**, 359–362.

[147] B. De Kruijff, P. Cullis and G. Radda, *Biochim. Biophys. Acta*, 1975, **406**, 6–20.

[148] S. B. Hladky, L. G. M. Gordon and D. A. Haydon, *Annu. Rev. Phys. Chem.*, 1974, **25**, 11–38.

[149] D. Z. Ting, P. S. Hagan, S. I. Chan, J. D. Doll and C. S. Springer Jr., *Biophys. J.*, 1981, **34**, 189–216.

[150] M. M. Pike, S. R. Simon, J. A. Balschi and C. S. Springer Jr., *Proc. Natl. Acad. Sci. U. S. A.*, 1982, **79**, 810–814.

[151] S. McLaughlin and M. Eisenberg, *Annu. Rev. Biophys. Bioeng.*, 1975, **4**, 335–366.

[152] M. M. Pike and C. S. Springer Jr., *J. Magn. Reson.*, 1982, **46**, 348–353.

[153] D. C. Buster, J. F. Hinton, F. S. Millett and D. C. Shungu, *Biophys. J.*, 1988, **53**, 145–152.

[154] F. Riddell and M. Hayer, *Biochim. Biophys. Acta*, 1985, **817**, 313–317.

[155] D. Shungu, D. Buster and R. Briggs, *J. Magn. Reson.*, 1990, **89**, 102–122.

[156] P. Juvvadi and E. Kalapaty, *J. Pept. Sci.*, 1998, **4**, 15–20.

[157] D. Shungu, *J. Magn. Reson.*, 1988, **77**, 491–503.

[158] C. C. Jao, B. G. Hegde, J. Chen, I. S. Haworth and R. Langen, *Proc. Natl. Acad. Sci. U. S. A.*, 2008, **105**, 19666–19671.

[159] M. Apostolidou, S. A. Jayasinghe and R. Langen, *J. Biol. Chem.*, 2008, **283**, 17205–17210.

[160] E. Sparr, M. F. M. Engel, D. V. Sakharov, M. Sprong, J. Jacobs, B. de Kruijff, J. W. M. Höppener and J. A. Killian, *FEBS Lett.*, 2004, **577**, 117–120.

[161] Y. A. Domanov and P. K. J. Kinnunen, *J. Mol. Biol.*, 2008, **376**, 42–54.

[162] B. D. van Rooijen, M. M. A. E. Claessens and V. Subramaniam, *FEBS Lett.*, 2008, **582**, 3788–3792.

[163] P. T. Wong, J. A. Schauerte, K. C. Wisser, H. Ding, E. L. Lee, D. G. Steel and A. Gafni, *J. Mol. Biol.*, 2009, **386**, 81–96.

[164] R. H. Ashley, T. A. Harroun, T. Hauss, K. C. Breen and J. P. Bradshaw, *BMC Struct. Biol.*, 2006, **6**, 21.

[165] F. Kamp and K. Beyer, *J. Biol. Chem.*, 2006, **281**, 9251–9259.

[166] A. Chattopadhyay and H. Raghuraman, *Curr. Sci.*, 2004, **87**, 175–180.

[167] L. A. Munishkina and A. L. Fink, *Biochim. Biophys. Acta*, 2007, **1768**, 1862–1885.

[168] M. Anguiano, R. J. Nowak and P. T. Lansbury, *Biochem.*, 2002, **41**, 11338–11343.

[169] T. L. Williams, I. J. Day and L. C. Serpell, *Langmuir*, 2010, **26**, 17260–17268.

[170] M. Volles and P. T. Lansbury, *Biochem.*, 2002, **41**, 4595–4602.

[171] M. Volles, S. Lee, J. Rochet and M. Shtilerman, *Biochem.*, 2001, **40**, 7812–7819.

[172] B. L. Kagan, R. Azimov and R. Azimova, *J. Membr. Biol.*, 2004, **202**, 1–10.

[173] N. Arispe, E. Rojas and H. B. Pollard, *Proc. Natl. Acad. Sci. U. S. A.*, 1993, **90**, 567–571.

[174] N. Arispe, H. B. Pollard and E. Rojas, *Proc. Natl. Acad. Sci. U. S. A.*, 1993, **90**, 10573–10577.

[175] N. Arispe, H. Pollard and E. Rojas, *Proc. Natl. Acad. Sci. U. S. A.*, 1996, **93**, 1710–1715.

[176] A. Quist, I. Doudevski, H. Lin, R. Azimova, D. Ng, B. Frangione, B. Kagan, J. Ghiso and R. Lal, *Proc. Natl. Acad. Sci. U. S. A.*, 2005, **102**, 10427–10432.

[177] H. Lin, R. Bhatia and R. Lal, *FASEB J.*, 2001, **15**, 2433–2444.

[178] H. A. Lashuel, D. Hartley, B. M. Petre, T. Walz and P. T. Lansbury Jr, *Nature*, 2002, **418**, 291.

[179] H. A. Lashuel, B. M. Petre, J. Wall, M. Simon, R. J. Nowak, T. Walz and P. T. Lansbury Jr, *J. Mol. Biol.*, 2002, **322**, 1089–1102.

[180] J. Seelig, *Biochim. Biophys. Acta*, 1978, **515**, 105–140.

[181] T. Lau, E. Ambroggio, D. Tew, R. Cappai, C. Masters, G. Fidelio, K. Barnham and F. Separovic, *J. Mol. Biol.*, 2006, **356**, 759–770.

[182] J. Madine, A. J. Doig and D. A. Middleton, *Biochem.*, 2006, **45**, 5783–5792.

[183] P. Cullis and B. De Kruijff, *Biochim. Biophys. Acta*, 1978, **507**, 207–218.

[184] E. Terzi, G. Hölzemann and J. Seelig, *Biochem.*, 1997, **36**, 14845–14852.

[185] J. D. Gehman, C. C. O'Brien, F. Shabanpoor, J. D. Wade and F. Separovic, *Eur. Biophys. J.*, 2008, **37**, 333–344.

[186] GE Healthcare, *Gel filtration: Principles and Methods*, 2010.

[187] Sigma-Aldrich, *Sephadex G-50 Superfine*, http://www.sigmaaldrich.com/catalog/product/sigma/g5050?lang=en&region=GB, Accessed 16th November 2012.

[188] Sigma-Aldrich, *Sunset Yellow FCF*, http://www.sigmaaldrich.com/catalog/product/aldrich/465224?lang=en&region=GB, Accessed 2nd January 2013.

[189] F. Delaglio, S. Grzesiek, G. W. Vuister, G. Zhu, J. Pfeifer and A. Bax, *J. Biomol. NMR*, 1995, **6**, 277–293.

[190] D. Hoult, *J. Magn. Reson.*, 1976, **21**, 337–347.

[191] G. Zheng and W. S. Price, *Prog. Nucl. Magn. Reson. Spectrosc.*, 2010, **56**, 267–288.

[192] M. D. Pelta, G. A. Morris, M. J. Stchedroff and S. J. Hammond, *Magn. Reson. Chem.*, 2002, **40**, S147–S152.

[193] M. D. Pelta, H. Barjat, G. A. Morris, A. L. Davis and S. J. Hammond, *Magn. Reson. Chem.*, 1998, **36**, 706–714.

[194] S. Viel, F. Ziarelli and S. Caldarelli, *Proc. Natl. Acad. Sci. U. S. A.*, 2003, **100**, 9696–9698.

[195] R. E. Hoffman, H. Arzuan, C. Pemberton, A. Aserin and N. Garti, *J. Magn. Reson.*, 2008, **194**, 295–299.

[196] K. F. Morris, P. Stilbs and C. S. Johnson Jr., *Anal. Chem.*, 1994, **66**, 211–215.

[197] R. Evans, S. Haiber, M. Nilsson and G. A. Morris, *Anal. Chem.*, 2009, **81**, 4548–4550.

[198] J. S. Kavakka, I. Kilpeläinen and S. Heikkinen, *Org. Lett.*, 2009, **11**, 1349–1352.

[199] J. S. Kavakka, V. Parviainen, K. Wähälä, I. Kilpeläinen and S. Heikkinen, *Magn. Reson. Chem.*, 2010, **48**, 777–781.

[200] S. Viel, G. Excoffier and F. Ziarelli, *Diff. Fund.*, 2007, **6**, 7–8.

[201] G. Pages, C. Delaurent and S. Caldarelli, *Angew. Chem., Int. Ed.*, 2006, **45**, 5950–5953.

[202] S. Caldarelli, *Magn. Reson. Chem.*, 2007, **45**, S48–S55.

[203] C. Pemberton, R. E. Hoffman, A. Aserin and N. Garti, *Langmuir*, 2011, **27**, 4497–4504.

[204] M. E. Zielinski and K. F. Morris, *Magn. Reson. Chem.*, 2009, **47**, 53–56.

[205] C. F. Tormena, R. Evans, S. Haiber, M. Nilsson and G. A. Morris, *Magn. Reson. Chem.*, 2010, **48**, 550–553.

[206] F. Asaro and N. Savko, *Magn. Reson. Chem.*, 2011, **49**, 195–198.

[207] R. E. Hoffman, A. Aserin and N. Garti, *J. Magn. Reson.*, 2012, **220**, 18–25.

[208] W. Yau, *Modern Size-Exclusion Liquid Chromatography*, John Wiley & Sons, New York, 1979.

[209] R. E. Joyce and I. J. Day, *J. Magn. Reson.*, 2012, **220**, 1–7.

[210] I. Teraoka, *Polymer Solutions: An Introduction to Physical Properties*, John Wiley & Sons, New York, 2002.

[211] P. Keifer, L. Baltusis, D. Rice, A. Tymiak and J. Shoolery, *J. Magn. Reson. A*, 1996, **75**, 65–75.

[212] C. Pemberton, R. Hoffman, A. Aserin and N. Garti, *J. Magn. Reson.*, 2011, **208**, 262–269.

[213] S. Viel, D. Capitani, L. Mannina and A. Segre, *Biomacromolecules*, 2003, **4**, 1843–1847.

[214] C. Carrara, S. Viel, C. Delaurent, F. Ziarelli, G. Excoffier and S. Caldarelli, *J. Magn. Reson.*, 2008, **194**, 303–306.

[215] P. T. Callaghan and D. N. Pinder, *Macromolecules*, 1985, **18**, 373–379.

[216] A. A. Bhalekar and J. B. F. N. Engberts, *Colloid Polym. Sci.*, 1993, **271**, 1068–1075.

[217] S. Ohashi, *Pure Appl. Chem.*, 1975, **44**, 415–438.

[218] J. N. Israelachvili, *Intermolecular and Surface Forces*, Academic Press, London, 1985.

[219] G. Paradossi, F. Cavalieri, E. Chiessi, C. Mondelli and M. Telling, *Chem. Phys.*, 2004, **302**, 143–148.

[220] L. Hagel, M. Ostberg and T. Andersson, *J. Chromatogr. A*, 1996, **743**, 33–42.

[221] H. Determann and W. Michel, *J. Chromatogr. A*, 1966, **25**, 303–313.

[222] D. Anderson and J. Stoddart, *Anal. Chim. Acta*, 1966, **34**, 401–406.

[223] J. V. Dawkins, *J. Polym. Sci. Polym. Phys. Ed.*, 1976, **14**, 569–571.

[224] T. Chang, *Anal. Chim. Acta*, 1968, **42**, 51–57.

[225] T. Kremmer and L. Boross, *Gel Chromatography*, John Wiley & Sons, Chichester, 1979.

[226] M. Stoll and T. Majors, *Phys. Rev. B*, 1981, **24**, 5–8.

[227] S. A. Bradley, J. Paschal and P. Kulanthaivel, *Magn. Reson. Chem.*, 2005, **43**, 31–35.

[228] S. Viel, F. Ziarelli and C. Carrara, *J. Magn. Reson.*, 2008, **190**, 113–123.

[229] J. M. Wieruszeski, G. Montagne, G. Chessari, P. Rousselot-Pailley and G. Lippens, *J. Magn. Reson.*, 2001, **152**, 95–102.

[230] T. D. W. Claridge, *High-Resolution NMR Techniques in Organic Chemistry*, Elsevier Ltd, Amsterdam, 2nd edn., 2009.

[231] R. E. Joyce and I. J. Day, *J. Phys. Chem. C.*, 2013, **117**, 17503–17508.

[232] S. K. Prasad, G. G. Nair, G. Hegde and V. Jayalakshmi, *J. Phys. Chem. B*, 2007, **111**, 9741–9746.

[233] H.-S. Park, S.-W. Kang, L. Tortora, Y. Nastishin, D. Finotello, S. Kumar and O. D. Lavrentovich, *J. Phys. Chem. B*, 2008, **112**, 16307–16319.

[234] S. Zhou, Y. Nastishin, M. Omelchenko, L. Tortora, V. Nazarenko, O. Boiko, T. Ostapenko, T. Hu, C. Almasan, S. Sprunt, J. Gleeson and O. Lavrentovich, *Phys. Rev. Lett.*, 2012, **109**, 1–5.

[235] F. Chami and M. R. Wilson, *J. Am. Chem. Soc.*, 2010, **132**, 7794–7802.

[236] GE Healthcare Life Sciences, *Sephadex Chromatography Media*, http://www.gelifesciences.com/webapp/wcs/stores/servlet/catalog/en/GELifeSciences-uk/products/AlternativeProductStructure_17400/, Accessed 2nd November 2012.

[237] Sigma-Aldrich, *Sephadex G-75 Superfine*, http://www.sigmaaldrich.com/catalog/product/sigma/g7550?lang=en&region=GB, Accessed 16th November 2012.

[238] Sigma-Aldrich, *Sephadex G-100 Superfine*, http://www.sigmaaldrich.com/catalog/product/sigma/g10050?lang=en&region=GB, Accessed 16th November 2012.

[239] GE Healthcare Life Sciences, *Sephadex G-75 Superfine*, http://www.gelifesciences.com/webapp/wcs/stores/servlet/catalog/en/GELifeSciences-uk/products/AlternativeProductStructure_17400/17005101.

[240] GE Healthcare Life Sciences, *Sephadex G-100 Superfine*, http://www.gelifesciences.com/webapp/wcs/stores/servlet/catalog/en/GELifeSciences-uk/products/AlternativeProductStructure_17400/17006101.

[241] H. P. Erickson, *Biol Proced Online*, 2009, **11**, 32–51.

[242] G. H. Sørland, J. G. Seland, J. Krane and H. W. Anthonsen, *J. Magn. Reson.*, 2000, **142**, 323–325.

[243] E. Pryor, J. A. Kotarek, M. A. Moss and C. N. Hestekin, *Int. J. Mol. Sci.*, 2011, **12**, 9369–9388.

[244] F. Dische, C. Wernstedt, G. Westermark, P. Westermark, M. Pepys, J. Rennie, S. Gilbey and P. Watkins, *Diabetologia*, 1988, **31**, 158–161.

[245] S. Yumlu, R. Barany, M. Eriksson and C. Röcken, *Hum. Pathol.*, 2009, **40**, 1655–1660.

[246] Y. Shikama, J.-I. Kitazawa, N. Yagihashi, O. Uehara, Y. Murata, N. Yajima, R. Wada and S. Yagihashi, *Intern. Med.*, 2010, **49**, 397–401.

[247] J. Brange, L. Andersen, E. D. Laursen, G. Meyn and E. Rasmussen, *J. Pharm. Sci.*, 1997, **86**, 517–525.

[248] E. J. Nettleton, P. Tito, M. Sunde, M. Bouchard, C. M. Dobson and C. V. Robinson, *Biophys. J.*, 2000, **79**, 1053–1065.

[249] L. N. Garriques, S. Frokjaer, J. F. Carpenter and J. Brange, *J. Pharm. Sci.*, 2002, **91**, 2473–2480.

[250] Q.-X. Hua and M. A. Weiss, *J. Biol. Chem.*, 2004, **279**, 21449–21460.

[251] D. F. Waugh, *J. Am. Chem. Soc.*, 1946, **68**, 247–250.

[252] V. du Vigneaud, R. H. Sifferd and R. R. Sealock, *J. Biol. Chem.*, 1933, **102**, 521–533.

[253] M. J. Burke and M. A. Rougvie, *Biochem.*, 1972, **11**, 2435–2439.

[254] M. Sorci, R. A. Grassucci, I. Hahn, J. Frank and G. Belfort, *Proteins*, 2009, **77**, 62–73.

[255] D. Waugh, *J. Am. Chem. Soc.*, 1944, **66**, 663.

[256] D. Waugh, *J. Am. Chem. Soc.*, 1948, **111**, 1850–1857.

[257] D. F. Waugh, R. E. Thompson and R. J. Weimer, *J. Biol. Chem.*, 1950, **185**, 85–95.

[258] D. F. Waugh, D. F. Wilhemson, S. L. Commerford and M. L. Sackler, *J. Am. Chem. Soc.*, 1953, **1048**, 2592–2600.

[259] F. Sanger, E. O. Thompson and R. Kitai, *Biochem. J.*, 1955, **59**, 509–518.

[260] A. Aguzzi and T. O'Connor, *Nat. Rev. Drug Discov.*, 2010, **9**, 237–248.

[261] Y. J. Zhu, H. Lin and R. Lal, *FASEB J.*, 2000, **14**, 1244–1254.

[262] R. El Jastimi, K. Edwards and M. Lafleur, *Biophys. J.*, 1999, **77**, 842–852.

[263] S. Thennarasu, D.-K. Lee, A. Poon, K. E. Kawulka, J. C. Vederas and A. Ramamoorthy, *Chem. Phys. Lipids*, 2005, **137**, 38–51.

[264] A. Andersson, J. Danielsson, A. Gräslund and L. Mäler, *Eur. Biophys. J.*, 2007, **36**, 621–635.

[265] H. Heerklotz and J. Seelig, *Eur. Biophys. J.*, 2007, **36**, 305–314.

[266] A. Chrzeszczyk, A. Wishnia and C. S. Springer Jr., *Biochim. Biophys. Acta*, 1977, **470**, 161–169.

[267] R. Cushley and B. Forrest, *Can. J. Chem.*, 1977, **16**, 220–226.

[268] S. A. Murphree, D. Murphy, A. Sartorelli and T. R. Tritton, *Biochim. Biophys. Acta*, 1982, **691**, 97–105.

[269] A. C. McLaughlin, P. R. Cullis, J. A. Berden and R. E. Richards, *J. Magn. Reson.*, 1975, **20**, 146–165.

[270] G. Da Costa, L. Mouret, S. Chevance, E. Le Rumeur and A. Bondon, *Eur. Biophys. J.*, 2007, **36**, 933–942.

[271] H. Hauser, E. G. Finer and D. Chapman, *J. Mol. Biol.*, 1970, **53**, 419–433.

[272] J. A. Berden, P. R. Cullis, D. I. Hoult, A. C. McLaughlin, G. K. Radda and R. E. Richards, *FEBS Lett.*, 1974, **46**, 55–58.

[273] M. Hope, M. Bally and G. Webb, *Biochim. Biophys. Acta*, 1985, **812**, 55–65.

[274] L. Mayer, M. Hope and P. Cullis, *Biochim. Biophys. Acta*, 1986, **858**, 161–168.

[275] B. J. Frisken, C. Asman and P. J. Patty, *Langmuir*, 2000, **16**, 928–933.

[276] S. Johnson, A. Bangham, M. Hill and E. Korn, *Biochim. Biophys. Acta*, 1971, **233**, 820–826.

[277] F. Szoka and D. Papahadjopoulos, *Annu. Rev. Biophys. Bioeng.*, 1980, **9**, 467–508.

[278] Malvern Instruments Ltd, *Dynamic Light Scattering : An Introduction in 30 Minutes*, Technical Note MRK656-01.

[279] J. R. Silvius, in *Lipid-Protein Interactions Volume 2*, ed. P. C. Jost and O. H. Griffith, John Wiley & Sons, New York, 1982.

[280] W. Pitcher III and W. Huestis, *Biochem. Biophys. Res. Commun.*, 2002, **296**, 1352–1355.

[281] M. Kiselev, T. Gutberlet, A. Hoell, V. Aksenov and D. Lombardo, *Chem. Phys.*, 2008, **345**, 181–184.

[282] Y. Su, R. Mani and M. Hong, *J. Am. Chem. Soc.*, 2008, **130**, 8856–8864.

[283] F. A. Nezil, S. Bayerl and M. Bloom, *Biophys. J.*, 1992, **61**, 1413–1426.

[284] O. Cruciani, L. Mannina, A. P. Sobolev, C. Cametti and A. Segre, *Molecules*, 2006, **11**, 334–344.

[285] B. S. Brown, *Biological Membranes*, The Biochemical Society, London, 1996.

[286] Avanti Polar Lipids, Inc., *Phase Transition Temperatures for Glycophospholipids*, http://avantilipids.com/index.php?option=com_content&view=article&id=1700&Itemid=419, Accessed 26th January 2013.

[287] J. L. Thewalt and M. Bloom, *Biophys. J.*, 1992, **63**, 1176–1181.

[288] E. Schnitzer, M. M. Kozlov and D. Lichtenberg, *Chem. Phys. Lipids*, 2005, **135**, 69–82.

[289] P. L. Yeagle, W. C. Hutton, C. Huang and R. B. Martin, *Proc. Natl. Acad. Sci. U. S. A.*, 1975, **72**, 3477–3481.

[290] A. Sakanishi, S. Mitaku and A. Ikegami, *Biochem.*, 1979, **18**, 2636–2642.

[291] B. De Kruijff, P. Cullis and G. Radda, *Biochim. Biophys. Acta*, 1976, **436**, 729–740.

[292] V. Kumar and W. Baumann, *Biochem. Biophys. Res. Commun.*, 1986, **139**, 25–30.

[293] Z. M. Anwar and H. A. Azab, *J. Chem. Eng. Data*, 2001, **46**, 613–618.

[294] M. Sokolowska and W. Bal, *J. Inorg. Biochem.*, 2005, **99**, 1653–1660.

[295] V. Hietapelto, R. S. Laitinen, J. Pursiainen and E. Rahkamaa, *Acta Chem. Scand.*, 1999, **53**, 7–14.

[296] K. Choi, J. Oh and Y. Lee, *Microchem. J.*, 1997, **55**, 357–366.

[297] C. E. Housecroft and E. C. Constable, *Chemistry*, Pearson Education Limited, Harlow, 3rd edn., 2006.

[298] Sigma-Aldrich, *Tris(hydroxymethyl)aminomethane*, http://www.sigmaaldrich.com/catalog/product/sial/252859?lang=en&region=GB, Accessed 14th February 2013.

[299] Sigma-Aldrich, *HEPES*, http://www.sigmaaldrich.com/catalog/product/sigma/h3375?lang=en&region=GB, Accessed 14th February 2013.

[300] D. Lichtenberg, R. Robson and E. Dennis, *Biochim. Biophys. Acta*, 1983, **737**, 285–304.

[301] M. le Maire, P. Champeil and J. V. Moller, *Biochim. Biophys. Acta*, 2000, **1508**, 86–111.

[302] M. T. Paternostre, M. Roux and J. L. Rigaud, *Biochem.*, 1988, **27**, 2668–2677.

[303] M. A. Partearroyo, M. A. Urbaneja and F. M. Gofii, *FEBS Lett.*, 1992, **302**, 138–140.

[304] A. de la Maza and J. L. Parra Juez, *J. Am. Oil Chem. Soc.*, 1993, **70**, 699–706.

[305] A. Memoli, L. Palermiti, V. Travagli and F. Alhaique, *Int. J. Pharm.*, 1995, **117**, 159–163.

[306] H. Ahyayauch, M. I. Collado, F. M. Goñi and D. Lichtenberg, *FEBS Lett.*, 2009, **583**, 2859–2864.

[307] T. M. Allen and L. G. Cleland, *Biochim. Biophys. Acta*, 1980, **597**, 418–426.

[308] M. R. R. de Planque, V. Raussens, S. A. Contera, D. T. S. Rijkers, R. M. J. Liskamp, J.-M. Ruysschaert, J. F. Ryan, F. Separovic and A. Watts, *J. Mol. Biol.*, 2007, **368**, 982–997.

[309] M. Sakono and T. Zako, *FEBS J.*, 2010, **277**, 1348–1358.

[310] R. Kayed, Y. Sokolov, B. Edmonds, T. M. McIntire, S. C. Milton, J. E. Hall and C. G. Glabe, *J. Biol. Chem.*, 2004, **279**, 46363–46366.

[311] A. Demuro, E. Mina, R. Kayed, S. C. Milton, I. Parker and C. G. Glabe, *J. Biol. Chem.*, 2005, **280**, 17294–17300.

[312] D. M. Walsh, I. Klyubin, J. V. Fadeeva, W. K. Cullen, R. Anwyl, M. S. Wolfe, M. J. Rowan and D. J. Selkoe, *Nature*, 2002, **416**, 535–539.

[313] M. Townsend, G. M. Shankar, T. Mehta, D. M. Walsh and D. J. Selkoe, *J. Physiol.*, 2006, **572**, 477–492.

[314] T. Bliss and G. Collingridge, *Nature*, 1993, **361**, 31–39.

[315] J. Weinstein, S. Yoshikami, P. Henkart, R. Blumenthal and W. Hagins, *Science*, 1977, **195**, 489–492.

[316] J. Wilschut, N. Duzgunes, R. Fraley and D. Papahadjopoulos, *Biochem.*, 1980, **19**, 6011–6021.

[317] Q. Fan, A. Relini, D. Cassinadri and A. Gliozzi, *Biochim. Biophys. Acta*, 1995, **1240**, 83–88.

[318] P. Tian, J. Ball, C. Zeng and M. Estes, *J. Virol.*, 1996, **70**, 6973–6981.

[319] T. Miura, K. Suzuki, N. Kohata and H. Takeuchi, *Biochem.*, 2000, **39**, 7024–7031.

[320] V. Minicozzi, F. Stellato, M. Comai, M. Dalla Serra, C. Potrich, W. Meyer-Klaucke and S. Morante, *J. Biol. Chem.*, 2008, **283**, 10784–10792.

[321] F. Thomas, G. Serratrice, C. Béguin, E. S. Aman, J. L. Pierre, M. Fontecave and J. P. Laulhere, *J. Biol. Chem.*, 1999, **274**, 13375–13383.

[322] S. Saito, T. Anada, S. Hoshi and K. Akatsuka, *Anal. Chem.*, 2005, **77**, 5332–5338.

Appendix A

Publications

A.1 Chromatographic NMR with size exclusion chromatography stationary phases

Rebecca E. Joyce and Iain J. Day
Journal of Magnetic Resonance
Year: 2012
Volume: 220
Pages: 1–7
Doi:10.1016/j.jmr.2012.04.017

A.2 In Situ Size Exclusion Chromatographic NMR of Sunset Yellow FCF in Solution

Rebecca E. Joyce and Iain J. Day
The Journal of Physical Chemistry C
Year: 2013
Volume: 117
Pages: 17503–17508
Doi:10.1021/jp4018794

Appendix B

Sunset Yellow NMR Data

B.1 ^{1}H Spectrum

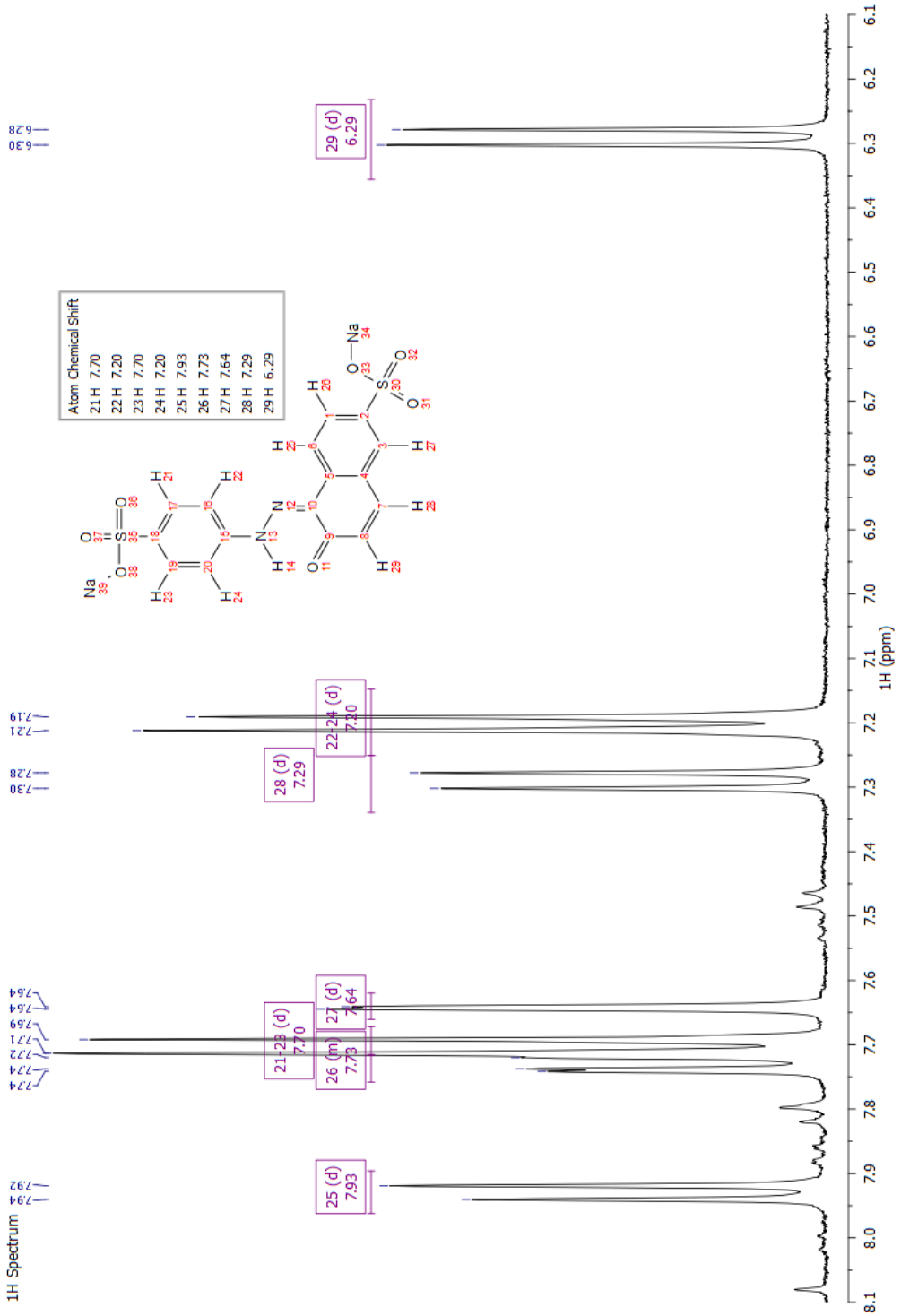

B.2 ^{13}C Spectrum

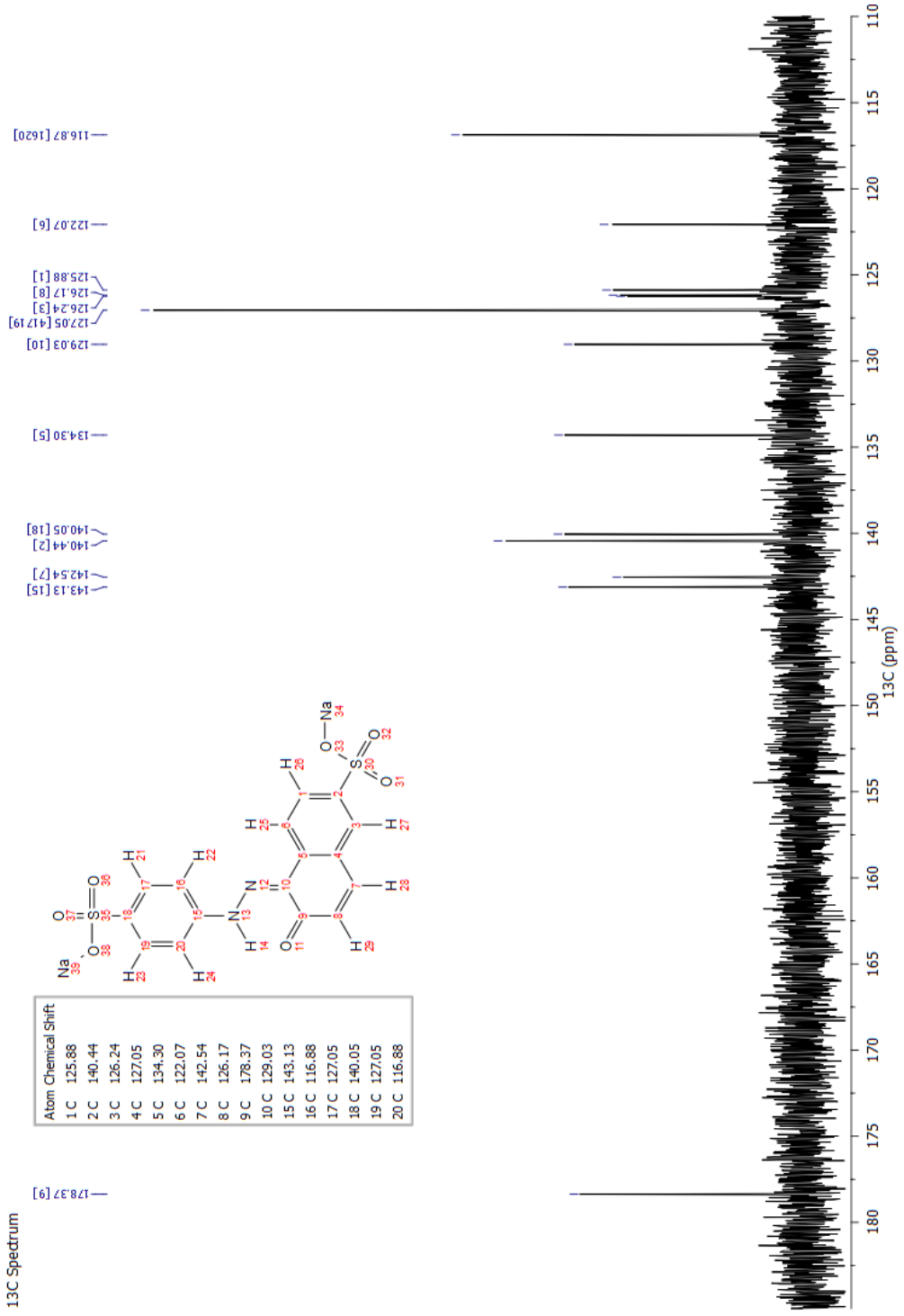

B.3 COSY Spectrum

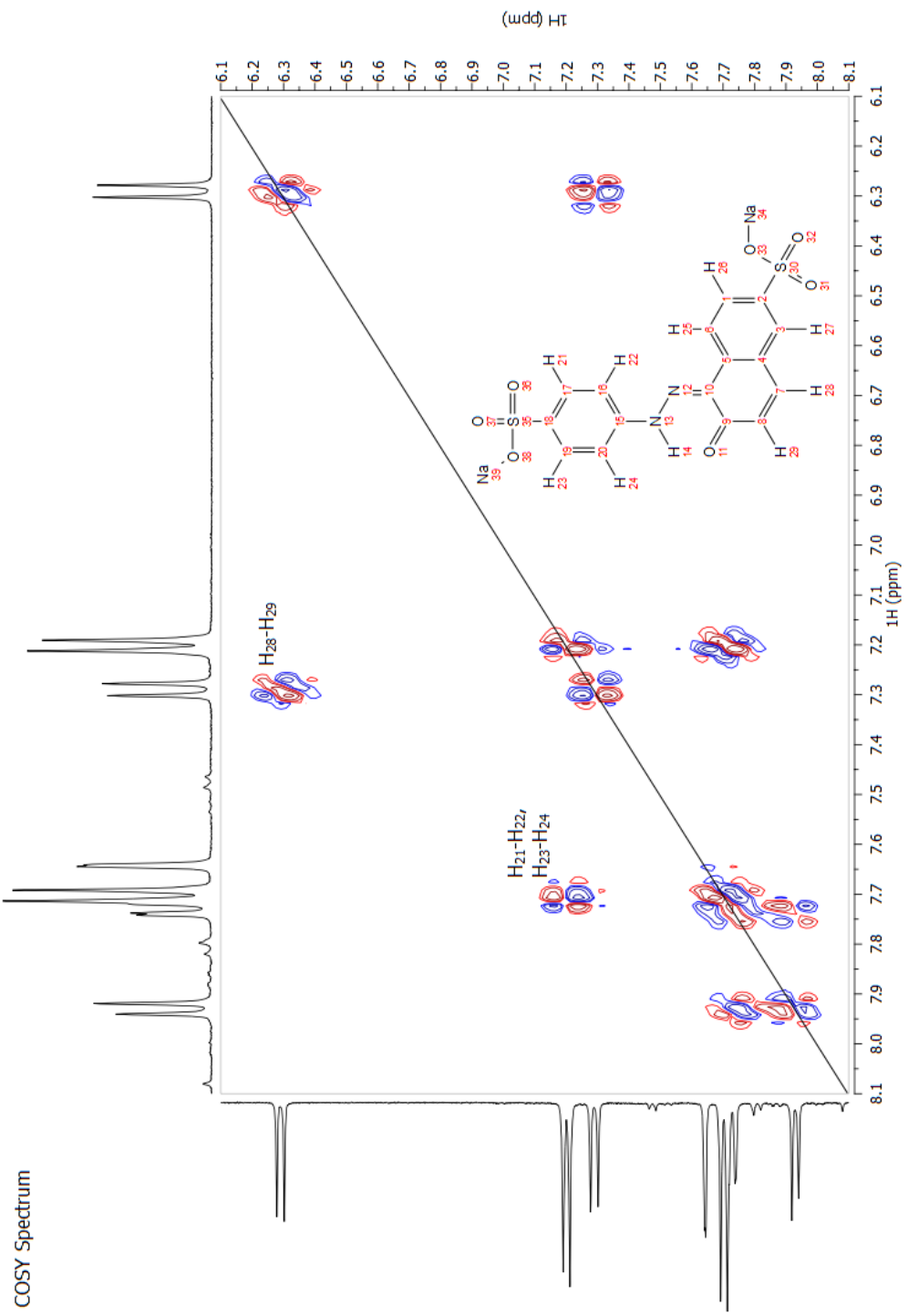

B.4 HSQC Spectrum

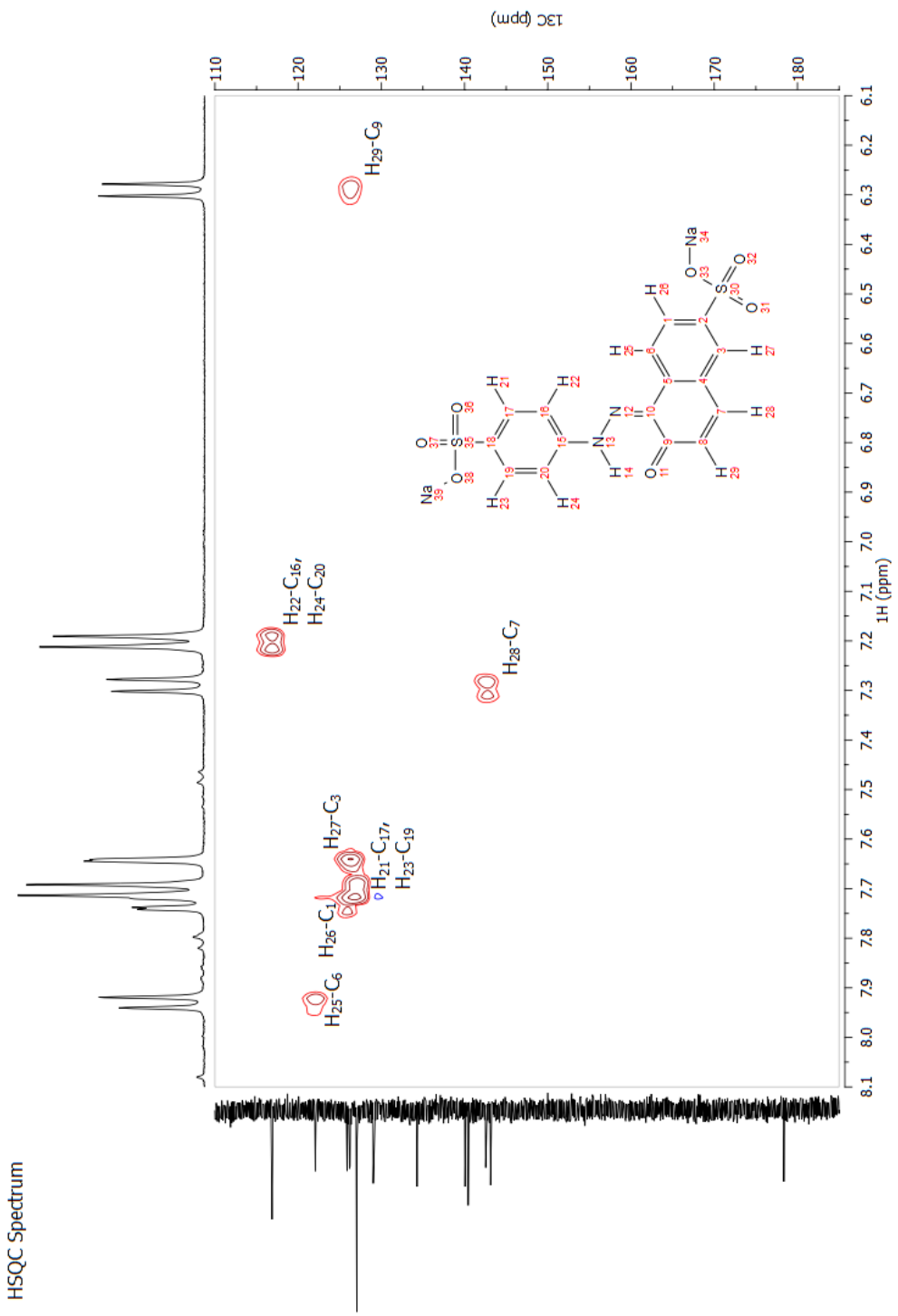

B.5 HMBC Spectrum